AWARD NUMBER: W81XWH-16-1-0073

TITLE: Targeting Breast Cancer Micrometastases: To Eliminate the Seeds of Evil

PRINCIPAL INVESTIGATOR: Xiang Zhang

CONTRACTING ORGANIZATION: Baylor College of Medicine, Houston, TX

REPORT DATE: January 2022

TYPE OF REPORT: Final

PREPARED FOR: U.S. Army Medical Research and Materiel Command
Fort Detrick, Maryland 21702-5012

REPORT DOCUMENTATION PAGE

Form Approved
OMB No. 0704-0188

1. REPORT DATE	**2. REPORT TYPE**	**3. DATES COVERED**
January 2022	Final	15Mar2016-14Sep2021

4. TITLE AND SUBTITLE

Targeting Breast Cancer Micrometastases: To Eliminate the Seeds of Evil

5a. CONTRACT NUMBER
W81XWH-16-1-0073

5b. GRANT NUMBER
BC150085

5c. PROGRAM ELEMENT NUMBER

6. AUTHOR(S)

Xiang Zhang

E-Mail: xiangz@bcm.edu

5d. PROJECT NUMBER

5e. TASK NUMBER

5f. WORK UNIT NUMBER

7. PERFORMING ORGANIZATION NAME(S) AND ADDRESS(ES)

Baylor College of Medicine
One Baylor Plaza
Houston, TX, 77030

8. PERFORMING ORGANIZATION REPORT NUMBER

9. SPONSORING / MONITORING AGENCY NAME(S) AND ADDRESS(ES)

U.S. Army Medical Research and Materiel Command
Fort Detrick, Maryland 21702-5012

10. SPONSOR/MONITOR'S ACRONYM(S)

11. SPONSOR/MONITOR'S REPORT NUMBER(S)

12. DISTRIBUTION / AVAILABILITY STATEMENT

Approved for Public Release; Distribution Unlimited

13. SUPPLEMENTARY NOTES

14. ABSTRACT A substantial proportion of breast cancer patients develop metastases despite surgeries and adjuvant therapies. Metastasis is incurable and responsible for over 90% of breast cancer-related death. Thus, the prevention of metastasis is an imperative clinical need. We seek to understand how microscopic metastases in distant organs (e.g., bone), before becoming overt malignancies, survive and progress by interacting with specific normal cells in that organ. The rationale is that such interaction may confer resistance to current adjuvant therapies and may also render the cancer cells vulnerable to novel treatments. To date, very few pre-clinical models of micrometastases exist. We have filled this gap by developing a series of techniques that allow us to monitor and quantitate the progression of micrometastases. In this application, we will further establish the authenticity of these models in reflecting biological properties of micrometastases. We will also use them to identify therapies that may eliminate metastatic seeds, especially in the bone. We will examine all breast cancer subtypes with an emphasis on estrogen receptor-positive breast cancer and investigate how the bone environment influences cancer cells' response to endocrine therapies. Specifically the three goals are: 1) To assess the differential responses of bone micrometastases to adjuvant therapies as compared to their parental tumors in the mammary gland, and dissect if and how such differences are attributable to the interaction with their adjacent normal cells.; 2) to further establish an experimental platform called "Bone-in-culture array" (BICA) that can mimic bone micrometastases and allow rapid testing of drug efficacies; and 3) to perform drug screening/discoveries to identify compounds that can be combined with current standard-of-care and eradicate bone micrometastases. The fulfillment of these goals will provide novel strategies that may significantly reduce bone or possibly other metastases in breast cancer. Moreover, the same techniques can be easily applied to other cancer, including lung cancer and some pediatric sarcomas.

15. SUBJECT TERMS
None listed.

16. SECURITY CLASSIFICATION OF:			**17. LIMITATION OF ABSTRACT**	**18. NUMBER OF PAGES**	**19a. NAME OF RESPONSIBLE PERSON**
a. REPORT	**b. ABSTRACT**	**c. THIS PAGE**			USAMRMC
Unclassified	Unclassified	Unclassified	Unclassified	86	**19b. TELEPHONE NUMBER** *(include area code)*

Table of Contents

Page

1. Introduction

In this project we aim to overcome the challenge of eliminating microscopic metastases of breast cancer, so that distant recurrences and related deaths can be significantly reduced in the foreseeable future. We will focus on bone micrometastases (BMM), which are precursors of overt bone metastases and possibly other metastases. In particular, we will delineate how breast cancer cells, when isolated in small quantity in a foreign milieu, react to therapies differently compared to the original primary tumor. We have designed and will continue to optimize various pre-clinical models to investigate the microenvironmental effects on BMM. These models will enable medium-throughput drug discovery/repositioning to expedite the elimination of breast cancer cells in the context of bone. The methodology may also be applied to metastases in other sites.

In the clinic, primary breast tumors are usually surgically removed soon after diagnosis, often leaving patients "tumor-free". However, 20-40% of breast cancer survivors will eventually suffer metastasis to distant organs, sometimes years after surgeries. Thus, the life-threatening enemy is typically not the bulk of primary tumors, but the dispersed metastatic seeds left behind, which have already disseminated to distant organs, may be temporarily dormant, and may resume aggressive outgrowth under certain yet-to-be-identified conditions. Current adjuvant therapies intend to eliminate these cells. However, the therapeutic decisions and strategies are usually based upon pathological features of primary tumors. Micrometastases are likely to differ from their parental primary tumors due to Darwinian selection and/or adaptation in a different milieu. In either case, the microenvironment in distant organs plays a critical role in driving the selection and/or in shaping the adaptive reaction of cancer cells. It is our vision that a critical barrier in curing breast cancer is the lack of knowledge about micrometastases and their microenvironment niches. Specifically, the key questions are the nature of the supporting pathways uniquely induced by cancer-niche interaction, and the mechanisms responsible for differential therapeutic responses as compared to parental primary tumors. To overcome this barrier, I propose to establish a series of pre-clinical models that recapitulate the cellular nature of micrometastases, mimic their habitat and allow expedited testing of their drug responses.

Three specific aims will be pursued. 1. To assess the differential responses of BMM to adjuvant therapies as compared to their parental tumors in the mammary gland, and dissect if and how such differences are attributable to the interaction with the microenvironment niche. 2. To establish the bone-in-culture array (BICA) platform, which aims to faithfully recapitulate the molecular profile, cell-biological behaviors, microenvironment niche, and therapeutic responses of BMM in vivo, and is amenable to medium-to-high throughput drug discovery/screening. 3. To identify and mechanistically investigate therapies against BMM by analyzing the omics data obtained from previous goals, and by screening pre-established libraries of FDA-approved drugs or small molecule inhibitors (SMIs).

2. Keywords:

Metastasis, microenvironment, drug discovery, therapeutic resistance, micrometastases, endocrine resistance

3. Accomplishment

All tasks have been accomplished within the grant period. Detailed results can be found in previous reports. In this final report, I would like to summarize the key findings made in the past five years under the support of this Era of Hope Award. In particular, bone molecular mechanisms and the corresponding therapeutic insights are tabulated. I am confident to say that this body of work has brought significant breakthroughs to breast cancer research. I am sincerely grateful for the support from DoD BCRP. Future investigations will continue to push the findings here to the clinic and hopefully lead to practice-changing advances.

Major Task 1 : Differential drug responses of bone micrometastases (BMM) as compared to the parental orthotopic tumors

Subtask 1: Tumor burden measurement (Month 1-24). We expect to use five PDXs (2 ER+, 1 Her2+ and 2 triple negative) and five cell lines (the same subtype distribution). The total # of models will be 10. Each model

will need 55 mice. PDXs will be transplanted into SCID/Beige mice and cell lines will be transplanted into Athymic nu/nu mice. These mice will be divided into treated and untreated. Treatments: tamoxifen, fulvestrant, ovariectomy, and lapatinib. Measurement: Weekly bioluminescence imaging and tumor volume measurement. Some mice will be euthanized at intermediate time points for Subtasks 2 and 3 below.

This subtask has been accomplished, as reported in previous years.

Subtask 2: Immunofluorescence staining to quantitate proliferation (e.g., Ki67+), survival (e.g., CC3) and self renewal (e.g., retention of H2B-GFP) (Month 1-18).
This subtask has been accomplished, as reported in previous years.

Major Task 2: Test if the abolishment of cancer-niche interaction in conditional N-cadherin KO mice reverses the therapeutic responses of BMM.

Subtask 1: Mouse breeding to generate animals with various genetic background (including immunodeficiency). We will breed TetO-Osx-cre-GFP with $Cdh2^{f/f}$ mice both purchased from Jackson Laboratories (Stock No: 006361 and 007611, respectively) to generate offsprings with both genetic alterations. The mice will also be crossed with Rag1-/- mice (Stock No: 002216) to generate immunodeficiency for human cancer cell transplantation. (Month 1-24).

This subtask has been accomplished, as reported in previous years.

Subtask 2: Repeat experiments in Major Task 1 in the conditional N-cadherin KO models, and Test if the abolishment of cancer-niche interaction in conditional N-cadherin KO mice reverses the therapeutic responses of BMM. TetO-Osx-cre-GFP; $Cdh2^{f/f}$ mice and TetO-Osx-cre-GFP; Cdh2f/f; Rag1-/- mice and their littermate female mice lacking Osx-Cre will be subjected to experiments as in Task #1. About 700 mice will be bred at this stage. Except that a few male mice carrying the wanted phenotype will be kept for strain maintaining, most male mice (estimated to be 340) will be euthanized right after genotyping. (Month 24-36)

This subtask has been accomplished, as reported in previous years.

Major Task 3: To establish and validate BICA

Subtask 1 : Characterize the cell-biological features of cancer cells in BICA (e.g., proliferation, self-renewal, and survival). We expect to use five PDXs (2 ER+, 1 Her2+ and 2 triple negative) and five cell lines (the same subtype distribution). The total # of models will be 10. Each model will need 20 mice. PDXs will be transplanted into SCID/Beige mice and cell lines will be transplanted into Athymic nu/nu mice. (Month 1-18)

This subtask has been finished, and results were updated in previous reports.

Subtask 2: To characterize the microenvironment niche in BICA using different subtypes of cancer models. This will be achieved by immunohistochemical and immunofluorescence staining of the following markers: ALP, Col-I, CTSK, Osterix, Runx2, CD31, NG2, and SOX9. The same numbers and PDXs and cell lines will be used as specified in Subtask 1 above. (Month 1-24).

This subtask has been finished, and results were updated in previous reports.

Subtask 3: To perform RNA-seq of cancer cells in BICA, and compared the profiles to cancer cells in intact bones and in mammary glands. For this task we will use 2 PDX (1 ER+ and 1 Her2+) and 2 cell lines (1ER+ and 1 Her2+). Each will be injected into 25 animals (5 for orthotopic tumors, 10 for intact bone metastases, and 10 for BICA). (Month 18-36)

This subtask has been finished, and results were updated in previous reports.

Subtask 4: To determine the therapeutic responses of cancer cells in BICA as compared to those of BMM in vivo and cancer cells in culture. We expect to use five PDXs (2 ER+, 1 Her2+ and 2 triple negative) and five cell lines (the same subtype distribution). The total # of models will be 10. Each model will need 50 mice. PDXs will be transplanted into SCID/Beige mice and cell lines will be transplanted into Athymic nu/nu mice. (Month 30-48)

This subtask has been accomplished, as reported in previous years.

Major Task 4: Analyze the RNA-seq data obtained from Specific Aim 1 to identify and validate candidate pathway/genes that can be targeted to eliminate BMMs

Subtask 1: Bioinformatics analyses to identify candidate pathways/genes. (Month 1-36)

This subtask has been accomplished, and several new findings have been made as reported before.

Subtask 2: Select candidates for functional validation in vivo and in BICA. (Month 36-60)

This effort has started and generated promising outcome. Representative results are shown in previous reports. We have summarized in **Table 1** below.

Major Task 5: Screening of small SMI libraries to identify FDA-approved drugs or new compounds that can eliminate BMM.

Subtask 1: Screening using BICA. We will use one ER+ PDX and one ER+ cell lines. Each model will be applied to 100 mice. This will generate approximately 5000 bone fragments, and can be used for screening of small drug libraries described in the proposal. Four libraries and BICA-screening will be performed. (Month 24-36)
This subtask has been accomplished, as reported in previous years.

Subtask 2: Identify and validate the efficacies of top candidates on BMM. We will use the same models as subtask 1. (Month 30-36)

This subtask has been accomplished and reported last year.

Subtask 3: Optimize and modify the compounds to achieve higher efficiency. We will use the same models as subtask 1. (Month 36-48)

This subtask has been accomplished, as reported in previous years.

Subtask 4: In-depth mechanistic studies of the validated compounds. We will perform RNAseq on BMM in vivo to delineate pathways affected by the compounds. We will then identify key genes that may mediate the compounds' effects. Genetic depletion will then be performed to perturb these genes. The models are the same as subtask 1. (Month 36-60)

We have made significant progress and uncovered several intriguing mechanisms underlying cancer-bone interactions and therapeutic resistance of bone metastases. These mechanisms have been reported in previous reports and have been summarized in **Table 1** below.

Table 1. Summary of key findings made within the grant period.

Year	Major mechanistic findings	Molecular targets	Therapeutic agents tested and results	References
2015 - 2021	Bone micrometastases form heterotypic adherens junctions with the osteogenic niche cells, which activates the mTOR pathway in cancer cells.	E-cadherin (cancer)	Anti-E-cadherin – delay bone colonization in vivo	(1)
		N-cadherin (osteogenic cells)	Anti-N-cadherin – impair cancer cell growth in co-culture with bone cells (N-cadherin KO in vivo inhibits bone colonization)	
		mTOR pathway (cancer)	mTOR inhibitors, rapamycin and Torin 1, inhibit bone metastasis in vivo.	

2016-2020	Bone micrometastases form gap junctions with the osteogenic niche cells, which activates the calcium pathway in cancer cells.	Cx43 (cancer and osteogenic cells)	Carbenoxolone and mefloquine inhibit bone metastasis in vivo. Arsenic trioxide inhibits expression of Cx43 in cancer cells.	(2, 3)
2015-2017	Bone-in-culture array (BICA) identified multiple potential targets that selectively mediate tumor growth in bone-like microenvironment.	Aurora kinase	Aurora kinase inhibitor, danusertib, impedes bone metastasis in BICA and in vivo. Arsenic trioxide inhibits cancer cell growth in BICA.	(4)
2016-2021	The bone microenvironment increases phenotypic plasticity of ER+ breast cancer cells and induces endocrine resistance through epigenomic reprogramming	EZH2	An EZH2 inhibitor, EPZ011989, reversed endocrine resistance and synergizes with fulvestrant in treating ER+ bone metastasis.	(5)
		FGFR	The FGFR inhibitor BGJ398 counteract endocrine resistance induced by osteogenic cells in vitro and in BICA.	
2016-2021	The bone microenvironment invigorates metastatic seeds for further dissemination	EZH2	The EZH2 inhibitor, EPZ011989, blocked cancer stemness induced by the bone microenvironment.	(6)
2018-2021	The bone microenvironment induces expression of Her2 in Her2- models and confer opportunities to target Her2 by bisphosphonate-conjugated trastusumab.	Her2	Bisphosphonate-conjugated trastusumab suppresses bone colonization of both Her2+ and Her2- cancer cells.	(7)

In addition to primary researches listed above, we have also published several reviews on related topics in first-rate journals, which are listed below.

1. Roberts L. Satcher and **Xiang H.-F. Zhang**. *Evolving cancer-niche interactions during bone metastasis progression and therapies.* **Nature Review Cancer**. DOI: 10.1038/s41568-021-00406-5.

2. Muscarella AM, Aguirre S, Hao X, Waldvogel SM, **Xiang H.-F. Zhang**. *Exploiting bone niches: progression of disseminated tumor cells to metastasis.* **Journal of Clinical Investigation** 2021 Mar 15;131(6):e143764. doi: 10.1172/JCI143764.

3. Wang H and **Xiang H.-F. Zhang.** (2020) "Molecules in the blood of older people promote Cancer Spread." **Nature**. 585(7824):187-188. doi: 10.1038/d41586-020-02381-7.

4. Wang H, Zhang W, Bado I, **Xiang H.-F. Zhang.** (2020) "Bone Tropism in Cancer Metastases." **Cold Spring Harb Perspect Med**. a036848. doi: 10.1101/cshperspect.a036848. PMID: 31615871

5. Bado I, **Xiang H.-F. Zhang**. (2020) "Senesce to Survive: YAP-Mediated Dormancy Escapes EGFR/MEK Inhibition." **Cancer Cell**, 13;37(1):1-2. doi: 10.1016/j.ccell.2019.12.008.

6. Gao Y, Bado I, Wang H, Zhang W, Rosen JM, and **Xiang H.-F. Zhang**. (2019). "Metastasis Organotropism: Redefining the Congenial Soil." **Dev Cell**, 2019, 49(3):375-391. PMID: 31063756 PMCID: PMC6506189

7. Zhang W, Lo HC, Bado I, Wang H, and **Xiang H.-F. Zhang**. (2019) *Bone metastasis: find your niche and fit in*. **Trends in Cancer**. 5(2):95-110.

4. Impact

The proposed research is innovative and distinctive in the field of breast cancer research for the following reasons. First, to date few experimental models can be used to test the therapeutic responses of BMM. The vast majority of pre-clinical research has been done using orthotopic tumor models, despite the fact that micrometastases are the major targets of adjuvant therapies. We have established unique in vivo and ex vivo models to fill this gap. We will use these models to elucidate how different subtypes of breast cancer respond to their respective adjuvant therapies as microscopic lesions embedded in the bone, a significant step toward full recapitulation of clinical scenarios. Second, BICA combines the complexity of bone microenvironment and the scalability of in vitro culturing. Compared to previous "tissue-in-culture" approaches, bone-in-culture represents a better mimicry of the counterpart organ because BMM are tightly integrated into the osteogenic niche and are difficult to be dissociated from the bone tissue. As a result, the cancer-niche crosstalk is preserved after tissue fragmentation. Thus, BICA provides distinctive opportunities to rapidly assay hundreds of compounds and reveal novel treatments of BMM. Third, the proposed research assembles a number of experts with different expertise including the-state-of-art breast cancer PDX models (Lewis), single/few cell RNA-seq (Zong), and drug design and synthesis (Song). This is expected to generate significant synergy.

The research outcomes from the first four grant years include the discovery of novel mechanisms underlying cancer-bone interactions and identification of potential novel therapies that may help eliminate bone micrometastases and prevent overt recurrences.

5. Changes/Problems

The Covid 19 pandemic has significantly impacted our ability to access lab and animal facilities. However, we have still made significant progress.

6. Products

Publications:

8. Tian Z#, Wu L#, Yu C, Chen Y, Xu Z, Bado IL, Loredo A, Wang L, Wang H, Wu K-L, Zhang W, **Xiang H-F Zhang***, Xiao H* (2021) Harnessing the power of antibodies to fight bone metastasis. **Science Advances**, 7 (26), eabf2051 (# indicates equal first-authorship, * indicates co-senior authors).

9. Bado IL, Zhang W, Hu J, Xu Z, Wang H, Sarkar, Li L, Wan Y-W, Liu J, Wu W, Lo H-C, Kim IS, Singh S, Janghorban M, Muscarella AM, Goldstein A, Singh P, Jeong H-H, Liu C, Schiff R, Huang S, Ellis MJ, Gaber MW, Gugala Z, Liu Z, **Xiang H.-F. Zhang** (2021) Impact of the bone microenvironment on phenotypic plasticity of ER+ breast cancer cells. **Developmental Cell**, 56(8):1100-1117.

10. Zhang W, Bado IL, Hu J, Wang Y-W, Wu L, Wang H, Gao Y, Jeong H-H, Xu Z, Hao X, Lege BM, Al-Ouran R, Li L, Li J, Yu L, Singh S, Lo H-C, Niu M, Liu J, Jiang W, Li Y, Wong STC, Cheng C, Liu Z, and **Xiang H.-F. Zhang** (2021). *The bone microenvironment invigorates metastatic seeds for further dissemination*. **Cell**, 184(9):2471-2486.

11. Roberts L. Satcher and **Xiang H.-F. Zhang**. *Evolving cancer-niche interactions during bone metastasis progression and therapies.* **Nature Review Cancer**. DOI: 10.1038/s41568-021-00406-5.

Grants:

1. DoD BCRP BC201371P1 Eliminating Bone Micrometastases by Bone-targeting Antibodies.
2. R01 CA271498 (Li/Zhang) Next Generation Rat Models of ER+ Breast Cancer, Pending (Impact Score: 11 (1%))

7. Participants & Other Collaborating Organizations

Name:	Chenghang Zong
Project Role:	Co-investigator
Researcher Identifier:	N/A
Nearest person month worked	0.36
Contribution	Dr. Zong is an expert of single-cell sequencing, and is helping us establish protocols to sequence BMM transcriptomes, which is critical to delineate molecular mechanisms underlying endocrine resistance of BMM.
Funding Support	Dr. Zong was also supported by NIH New Innovator1DP2EB020399-01
Name:	Yongcheng Song
Project Role:	Co-investigator
Researcher Identifier:	N/A
Nearest person month worked	0.6
Contribution	Dr. Song is an expert of chemical synthesis and modification of drugs. He is helping us to improve bioavailability and pharmacokinetics of potential bone metastasis drugs.
Funding Support	Dr. Song was also supported by NIH R01NS080963, Cancer Prevention and Research Institute of Texas RP140469 and RP150129
Name:	Michael Lewis
Project Role:	Co-investigator
Researcher Identifier:	N/A
Nearest person month worked	0.6
Contribution	Dr. Lewis established a cohort of PDX models. He is helping us utilize PDX models to generate metastasis models for mechanistic and therapeutic studies.
Funding Support	Dr. Lewis is also supported by fundings from NSF (1263742),

	NIH (CA179720) and Helis Foundation.
Name:	Hai Wang
Project Role:	Instructor
Researcher Identifier:	N/A
Nearest person month worked	12
Contribution	Dr. Wang specialize in bone metastasis research techniques and is leading the efforts of establishing BICA.
Name:	Yang Gao
Project Role:	Postdoctoral Fellow
Researcher Identifier:	N/A
Nearest person month worked	6
Contribution	Dr. Yang focuses on the role of estrogen receptors in driving bone microenvironment-dependent endocrine resistance.
Name:	Zhan Xu
Project Role:	Postdoctoral Fellow
Researcher Identifier:	N/A
Nearest person month worked	12
Contribution	Dr. Xu focuses on the roles of various bone microenvironment niches during bone metastasis colonization.

Name:	Xiang Zhang
Project Role:	PI/PD
Researcher Identifier:	N/A
Nearest person month worked	3.0
Contribution	Dr. Zhang designed and supervised the experiments described in this report.
Funding Support	Dr. Zhang is also supported by NIH/NCI, Breast Cancer Research Foundation, and McNair Medical Institute.

All collaborators and participants are at Baylor College of Medicine.

8. Special Reporting Requirements

None.

9. Appendices

A copy of the publications that have not been included

REFERENCES

1. Wang H, Yu C, Gao X, Welte T, Muscarella AM, Tian L, Zhao H, Zhao Z, Du S, Tao J, Lee B, Westbrook TF, Wong ST, Jin X, Rosen JM, Osborne CK, Zhang XH. The osteogenic niche promotes early-stage bone colonization of disseminated breast cancer cells. Cancer Cell. 2015;27(2):193-210. Epub 2015/01/21. doi: 10.1016/j.ccell.2014.11.017. PubMed PMID: 25600338; PMCID: PMC4326554.
2. Wang H, Tian L, Liu J, Goldstein A, Bado I, Zhang W, Arenkiel BR, Li Z, Yang M, Du S, Zhao H, Rowley DR, Wong STC, Gugala Z, Zhang XH. The Osteogenic Niche Is a Calcium Reservoir of Bone Micrometastases and Confers Unexpected Therapeutic Vulnerability. Cancer Cell. 2018;34(5):823-39 e7. Epub 2018/11/14. doi: 10.1016/j.ccell.2018.10.002. PubMed PMID: 30423299; PMCID: PMC6239211.
3. Muscarella AM. Unique cellular protrusions mediate breast cancer cell migration by tethering to osteogenic cells. npj Breast Cancer. 2020. doi: 10.1038/s41523-020-00183-8.
4. Wang H, Tian L, Goldstein A, Liu J, Lo HC, Sheng K, Welte T, Wong STC, Gugala Z, Stossi F, Zong C, Li Z, Mancini MA, Zhang XH. Bone-in-culture array as a platform to model early-stage bone metastases and discover anti-metastasis therapies. Nat Commun. 2017;8:15045. Epub 2017/04/22. doi: 10.1038/ncomms15045. PubMed PMID: 28429794; PMCID: PMC5413944.
5. Bado IL, Zhang W, Hu J, Xu Z, Wang H, Sarkar P, Li L, Wan YW, Liu J, Wu W, Lo HC, Kim IS, Singh S, Janghorban M, Muscarella AM, Goldstein A, Singh P, Jeong HH, Liu C, Schiff R, Huang S, Ellis MJ, Gaber MW, Gugala Z, Liu Z, Zhang XH. The bone microenvironment increases phenotypic plasticity of ER(+) breast cancer cells. Dev Cell. 2021;56(8):1100-17 e9. Epub 2021/04/21. doi: 10.1016/j.devcel.2021.03.008. PubMed PMID: 33878299; PMCID: PMC8062036.
6. Zhang W, Bado IL, Hu J, Wan YW, Wu L, Wang H, Gao Y, Jeong HH, Xu Z, Hao X, Lege BM, Al-Ouran R, Li L, Li J, Yu L, Singh S, Lo HC, Niu M, Liu J, Jiang W, Li Y, Wong STC, Cheng C, Liu Z, Zhang XH. The bone microenvironment invigorates metastatic seeds for further dissemination. Cell. 2021;184(9):2471-86 e20. Epub 2021/04/21. doi: 10.1016/j.cell.2021.03.011. PubMed PMID: 33878291; PMCID: PMC8087656.
7. Tian Z, Wu L, Yu C, Chen Y, Xu Z, Bado I, Loredo A, Wang L, Wang H, Wu KL, Zhang W, Zhang XH, Xiao H. Harnessing the power of antibodies to fight bone metastasis. Sci Adv. 2021;7(26). Epub 2021/06/25. doi: 10.1126/sciadv.abf2051. PubMed PMID: 34162538.

Cell

The bone microenvironment invigorates metastatic seeds for further dissemination

Graphical abstract

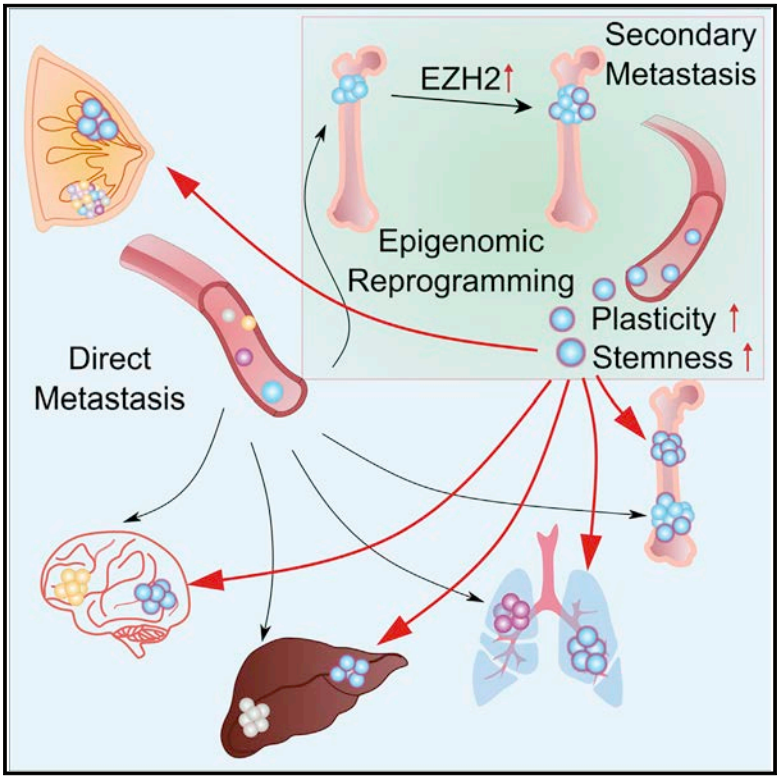

Highlights

- Experimental bone metastases (BoM) spread to other organs in mouse models
- Evolving barcodes delineate further spread from BoM in spontaneous metastasis
- BoM spurs metastatic seeds with increased stemness and reduced organotropism
- EZH2 mediates secondary metastasis invigorated by the bone microenvironment

Authors

Weijie Zhang, Igor L. Bado, Jingyuan Hu, ..., Chonghui Cheng, Zhandong Liu, Xiang H.-F. Zhang

Correspondence

xiangz@bcm.edu

In brief

Delineation of cancer cell spreading from primary bone metastasis by an evolving barcode system highlights the impact of the bone microenvironment in shaping secondary metastasis through mechanisms distinct from clonal selection.

Zhang et al., 2021, Cell *184*, 1–16
April 29, 2021
https://doi.org/10.1016/j.cell.2021.03.011

CellPress

Please cite this article in press as: Zhang et al., The bone microenvironment invigorates metastatic seeds for further dissemination, Cell (2021), https://doi.org/10.1016/j.cell.2021.03.011

Cell

CellPress

Article

The bone microenvironment invigorates metastatic seeds for further dissemination

Weijie Zhang,[1,2,3,11] Igor L. Bado,[1,2,3,11] Jingyuan Hu,[4,5] Ying-Wooi Wan,[4,6] Ling Wu,[1,2,3] Hai Wang,[1,2,3] Yang Gao,[1,2,3] Hyun-Hwan Jeong,[4,6] Zhan Xu,[1,2,3] Xiaoxin Hao,[1,2,3] Bree M. Lege,[1,6] Rami Al-Ouran,[4,7] Lucian Li,[4,7] Jiasong Li,[8] Liqun Yu,[1,2,3] Swarnima Singh,[1,2,3] Hin Ching Lo,[1,2,3] Muchun Niu,[9] Jun Liu,[1,2,3] Weiyu Jiang,[1,2,3] Yi Li,[1,2,3] Stephen T.C. Wong,[2,3,8] Chonghui Cheng,[1,6] Zhandong Liu,[4,6] and Xiang H.-F. Zhang[1,2,3,10,12,*]

[1]Lester and Sue Smith Breast Center, Baylor College of Medicine, Houston, TX 77030, USA
[2]Dan L. Duncan Cancer Center, Baylor College of Medicine, Houston, TX 77030, USA
[3]Department of Molecular and Cellular Biology, Baylor College of Medicine, Houston, TX 77030, USA
[4]Jan and Dan Duncan Neurological Research Institute, Texas Children's Hospital, Houston, TX 77030, USA
[5]Quantitative and Computational Biosciences Program, Baylor College of Medicine, Houston, TX 77030, USA
[6]Department of Molecular and Human Genetics, Baylor College of Medicine, Houston, TX 77030, USA
[7]Department of Pediatrics, Baylor College of Medicine, Houston, TX 77030, USA
[8]Department of Systems Medicine and Bioengineering and Translational Biophotonics Laboratory, Houston Methodist Cancer Center, Houston, TX 77030, USA
[9]Integrative Molecular and Biomedical Sciences Graduate Program, Baylor College of Medicine, Houston, TX 77030, USA
[10]McNair Medical Institute, Baylor College of Medicine, Houston, TX 77030, USA
[11]These authors contributed equally
[12]Lead contact
*Correspondence: xiangz@bcm.edu
https://doi.org/10.1016/j.cell.2021.03.011

SUMMARY

Metastasis has been considered as the terminal step of tumor progression. However, recent genomic studies suggest that many metastases are initiated by further spread of other metastases. Nevertheless, the corresponding pre-clinical models are lacking, and underlying mechanisms are elusive. Using several approaches, including parabiosis and an evolving barcode system, we demonstrated that the bone microenvironment facilitates breast and prostate cancer cells to further metastasize and establish multi-organ secondary metastases. We uncovered that this metastasis-promoting effect is driven by epigenetic reprogramming that confers stem cell-like properties on cancer cells disseminated from bone lesions. Furthermore, we discovered that enhanced EZH2 activity mediates the increased stemness and metastasis capacity. The same findings also apply to single cell-derived populations, indicating mechanisms distinct from clonal selection. Taken together, our work revealed an unappreciated role of the bone microenvironment in metastasis evolution and elucidated an epigenomic reprogramming process driving terminal-stage, multi-organ metastases.

INTRODUCTION

Metastasis to distant organs is the major cause of cancer-related deaths. Bone is the most frequent destination of metastasis in breast cancer and prostate cancer (Gundem et al., 2015; Kennecke et al., 2010; Smid et al., 2008). In the advanced stage, bone metastasis is driven by the paracrine crosstalk among cancer cells, osteoblasts, and osteoclasts, which together constitute an osteolytic vicious cycle (Esposito et al., 2018; Kang et al., 2003; Kingsley et al., 2007; Weilbaecher et al., 2011). Specifically, cancer cells secrete molecules such as PTHrP, which act on osteoblasts to modulate the expression of genes including RANKL and OPG (Boyce et al., 1999; Juárez and Guise, 2011). The alterations of these factors, in turn, boost osteoclast maturation and accelerate bone resorption. Many growth factors (e.g., IGF1) deposited in the bone matrix are then released and reciprocally stimulate tumor growth. This knowledge laid the foundation for clinical management of bone metastases (Coleman et al., 2008).

The urgency of bone metastasis research is somewhat controversial. It has long been noticed that, at the terminal stage, breast cancer patients usually die of metastases in multiple organs. In fact, compared to metastases in other organs, bone metastases are relatively easier to manage. Patients with the skeleton as the only site of metastasis usually have better prognosis than those with visceral organs affected (Coleman and Rubens, 1987; Coleman et al., 1998). These facts argue that perhaps metastases in more vital organs should be prioritized in research. However,

Please cite this article in press as: Zhang et al., The bone microenvironment invigorates metastatic seeds for further dissemination, Cell (2021), https://doi.org/10.1016/j.cell.2021.03.011

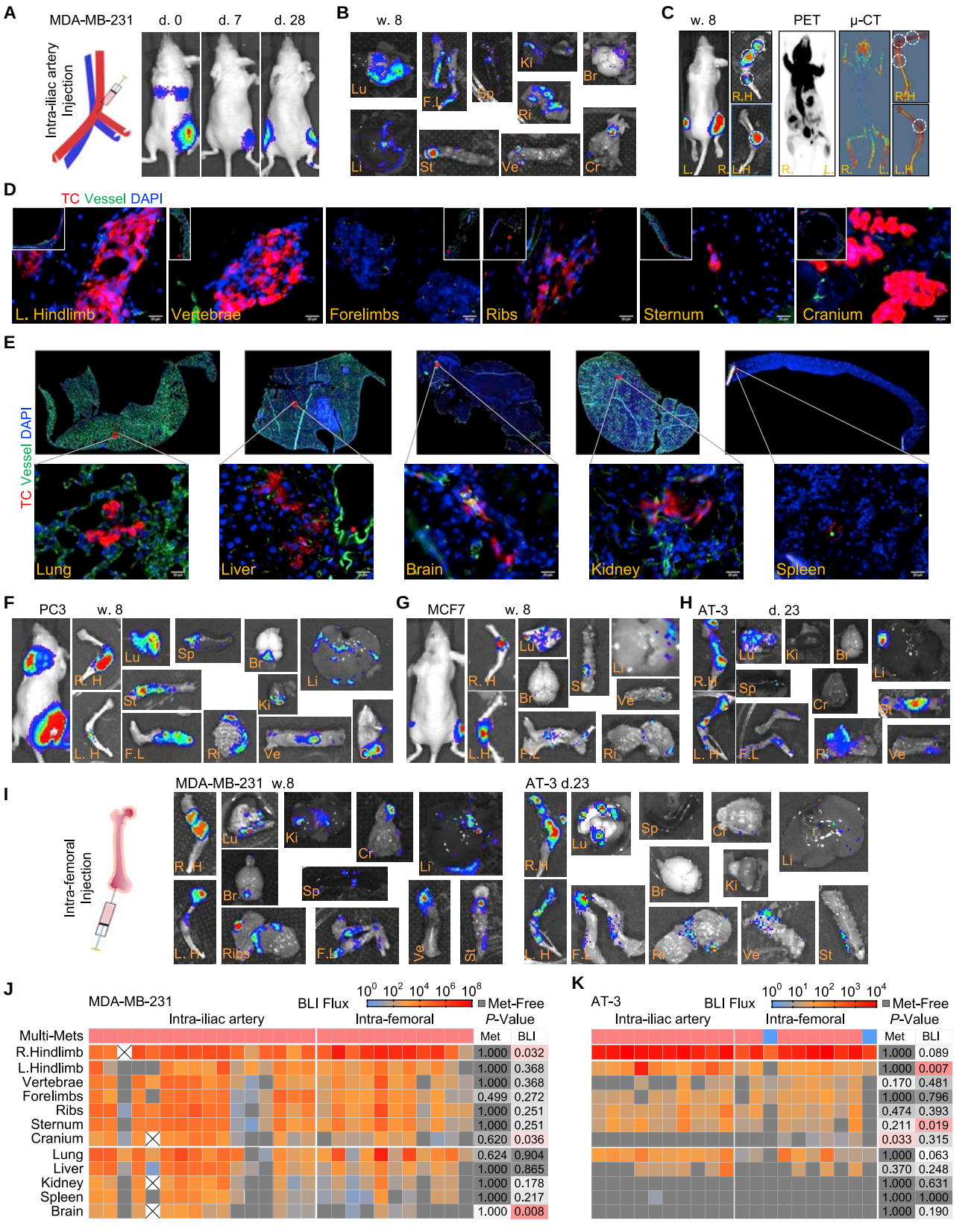

(legend on next page)

Please cite this article in press as: Zhang et al., The bone microenvironment invigorates metastatic seeds for further dissemination, Cell (2021), https://doi.org/10.1016/j.cell.2021.03.011

metastases usually do not occur synchronously. In 45% of metastatic breast cancer cases, bone is the first organ that shows signs of metastasis, much more frequently compared to the lungs (19%), liver (5%), and brain (2%) (Coleman and Rubens, 1987). More importantly, in more than two-thirds of cases, metastases will not be limited to the skeleton, but rather subsequently occur to other organs and eventually cause death (Coleman, 2006; Coleman and Rubens, 1987; Coleman et al., 1998). This raises the possibility of secondary dissemination from the initial bone lesions to other sites. Indeed, recent genomic analyses concluded that the majority of metastases result from seeding from other metastases, rather than primary tumors (Brown et al., 2017; Gundem et al., 2015; Ullah et al., 2018). Thus, it is imperative to investigate further metastatic seeding from bone lesions, as it might lead to prevention of the terminal stage, multi-organ metastases that ultimately cause the vast majority of deaths.

Despite its potential clinical relevance, little is known about metastasis-to-metastasis seeding. Current preclinical models focus on seeding from primary tumors but cannot distinguish between additional sites of dissemination. We have recently developed an approach, termed intra-iliac artery injection (IIA), that selectively deliver cancer cells to hind limb bones via the external iliac artery (Wang et al., 2015, 2018; Yu et al., 2016). Although it skips the early steps of the metastasis cascade, it focuses on the initial seeding of tumor cells in the hind limbs, and allows the tracking of secondary metastases from bone to other organs. It is therefore a suitable model to investigate the clinical and biological roles played by bone lesions in multi-organ metastasis-to-metastasis seeding.

RESULTS

Temporally lagged multi-organ metastases in mice carrying IIA-introduced bone lesions of breast and prostate cancers

IIA injection has been employed to investigate early-stage bone colonization. Both aggressive (e.g., MDA-MB-231) and relatively indolent (e.g., MCF7) breast cancer cells can colonize bones albeit following different kinetics. In both cases, cancer cell distribution is highly bone-specific at early time points, allowing us to dissect cancer-bone interactions without the confounding effects of tumor burden in other organs (Figure 1A) (Wang et al., 2015, 2018). However, as bone lesions progress, metastases, as indicated by bioluminescence signals, begin to appear in other organs, including additional bones, lung, liver, kidney, and brain, usually 4–8 weeks after IIA injection of MDA-MB-231 cells (Figure 1B). Bioluminescence imaging provides sufficient sensitivity to detect metastases (Deroose et al., 2007). However, many factors such as lesion depth and optical properties of tissues may influence signal penetration. Thus, we used a number of other approaches to validate the presence of metastases in multiple types of tissues. These include positron emission tomography (PET) (Figure 1C), micro computed tomography (μCT) (Figures 1C and S1A), whole-tissue two-photon imaging (Figure S1B), immunofluorescence staining (Figure 1D and 1E), and histological staining (H&E) (Figure S1C). Compared to bioluminescence imaging, these approaches provided independent evidence, but are either less sensitive or non-quantitative (Deroose et al., 2007) (Figure S1A). Therefore, we also used quantitative PCR (qPCR) to detect human-specific DNA in dissected mouse tissues and confirmed that qPCR results and bioluminescence signal intensity values are highly correlative (Figures S1D and S1E). Of note, the spectrum of metastases covers multiple other bones (Figure 1D) and soft-tissue organs (Figure 1E). Taken together, our data support occurrence of multi-organ metastases in animals with IIA-introduced bone lesions.

This phenomenon is not specific for the highly invasive MDA-MB-231 cells, but was also observed in more indolent MCF7 cells and PC3 prostate cancer cells, as well as murine mammary carcinoma AT-3 cells in immunocompetent mice, albeit after a longer lag period for PC3 cells (8–12 weeks) (Figures 1F–1H and S1F).

As an independent approach to introduce bone lesions, we used intra-femoral (IF) injection that delivers cancer cells directly to bone marrow, bypassing the artery circulation involved in IIA injection. This approach also resulted in multi-organ metastases at late time points in both MDA-MB-231 and AT-3 models (Figures 1I and S1G). The frequency and distribution patterns of metastases were similar between intra-femoral and IIA injection models (Figures 1J and 1K). Thus, we hypothesize cancer cells in the bone microenvironment may gain capacity to further metastasize.

Figure 1. Multi-organ metastases in mice with bone lesions

(A) Diagram of intra-iliac artery (IIA) injection and representative bioluminescent images (BLI) showing the *in vivo* distribution of tumor cells after IIA injection of 1E5 MDA-MB-231 fLuc-mRFP cells.

(B and C) Representative *ex vivo* BLI images (B) and PET-μCT (C) on hindlimb and other tissues of the same animal with MDA-MB-231 cells inoculated in the right hindlimb after 8 weeks. R.H, right hindlimb; Lu, lung; L.H, left hindlimb; Li, liver; Ki, kidney; Sp, spleen; Br, brain; Ve, vertebrae; F.L, forelimbs; Ri, ribs; St, sternum; Cr, cranium.

(D and E) Representative immunofluorescent images of tumor lesions in various bones (D) and other organs (E). To obtain complete views of entire organs, smaller fields were acquired in tiles by mosaic scanning and then stitched by Zen. Scale bar, 20 μm.

(F–H) Representative BLI images of animals and tissues after IIA injection of 2E5 prostate cancer cells PC3 (F), 1E5 ER^+ breast cancer cells MCF7 (G), and 1E5 murine mammary carcinoma cells AT-3 (H) at the indicated time.

(I) Diagram of intra-femoral injection (IF) (left) and representative *ex vivo* BLI images of tissues from animals received 1E5 MDA-MB-231 cells (middle) or AT-3 cells (right) via IF injection.

(J and K) Heatmap of *ex vivo* BLI intensity and status of metastatic involvement on various types of tissues from animals carried MDA-MB-231 (J) and AT-3 (K) bone tumors. Columns, individual animal; rows, various tissues or status of multi-site metastases; Gray, no detectable lesion. n (# of mice): MDA-MB-231, 16 (IIA), 11 (IF); AT-3, 10 (IIA), 10 (IF). p values were assessed by Fisher's exact test on the ratio of metastasis while by Mann-Whitney test on the tumor burden.
See also Figure S1.

Please cite this article in press as: Zhang et al., The bone microenvironment invigorates metastatic seeds for further dissemination, Cell (2021), https://doi.org/10.1016/j.cell.2021.03.011

Bone lesions more readily give rise to multi-organ metastasis

The later-appearing multi-organ metastases may result from further dissemination of cancer cells in the initial bone lesions. Alternatively, they could also arise from cancer cells that leaked and escaped from bone capillaries during IIA or IF injection. In the latter case, the leaked cancer cells would enter the iliac vein and subsequently arrive in the lung capillaries. Indeed, there did appear to be bioluminescence signals in the lungs upon IIA injection (Figure 1A). To distinguish these probabilities, we performed intra-iliac vein (IIV) injection and compared the results to those of IIA injection at late time points. The IIV injection procedure should mimic the "leakage" from IIA injection, although this would allow many more cells to enter the venous system and be arrested in the lung capillaries (Figures 2A and S2A–S2C, compared to Figure 1A). As another relevant comparison, we also examined metastasis from orthotopic tumors transplanted into mammary fat pad (MFP) (Figures 2B, S2A, S2B, and S2D). Furthermore, in the case of ER^+ cells, recent studies suggest that intra-ductal injection provides a more "luminal" microenvironment and may promote spontaneous metastasis to other organs (Sflomos et al., 2016). As a result, specifically for MCF7 cells, the only ER^+ cancer model used in our study, we also included mouse intra-ductal (MIND) injection as an additional model. In all experiments, we used total bioluminescence signal intensity to evaluate tumor burdens at hind limbs (IIA and IF), lungs (IIV), and mammary fat pads (MFP and MIND), respectively. We attempted to assess multi-organ metastasis when the "primary lesions" reach a comparable level of bioluminescent intensity, simply to rule out the source tumor burden as a confounding factor in our comparisons. This was feasible for some models such as mammary tumors and bone lesions derived from MCF7 (Figure S2E). However, in other models, mammary tumors tend to grow much faster compared to lesions growing in other sites (Figures S2F and S2G). Therefore, we chose to end experiments at the same time point for all conditions. In all experiments, multi-organ metastases were examined well before animals became moribund. Taken together, we asked if secondary metastasis from bone lesions follows a faster kinetics and reaches a wider spectrum of target organs as compared to that from orthotopic tumors or lungs.

Strikingly, the answer to this question is evidently positive in all three tumor models examined (Figures 2C–2H). We assessed 11 organs including six other bones and five soft tissue organs for metastasis. Curiously, in many cases, counter-lateral hind limbs (designated as "L.Hindlimb" for "left hind limb" as the initial bone lesions were introduced to the right hind limb) are most frequently affected among all organs in IIA models. Lungs are also frequently affected in MDA-MB-231 and AT-3 models, by metastasis from both bone lesions and orthotopic tumors. However, it is striking to note that lung metastasis in IIA and IF models is comparable or even more severe as compared to that in IIV models, despite the fact that IIV injection delivers more cancer cells directly to lungs (Figure S2H). In fact, the normalized increase of tumor burden at lungs through IIA and IF are at least 10-fold more than that through IIV injection (e.g., Figure S2H), which strongly argue that bone microenvironment promotes secondary metastasis.

Cross-seeding of cancer cells from bone lesions to orthotopic tumors

Cancer cells may enter circulation and seed other tumor lesions or re-seed the original tumors (Kim et al., 2009). By using MDA-MB-231 cells tagged with different fluorescent proteins, we asked if bone lesions can cross-seed mammary tumors (Figure 3A). Interestingly, we observed that although orthotopic tumors can be readily seeded by cells derived from bone lesions, the reverse seeding rarely occurs (Figures 3B and 3C). This difference again highlights the enhanced metastatic aggressiveness of cancer cells in the bone microenvironment.

Parabiosis models support enhanced capacity of cancer cells to metastasize from bone to other organs

It is possible that IIA injection disturbs bone marrow and stimulates systemic effects that allow multi-organ metastases. For example, the injection might cause a transient efflux of bone marrow cells that can arrive at the distant organ to form pre-metastatic niche. To test this possibility, we used parabiosis to fuse the circulation between a bone lesion-carrying mouse (donor) and tumor-free mouse (recipient) 1 week after IIA injection. In parallel, we also performed parabiosis on donors that have received MFP injection and tumor-free recipients (Figure 3D). After 7 weeks, surgical separation was performed to allow time for metastasis development in the recipients. Subsequently, the organs of originally tumor-free recipients were collected and examined for metastases 4 months later. Only ~20% of recipients in the IIA group were found to harbor cancer cells in various organs (Figures 3E and 3F), mostly as microscopic disseminated tumor cells (Figure 3G), indicating that the fusion of circulation system is not efficient for metastatic seeds to cross over from donor to recipient. However, in the MFP comparison group, no metastatic cells were detected (Figures 3F, S3A, and S3B), and the difference is statistically significant. Therefore, the parabiosis data also support the hypothesis that the bone microenvironment invigorates further metastasis, and this effect is unlikely to be due to IIA injection-related systemic influence.

An evolving barcode system revealed the phylogenetic relationships between initial bone lesions and secondary metastases

Barcoding has become widely used to elucidate clonal evolution in tumor progression and therapies. An evolving barcoding system has recently been invented for multiple parallel lineage tracing (Kalhor et al., 2017, 2018). It is based on CRISPR/Cas9 system but utilizes guide RNAs that are adjacent to specific protospacer adjacent motif (PAM) in their genomic locus, thereby allowing Cas9 to mutate its own guide RNAs. These variant guide RNAs are named homing guide RNAs (hgRNAs). When Cas9 is inducibly expressed, hgRNA sequences will randomly drift, serving as evolving barcodes (Figure 4A). A preliminary *in vitro* experiment demonstrated that the diversity of barcodes (measured as Shannon entropy) is a function of duration of Cas9 expression (Figures 4B and S4A).

We introduced this system into MDA-MB-231 and AT-3 cells, and transplanted them into mammary fat pads of nude and wild-type C57BL/6 mice, respectively. When orthotopic tumors

Please cite this article in press as: Zhang et al., The bone microenvironment invigorates metastatic seeds for further dissemination, Cell (2021), https://doi.org/10.1016/j.cell.2021.03.011

CellPress

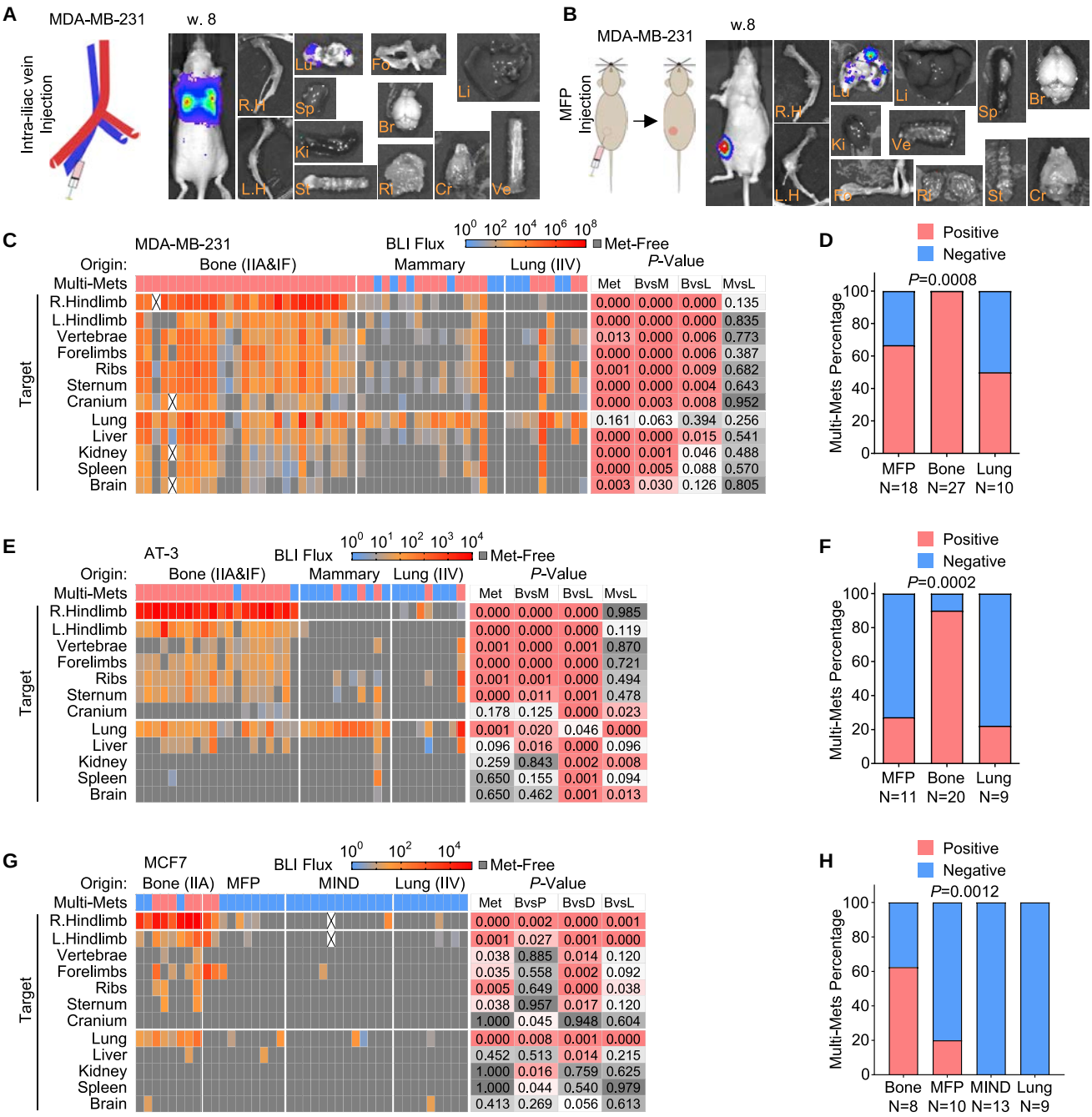

Figure 2. Bone microenvironment promotes further metastasis

(A) Diagram of intra-iliac vein (IIV) injection and representative BLI images of animals and tissues 8 weeks after IIV injection of 1E5 MDA-MB-231 cells.

(B) Diagram of mammary fat pad (MFP) implantation and representative BLI images of animals and tissues 8 weeks after MFP implantation of 1E5 MDA-MB-231 cells.

(C and D) Comparison of metastatic pattern and tumor burden (C) and the ratio of multi-site metastasis (D) in animals with bone (IIA/IF), lung (IIV) or mammary (MFP) tumors of MDA-MB-231 cells. n (# of mice) = 27 (bone); 18 (MFP); 10 (lung).

(E and F) Comparison of metastatic pattern and tumor burden (E) and the ratio of multi-site metastasis (F) in animals with bone (IIA/IF), lung (IIV) or mammary (MFP) tumors of AT-3 cells. n (# of mice) = 20 (bone); 11 (MFP); 9 (lung).

(G and H) Comparison of metastatic pattern and tumor burden (G) and the ratio of multi-site metastasis (H) in animals with bone (IIA), lung (IIV) or mammary (MFP or MIND) tumors of MCF7 cells. n (# of mice) = 8 (bone); 10 (MFP); 13 (MIND); 9 (lung).

p values were assessed by χ^2 test in (C)–(H) on the ratio of metastasis; by uncorrected Dunn's test following Kruskal-Wallis test in (C), (E), and (H) on the tumor burden.

See also Figure S2.

Please cite this article in press as: Zhang et al., The bone microenvironment invigorates metastatic seeds for further dissemination, Cell (2021), https://doi.org/10.1016/j.cell.2021.03.011

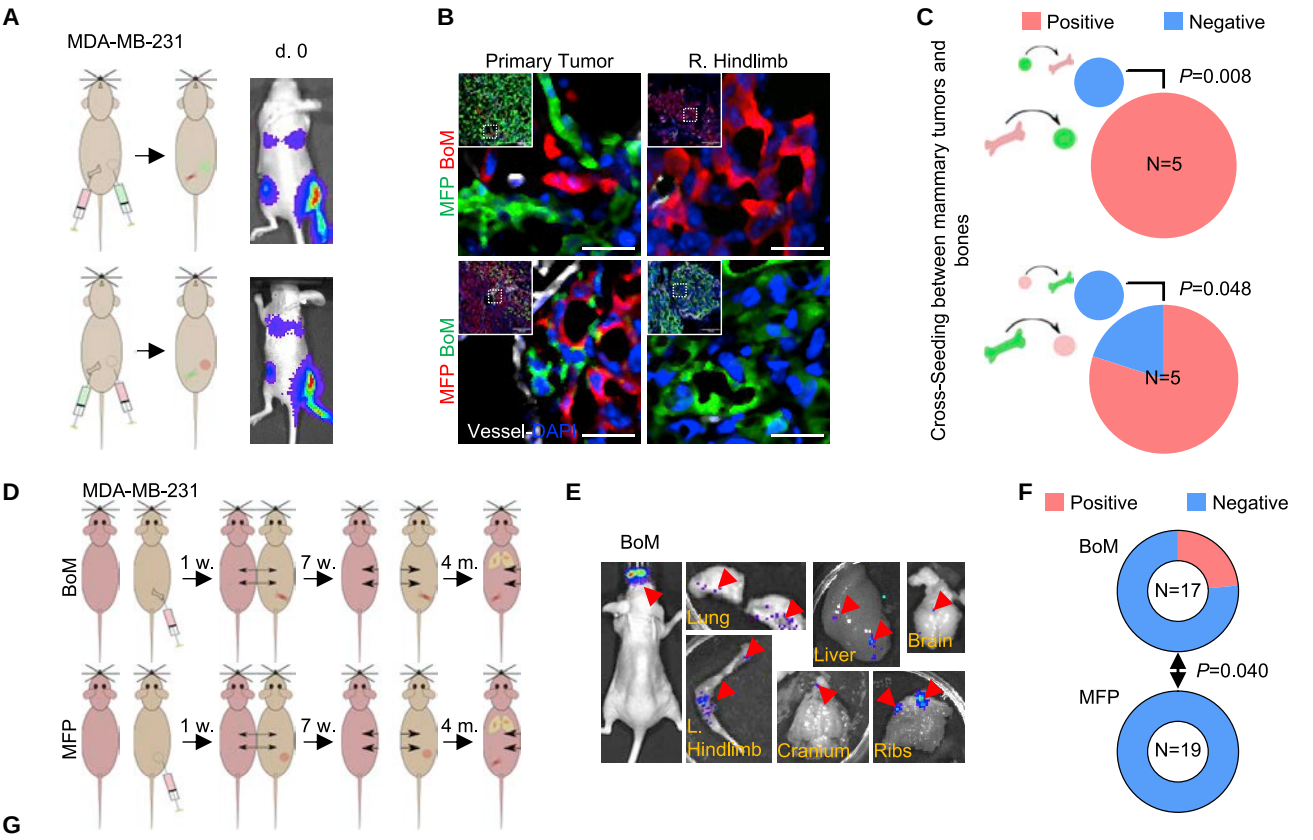

Figure 3. Cross-seeding and parabiosis experiments support the promoting effects of bone microenvironment on further dissemination

(A) Experimental design of cross-seeding experiment between mammary and bone tumors of mRFP or EGFP tagged MDA-MB-231 cells. Upper: mRFP (IIA), EGFP (MFP). Lower: EGFP (IIA), mRFP (MFP).

(B) Representative confocal images showing the cross-seeding between bone and mammary tumors. Scale bar, 20 μm. n (# of mice) = 5 for each arm.

(C) Incidence of cross-seeding between bone and mammary tumors.

(D) Experimental design of parabiosis models to compare the metastatic capacity of bone and mammary tumors. n (# of mice) = 17 (BoM); 19 (MFP).

(E) Representative BLI images of metastatic lesions in recipient mice parabiotic with mice bearing bone metastases.

(F) Ratio of recipients with metastasis in bone and mammary tumor groups, as determined by BLI imaging.

(G) Representative immunofluorescent images on tissues from recipients of bone tumor group. To obtain complete views of entire organs, smaller fields were acquired in tiles by mosaic scanning and then stitched by Zen. Scale bar, 20 μm. Tissues from 6 animals were examined.

p values were assessed by Fisher's exact test in (C) and (F).

See also Figure S3.

reach 1 cm^3, we resected the tumors and induced Cas9 by doxycycline. It should be noted that the orthotopic tumors already harbored a high diversity of mutant barcodes presumably due to leakage of Cas9 expression. This served as an initial barcode repertoire that enabled us to distinguish distinct clones that metastasize from orthotopic tumors to various organs. Further Cas9 expression yielded new mutations for delineation of parent-child relationship among lesions (Figure 4C). We rationalize that the diversity of barcodes, or the Shannon entropy, in a metastasis should reflect the "age" of metastasis. When secondary metastasis occurs, child metastases will inherit only a subset of barcodes causing a reduction of Shannon entropy. Therefore, among genetically related metastases indicated by sharing common mutant barcodes, those with higher Shannon entropy are more likely to be parental (Figure 4C). This can be supported by the observation that primary bone lesions possess higher entropy than those secondary metastases in IIA model (Figure S4B).

Please cite this article in press as: Zhang et al., The bone microenvironment invigorates metastatic seeds for further dissemination, Cell (2021), https://doi.org/10.1016/j.cell.2021.03.011

CellPress

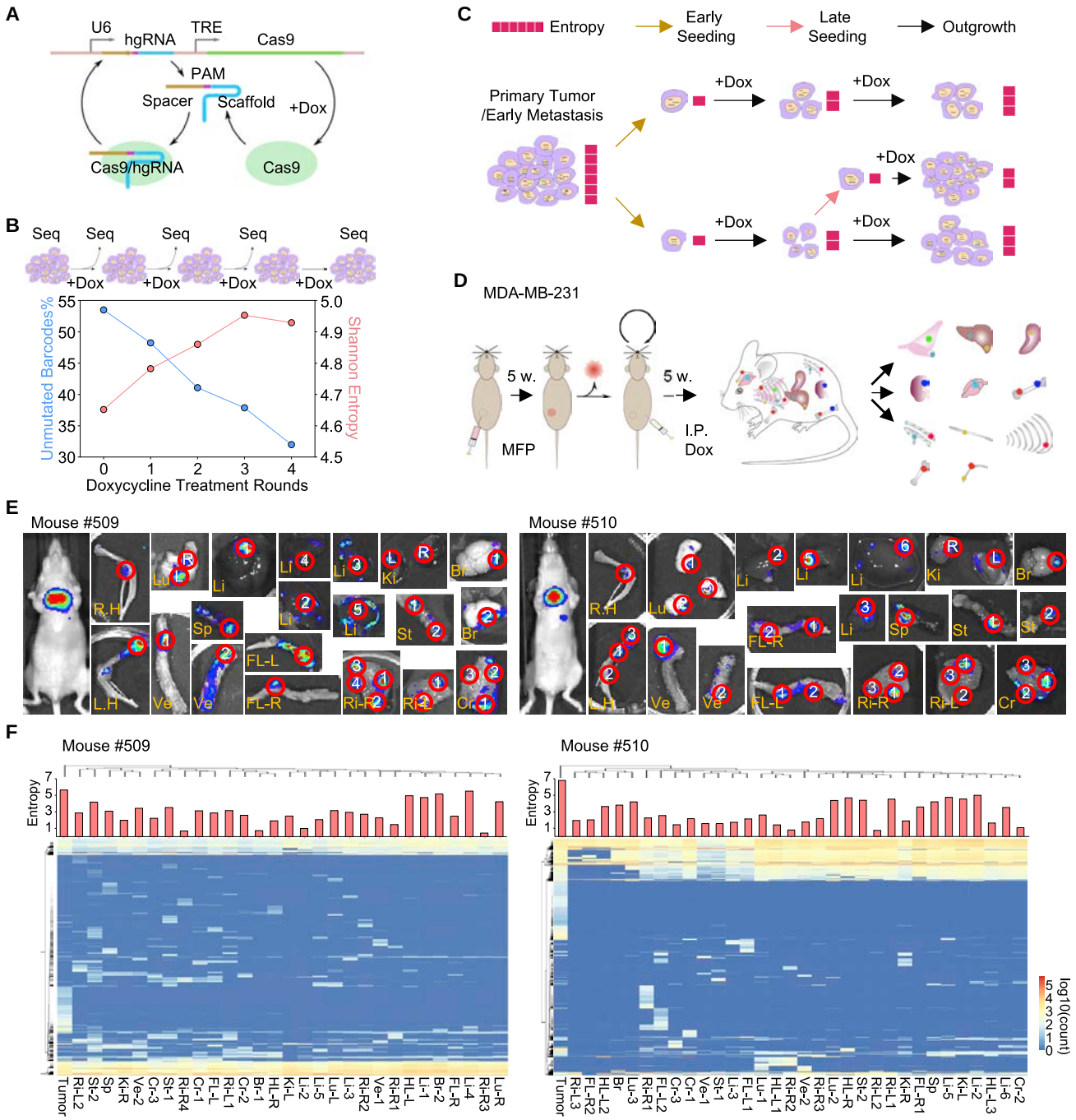

Figure 4. *In vivo* barcoding of spontaneous metastases with hgRNAs

(A) Principle of the evolving barcode system comprised of hgRNAs and inducible Crispr-Cas9.

(B) Ratio of unmutated barcode and Shannon entropy in MDA-MB-231 cells upon multiple rounds of doxycycline treatment *in vitro*.

(C) Schematics showing the rationale of using evolving barcodes to infer the evolution of metastatic lesions and the timing of seeding events. Barcode diversity decreases during the seeding process. Children metastases inherit a subset of signature barcodes from parental tumors. Upon Cas9 activation, barcodes start evolving and regain diversity. Diversity of barcodes can therefore infer the relative timing of seeding, and phylogenetically related metastases share a subset of signature barcodes.

(D and E) Design of *in vivo* barcoding experiment (D) and representative BLI images (E) of metastatic lesions from MDA-MB-231 tumors.

(F) Feature matrix of mutation events in MDA-MB-231 metastatic samples.

See also Figure S4 and Table S1.

Please cite this article in press as: Zhang et al., The bone microenvironment invigorates metastatic seeds for further dissemination, Cell (2021), https://doi.org/10.1016/j.cell.2021.03.011

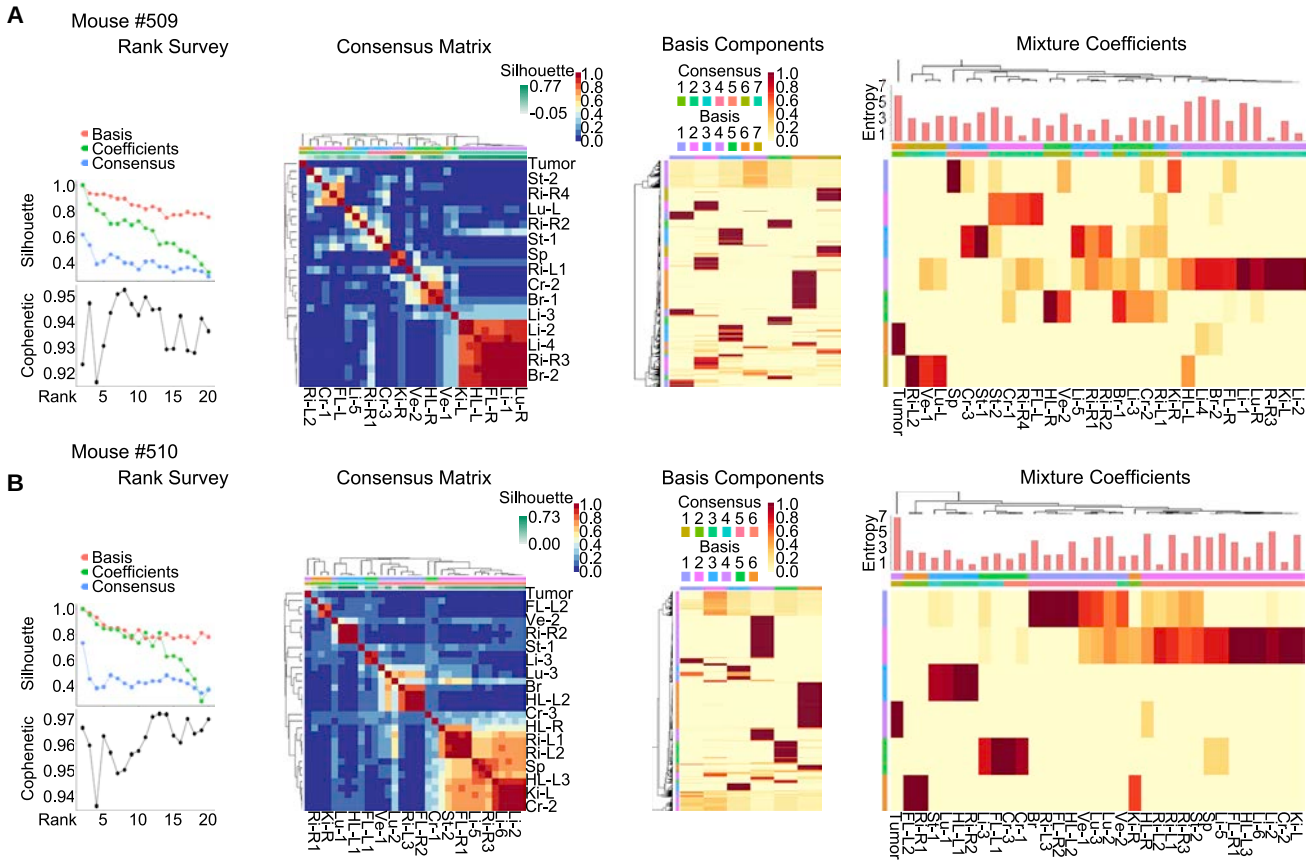

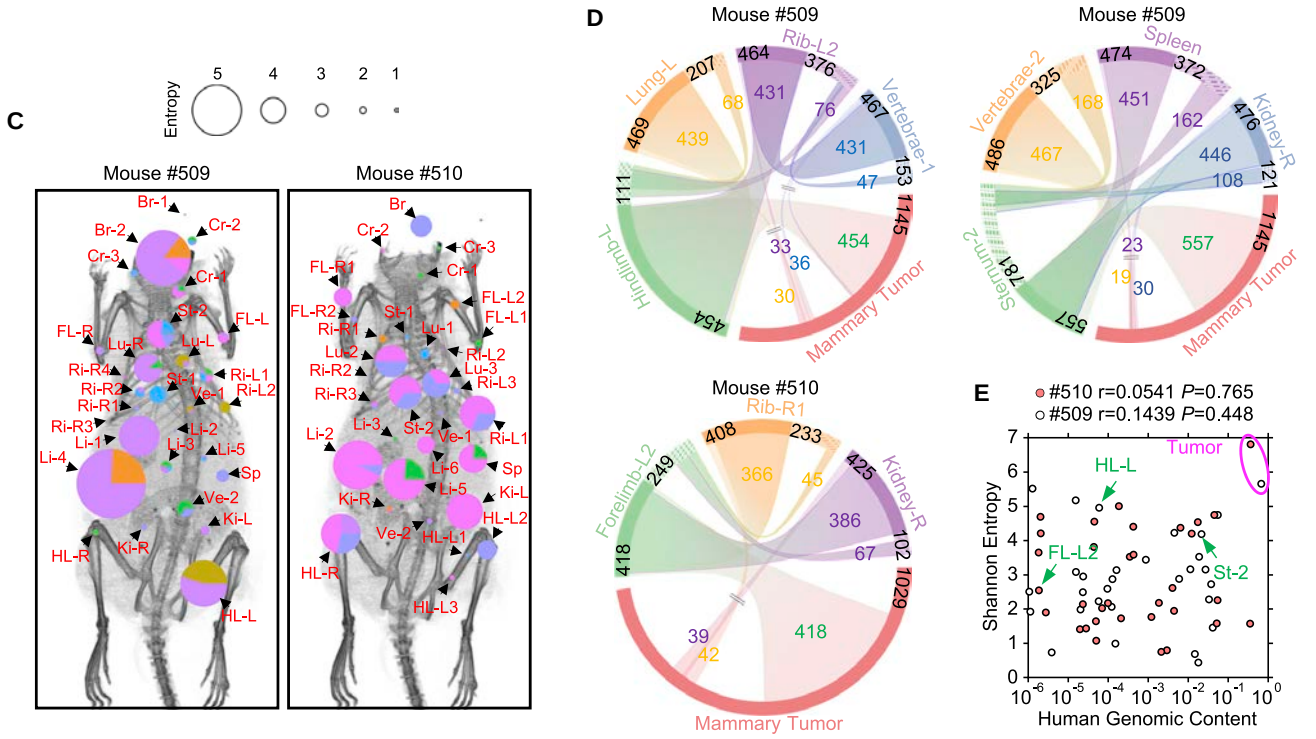

(legend on next page)

Please cite this article in press as: Zhang et al., The bone microenvironment invigorates metastatic seeds for further dissemination, Cell (2021), https://doi.org/10.1016/j.cell.2021.03.011

We isolated 29, 32, 9, and 17 metastases from two mice bearing MDA-MB-231 and two mice bearing AT3 tumors, respectively (Figures 4D, 4E, and S4C; Table S1). Sequencing of the barcodes carried by these metastases in combination of the analysis of the timing of seeding as indicated by the Shannon entropy of barcodes led to profound findings. First, in line with a previous study (Echeverria et al., 2018), multi-organ metastases are not genetically grouped according to sites of metastases at the terminal stage (Figures 4F and S4D). Nonnegative matrix factorization (NMF) analysis of mutant barcodes suggested the early disseminated metastases, which have the highest level of Shannon entropy, were featured with a common cluster of mutant barcodes irrespective of their locations, especially in AT-3 models (Figures 5A–5C and S5A–S5C). This is evidence against organotropism in the late stage of metastatic progression in mouse models. Second, most metastases are potentially multiclonal as indicated by multiple clusters of independent mutant barcodes (Figures 5C and S5C). Third, putative parent-child relationship between metastases with unique mutant barcodes clearly exemplified secondary metastatic seeding from bone to other distant sites (Figures 5D and S5D) in both models. Finally, we did not observe a clear correlation between tumor burden and Shannon entropy across different metastases, and the putative funder metastases can be small in tumor burden while diversified in barcode composition, suggesting that asymptomatic metastases might also seed further metastases (Figures 5E and S5E). Taken together, these data reveal potential widespread metastasis-to-metastasis seeding and support that secondary metastases from the bone to other distant organs happen in a natural metastatic cascade.

The bone microenvironment promotes further metastasis by enhancing cancer cell stemness and plasticity

Organotropism is an important feature of metastasis. Clonal selection appears to play an important role in organ-specific metastasis, which has been intensively studied (Bos et al., 2009; Kang et al., 2003; Minn et al., 2005; Vanharanta and Massagué, 2013). Here, the metastasis-promoting effects of the bone microenvironment appear to be multi-organ and do not show specific organ-tropism. In an accompanied study, we discovered profound phenotypic shift of ER^+ breast cancer cells in the bone microenvironment, which included loss of luminal features and gain of stem cell-like properties (Bado et al., 2021). This shift is expected to promote further metastases (Gupta et al., 2019; Ye and Weinberg, 2015). Therefore, we hypothesize that the enhancement of metastasis may be partly through an epigenomic dedifferentiation process.

To test this possibility, we compared the metastasis capacity of a genetically identical SCP of MDA-MB-231 cells and its derivatives entrained by different microenvironments (Figures S6A and S6B). Based on a previous study (Minn et al., 2005), we picked a non-metastatic SCP termed SCP21. SCP21 cells were introduced to mammary fat pads, lungs, and hind limb bones to establish tumors. After 6 weeks, entrained cancer cells were extracted from these organs for further experiments (Figure 6A). We used intra-cardiac injection to simultaneously deliver cancer cells to multiple organs (Figure 6A). Compared to the mammary fat pad- and lung-entrained counterparts, bone-entrained SCP21 was more capable of colonizing distant organs and gave rise to much higher tumor burden in multiple sites as determined by bioluminescence (Figures 6A–6C). In mice subjected to dissection and *ex vivo* bioluminescent imaging, significantly more and bigger lesions were observed from mice received bone-entrained SCP21 cells in both skeletal and visceral tissues (Figures S6C–S6E), suggesting an increase of overall metastatic capacity rather than bone tropism in tumor cells exposed to bone environment.

Inspired by the accompanied study (Bado et al., 2021), we examined stemness markers (Al-Hajj et al., 2003; Charafe-Jauffret et al., 2009) of SCP21 cells entrained in different microenvironments. Interestingly, bone-entrained cells appeared to express a higher level of both ALDH1 activity and CD44 expression (Figures 6D and 6E). In addition, bone-entrained SCP21 cells increased expression of multiple proteins involved in epithelial-mesenchymal transition (EMT) and in pathways shown to mediate the effects of bone microenvironment on ER^+ cancer cells in our accompanied study, including FGFR1, PDGFRβ, EZH2, SLUG, and ZEB1 (Figures 6F and S6F). These data suggest that similar mechanisms may be at work to induce cancer cell stemness and plasticity in this ER^- model.

Indeed, when the same approaches were applied to the SCP2 derivatives of MCF7 cells. Bone entrained MCF7-SCP2 cells showed increased initial survival and faster metastatic growth after intra-cardiac injection (Figures 6G–6I) and increased level of ALDH1 activity and CD44 expression (Figures 6J and 6K). In this epithelial model, we also observed a hybrid EMT phenotype (Figure S6G), as also elaborated in our associated study (Bado et al., 2021). It should be noted that, in this series of experiments, lung-derived subline was not developed due to the lack of lung colonization for MCF7-SCP2 cells.

In addition to cancer cells that are manually extracted from various organs, we examined naturally occurred circulating tumor cells (CTCs) emitted from bone lesions versus mammary tumors. Not surprisingly, bone lesions generated a higher number of CTCs, probably due to the more permeable vascular structures or survival advantage conferred by the bone.

Figure 5. NMF analysis of evolving barcodes delineates metastatic spread

(A and B) Plots of NMF rank survey, consensus matrix, basis components matrix and mixture coefficients matrix of 200 NMF runs on the barcodes from MDA-MB-231 metastatic lesions.

(C) Body map depicting the basis composition of MDA-MB-231 metastatic lesions.

(D) Chord diagrams illustrating the composition flow of barcode mutations between primary tumors and selected MDA-MB-231 metastatic lesions.

(E) Correlation plot of Shannon entropy and tumor burden on MDA-MB-231 samples. The tumor burden was indicated by human genomic content determined by q-PCR. Spearman r and p values were indicated.

See also Figure S5.

Please cite this article in press as: Zhang et al., The bone microenvironment invigorates metastatic seeds for further dissemination, Cell (2021), https://doi.org/10.1016/j.cell.2021.03.011

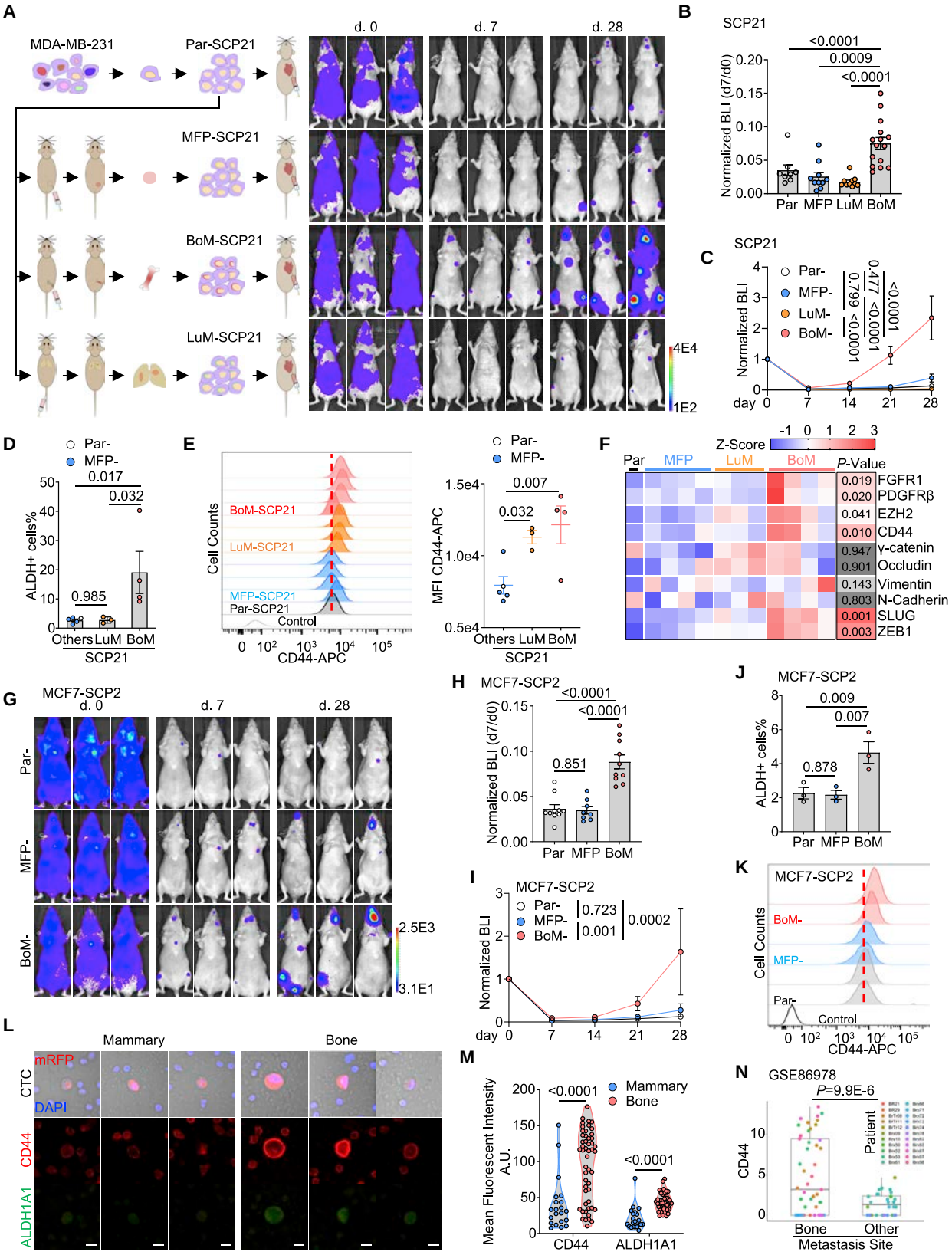

(legend on next page)

Please cite this article in press as: Zhang et al., The bone microenvironment invigorates metastatic seeds for further dissemination, Cell (2021), https://doi.org/10.1016/j.cell.2021.03.011

However, on top of the higher number, CTCs from bone lesions also express higher quantity of CD44 and ALDH1 (Figures 6L and 6M), suggesting increased stemness.

Finally, we also interrogated CD44 expression in a single-cell RNA sequencing (RNA-seq) dataset of CTCs derived from breast cancer patients. When patients were divided into two groups—those carrying bone metastasis versus those carrying other metastases, significantly higher expression of CD44 was observed in the former (Figure 6N) (Aceto et al., 2018), providing clinical support for our hypothesis that the bone microenvironment promotes tumor cell stemness and plasticity, and thereby invigorate further metastasis.

EZH2 in cancer cells orchestrates the effect of bone microenvironment in secondary metastasis

Because EZH2 was revealed to play a central role in loss of ER and gain of plasticity in ER$^+$ models in the accompanied study (Bado et al., 2021), we asked if it also mediates secondary metastasis. The frequency of ALDH1$^+$ cells and the expression of mesenchymal and stemness markers in bone-entrained SCP21 cells were also significantly decreased upon treatment of an EZH2 inhibitor (EPZ) used in our accompanied study (Figures S7A–S7C), supporting EZH2 as an upstream regulator the observed phenotypic shift.

In addition to expression, we used an EZH2 target gene signature (Lu et al., 2010) to deduce EZH2 activities. This signature was then applied to RNA-seq transcriptomic profiling of SCP21 cells subjected to various treatments or entrained in different organs. EPZ treatment relieved the suppression of signature genes, resulting in higher expression (Figure S7D), which supported the validity of the signature. We then compared cells entrained in bone lesions versus mammary gland tumors or lung metastasis and observed significantly higher EZH2 activity in the bone-entrained cells (Figure 7A). Importantly, bone-induced changes to both EZH2 activity and frequency of ALDH1$^+$ cells appeared to be reversible, as *in vitro* passages led to progressive loss of these traits (Figures 7B and 7C). Other bone microenvironment-induced factors upstream of EZH2 (e.g., FGFR1 and PDGFRβ) (Kottakis et al., 2011; Yue et al., 2019) also exhibited transient increased expression in bone-entrained cells (Figures 7D and S7E). Taken together, these data further suggest the potential role of EZH2 in secondary metastasis from bone lesions.

Remarkably, transient treatment of EPZ before intra-cardiac injection, which did not suppress the growth of tumor cells *in vitro* (Figure S7F), completely abolished the enhanced metastasis of bone-entrained SCP21 cells (Figures 7E–7G) and MCF7-SCP2 cells (Figures 7H–7K) *in vivo*, again demonstrating that the observed effects of bone microenvironment is not through clonal selection, but rather epigenomic reprogramming driven by EZH2.

Finally, to confirm the cancer cell-intrinsic role of EZH2 during this process, we generated inducible knockdown of EZH2 (Figure S7G), that also slightly affected downstream expression of plasticity factors and stem cell markers (Figures S7G and S7H), but did not alter cancer cell growth rate *in vitro* (Figure S7I). Induction of knockdown was initiated after bone lesions were introduced for one week (Figures 7L, and S7J). Interestingly, whereas EZH2 knockdown did not alter primary bone lesion development (Figure 7M), it dramatically reduced secondary metastasis to other organs (Figure 7N). Taken together, these aforementioned results strongly implicate EZH2 as a master regulator of secondary metastases from bone lesions.

DISCUSSION

In this study, based on the IIA injection technique and through multiple independent approaches, we demonstrated that the bone microenvironment not only permits cancer cells to further disseminate but also appears to augment this process. A key question that remains is the timing of secondary metastasis spread out of the initial bone lesions: whether this occurs before or after the bone lesions become symptomatic and clinically detectable. The answer will determine if therapeutic interventions should be implemented in adjuvant or metastatic settings, respectively. Moreover, if further seeding occurs before bone lesions become overt, it raises the possibility that metastases in other organs might arise from asymptomatic bone metastases, which might warrant further investigations. Indeed, it has been reported that DTCs in bone marrow of early breast cancer patients enrich stem cell-like population (Alix-Panabieres et al.,

Figure 6. Bone-entraining boosts the metastatic capacity of single cell-derived cancer cells

(A) Experimental design (left) and representative BLI images (right) to test the metastatic capacity of mammary, lung, or bone-entrained SCP21s.

(B) Normalized whole-body BLI intensity 7 days after intra-cardiac (IC) injection of same number of MFP-, LuM-, BoM-, or Par-SCP21 cells.

(C) Colonization kinetics of MFP-, LuM-, BoM-, and Par-SCP21 cells after IC injection. n (# of mice) = 8 (Par); 10 (MFP); 15 (BoM); 10 (LuM).

(D) Percentage of ALDH$^+$ population in MFP-, LuM-, BoM-, and Par-SCP21 cells by flow cytometry.

(E) Histogram (left) and median fluorescent intensity (MFI) (right) of surface CD44 protein in MFP-, LuM-, BoM- and Par-SCP21 cells by flow cytometry.

(F) Expression levels of proteins in Par- and organ-entrained SCP21s. Protein levels were quantified and converted into *Z* score from three or four western blottings.

(G–I) Representative BLI images (G), normalized BLI intensity at day 7 (H), and the colonization kinetics (I) of MFP-, BoM-, and Par- MCF7-SCP2 cells after I.C. injection. n (# of mice) = 10 (Par); 8 (MFP); 10 (BoM).

(J and K) Percentage of ALDH$^+$ population (J) and expression of surface CD44 (K) in MFP-, BoM-, and Par- MCF7-SCP2 cells by flow cytometry. n (# of repeats) = 3 (J); 2 (K).

(L and M) Representative fluorescent images (L) and quantification (M) of CD44 and ALDH1A1 expression on CTCs from NRG mice bearing MDA-MB-231 cells derived mammary or bone tumors. CTCs were pooled from 5 blood samples. Scale bar, 10 μm.

(N) Expression levels of CD44 mRNA in CTCs from breast cancer patients with bone metastases or other metastases (GSE86978).

Data are represented as mean ± SEM in (B), (C), (D), (E), (H), (I) and (J). p values were assessed by Fisher's LSD test following one-way ANOVA test in (B), (D), (E), (H), and (J); by Fisher's LSD test post two-way ANOVA test in (C) and (I); by Student's t test in (F); by Mann-Whitney test in (M) and (N).

See also Figure S6.

Please cite this article in press as: Zhang et al., The bone microenvironment invigorates metastatic seeds for further dissemination, Cell (2021), https://doi.org/10.1016/j.cell.2021.03.011

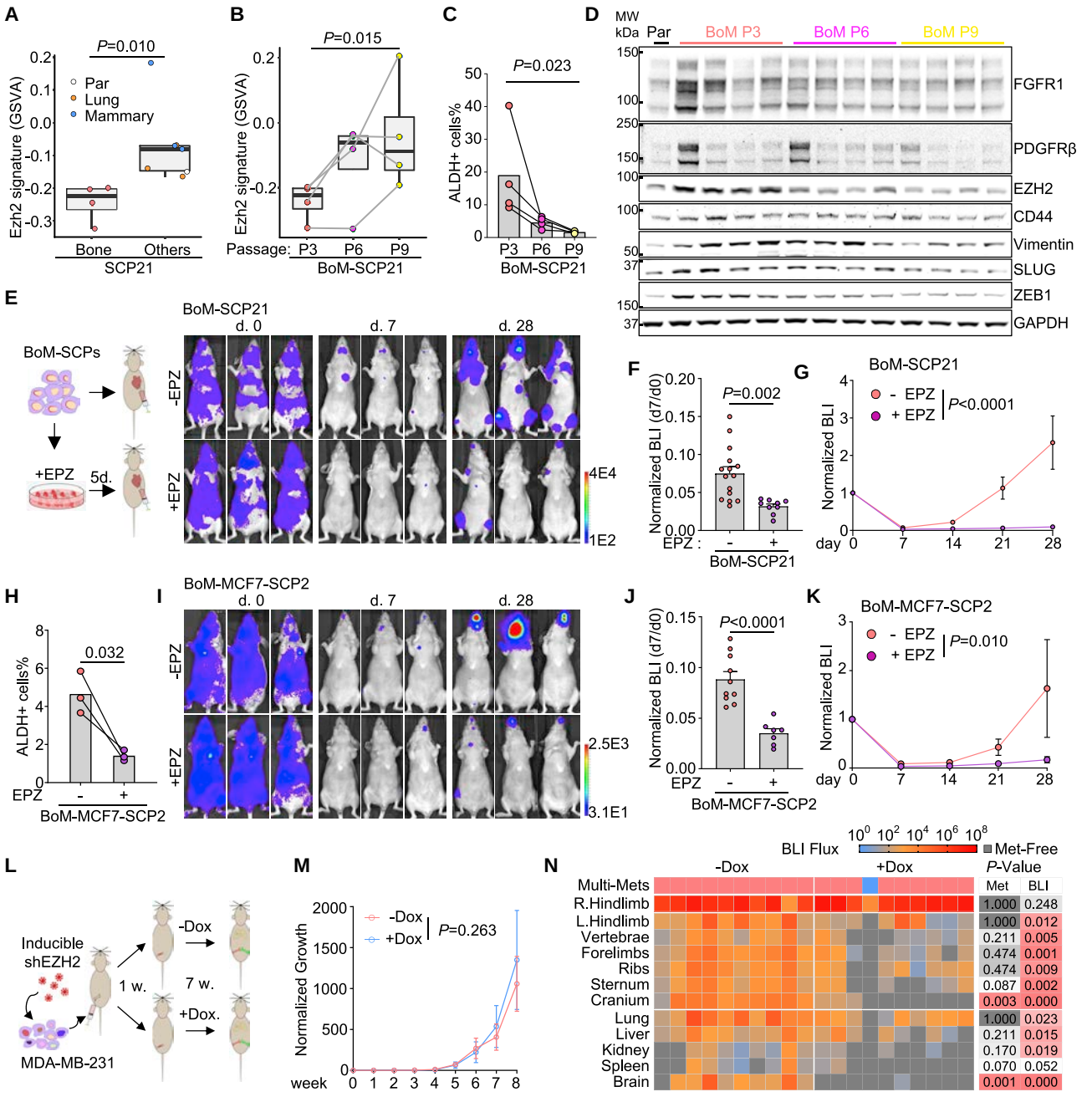

Figure 7. Secondary metastasis from bone lesions is dependent on EZH2 mediated epigenomic reprograming

(A) Levels of EZH2 signature genes (GSVA) in bone entrained and other SCP21 cells.

(B) Levels of EZH2 signature genes in bone entrained-SCP21 cells after different passages *in vitro*.

(C) Percentage of ALDH1$^+$ population in bone entrained-SCP21 cells at different passages.

(D) Representative western blotting of proteins in bone entrained-SCP21 cells after different passages.

(E–G) The schematic diagram and representative BLI images (E), normalized BLI intensity at day 7 (F), and the colonization kinetics (G) of BoM-SCP21 cells with *in vitro* EPZ011989 (EPZ) treatment before IC injection. Non-treated BoM-SCP21 cells were used as control. n (# of mice) = 15 (−EPZ); 9 (+EPZ).

(H) Comparison of ALDH1+ cells in EPZ treated and non-treated BoM-MCF7-SCP2 cells by flow cytometry. n (# of replicate) = 3.

(I–K) Representative BLI images (I), normalized BLI intensity at day 7 (J), and the colonization kinetics (K) of BoM-MCF7-SCP2 cells with *in vitro* treatment of EPZ before IC injection. Non-treated BoM-MCF7-SCP2 cells were used as control. n (# of mice) = 10 (−EPZ); 7 (+EPZ).

(L) Experimental design assessing the multi-site metastases from bone lesions with inducible depletion of EZH2.

(M) Growth kinetics of the primary bone lesions in mice receiving doxycycline or control water, assessed by *in vivo* BLI imaging. BLI intensities at right hindlimbs were normalized to the mean intensity at day 0. n (# of mice) = 10 for each arm.

(legend continued on next page)

Please cite this article in press as: Zhang et al., The bone microenvironment invigorates metastatic seeds for further dissemination, Cell (2021), https://doi.org/10.1016/j.cell.2021.03.011

2007; Balic et al., 2006), supporting that asymptomatic bone micrometastases are potentially capable of metastasizing before being diagnosed. In this study, our evolving barcode strategy exemplified potential metastases from bone to other organs. Interestingly, we found that the putative parental metastases could remain small (Figures 5E and S5E), which may suggest that further dissemination might occur before diagnosis of existing lesions. Future studies will be needed to precisely determine the onset of secondary metastasis from bones.

The fact that the genetically homogeneous SCP cells became more metastatic after lodging into the bone microenvironment suggests a mechanism distinct from genetic selection. Remarkably, this phenotype persists even after *in vitro* expansion, so it is relatively stable and suggests an epigenomic reprogramming process. We propose that this epigenetic mechanism may act in concert with the genetic selection process. Specifically, the organ-specific metastatic traits may pre-exist in cancer cell populations (Minn et al., 2005; Zhang et al., 2013) and determine the first site of metastatic seeding. The epigenomic alterations will then occur once interactions with specific microenvironment niches are established and when cancer cells become exposed chronically to the foreign milieu of distant organs. Our data suggest that such alterations drive a second wave of metastases in a less organ-specific manner. This may explain why terminal stage of breast cancer is often associated with multiple metastases (Disibio and French, 2008).

Here, we suggested that the enhanced EZH2 activity underpins the epigenetic reprograming of tumor cells in bone microenvironment for further metastases. EZH2 maintains the de-differentiated and stem cell-like status of breast cancer cells by repressing the lineage-specific transcriptional programs (Chang et al., 2011; Gonzalez et al., 2014). Pharmacologically or genetically targeting EZH2 has been reported to inhibit tumor growth, therapeutic resistance, and metastases with different efficacies in preclinical models (Hirukawa et al., 2018; Ku et al., 2017; Ma et al., 2020; Zhang et al., 2020). It was noted that in our models, EZH2 inhibition could not suppress the cell growth *in vitro* or in the primary injection site, whereas both the transient treatment of EZH2 inhibitor or inducible knockdown of EZH2 in cancer cells dramatically decreased secondary metastasis, suggesting targeting EZH2 may block the metastatic spread rather than the tumor growth.

In the clinic, some bone metastases can be managed for years without further progression, while others quickly develop therapeutic resistance and are associated with subsequent metastases in other organs (Coleman, 2006). These different behaviors may suggest different subtypes of cancers that are yet to be characterized and distinguished. Alternatively, there may be a transition between these phenotypes. In fact, depending on different interaction partners, the same cancer cells may exist in different status in the bone. For instance, although endothelial cells may keep cancer cells in dormancy (Ghajar et al., 2013; Price et al., 2016), osteogenic cells promote their proliferation and progression toward micrometastases (Wang et al., 2015, 2018). Therefore, it is possible that the transition from indolent to aggressive behaviors is underpinned by an alteration of specific microenvironment niches. Detailed analyses of such alteration will lead to unprecedented insights into the metastatic progression.

Limitations the study

In this study, we did not provide direct clinical evidence that bone metastasis can seed other metastases in cancer patients. Although this is reported in several previous studies (Brown et al., 2017; Gundem et al., 2015; Ullah et al., 2018), the prevalence of secondary metastases seeded from bone lesions remains to be determined in patients. Future genomic studies with improved depth and informatics will likely dissect this process in greater depth and elucidate spatiotemporal paths of metastasis. The evolving barcode strategy was useful in tracing metastatic evolution. The most striking and robust finding from these experiments is that genetically closely related metastases do not localize in the same type of tissues and are usually highly distinct from orthotopic tumors. This in principle argues against independent seeding events from primary tumors and supports metastasis-to-metastasis seeding. However, the deduction of specific parental-child relationship based on Shannon entropy is intuitive and qualitative, and needs to be analyzed by more quantitative models in future work.

We principally demonstrated that compared to lungs, bones are more capable of promoting secondary metastasis. However, further studies will be required to determine whether other organs, such as liver and lymph nodes, might also exert similar effects on metastatic spread. We postulate that two factors may regulate an organ's capacity to promote secondary metastases. First, the initial wave of organotropic metastasis will pose a selection of metastatic seeds that arrive and survive in a specific organ. Second, the subsequent interactions with resident cells will induce adaptive epigenetic changes on top of the genetic selection, which together dictate whether the metastatic journey may extend to other organs.

Although data presented in this study indicate that cancer cells colonizing the bone acquire intrinsic traits for further dissemination, we cannot rule out systemic effects that may also contribute to this process. At the late stage, bone metastases are known to cause strong systemic abnormality such as cachexia (Waning et al., 2015), which may influence secondary metastasis. Even at early stages before bone metastases stimulate severe symptoms, the disturbance of micrometastases to hematopoietic cell niches may mobilize certain blood cells to migrate to distant organs, which may in turn result in altered metastatic behaviors (Peinado et al., 2017). These possibilities will need to be tested in future research.

(N) Heatmap of *ex vivo* BLI intensity and status of metastatic involvement in tissues from animals with EZH2 depleted or control bone metastases.
Data are represented as mean ± SEM in (F), (G), (J), (K), and (M). p values were assessed by Student's t test in (A), (F), and (J); by test for linear trend following repeat measure one-way ANOVA in (B) and (C); by LSD test following two-way ANOVA in (G), (K), and (M); by ratio paired t test in (H); by Fisher's exact test on the ratio of metastatic involvement and Mann-Whitney test on BLI intensity in (N).
See also Figure S7.

STAR★METHODS

Detailed methods are provided in the online version of this paper and include the following:

- KEY RESOURCES TABLE
- RESOURCE AVAILABILITY
  - Lead contact
  - Materials availability
  - Data and code availability
- EXPERIMENTAL MODEL AND SUBJECT DETAILS
  - Cell lines and Cell Culture
  - Animals
- METHOD DETAILS
  - Plasmid Construction
  - Lentiviral Production and Transduction
  - *In vitro* activation of hgRNA barcodes
  - Intra-iliac artery and Intra-iliac vein Injection
  - Intra-femoral and Intra-Cardiac Injection
  - Mammary Fat Pad and Intra-Ductal Injection
  - Parabiosis and Reverse Procedure
  - *In vivo* activation of hgRNA barcodes
  - Bioluminescence Imaging and Tissue Collection
  - Small Animal PET-CT Scanning
  - Deep Imaging of Intact Tissues
  - Immunofluorescent Staining
  - Genomic DNA Extraction from Tissues and Cells
  - Amplification and Sequencing of hgRNA Barcodes
  - Evolving Barcode Data Processing
  - Non-negative matrix factorization analysis
  - Assessment of Metastasis of Organ-entrained SCPs
  - Flow Cytometry
  - RNA and Protein Extraction and Quantification
  - RNA-Sequencing and Whole Exome Sequencing
  - Capture and Staining of CTCs
- QUANTIFICATION AND STATISTICAL ANALYSIS

SUPPLEMENTAL INFORMATION

Supplemental information can be found online at https://doi.org/10.1016/j.cell.2021.03.011.

ACKNOWLEDGMENTS

We would like to thank Zhang Laboratory members Dr. Lin Tian and Dr. Reza Kalhor for insightful discussion. Thanks also go to Epizyme (Cambridge, MA) for providing the EZH2 inhibitor EPZ-011989. We also acknowledge the Pathology Core of Lester and Sue Smith Breast Center, the Optical Imaging & Vital Microscopy (OiVM) core, the Genomic and RNA profiling core at Baylor College of Medicine, and Small Animal Imaging Facility (SAIF) core at Texas Children Hospital. X.H.-F.Z. is supported by US Department of Defense (DAMD W81XWH-16-1-0073 and DAMD W81XWH-20-1-0375), NCI (CA183878, CA227904, CA221946, and CA251950), the Breast Cancer Research Foundation, and McNair Foundation. S.S. is a recipient of CPRIT Training Grant (RP160283). S.T.C.W. and Jiasong Li are supported in part by NCI (U01CA252553), the John S. Dunn Research Foundation, and T.T. and W.F. Chao Center for BRAIN. C.C. is supported by the CPRIT Scholar Award (RR160009). This project was supported by the RNA In Situ Hybridization Core with a Shared Instrumentation grant from the NIH (1S10OD016167), the Cytometry and Cell Sorting Core with funding from the CPRIT Core Facility Support Award (CPRIT-RP180672), and the expert assistance of Dr. Cecilia Ljungberg and Joel M. Sederstrom at Baylor College of Medicine.

AUTHOR CONTRIBUTIONS

Conceptualization and Methodology, W.Z., I.L.B., J.H., H.W., Z.L., and X.H.-F.Z.; Investigation, Formal Analysis and Validation, W.Z., I.L.B., J.H., Y.-W.W., L.W., H.W., Y.G., Z.X., X.H., B.M.L., R.A.-O., L.L., Jiasong Li, L.Y., H.C.L., M.N., Jun Liu, W.J., Z.L., and X.H.-F.Z.; Resources, Y.L., S.T.C.W., C.C., Z.L., and X.H.-F.Z.; Software, Data Curation, and Visualization, W.Z., I.L.B., J.H., Y.-W.W., H.-H.J., R.A.-O., L.L, S.S., Z.L., and X.H.-F.Z.; Writing – Original Draft, W.Z., I.L.B., J.H., and X.H.-F.Z.; Writing – Review & Editing, W.Z., H.C.L., S.T.C.W., and X.H.-F.Z.; Supervision, X.H.-F.Z.; Project Administration, W.Z. and X.H.-F.Z.; Funding Acquisition, S.T.C.W., C.C., and X.H.-F.Z.

DECLARATION OF INTERESTS

The authors declare no competing interests.

Received: September 12, 2019
Revised: November 30, 2020
Accepted: March 4, 2021
Published: April 19, 2021

REFERENCES

Aceto, N., Bardia, A., Wittner, B.S., Donaldson, M.C., O'Keefe, R., Engstrom, A., Bersani, F., Zheng, Y., Comaills, V., Niederhoffer, K., et al. (2018). AR expression in breast cancer CTCs associates with bone metastases. Mol. Cancer Res. *16*, 720–727.

Afgan, E., Baker, D., Batut, B., van den Beek, M., Bouvier, D., Cech, M., Chilton, J., Clements, D., Coraor, N., Grüning, B.A., et al. (2018). The Galaxy platform for accessible, reproducible and collaborative biomedical analyses: 2018 update. Nucleic Acids Res. *46* (W1), W537–W544.

Al-Hajj, M., Wicha, M.S., Benito-Hernandez, A., Morrison, S.J., and Clarke, M.F. (2003). Prospective identification of tumorigenic breast cancer cells. Proc. Natl. Acad. Sci. USA *100*, 3983–3988.

Alix-Panabières, C., Vendrell, J.-P., Pellé, O., Rebillard, X., Riethdorf, S., Müller, V., Fabbro, M., and Pantel, K. (2007). Detection and characterization of putative metastatic precursor cells in cancer patients. Clin. Chem. *53*, 537–539.

Andor, N., Harness, J.V., Müller, S., Mewes, H.W., and Petritsch, C. (2014). EXPANDS: expanding ploidy and allele frequency on nested subpopulations. Bioinformatics *30*, 50–60.

Bado, I.L., Zhang, W., Hu, J., Xu, Z., Wang, H., Sarkar, P., Li, L., Wan, Y.-W., Liu, J., Wu, W., et al. (2021). Impact of the bone microenvironment on phenotypic plasticity of ER+ breast cancer cells. Dev. Cell *56*, 1100–1117.

Balic, M., Lin, H., Young, L., Hawes, D., Giuliano, A., McNamara, G., Datar, R.H., and Cote, R.J. (2006). Most early disseminated cancer cells detected in bone marrow of breast cancer patients have a putative breast cancer stem cell phenotype. Clin. Cancer Res. *12*, 5615–5621.

Barger, C.J., Branick, C., Chee, L., and Karpf, A.R. (2019). Pan-Cancer Analyses Reveal Genomic Features of FOXM1 Overexpression in Cancer. Cancers (Basel) *11*, 251.

Bos, P.D., Zhang, X.H.F., Nadal, C., Shu, W., Gomis, R.R., Nguyen, D.X., Minn, A.J., van de Vijver, M.J., Gerald, W.L., Foekens, J.A., and Massagué, J. (2009). Genes that mediate breast cancer metastasis to the brain. Nature *459*, 1005–1009.

Boyce, B.F., Yoneda, T., and Guise, T.A. (1999). Factors regulating the growth of metastatic cancer in bone. Endocr. Relat. Cancer *6*, 333–347.

Brown, D., Smeets, D., Székely, B., Larsimont, D., Marcell Szász, A., Adnet, P.Y., Rothé, F., Rouas, G., Nagy, Z.I., Faragó, Z., et al. (2017). Phylogenetic analysis of metastatic progression in breast cancer using somatic mutations and copy number aberrations. Nat. Commun. *8*, 25–29.

Chang, C.J., Yang, J.Y., Xia, W., Chen, C.T., Xie, X., Chao, C.H., Woodward, W.A., Hsu, J.M., Hortobagyi, G.N., and Hung, M.C. (2011). EZH2 promotes expansion of breast tumor initiating cells through activation of RAF1-β-catenin signaling. Cancer Cell *19*, 86–100.

Charafe-Jauffret, E., Ginestier, C., Iovino, F., Wicinski, J., Cervera, N., Finetti, P., Hur, M.H., Diebel, M.E., Monville, F., Dutcher, J., et al. (2009). Breast cancer cell lines contain functional cancer stem cells with metastatic capacity and a distinct molecular signature. Cancer Res. *69*, 1302–1313.

Coleman, R.E. (2006). Clinical features of metastatic bone disease and risk of skeletal morbidity. Clin. Cancer Res. *12*, 6243s–6249s.

Coleman, R.E., and Rubens, R.D. (1987). The clinical course of bone metastases from breast cancer. Br. J. Cancer *55*, 61–66.

Coleman, R.E., Smith, P., and Rubens, R.D. (1998). Clinical course and prognostic factors following bone recurrence from breast cancer. Br. J. Cancer *77*, 336–340.

Coleman, R.E., Guise, T.A., Lipton, A., Roodman, G.D., Berenson, J.R., Body, J.J., Boyce, B.F., Calvi, L.M., Hadji, P., McCloskey, E.V., et al. (2008). Advancing treatment for metastatic bone cancer: consensus recommendations from the Second Cambridge Conference. Clin. Cancer Res. *14*, 6387–6395.

Deroose, C.M., De, A., Loening, A.M., Chow, P.L., Ray, P., Chatziioannou, A.F., and Gambhir, S.S. (2007). Multimodality imaging of tumor xenografts and metastases in mice with combined small-animal PET, small-animal CT, and bioluminescence imaging. J. Nucl. Med. *48*, 295–303.

Disibio, G., and French, S.W. (2008). Metastatic patterns of cancers: results from a large autopsy study. Arch. Pathol. Lab. Med. *132*, 931–939.

Echeverria, G.V., Powell, E., Seth, S., Ge, Z., Carugo, A., Bristow, C., Peoples, M., Robinson, F., Qiu, H., Shao, J., et al. (2018). High-resolution clonal mapping of multi-organ metastasis in triple negative breast cancer. Nat. Commun. *9*, 5079.

Esposito, M., Guise, T., and Kang, Y. (2018). The Biology of Bone Metastasis. Cold Spring Harb. Perspect. Med. *8*, a031252.

Gaujoux, R., and Seoighe, C. (2010). A flexible R package for nonnegative matrix factorization. BMC Bioinformatics *11*, 367.

Ghajar, C.M., Peinado, H., Mori, H., Matei, I.R., Evason, K.J., Brazier, H., Almeida, D., Koller, A., Hajjar, K.A., Stainier, D.Y.R., et al. (2013). The perivascular niche regulates breast tumour dormancy. Nat. Cell Biol. *15*, 807–817.

Gonzalez, M.E., Moore, H.M., Li, X., Toy, K.A., Huang, W., Sabel, M.S., Kidwell, K.M., and Kleer, C.G. (2014). EZH2 expands breast stem cells through activation of NOTCH1 signaling. Proc. Natl. Acad. Sci. USA *111*, 3098–3103.

Gundem, G., Van Loo, P., Kremeyer, B., Alexandrov, L.B., Tubio, J.M.C., Papaemmanuil, E., Brewer, D.S., Kallio, H.M.L., Högnäs, G., Annala, M., et al.; ICGC Prostate Group (2015). The evolutionary history of lethal metastatic prostate cancer. Nature *520*, 353–357.

Gupta, P.B., Pastushenko, I., Skibinski, A., Blanpain, C., and Kuperwasser, C. (2019). Phenotypic Plasticity: Driver of Cancer Initiation, Progression, and Therapy Resistance. Cell Stem Cell *24*, 65–78.

Hirukawa, A., Smith, H.W., Zuo, D., Dufour, C.R., Savage, P., Bertos, N., Johnson, R.M., Bui, T., Bourque, G., Basik, M., et al. (2018). Targeting EZH2 reactivates a breast cancer subtype-specific anti-metastatic transcriptional program. Nat. Commun. *9*, 2547.

Hu, J., Al-Ouran, R., Zhang, X., Liu, Z., and Jeong, H.-H. (2020). TraceQC: An R package for quality control of CRISPR lineage tracing data. bioRxiv, doi: 2020.06.05.137141.

Juárez, P., and Guise, T.A. (2011). TGF-β in cancer and bone: implications for treatment of bone metastases. Bone *48*, 23–29.

Kalhor, R., Mali, P., and Church, G.M. (2017). Rapidly evolving homing CRISPR barcodes. Nat. Methods *14*, 195–200.

Kalhor, R., Kalhor, K., Mejia, L., Leeper, K., Graveline, A., Mali, P., and Church, G.M. (2018). Developmental barcoding of whole mouse via homing CRISPR. Science *361*, eaat9804.

Kamran, P., Sereti, K.I., Zhao, P., Ali, S.R., Weissman, I.L., and Ardehali, R. (2013). Parabiosis in mice: a detailed protocol. J. Vis. Exp. (80), 50556.

Kang, Y., Siegel, P.M., Shu, W., Drobnjak, M., Kakonen, S.M., Cordón-Cardo, C., Guise, T.A., and Massagué, J. (2003). A multigenic program mediating breast cancer metastasis to bone. Cancer Cell *3*, 537–549.

Kennecke, H., Yerushalmi, R., Woods, R., Cheang, M.C.U., Voduc, D., Speers, C.H., Nielsen, T.O., and Gelmon, K. (2010). Metastatic behavior of breast cancer subtypes. J. Clin. Oncol. *28*, 3271–3277.

Kim, M.Y., Oskarsson, T., Acharyya, S., Nguyen, D.X., Zhang, X.H.F., Norton, L., and Massagué, J. (2009). Tumor self-seeding by circulating cancer cells. Cell *139*, 1315–1326.

Kingsley, L.A., Fournier, P.G.J., Chirgwin, J.M., and Guise, T.A. (2007). Molecular biology of bone metastasis. Mol. Cancer Ther. *6*, 2609–2617.

Koboldt, D.C., Zhang, Q., Larson, D.E., Shen, D., McLellan, M.D., Lin, L., Miller, C.A., Mardis, E.R., Ding, L., and Wilson, R.K. (2012). VarScan 2: somatic mutation and copy number alteration discovery in cancer by exome sequencing. Genome Res. *22*, 568–576.

Kottakis, F., Polytarchou, C., Foltopoulou, P., Sanidas, I., Kampranis, S.C., and Tsichlis, P.N. (2011). FGF-2 regulates cell proliferation, migration, and angiogenesis through an NDY1/KDM2B-miR-101-EZH2 pathway. Mol. Cell *43*, 285–298.

Ku, S.Y., Rosario, S., Wang, Y., Mu, P., Seshadri, M., Goodrich, Z.W., Goodrich, M.M., Labbé, D.P., Gomez, E.C., Wang, J., et al. (2017). Rb1 and Trp53 cooperate to suppress prostate cancer lineage plasticity, metastasis, and antiandrogen resistance. Science *355*, 78–83.

Li, H., Handsaker, B., Wysoker, A., Fennell, T., Ruan, J., Homer, N., Marth, G., Abecasis, G., and Durbin, R.; 1000 Genome Project Data Processing Subgroup (2009). The Sequence Alignment/Map format and SAMtools. Bioinformatics *25*, 2078–2079.

Lu, C., Han, H.D., Mangala, L.S., Ali-Fehmi, R., Newton, C.S., Ozbun, L., Armaiz-Pena, G.N., Hu, W., Stone, R.L., Munkarah, A., et al. (2010). Regulation of tumor angiogenesis by EZH2. Cancer Cell *18*, 185–197.

Ma, A., Stratikopoulos, E., Park, K.S., Wei, J., Martin, T.C., Yang, X., Schwarz, M., Leshchenko, V., Rialdi, A., Dale, B., et al. (2020). Discovery of a first-in-class EZH2 selective degrader. Nat. Chem. Biol. *16*, 214–222.

Martin, M. (2011). Cutadapt removes adapter sequences from high-throughput sequencing reads. EMBnet. J. *17*, 10.

Minn, A.J., Kang, Y., Serganova, I., Gupta, G.P., Giri, D.D., Doubrovin, M., Ponomarev, V., Gerald, W.L., Blasberg, R., and Massagué, J. (2005). Distinct organ-specific metastatic potential of individual breast cancer cells and primary tumors. J. Clin. Invest. *115*, 44–55.

Nguyen, D.-A., Beeman, N., Lewis, M., Schaack, J., and Neville, M.C. (2000). Intraductal Injection into the Mouse Mammary Gland. In Methods in Mammary Gland Biology and Breast Cancer Research (Springer US), pp. 259–270.

Peinado, H., Zhang, H., Matei, I.R., Costa-Silva, B., Hoshino, A., Rodrigues, G., Psaila, B., Kaplan, R.N., Bromberg, J.F., Kang, Y., et al. (2017). Pre-metastatic niches: organ-specific homes for metastases. Nat. Rev. Cancer *17*, 302–317.

Price, T.T., Burness, M.L., Sivan, A., Warner, M.J., Cheng, R., Lee, C.H., Olivere, L., Comatas, K., Magnani, J., Kim Lyerly, H., et al. (2016). Dormant breast cancer micrometastases reside in specific bone marrow niches that regulate their transit to and from bone. Sci. Transl. Med. *8*, 340ra73.

Sflomos, G., Dormoy, V., Metsalu, T., Jeitziner, R., Battista, L., Scabia, V., Raffoul, W., Delaloye, J.-F., Treboux, A., Fiche, M., et al. (2016). A Preclinical Model for ERα-Positive Breast Cancer Points to the Epithelial Microenvironment as Determinant of Luminal Phenotype and Hormone Response. Cancer Cell *29*, 407–422.

Smid, M., Wang, Y., Zhang, Y., Sieuwerts, A.M., Yu, J., Klijn, J.G., Foekens, J.A., and Martens, J.W. (2008). Subtypes of breast cancer show preferential site of relapse. Cancer Res. *68*, 3108–3114.

Ullah, I., Karthik, G.M., Alkodsi, A., Kjällquist, U., Stålhammar, G., Lövrot, J., Martinez, N.F., Lagergren, J., Hautaniemi, S., Hartman, J., and Bergh, J. (2018). Evolutionary history of metastatic breast cancer reveals minimal seeding from axillary lymph nodes. J. Clin. Invest. *128*, 1355–1370.

Vanharanta, S., and Massagué, J. (2013). Origins of metastatic traits. Cancer Cell *24*, 410–421.

Wang, H., Yu, C., Gao, X., Welte, T., Muscarella, A.M., Tian, L., Zhao, H., Zhao, Z., Du, S., Tao, J., et al. (2015). The osteogenic niche promotes early-stage bone colonization of disseminated breast cancer cells. Cancer Cell *27*, 193–210.

Wang, H., Tian, L., Liu, J., Goldstein, A., Bado, I., Zhang, W., Arenkiel, B.R., Li, Z., Yang, M., Du, S., et al. (2018). The osteogenic niche is a calcium reservoir of bone micrometastases and confers unexpected therapeutic vulnerability. Cancer Cell *34*, 823–839.e7.

Waning, D.L., Mohammad, K.S., Reiken, S., Xie, W., Andersson, D.C., John, S., Chiechi, A., Wright, L.E., Umanskaya, A., Niewolna, M., et al. (2015). Excess TGF-β mediates muscle weakness associated with bone metastases in mice. Nat. Med. *21*, 1262–1271.

Weilbaecher, K.N., Guise, T.A., and McCauley, L.K. (2011). Cancer to bone: a fatal attraction. Nat. Rev. Cancer *11*, 411–425.

Ye, X., and Weinberg, R.A. (2015). Epithelial-Mesenchymal Plasticity: A Central Regulator of Cancer Progression. Trends Cell Biol. *25*, 675–686.

Yu, C., Wang, H., Muscarella, A., Goldstein, A., Zeng, H.C., Bae, Y., Lee, B.H.I., and Zhang, X.H.F. (2016). Intra-iliac artery injection for efficient and selective modeling of microscopic bone metastasis. J. Vis. Exp. *2016*, 1–7.

Yue, Z., Chen, J., Lian, H., Pei, J., Li, Y., Chen, X., Song, S., Xia, J., Zhou, B., Feng, J., et al. (2019). PDGFR-β Signaling Regulates Cardiomyocyte Proliferation and Myocardial Regeneration. Cell Rep. *28*, 966–978.e4.

Zhang, X.H.F., Jin, X., Malladi, S., Zou, Y., Wen, Y.H., Brogi, E., Smid, M., Foekens, J.A., and Massagué, J. (2013). Selection of bone metastasis seeds by mesenchymal signals in the primary tumor stroma. Cell *154*, 1060–1073.

Zhang, L., Yao, J., Wei, Y., Zhou, Z., Li, P., Qu, J., Badu-Nkansah, A., Yuan, X., Huang, Y.W., Fukumura, K., et al. (2020). Blocking immunosuppressive neutrophils deters pY696-EZH2-driven brain metastases. Sci. Transl. Med. *12*, 5387.

Article

Developmental Cell

The bone microenvironment increases phenotypic plasticity of ER+ breast cancer cells

Graphical abstract

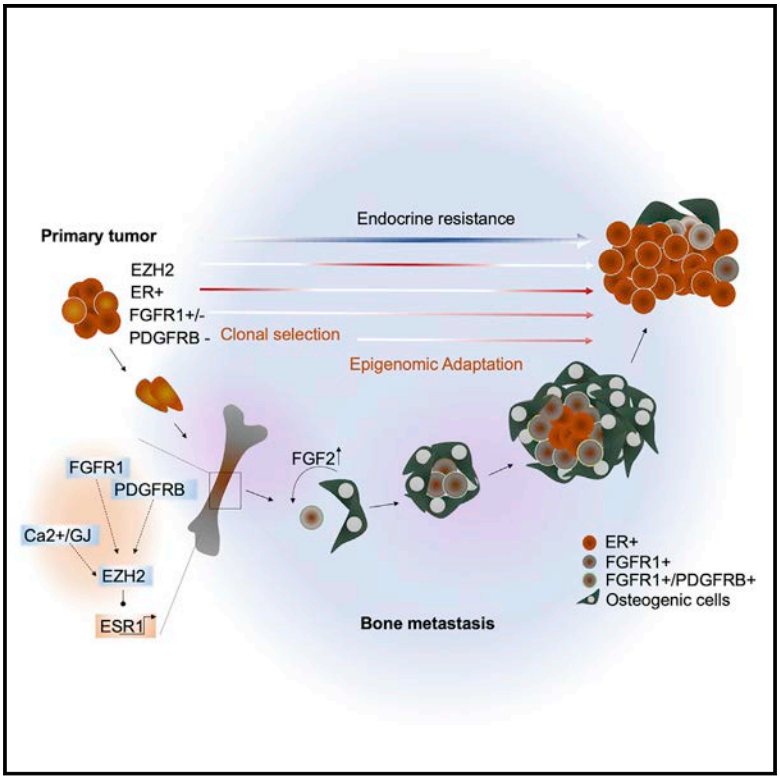

Highlights

- ER+ breast cancer cells transiently reduce ER expression in bone micrometastases
- Interaction with osteogenic cells causes reversible ER loss and endocrine resistance
- Epigenomic mechanisms lead to ER reduction, cancer stemness, and cellular plasticity
- EZH2 mediates the impact of bone and is a target to alleviate endocrine resistance

Authors

Igor L. Bado, Weijie Zhang, Jingyuan Hu, ..., Zbigniew Gugala, Zhandong Liu, Xiang H.-F. Zhang

Correspondence

xiangz@bcm.edu

In brief

Bado et al. demonstrate that the osteogenic niche enhances the phenotypic plasticity of metastatic ER+ breast cancer cells through an EZH2-mediated epigenomic reprogramming. The resulting spatiotemporal heterogeneity of ER expression leads to increased stemness and endocrine resistance. Targeting EZH2 restores endocrine sensitivity and synergizes with standard anti-ER therapies.

Bado et al., 2021, Developmental Cell *56*, 1100–1117
April 19, 2021
https://doi.org/10.1016/j.devcel.2021.03.008

CellPress

CellPress

Developmental Cell

Article

The bone microenvironment increases phenotypic plasticity of ER+ breast cancer cells

Igor L. Bado,[1,2,3,11] Weijie Zhang,[1,2,3,11] Jingyuan Hu,[4,5,6] Zhan Xu,[1,2,3] Hai Wang,[1,2,3] Poonam Sarkar,[5] Lucian Li,[5,6] Ying-Wooi Wan,[5,6,7] Jun Liu,[1,2,3] William Wu,[7] Hin Ching Lo,[1,2,3] Ik Sun Kim,[1,2,3] Swarnima Singh,[2,3] Mahnaz Janghorban,[2,3] Aaron M. Muscarella,[1,2,3] Amit Goldstein,[1,2,3] Purba Singh,[1,2,3] Hyun-Hwan Jeong,[8] Chaozhong Liu,[5,6] Rachel Schiff,[1,2] Shixia Huang,[3] Matthew J. Ellis,[1,2,3] M. Waleed Gaber,[5] Zbigniew Gugala,[9] Zhandong Liu,[6,7] and Xiang H.-F. Zhang[1,2,3,10,12,*]

[1]Lester and Sue Smith Breast Center, Baylor College of Medicine, One Baylor Plaza, Houston, TX 77030, USA
[2]Dan L. Duncan Cancer Center, Baylor College of Medicine, One Baylor Plaza, Houston, TX 77030, USA
[3]Department of Molecular and Cellular Biology, Baylor College of Medicine, One Baylor Plaza, Houston, TX 77030, USA
[4]Program in Quantitative and Computational Biosciences, Baylor College of Medicine, One Baylor Plaza, Houston, TX 77030, USA
[5]Department of Pediatrics, Baylor College of Medicine, One Baylor Plaza, Houston, TX 77030, USA
[6]Jan and Dan Duncan Neurological Research Institute, Texas Children's Hospital, Houston, TX 77030, USA
[7]Department of Molecular and Human Genetics, Baylor College of Medicine, One Baylor Plaza, Houston, TX 77030, USA
[8]Center for Precision Health, School of Biomedical Informatics, the University of Texas Health Science Center at Houston, Houston, TX 77030, USA
[9]Department of Orthopedic Surgery and Rehabilitation, University of Texas Medical Branch, 301 University Boulevard, Galveston, TX 77555, USA
[10]McNair Medical Institute, Baylor College of Medicine, BCM600, One Baylor Plaza, Houston, TX 77030, USA
[11]These authors contributed equally
[12]Lead contact
*Correspondence: xiangz@bcm.edu
https://doi.org/10.1016/j.devcel.2021.03.008

SUMMARY

Estrogen receptor-positive (ER+) breast cancer exhibits a strong bone tropism in metastasis. How the bone microenvironment (BME) impacts ER signaling and endocrine therapy remains poorly understood. Here, we discover that the osteogenic niche transiently and reversibly reduces ER expression and activities specifically in bone micrometastases (BMMs), leading to endocrine resistance. As BMMs progress, the ER reduction and endocrine resistance may partially recover in cancer cells away from the osteogenic niche, creating phenotypic heterogeneity in macrometastases. Using multiple approaches, including an evolving barcoding strategy, we demonstrated that this process is independent of clonal selection, and represents an EZH2-mediated epigenomic reprogramming. EZH2 drives ER+ BMMs toward a basal and stem-like state. EZH2 inhibition reverses endocrine resistance. These data exemplify how epigenomic adaptation to BME promotes phenotypic plasticity of metastatic seeds, fosters intra-metastatic heterogeneity, and alters therapeutic responses. Our study provides insights into the clinical enigma of ER+ metastatic recurrences despite endocrine therapies.

INTRODUCTION

Estrogen receptor-positive (ER+) breast cancer (BC) accounts for over 70% of all BCs, and after recurring, causes over 24,000 deaths per year in the US. Adjuvant endocrine therapies target ER and significantly reduce recurrences. However, 20%–40% of patients still develop metastases, often after a prolonged latency (Lim et al., 2012; Zhang et al., 2013). Thus, it is imperative to understand how ER+ cancer cells escape endocrine therapies in distant organs and to identify therapies to eliminate these cells.

Bone is the most frequently affected organ by ER+ BC, which is usually luminal-like subtype. Compared with the basal-like subtype, luminal BC exhibits a 2.5-fold increased frequency of bone metastasis (BoM), but a 2.5-fold decreased frequency of lung metastasis (Kennecke et al., 2010; Smid et al., 2008). BoMs of luminal-like BC are usually late onset, occurring beyond 5 years after surgery. Current tumor-intrinsic biomarkers in primary tumors can predict recurrences within 5 years, but not beyond (Sgroi et al., 2013), suggesting that the capacity of developing late-onset metastasis may not be encoded in cancer cells. We hypothesize that unique interactions between the bone microenvironment (BME) and ER+ disseminated tumor cells (DTCs) may facilitate survival and therapeutic resistance.

Little is known about how the BME affects ER+ BC cells. There is a paradoxically high discordance rate of ER status between primary tumors and DTCs, suggesting loss of ER in DTCs

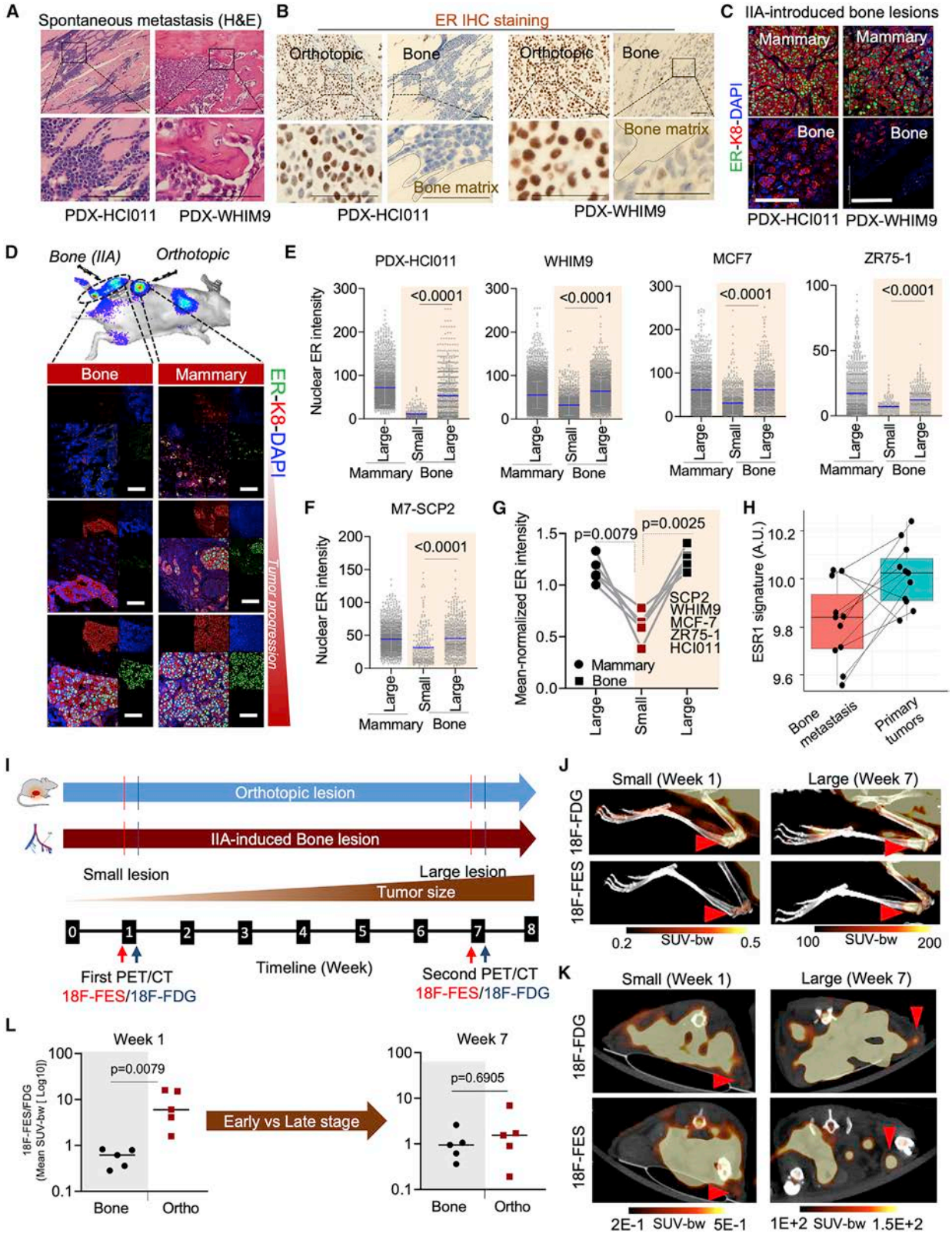

Figure 1. BME induces transient loss of ER expression in ER$^+$ breast cancer cells

(A) H&E staining of spontaneous metastases of HCI011 and WHM9 tumors to spine and hind limb, respectively. Scale bar: 100 μm.

(B) Human-specific ER IHC staining are shown for spontaneous metastasis of HCI011 and WHIM9, respectively. Scale bar: 50 μm.

(legend continued on next page)

(Fehm et al., 2008; Jäger et al., 2015). However, most overt BoMs (>85%) remain positive for ER (Hoefnagel et al., 2013), seemingly contradicting the DTC findings. ER$^+$ BoMs can still respond to endocrine therapies, although resistance almost invariably develops.

We have previously developed a series of models and techniques to investigate cancer-bone interaction at a single-cell resolution. Herein, we aim to investigate the impact of BME on the ER signaling in ER$^+$ BC cells.

RESULTS

BMMs transiently lose ER expression

To study how ER$^+$ BC cells interact with BME, we identified two patient-derived xenograft models (PDXs), HCI011 and WHIM9, from patients with BoMs (Derose et al., 2011; Li et al., 2013). In immunodeficient mice, orthotopic HCI011 and WHIM9 tumors spontaneously metastasized to bones 5–6 months after surgeries (Figure 1A). Spontaneous BoMs exhibited reduced ER expression in both PDX models (Figure 1B). The BoM size positively correlated with an average intensity of nuclear ER by IHC staining (Figures S1A and S1B).

Next, we performed intra-iliac artery (IIA) injection of dissociated PDXs or established ER$^+$ cell lines (MCF-7 and ZR75-1) to introduce experimental BoMs. This approach synchronizes the onset of colonization and enriches BMMs, thereby allowing quantitative examination of bone colonization of relatively indolent cancer cells at different stages (Figures 1C and 1D) (Yu et al., 2016). As in spontaneous BoMs, a strong correlation was found between ER expression and the size of IIA-induced BoMs (Figure S1C) but not orthotopic tumors (Figure S1D). When we classified BoMs by size, the expression of ER diminished in small lesions compared with mammary tumors but was restored in large lesions (Figure 1E). Thus, in both spontaneous and experimental BoM models, lesion size seems to be associated with ER expression (Figures 1E–1G).

Two possible mechanisms might explain the above association. First, genetically distinct ER^{low} and ER^{high} cancer cells may pre-exist, and the former progresses at a slower rate and form small lesions. Second, there may be a transient loss and a subsequent recovery of ER in ER$^+$ cancer cells in BME. To distinguish these, we collected four single-cell-derived populations from MCF-7 cells (M7-SCPs). Exome sequencing validated their genetic purity (Figure S1E). The expression of ER in M7-SCPs is still variable from cell to cell, although to a lesser degree compared with parental cells (Figure S1F), suggesting a baseline level of cellular plasticity among ER$^+$ BC cells. Using an M7-SCP of the best clonality (M7-SCP2), we compared the ER expression between BMMs and macrometastases. Like parental MCF7, M7-SCP2 cells exhibited decreased ER expression in small BoMs (Figures 1F, S1G, and S1H). Taken together, multiple ER$^+$ models supported that BME induces a loss of ER expression specifically in BMMs (Figure 1G).

The loss of ER was also observed in clinical specimens. In a study comparing patient-matched primary BCs and BoMs, ESR1 was found to be one of the top genes downregulated in BoMs (Priedigkeit et al., 2017). Gene set variation analysis (GSVA) further suggests that there is an even stronger downregulation of acute ER signaling (Figure 1H).

We next monitored the longitudinal alteration of ER signaling during BoM progression using positron emission tomography-computed tomography (PET-CT) imaging. A radiolabeled 18F-fluoroestradiol (18F-FES) PET/CT imaging strategy was adopted (Figures 1I and S1I–S1K) to measure the uptake of estrogen by tumors in parallel with glucose consumption (18F-FDG) (Kurland et al., 2017). We found a significant reduction in estrogen uptake in early lesions of BoM (Figure 1J) compared with mammary tumors (Figures 1K and S1I). The difference was reduced at a later time point (Figures 1J–1L), suggesting a reversible process.

An evolving barcode strategy to trace clonal evolution of ER$^+$ BC cells

ER heterogeneity is often observed in the clinic. However, the phylogenetic relationship between ER$^+$ and ER$^-$ cancer cells is not defined. We used an evolving barcode system (Kalhor et al., 2017, 2018) to trace the evolution of ER$^+$ cancer cells in BME. This is a variant of the widely used CRISPR-Cas9 system. Here, the PAM site is mutated such that Cas9 can target the locus encoding guide RNAs (termed "home-guide RNAs" or hgRNAs). As a result, mutations are iteratively introduced to drive the evolution of hgRNAs. This provides an opportunity for multiple parallel lineage tracing in cancer.

(C) IF staining of ER, keratin 8 (K8), and DAPI in orthotopic (mammary) and IIA-induced BoM models of ER$^+$ PDXs (HCI011 and WHIM9). Scale bars: 100 μm.
(D) IF images of MCF7 cells following orthotopic and bone transplantation. Changes in ER expression are illustrated at different stages of tumor progression. Scale bars: 50 μm.
(E) Dot plot depicting nuclear ER intensity of single cells (SCs) in orthotopic and BoM specimens from PDXs (HCI011, WHIM9) and cell lines (MCF7, ZR75-1), following IF staining as illustrated in (C and D) (n = 3–6 mice per model). Error bars: mean ± SD.
(F) Dot plot depicting nuclear ER intensity of SCs in orthotopic and BoM specimens from M7-SCP2. Bone lesions were classified into "small" and "large" as defined in (E); (n = 4 mice). Error bars: mean ± SD.
(G) Connected scatterplots showing the mean-normalized ER intensity of all cancer models used from 1E to 1F. (n = 5 cell lines).
(H) Boxplot depicting changes in ESR1 early signature in matched BoM and primary specimens from BC patients (Github: https://github.com/npriedig/).
(I) Scheme describing the PET-CT experiment on MCF7 orthotopic or IIA-induced BoM models. 18F-FES and 18F-FDG imaging were performed 48 h apart, at week 1 and 7 post tumor transplantation.
(J) PET/CT scans showing the maximum intensity projection (MIP) of 18F-FDG and 18F-FES in bone as described in I. MCF7 BoMs were generated using IIA injection. Red arrows indicate tumor location. Scale: 0.2–0.5 SUV-bw (week 1) and 100–200 SUV-bw (week 7).
(K) Axial view of PET/CT scans depicting the uptake of 18F-FDG and 18F-FES in small and large lesions of MCF7 orthotopic tumors. Early time point (week 1) and late time point (week 7) were used to depict non-palpable orthotopic tumor stage (small <2 mm) and the palpable tumor stage. Red arrows and scale: as in (J).
(L) Relative quantification of radiolabeled 18F-FES uptake in small and large lesions of orthotopic and BoMs. Each dot represents the mean standard uptake values (mean SUV-bw) of 18F-FES normalized to the mean SUV of 18F-FDG for each mouse. Mann-Whitney U test is used for statistical analysis; n = 5 mice per group.
(A–L) p values were computed by two-tailed unpaired Student's t tests unless otherwise noted.

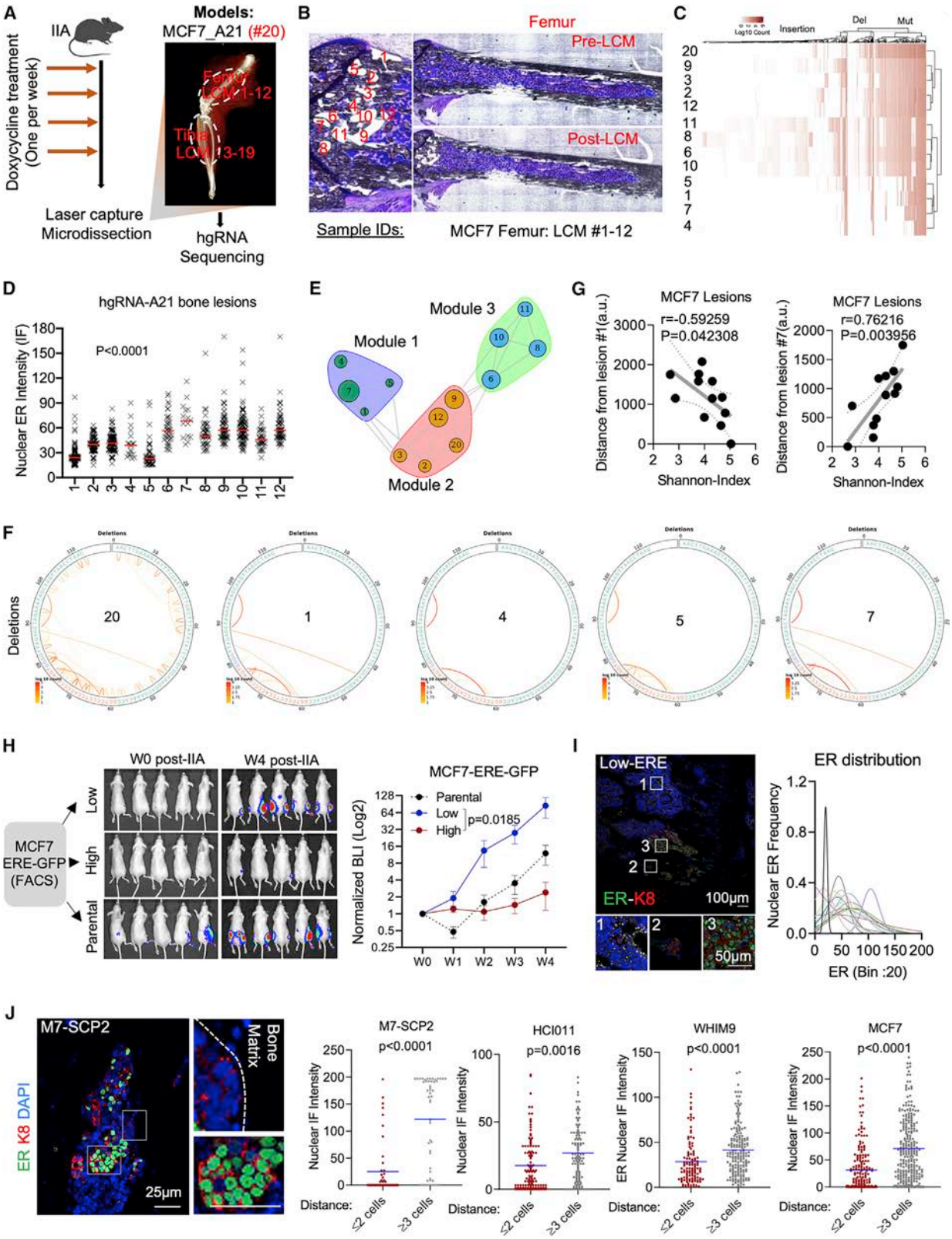

(legend on next page)

The evolving barcode system was introduced to MCF-7 cells and was allowed to accumulate mutations before tumor transplantation to the bone by IIA injection (Figure 2A). This created a baseline barcode diversity so that independent clones in the bone can be distinguished. Further evolution after IIA injection helps deduce the parent-child relationship between clones. We used laser-captured micro-dissection (LCM) to isolate cancer cells in different regions of established BoMs (Figures 2B and S2A). DNA purification and PCR-mediated enrichment of hgRNA sequences were performed before sequencing (Figures 2A, 2B, and S2A). The hgRNAs were then used to deduce the phylogenetic relationship among cancer cells in different lesions (Figures 2C and S2B). A consecutive section of the bone was used for immunofluorescence (IF) staining of ER so that the nuclear ER expression of each lesion could be superimposed with the barcodes. ER expression was highly variable across different lesions in the femur (Figures 2D and S2C) and tibia (Figure S2D), indicating an increased phenotypic heterogeneity of the BoM.

In the metaphyseal area of femur, 12 lesions were grouped into three clusters (Figure S2E). Interestingly, ER expression varies within each cluster, which provides strong evidence against genetic traits as a determinant of the ER level in BoM (Figure 2E). Similar observations were found in lesions derived from tibia (Figure S2F). A notable example was the *module 1*, a cluster formed by lesions #1, #4, #5, and #7. The barcodes of these lesions are highly similar (Figures 2F and S2G), indicating close phylogenetic distance. Additionally, these lesions have a distinct spatial distribution with a close proximity to the growth plate (Figure S2H). Lesion #1 exhibited a low ER expression but the highest Shannon entropy among all 12 lesions, whereas lesion #7 was the opposite. Both ER expression and Shannon entropy of other lesions varied as functions of distance to these two extreme lesions (Figure 2G). Considering that the Shannon entropy is correlated with the ''age'' of cancer cells (Zhang et al., 2021), lesion #1 is likely to be parental to legions #4, #5, and #7. The fact that their ER levels greatly varies, support our hypothesis that ER^{-} lesions may give rise to ER^{+} lesions as BoMs progresses.

The analysis of all lesions (#1–19) derived from the same hind limb revealed surprising similarities between lesions from femur and tibia (Figure S2E). Despite physical barriers, lesion #15 from tibia shared similar mutations with lesions #6, #8, #10, and #11 from femur, suggesting a femur-to-tibia seeding (Figure S2E). This metastasis-to-metastasis seeding is further investigated in our accompanied study (Zhang et al., 2021).

ERE-GFP^{Low} cells drive BoM progression and reconstitute ER heterogeneity

As an independent approach to trace the fate of ER^{-} cancer cells in BoM, we introduced a reporter system, namely, GFP expression driven by the estrogen-responsive elements (ERE-GFP). We performed IIA injection of ERE-GFP^{high} and ERE-GFP^{low} cells, respectively. The bone colonization capacity of ERE-GFP^{Low} cells was over 30-fold higher compared with ERE-GFP^{high} cells (Figures 2H and S2I), consistent with the finding that the ER^{-} subset of MCF-7 cells enrich stemness (Fillmore et al., 2010). Interestingly, BoMs established by ERE-GFP^{Low} cells exhibited heterogeneous ER expression, similar to those derived from parental cells (Figures 2I and S2J) and lesion sizes were associated with ER expression (Figure S2K). This experiment provides additional support for the conclusion that ER^{Low} cells may generate ER^{high} cells in BME.

BC lesions tend to associate with areas of new bone matrix deposition (Figure S2L). We examined the spatial distribution of ER expression relative to bone matrix. Cancer cells apart from lesion borders were more likely to restore ER expression compared with those at the border (Figure 2J). Thus, ER recovery tends to occur first toward the center of a BoM lesion, leading to the hypothesis that the interactions between metastatic cells and adjacent bone cells drive the transient loss of ER.

Direct interaction with OGs mediates the loss of ER expression

To identify bone cells that causes ER loss in BMMs, we assessed the spatial relationship between ER expression and various bone cells, including osteoclasts ($RANK^{+}$), endothelial cells ($CD31^{+}$), myofibroblasts/bone stromal cells (αSMA^{+}), and OGs (ALP^{+}). In WHIM9, HCI011, and MCF-7 models, RANK expression exhibited a positive association with nuclear ER intensity at a single-cell level (Figure 3A). In contrast, negative associations were observed for endothelial, fibroblasts, and OGs (Figures 3B and 3C). Among these, the correlation of ALP^{+} OGs is most consistent across different models (Figure 3C), suggesting that OGs may be the cell types driving the loss of ER.

Figure 2. Tracing ER expression in bone metastases by evolving barcodes and ERE-reporter

(A) Experimental design of BoM lineage tracing using an inducible CRISPR-Cas9 hgRNA evolving barcoding system. iCas9-expressing MCF7 cells were stably transduced with homing guide RNA A21 (hgRNA-A21) before transplantation to bone and induced weekly for 4 weeks before LCM and targeted sequencing. We collected 19 lesions from femur (#1–12) and tibia (#13–19). Barcoded parental cells were labeled as #20.

(B) Exact map of mouse femur before and after LCM of metastatic lesions #1–12.

(C) Heatmap showing hierarchical clustering of bone lesions #1–12, based on hgRNA-A21 mutations.

(D) IF quantification of SCs nuclear ER in lesions #1–12 (femur). (n = 12 lesions); p value: ordinary one-way ANOVA.

(E) Modular organization of lesions #1–12 following a high-dimensional undirected analysis of barcode mutations. Node sizes represent mean intensity of ER expression.

(F) Circus plot showing barcode deletions in bone lesions clustered in module 1 (see E). #20: Pre-injected cells.

(G) Scatter plot showing Pearson correlation (R) between the Shannon index of bone lesions and their relative distance to lesion #1 or #7. p value: two-tailed t test.

(H) IIA-induced BoM from ERE-GFP reporter MCF7 cells. ERE-GFP^{Low}, and ERE-GFP^{high} MCF7 cells were sorted based of their GFP expression. Tumor growth was measured by bioluminescence. (n = 5–8 mice); p value: two-way ANOVA. Error bars: mean ± SEM.

(I) IF staining of ER in BoM derived from ERE-GFP^{Low} MCF7 cells. The Gaussianized ER distribution is based on nuclear intensity of SCs; peak: mean ER expression per lesion.

(J) IF staining depicting a spatial distribution of ER based on the location of M7-SCP2 lesions relatively to the bone matrix. Scale bars: 25 μm. Dot plots represent nuclear ER expression in cells proximal ($\leq$ 2 cell distance) or distal ($\geq$3 distance) to the bone matrix. p *values*: two-tailed unpaired Student's t tests.

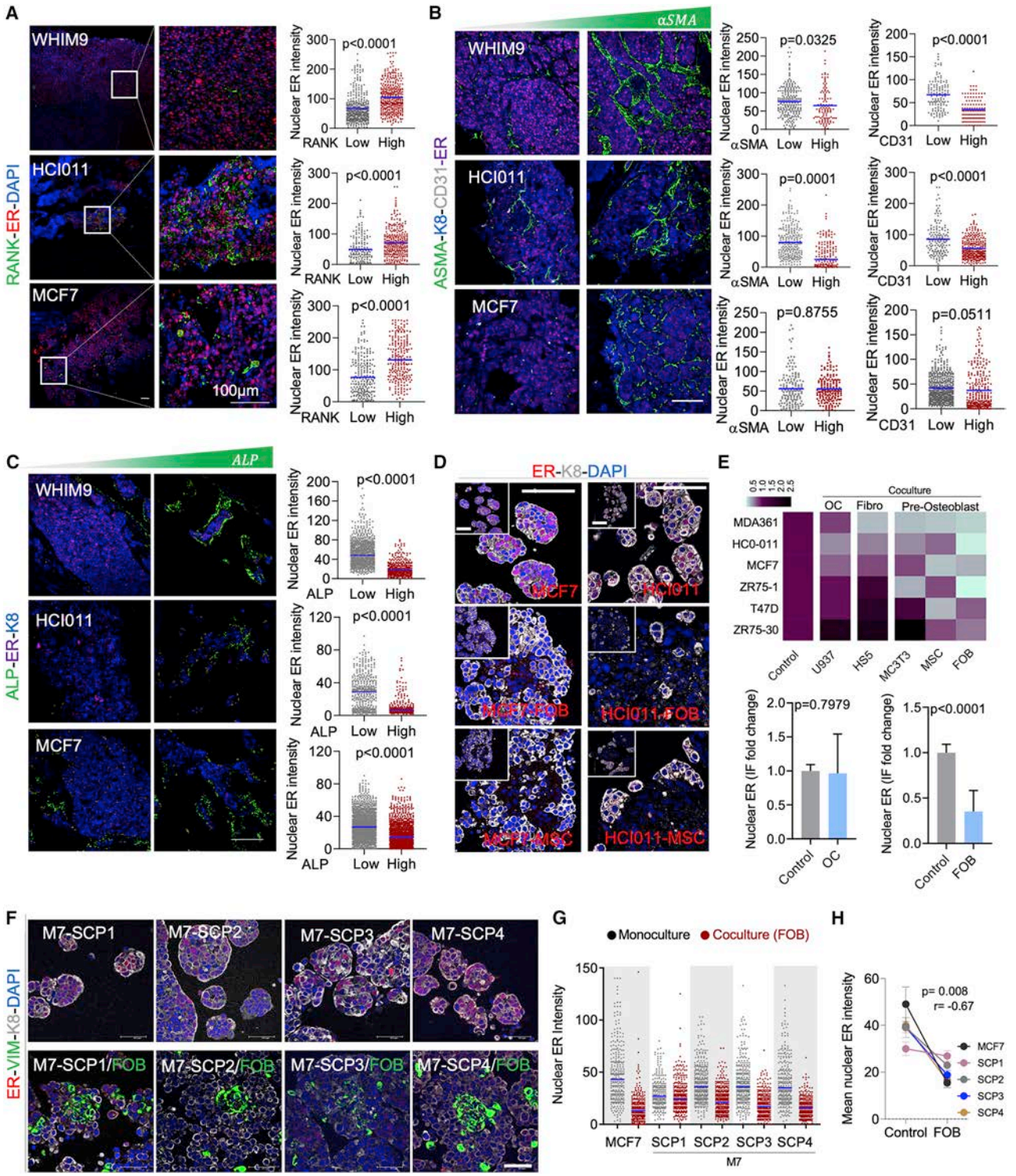

Figure 3. OGs promote the loss of ER expression and reduction of ER activities during early stages of bone colonization

(A) IF of BoMs showing ER expression in PDXs (HCI011 and WHIM9) and MCF7 cells, relatively to receptor activator of nuclear factor-KB (RANK) expression in osteoclasts. Scale bars: 100 μm. Dot plots show ER quantification in SCs. (n = 3–5 lesions).

(B) IF as in (A). ER is co-stained with alpha smooth muscle actin (αSMA) and cluster of differentiation 31 (CD31) to depict endothelial cells. Dot plots show ER quantification in SCs. (n = 3–5 lesions).

(C) IF as in (A). ER is co-stained with alkaline phosphatase (ALP). Dot plots show ER quantification in SCs. (n = 3–5 lesions).

(D) IF images of HCI011-derived primary cells and MCF7 cells in 3D monoculture and co-culture with FOBs and MSCs. Scale bars: 100 μm.

(legend continued on next page)

To further study this interaction, we employed a fetal OB line (FOB) and a human MSC line to represent OGs. Luminal-like cancer cells and OGs form heterotypic organoids in 3D suspension co-culture, which recapitulated several aspects of cancer-niche interaction (Wang et al., 2015). Co-staining of ER and keratin 8 (K8, a marker of luminal cells) in 3D co-cultures revealed a loss of ER in MCF-7 cell line and HCI011 PDX-derived organoids (Figure 3D) similar to *in vivo* BMMs. MSCs and FOB both induced consistent loss of ER expression across multiple models (Figure 3E). In contrast, U937, a human monocytic cell line that is often used to model osteoclast precursors, did not cause the same changes to the ER expression, supporting the specificity of OGs (Figure 3E).

Importantly, M7-SCPs also exhibited the same alterations upon interacting with FOB (Figures 3F and 3G). In M7-SCP2, -SCP3, and -SCP4, the degree of ER downregulation is comparable with parental MCF-7 cells. In contrast, M7-SCP1 exhibited a lesser decrease (Figures 3G and 3H). Interaction with OGs confers growth advantage on cancer cells, as we previously showed (Wang et al., 2015, 2018). Similar to MCF-7 cells (Figures S3A and S3B), M7-SCP1, 2, and 3 also displayed such an advantage in 3D co-cultures as compared with monocultures. In contrast, the growth of M7-SCP4 was suppressed by FOB (Figure S3C). Thus, different M7-SCPs possess a variable capacity of orthotopic tumor initiation, bone colonization, FOB-mediated growth promotion, and ER downregulation (Figure S3D). This pre-existing heterogeneity supports the importance of clonal selection in metastasis, which has been repeatedly demonstrated in previous studies (Bos et al., 2009; Kang et al., 2003; Minn et al., 2005). However, the BME-induced, adaptive change is less appreciated (Figures 3F–3H).

Hyperactive ER activities can lead to ER protein degradation (Nawaz et al., 1999). Therefore, decreased ER expression could paradoxically suggest an enhanced ER signaling. Upon co-culturing with FOB, cancer cells reduced the transcription of ER mRNA (Figure 4A), as well as ER transcription activities as indicated by a luciferase reporter driven by a promoter containing ER-responsive elements (ERE-luciferase) (Figure 4B). The ER target progesterone (PR) was also downregulated in BMMs (Figure 4C). These data indicate that the transient loss of ER is not a reflection of hyperactive ER signaling, but rather the cause of decreased ER signaling.

Interaction with OGs in the BME leads to resistance to endocrine therapies

Downregulation of ER may impact endocrine therapies. We examined the effects of fulvestrant, tamoxifen, and estradiol on ER$^+$ cancer cells with or without co-culture of FOB. The presence of FOB diminished the effects of these agents on ER nuclear localization (Figure 4D) and blunted the anti-proliferative effects of tamoxifen and fulvestrant (Figure 4E). The same results were observed using M7-SCPs (Figure 4F), indicating a process independent of genetic selection. We next examined the reversibility of "bone-entrained" effects by inoculating M7-SCP2 cells into bone via IIA. Cancer cells were retrieved after establishment of BMMs, resulting in "bone-entrained" M7-SCP2 cells (M7-SCP2-Bo) (Figure S4A). M7-SCP2-Bo cells remained resistant to fulvestrant in early passages, but this resistance diminished as cells were expanded in cultures (Figure 4G), suggesting that BME-induced phenotypic shift is not stably inherited.

We next examined responses of ER$^+$ cancer cells to estrogen deprivation in BME (Figure S4B). Combined ovariectomy and letrozole treatment could significantly impede orthotopic tumor growth in both MCF-7 and ZR75-1 models (Figures S4C and S4D) but failed to reduce BoM colonization at early time points (Figures 4H–4M). The response to estrogen deprivation was partially recovered in MCF-7 cells after week 3 (Figures 4H–4J), further supporting that the resistance may be reversible as metastases further progress. However, ZR75-1 bone lesions remained resistant at later time points (Figures 4K–4M). Hence, not all BoMs restore endocrine sensitivity. In ZR75-1, despite the partial reversion of ER expression in macrometastases, PR expression remained repressed (Figures S4E and S4F). Thus, downstream ER signaling may not recover together with ER expression during BoM progression.

Downregulation of ER in BoM is partially mediated by direct cell-cell contact and gap junctions

We previously reported that heterotypic gap junctions between cancer cells and OGs mediate calcium influx to the former and activates calcium signaling (Wang et al., 2018). We asked if the gap junction and calcium signaling may mediate ER downregulation and endocrine resistance. Suppression of gap junction by a peptide, GAP19, or calcium signaling by a small molecule inhibitor, FK506, partially restored ER expression in co-cultures with FOBs (Figure S5A). This effect was small but noticeable and was further supported by a converse experiment showing that high [Ca2+] in the medium decreased ER expression (Figure S5B). Inhibition of calcium signaling also reduced the grow advantage conferred by FOB (Figure S5C), and enhanced endocrine therapies in bone-in-culture array (BICA) (Figure S5D), which is an *ex vivo* platform that recapitulate BME and cancer-niche interactions (Wang et al., 2017). Taken together, gap junction and calcium signaling contribute to inhibit ER expression in BMMs.

Unbiased profiling uncovered global phenotypic shift of ER$^+$ cancer cells

We used multiple approaches to discover additional mechanisms underpinning BME-induced ER downregulation (Figure 5A). Translating ribosome affinity purification followed by

(E) Heatmap showing the mean intensity of ER in primary cells (HCI011) and BC cell lines (MDA-MB-361, MCF7, ZR75-1, T47D, ZR75-30) in 3D monoculture (control) or co-culture with osteoclast precursors (U937), bone marrow stromal cells (Hs5), mouse pre-osteoblasts (MC3T3), human mesenchymal stem cells (MSC) and human pre-osteoblast (FOB). Histogram shows ER expression in monoculture versus co-culture of multiple cell lines with U937 or FOB cells; (n = 3 biological replicates). Error bars: mean ± SD.

(F) IF showing ER expression in M7-SCPs in 3D monoculture or co-culture with FOB cells. Vimentin (VIM). Scale bars: 50 μm.

(G) IF quantification of ER expression in M7-SCP1 to 4; (n = 3 biological replicates).

(H) Graph representing ER expression in cancer cells alone or in co-cultured with FOB cells. Spearman correlation (R); (n = 5 cell lines); Error bars: mean ± SEM.

(A–H) p values were computed by two-tailed unpaired Student t tests unless otherwise noted.

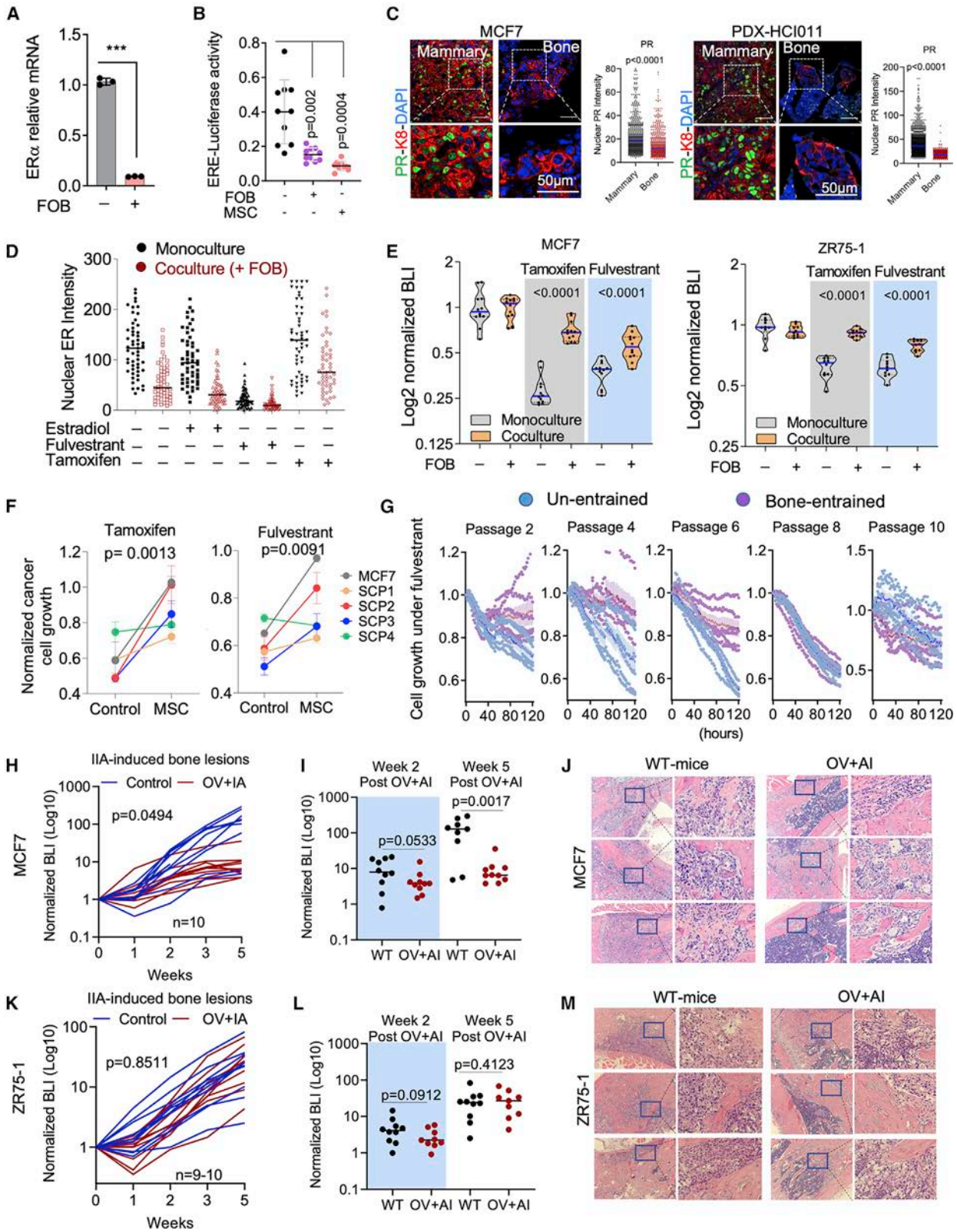

(legend on next page)

RNA-seq (TRAP-seq) was applied to profile transcriptome in cancer cells interacting with OGs in 3D suspension co-cultures without dissociating the two cell types. TRAP-seq revealed that MSCs diminished the impact of endocrine perturbations on ER$^+$ cancer cells (Figure S5E). We also validated that GJA1, the gene encoding connexin 43, was upregulated by MSCs in co-cultures and exhibited a strong inverse correlation with ER expression (Figure S5F), further indicating a role of gap junctions in downregulating ER. However, the conditioned medium of OGs also causes ER downregulation and endocrine resistance (Figure S5G), indicating paracrine mechanisms.

According to TRAP-seq, over 1,100 genes are significantly increased by MSC co-cultures (FDR <0.05 and fold change >2), which indicates a global phenotypic alteration. Using PAM50 signatures, we observed a shift from luminal to basal subtype (Figure 5B). Several pathways changed significantly in MSC-interacting cancer cells, including the decrease in ER signaling and increase in epithelial to mesenchymal transition (EMT) and STAT3 signaling (Figure 5B), all of which indicated dedifferentiation and stem-like activities (Mani et al., 2008; Marotta et al., 2011; Pfefferle et al., 2015). The PANTHER classification system identified a number of pathways overrepresented in the altered genes, including several related to epigenomic regulation of gene expression (e.g., PRC2), stemness-related pathways (e.g., WNT and Notch), and receptor tyrosine kinase (RTK) signaling (Figures 5C and S5H). Some of these pathways have been previously implicated in BoM and therapeutic resistance (Andrade et al., 2017; Esposito et al., 2019; Sethi et al., 2011; Zheng et al., 2017). These findings indicate that OGs induce an epigenomic landscape alteration in ER$^+$ BC cells toward more ER-independent and stem-like states.

Reverse phase protein array (RPPA) was used to profile over 236 key proteins and phospho-proteins in cancer cells that have been extracted from BME. Comparisons were made between MCF-7 and MCF-7-Bo and between M7-SCP2 and M7-SCP2-Bo. We identified the proteins and phospho-proteins that are significantly altered (Figures S5I and S5J). The bone-entrained cells exhibited reduced ER signaling (Figure 5D), enhanced stemness (Figure 5D), increased mesenchymal markers (Figure 5E), and increased RTK expression (Figure 5F). The most upregulated protein in both MCF-7-Bo and M7-SCP2-Bo was PDGFRβ (Figures S5J and S5J). Overall, these changes revealed a global phenotypic shift toward a more dedifferentiated status (Ginestier et al., 2007; Guo et al., 2012; Mani et al., 2008; Tam et al., 2013; Ithimakin et al., 2013). One notable osteogenic cell-induced change is the acquisition of a hybrid EMT status (Figure 5E). We performed co-IF staining of epithelial markers (E-cadherin and cytokeratin 8) and a mesenchymal marker (Vimentin). A small proportion of double-positive cells were observed, usually located at the border between metastases and bone matrix, where OGs are located (Figure 5G). Thus, the interaction with OGs does not simply cause EMT, but rather induce phenotypic plasticity and confer stemness.

Assay for transposase-accessible chromatin using sequencing (ATAC-seq) (Buenrostro et al., 2015) was used to evaluate epigenetic changes occurring at the chromatin level of cancer cells extracted from bone. The differentially accessible regions (DAR) between parental and bone-entrained cells were decreased in the latter in general (Figures 5H–5J), indicating a global shift toward heterochromatin formation. This was further supported by a global decrease in chromatin accessibility (Figure 5K). We identified two major peaks around ESR1 gene with reduced chromatin accessible in bone-entrained cells (Figure 5L) (Peaks 1 and 3). The reduction reversed over multiple passages *in vitro* (Figures 5L and S5K). Overall, these results indicate a reversible epigenetic reprogramming in cancer cells interacting with BME.

FGFR and PDGFR pathways contribute to phenotypic changes in BMMs

Among all pathways altered in BME, PDGFRβ and FGFR1 pathways are of particular interest. PDGFRβ exhibited the highest

Figure 4. OGs confer endocrine resistance

(A) Relative mRNA expression of ESR1 in 3D monoculture or co-culture of MCF7 with FOB. Data result from FACS-sorted MCF7. (n = 3 technical replicates). Error bars: mean ± SD.

(B) Dot plot representing ER transcriptional activity in MCF7 cells expressing PGL2 ERE-luciferase reporter. MCF7 cells were cultured in 3D with or without OGs (FOB and MSC) for 7 days. (n = 10 technical replicates); Error bars: mean ± SD.

(C) Confocal images showing the expression of progesterone receptor (PR) in IIA-induced BoM from MCF7 and HCI011. Dot plots show nuclear PR IF intensity. (n = 3 lesions).

(D) Dot plots depicting ER intensity in 3D mono- and co-culture of MCF7 cells with FOB following 24 h treatment with 10 nM 17β-estradiol, 20 nM fulvestrant, and 100 nM 4-hydroxytamoxifen (tamoxifen); n = 5 fields.

(E) Violin plot showing the response of luciferase-labeled MCF7 and ZR75-1 cells to 100 nM of 4-hydroxytamoxifen (tamoxifen) and 20 nM of fulvestrant in 3D mono- or co-culture with OGs (FOB). Bioluminescence was acquired 72 h post-treatment. (n = 12 and 10 technical replicates for and ZR75-1).

(F) Graphs representing the proliferation of MCF7 cells and M7-SCP1-4 in monoculture and MSC co-culture following 1 week of treatment with 20 nM fulvestrant or 100 nM tamoxifen; n = 5 cell lines. Error bars: mean ± SEM.

(G) Time course experiment depicting growth kinetics of un-entrained and bone-entrained M7-SCP2 cells in vehicle or 20 nM fulvestrant conditions; n = 6 technical replicates.

(H) Growth curve showing response of IIA-induced MCF7 BoMs to estrogen depletion. Ovariectomized (OV) mice were additionally treated with letrozole (OV+AI), daily. Results are based on BLI. (n = 10 mice); p value: two-way ANOVA.

(I) Dot plot showing BoM growth in wild-type (WT) and OV+AI mice at week 2 and week 5 post tumor transplantation; n = 10 mice. p value: two-tailed unpaired Student's t test.

(J) H&E staining showing MCF7 metastatic lesions in wild-type (WT) and "OV+AI" groups.

(K) Growth curve depicting the response of ZR75-1-derived BoM as in (H). (n=9–10 mice); p value: two-way ANOVA.

(L) Dot plot showing statistical growth differences in ZR75-1 as in (I).

(M) H&E staining of ZR75-1 metastatic lesions as in (J).

(A–M) p values were computed by two-tailed unpaired Student's t tests unless otherwise noted.

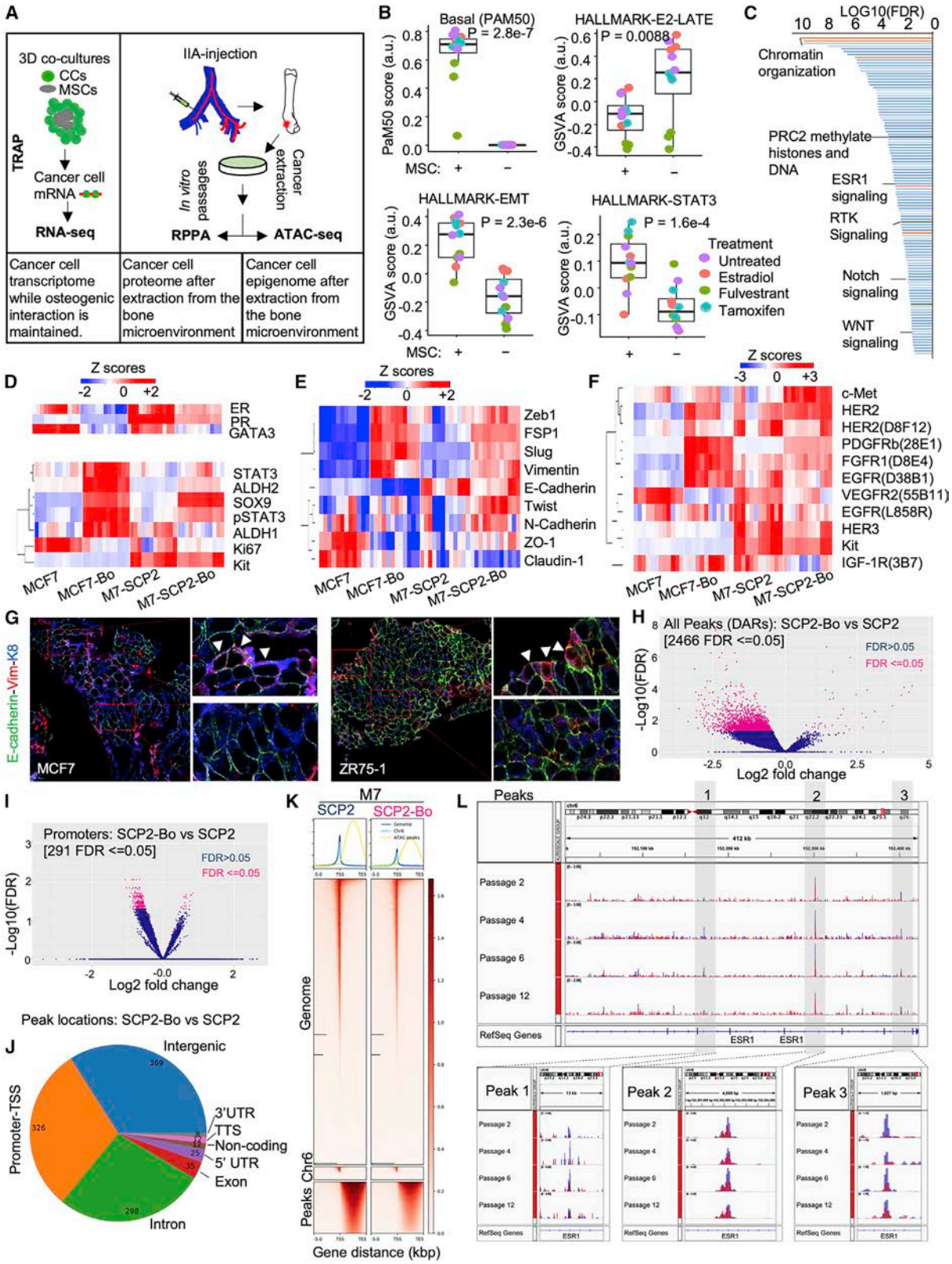

(legend on next page)

fold change in both models (Figures S5I and 5J) and was shown to determine the subtype of BC and mediate cancer stem cell activities (Lehmann et al., 2011; Tam et al., 2013). Multiple FGF ligands and receptors were upregulated in human BoMs compared with matched primary tumors (Priedigkeit et al., 2017). FGF signaling regulates stem cell compartment in ER^+ BC (Fillmore et al., 2010). Using a literature-based network analysis platform (https://string-db.org/)(von Mering et al., 2005), we found that FGF2 connects ER, FGFR1, and PDGFRB (Figure 6A), suggesting a pivotal role of FGF2 in ER downregulation and endocrine resistance.

FGF2 is the highest expressed FGF ligands by FOB cells (Figure 6B). IF staining of FGF2 in BMMs revealed a positive correlation with ALP+ OGs (Figures 6C and S6A) and a negative correlation with nuclear intensity of ER (Figures 6D and 6E). Functionally, recombinant FGF2 treatment decreased ER expression in multiple cell lines including M7-SCPs (Figure 6F), and induced resistance to fulvestrant (Figure 6G). Conversely, a potent FGFR inhibitor, BGJ398, reversed the fulvestrant resistance of ER^+ cancer cells in BICA (Figure 6H).

PDGFRB is highly expressed in the bone-entrained cells at both protein and mRNA levels (Figure S6B). Direct interaction between cancer cells and OGs was required for PDGFRB upregulation (Figure S6C). Among all PDGF ligands, PDGF-DD, but not PDGF-BB or PDGF-CC, significantly promoted the therapeutic resistance (Figures S6D and S6E), while suppressing the ER expression (Figures S6F and S6G). Like FGFR, the inhibition of PDGFR signaling by sunitinib partially abolished the cancer-promoting effects of FOB cells in 3D co-cultures (Figure S6H), further supporting the important roles of both FGFR and PDGFR signaling in the BME-induced endocrine resistance.

The complicated impact of BME converges on an EZH2

We next asked how the discovered pathways cooperate to silence ER and increase phenotypic plasticity. In the Epigenomic Roadmap database, FGF2-regulated genes are enriched with tri-methylation of H3K27, and sensitive to perturbation of EZH2 (Figure 6I). Consistently, PRC2 methyltransferase activity is enhanced in cancer cells co-cultured with MSCs (Figure 5G). Treatment of recombinant FGF2 increased H3K27me3 and EZH2 (Figures 6J, 6K, and S6I) but did not affect other H3 modifications (Figure S6J). Conversely, treatment of BGJ398 decreased EZH2 expression in 3D cancer-MSC co-cultures (Figure 6J). PDGF-DD yielded similar effects (Figures S6I and S6J). Furthermore, calcium signaling affected EZH2 expression at the RNA level (Figure S6K). Thus, the pathways that downregulate ER seem to converge on the regulation of EZH2.

EZH2 is a reliable marker for cancer stemness (Kim and Roberts, 2016; Zhou et al., 2002). In ER^+ cancer cells, the PRC2 target genes were concertedly downregulated, whereas a stemness signature (Varambally et al. 2020) was upregulated, by co-culturing of OGs (Figures S6L–S6N), validating the connection of EZH2 to cancer stemness. In addition, cancer-cell-intrinsic EZH2 expression was specifically increased in BME compared with other organs (Figure 6L).

EZH2 has been shown to silence ER expression in previous studies (Reijm et al., 2011). To validate this, we carried out IF staining in 3D co-cultures and observed an inverse correlation between EZH2 and ER expression both in 3D cultures and in bone lesions at a single-cell level (Figures 6M and 6N). Inhibition of EZH2 enzymatic activity by an EZH2 inhibitor (EPZ011989) (Campbell et al., 2015) led to restoration of ER expression at the RNA level (Figure 6O). The inverse changes of ER and EZH2 were also observed *in vivo* between BMMs and macrometastases (Figure 6P). Finally, the BME-induced increase in H3K27me3 was reversible after several passages *in vitro*, again suggesting a transient impact (Figure 6Q).

EZH2 inhibition induced ER expression in a murine model, which is abolished by OGs in bone lesions

We sought to validate our findings in immunocompetent hosts. Most murine BC cell lines are ER^-, thereby limiting the possibility of syngeneic experiments (Derose et al., 2011). However, some murine models express ER in early-stage tumor progression, e.g., MMTV-PyMT (Lin et al., 2003; Medina et al., 2002). AT3 is a cell line derived from MMTV-PyMT (Guy et al., 1992). We reasoned that it might express ER at some stage and examined if EZH2 inhibition restores ER expression in AT3. In mammary tumors, the transient treatment of EZH2 inhibitor increased ER expression in a durable fashion and to a level exceeding the threshold defining

Figure 5. BME drives a global phenotypic shift involving multiple pathways

(A) Experimental summary diagram to evaluate molecular in cancer cells exposed to BME. TRAP-seq was performed on 3D co-culture of MCF7 and OGs (MSCs), RPPA on un-entrained (MCF7 and M7-SCP2) and bone-entrained cells (MCF7-Bo and M7-SCP2-Bo), and ATAC-seq on un-entrained (M7-SCP2) or bone-entrained (M7-SCP2-Bo) cells.

(B) Box plot depicting gene signature alternations in MCF7 monoculture (MSC-) and co-cultures (MSC) from TRAP-seq. Analysis was performed using a non-parametric and unsupervised GSVA (Hänzelmann et al., 2013). Specific colors represent different treatment conditions. (n = 4 biological replicates each with 3 technical replicates); p value: two-tailed unpaired Student's t test.

(C) Waterfall plot showing the gene ontology analysis of TRAP-seq data from PANTHER classification system, based on false discovery rate (FDR).

(D) Heatmap depicting expression changes in luminal and stemness-related markers from RPPA data. Parental cells (MCF7 and M7-SCP2), and bone-entrained BC cells (MCF7-Bo and M7-SCP2-Bo) are compared; N: 4 biological replicates and 3 technical replicates.

(E) Heatmap depicting EMT/MET markers from RPPA data as described in (D).

(F) Heatmap depicting receptor tyrosine kinases from RPPA data as described in (D).

(G) IF showing vimentin, E-cadherin, and keratin 8 expression in IIA-induced bone MCF7 and ZR75-1 BoMs.

(H) Volcano plot showing epigenetic reprogramming of bone-entrained M7-SCP2 cells based on differentially enriched peaks from ATAC sequencing analysis. 2,644 peaks were significantly altered in bone-entrained M7-SCP2 (FDR $\leq$ 0.05) and highlighted in pink.

(I) Volcano plot based on opened promotors identified by ATAC-seq analysis. FDR < 0.05 is highlighted in pink.

(J) Pie chart depicting the genomic distribution of differentially altered peaks between un-entrained and bone-entrained M7-SCP2 cells.

(K) Heatmaps and summary plots showing chromatin opening near the transcription start site TSS. 5,000 bp before and after TSS are represented.

(L) Genomic track showing peak variations in the ESR1 gene of un-entrained (M7-SCP2) and bone-derived (M7-SCP2-Bo) cells in blue and red color, respectively. 3 major peaks are highlighted epigenetic reversibility in M7-SCP2-Bo *in vitro*.

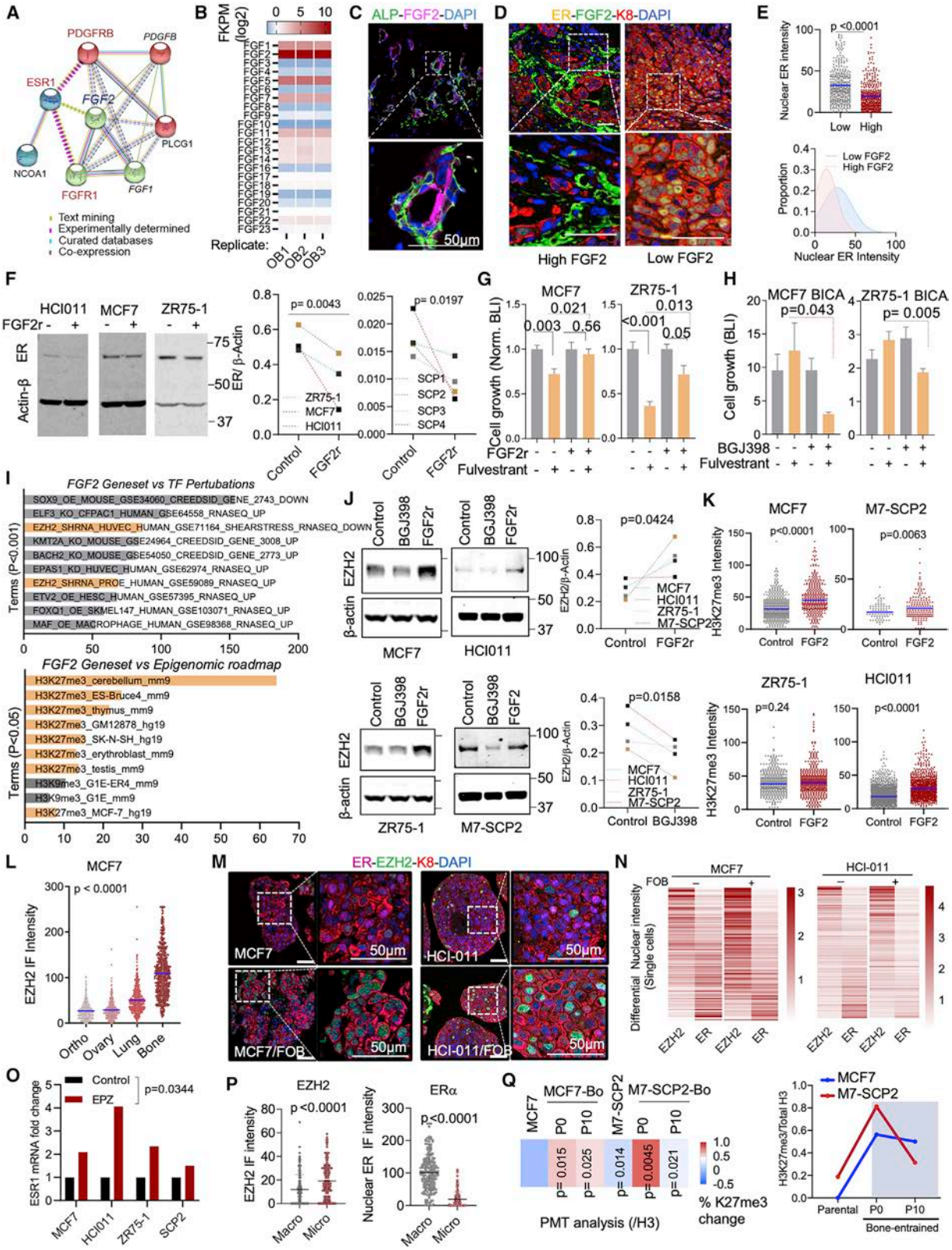

Figure 6. Osteogenic cell-secreted FGFs promote endocrine resistance

(A) Network depicting functional protein association between FGFR1, PDGFRB, and ER using the STRING database. *K* means clustering (k = 3) was used to represent 3 major centroids (depicted as red, green, and cyan spheres) and their most closely associated proteins based on unsupervised data mining.

(legend continued on next page)

ER$^+$ tumors (Figures 7A, 7B, and S7A). Although the re-expression of ER could not restore downstream estrogen signaling, it recapitulated upstream regulation of ER expression by EZH2. Therefore, we went on to determine how the aberrant expression of ER in AT3 cells might respond to BME. After IIA injection, ER expression in AT3 was lost again in syngeneic mice, and this loss was especially pronounced in regions adjacent to bone matrix (Figures 7C and 7D). Importantly, inducible depletion of osterix-expressing osteoprecursor cells abolished the loss of ER (Figures 7C and 7D). Taken together, these data validated that the OGs suppress ER expression in BME.

Short-term inhibition of EZH2 restores sensitivity of BMMs to endocrine therapies

Since EZH2 mediates the BME-induced endocrine resistance, we hypothesized that inhibition of EZH2 should reverse this resistance and synergize with endocrine therapies. Using the EZH2 inhibitor EZP011989, we confirmed our hypothesis *in vitro* using MCF-7 cells. The synergy is especially strong on MCF-7-Bo cells (Figure S7B). Next, a four-arm *in vivo* experiment was used to ask if combinatory treatment of EPZ011989 and fulvestrant at the microscopic metastasis stage (to mimic adjuvant therapy) could lead to decreased bone colonization. EPZ011989 and fulvestrant had little-to-modest effects when used as single agents. However, the combined treatment inhibited bone colonization and rendered 50% of mice tumor free on the basis of bioluminescence signals (Figure 7E) and microCT (Figures 7F, S7C, and S7D). This is a remarkable effect considering that EPZ011989 treatment only lasts for 3 weeks. EPZ011989 treatment also sensitized ZR75-1 bone lesions to fulvestrant treatment (Figure 7G). Finally, we tested the combinatory treatment on PDX-based spontaneous BoM models using PET imaging. Pretreatment of mice with EPZ011989 inhibited spontaneous metastasis to bone, as shown in the reduced 18F-FDG update (Figures 7H and S7E).

DISCUSSION

Phenotypic plasticity has been recognized as a major driving force of normal development, tumor initiation, and tumor progression (Dravis et al., 2018; Gupta et al., 2019; Lambert et al., 2017). The heterogeneity of ER expression in ER$^+$ tumors has long been noticed and may reflect such plasticity. In this study, our data demonstrate that even genetically identical ER$^+$ cancer cells exhibit a substantial level of variation in ER expression. We uncovered that the OGs trigger an adaptive epigenomic change in ER$^+$ metastatic seeds through both paracrine signaling and direct cell-cell contact and leads to increased phenotypic plasticity and therapeutic resistance. These changes form a transient and reversible effect on cancer cells, including those that are genetically homogeneous, which distinguishes this process from the clonal selection investigated in the past (Bos et al., 2009; Kang et al., 2003; Minn et al., 2005). Indeed, our data suggest a coordinated action between epigenomic adaptation and genetic selection.

Our study identified a number of pathways that are altered in cancer cells by BME. Among these pathways, EZH2-mediated epigenomic reprogramming is a leading candidate for therapeutic intervention. It integrates multiple signals from OGs (e.g., FGF2 and PDGF-DD), and in turn, broadly impacts several downstream pathways related to cancer stemness and metastasis (e.g., WNT and Notch)(Gonzalez et al., 2014; Shi et al.,

(B) Graph showing the expression of all human 22 fibroblast growth factor (FGF) family proteins (FGF1-23) in OGs (FOB) RNA sequencing dataset (n = 3 technical triplicates).
(C) IF images of alkaline phosphatase (ALP) and basic fibroblast growth factor (FGF2/bFGF) in normal bone tissue. Nuclei is shown in blue (DAPI). Scale bar: 50 μm
(D) IF images showing decreased ER expression in tumors established in FGF2 enriched BME.
(E) The scatter dot plot represents ER quantification from tumors according to FGF2 enrichment (Low and High) in adjacent stromal cells (n = 3–4 lesions). Mean expression is represented in blue. The Gaussian curve simulates ER distribution based on nuclear intensity. Peaks: mean expression of ER.
(F) Immunoblots depicting the effect of recombinant FGF2 (20ng/ml) on ER expression in multiple BC models including PDX HCI011. Cells were treated for 24 h. ER expression was summarized as connected dot plot graphs; n = 3 and 4 cell lines. p values: one-tailed unpaired Student's t tests.
(G) Histogram showing effect of recombinant FGF2 (20ng/ml) on MCF7 and ZR75-1 cell growth in 3D; n = 6 technical replicates.
(H) Bone-in-culture-array (BICA) assay showing synergistic effects between 2.5 μM pan FGFR inhibitor (BGJ398) and 20 nM fulvestrant in MCF7 and ZR75-1 models. n = 6 technical replicates.
(I) Annotated bar plot showing the association of histone modifications with basic FGF (FGF2) gene signatures using the Enrichr platform (https://amp.pharm.mssm.edu/Enrichr/). Processed ChIP-sequencing data were obtained from Epigenomic Roadmap Project (Roadmap Epigenomics Consortium et al., 2015). Histograms represent the association score with FGF2 signaling. Signatures are sorted based on p value ranking. Only p values < 0.05 and <0.01 were shown for the top and bottom panel, respectively.
(J) Immunoblotting showing alteration of EZH2 expression in multiple cells following a 24 h treatment with 1 μM pan FGFR inhibitor (BGJ398) or 20 nM FGF2 recombinant (FGF2r). Primary cells generated from HCI011 (ER$^+$ PDX) were cultured in 3D and treated with 1 μM pan FGFR inhibitor (BGJ398) or vehicle for 24 h. Normalized EZH2 expression (/β-actin) was shown as dot plots. (n = 4 cell lines); p value: one-tailed unpaired Student's t test.
(K) Dot plots depicting the effect of 20 nM recombinant FGF2 on H3k27me3 of multiple ER$^+$ BC 3D models, based on quantified IF images (n = 3 technical replicates). p values: one-tailed paired Student's t tests.
(L) IF quantification of EZH2 expression in paired metastases and orthotopic tumor. MCF7 cells were transplanted to bone and to mammary gland of nude mice, which led to tumor formation at multiples sites, including lung, ovary, bone, and mammary gland. Metastatic tissues were harvested for IF quantification and shown as a dot plot graph. (n = 3 images); Error bars: mean ± SD.
(M) IF showing co-expression of ER and EZH2 in 3D monocultures and co-cultures (+FOB) models of MCF7 and PDX HCI011. Scale bars: 50 μm.
(N) Heatmap showing relative expression of nuclear ER and EZH2 in MCF7 and PDX HCI011 SCs as depicted in (M).
(O) Effect of the EZH2 inhibitor EPZ011989 on ESR1 mRNA expression after 24 h of treatment; n = 4 cell lines.
(P) Dot plots showing IF quantification of EZH2 and ER in MCF7 BMMs and macrometastases (n = 3–5 lesions). Error bars: mean ± SD.
(Q) Reversibility of epigenetic changes based on post-translational modification (PTM) analysis. The percent changes in H3k27me3 between parental cells (MCF7), M7-SCP2 and bone-derived (MCF7-Bo and M7-SCP2-Bo) after multiple passages *in vitro* (Passages: P0 and P10). (n = 4 biological replicates); p values are relatively to parental cells. The right panel depicts the temporal epigenetic changes (H3k27me3/H3)
(A–Q) p values were computed by two-tailed unpaired Student's t tests unless otherwise noted.

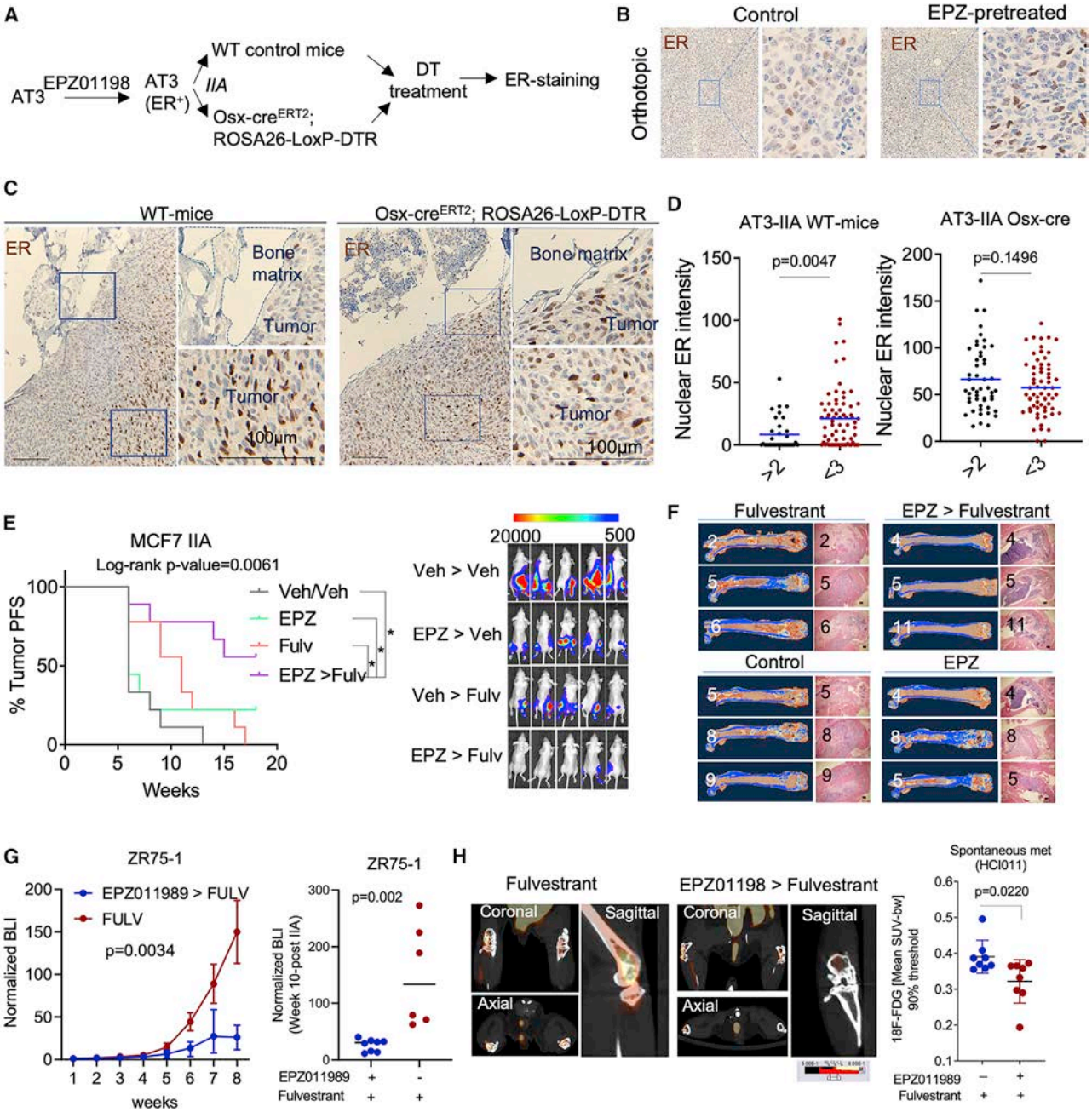

Figure 7. EZH2 integrates multiple signals from BME and drives the phenotypic shift of ER$^+$ breast cancer cells

(A) Scheme to evaluate ER loss in syngeneic murine models. AT3 cells were pretreated with EZH2 inhibitor (EPZ011989) for 2 weeks before being transplanted to bone of wild-type or osterix-depleted C57BL/6 mice (Osx-cre^{ERT2} ROSA-LoxP-DTR).

(B) IHC staining depicting ER expression in orthotopic tumors derived from EZP011989 pretreated AT3 cells.

(C) IHC staining of ER in BoM models presented in (A).

(D) Dot plots showing ER expression in IIA-induced AT3 BoM in control (WT-mice) and osteoprogenitor-depleted (Osx- cre^{ERT2} ROSA-LoxP-DTR) mice at the SC level.

(E) Progression free survival (PFS) curve of IIA-induced BoMs following treatment with the EZH2 inhibitor EPZ011989 or the ER inhibitor fulvestrant in combination or as single agents. BL images show the effect of combination treatment on IIA-induced BoMs. (n = 9–10 mice); Log-rank test was used for survival analysis. *p < 0.05.

(F) microCT and H&E images depicting tumor burden after pre-clinical experiment described in E. All groups revealed BoM formation except for combination treatment group (EPZ > Fulvestrant).

(G) Growth curve showing the effect of EPZ011989 pretreatment on the fulvestrant response of endocrine resistant ZR75-1 BoMs. Single agent and combination treatment groups are shown in blue and red, respectively. Multiple ANOVA was used for statistical analysis. BLI of metastatic burden at week 8 was shown as dot plot. (n = 6 and 8 mice for fulvestrant and combination group, respectively. Error bars: mean ± SD.

(legend continued on next page)

2007). Moreover, potent and selective EZH2 inhibitors are available and are being clinically investigated in other diseases (Italiano et al., 2018), making it relatively easy for future clinical applications. Pharmacological inhibition of EZH2 promotes a global landscape change of histone marks (Huang et al., 2018). Tumors that developed resistance to histone demethylase KDM5A/B had increased EZH2 expression (Hinohara et al., 2018). Hence, BME induction of EZH2 in BMMs may trigger an epigenomic disturbance beyond H3K27me3.

The loss of ER expression during BoM appears to be transient. In the advanced stage when the osteolytic vicious cycle starts (Boyce et al., 1999; Kozlow and Guise, 2005; Weilbaecher et al., 2011), ER expression may recover, perhaps driven by the stimulatory effects of other stromal cells recruited to macrometastases. The positive spatial correlation between RANK and ER supports this possibility. However, the BME-conferred endocrine resistance may persist in cells maintaining interactions with OGs suggesting that additional mechanisms may be involved (Eyre et al., 2019). Thus, overt BoMs may be heterogeneous, including a subset whose ER signaling remains repressed, which may be responsible for the rapid development of resistance observed during metastatic treatments (Johnston, 2010).

Although our experiments focused on BoMs, we are not ignoring the fact that other metastases also need to be prevented and cured. Recent genomic analyses revealed frequent metastasis-to-metastasis seeding (Brown et al., 2017; Ullah et al., 2018), suggesting that bone may not be the final destination for cancer cell dissemination. In fact, over two-thirds of bone-only metastases subsequently develop other metastases (Coleman, 2001). The enhancement of stem cell signaling in BME raises the possibility that bone may invigorate DTCs for further metastases, and this possibility has recently gained support in our co-submitted manuscript (Zhang et al., 2021). Therefore, investigations on BoMs may have much broader impacts.

Limitations of study

Our data did not address the question of whether the observed effects are specific to the BME. It is possible that in non-bone organs similar mechanisms also lead to increased phenotypic plasticity via other cell types. Our study is also limited by the lack of naturally occurring murine ER^+ models that recapitulate endocrine responses and development of resistance, as well as inability to stably tag all PDX models for linage tracing.

STAR★METHODS

Detailed methods are provided in the online version of this paper and include the following:

- KEY RESOURCES TABLE
- RESOURCE AVAILABILITY
  - Lead contact
  - Material availability
  - Data and code availability
- EXPERIMENTAL MODEL AND SUBJECT DETAILS
  - Animal studies
  - Patient-derived xenografts (PDXs) and primary cells
  - Cell lines
- METHOD DETAILS
  - Ovariectomy and aromatase inhibition
  - Intra-iliac-artery (IIA) and mammary fat pad (MFP) injections
  - Spontaneous metastasis from PDX models
  - Drug treatments
  - Immunohistochemistry, immunofluorescence, and immunoblotting
  - Image acquisition and quantification
  - Tumor classification
  - Recombinant protein and calcium treatments
  - Live imaging
  - Reverse phase protein arrays (RPPA)
  - PET/CT imaging and analysis
  - microCT imaging and analysis
  - Mammosphere and coculture assays
  - Quantitative real-time PCR
  - Bulk ATAC sequencing (ATAC-seq) and analysis
  - ATAC-seq analysis
  - Whole-exome sequencing (WES)
  - Histone protein post-translational modification (PTM) analysis
  - Translating ribosome affinity purification (TRAP) sequencing (TRAP-seq)
  - Tracing metastasis expansion in bone using CRISPR-Cas9/hgRNA system
- QUANTIFICATION AND STATISTICAL ANALYSIS

SUPPLEMENTAL INFORMATION

Supplemental Information can be found online at https://doi.org/10.1016/j.devcel.2021.03.008.

ACKNOWLEDGMENTS

We thank the Breast Center Pathology Core, the Antibody-Based Proteomics Core (CPRIT Core Facility award [RP170005] and P30 Cancer Center Support Grant [NCI-CA125123]), the Small Animal Imaging Facility (SAIF) at Texas Children Hospital, and the Genomic and RNA Profiling core (GARP) for their technical support. We also thank Epizyme (Cambridge, MA) for providing the EZH2 inhibitor EPZ-011989. We express our gratitude to Drs. Rosen Jeffrey, Michael Lewis, and Xi Chen for advice and technical support. This project was supported by the Cytometry and Cell Sorting Core at Baylor College of Medicine with funding from the CPRIT Core Facility Support Award (CPRIT-RP180672) and the NIH (CA125123 and RR024574) and the assistance of Joel M. Sederstrom. X.H.-F.Z. is supported by US Department of Defense DAMD W81XWH-16-1-0073 (Era of Hope Scholarship), NCI CA183878, NCI CA251950, NCI CA221946, DAMD W81XWH-20-1-0375, Breast Cancer Research Foundation, and McNair Medical Institute.

AUTHOR CONTRIBUTIONS

Conceptualization, I.L.B., W.Z., M.W.G., S.H., H.W., P.S., and X.H.-F.Z.; methodology, I.L.B., W.Z., H.W., P. Sarkar, Z.G., Z.X., Z.G., Z.L., Y.-W.W., J.L.,

(H) PET-CT images showing 18F-FDG uptake in spontaneous BoMs (hind limbs) following single agent (fulvestrant) or combination (EPZ > fulvestrant) treatment. (n = 4 mice). Error bars: mean ± SD.
(A–H) p values were computed by two-tailed unpaired Student's t tests unless otherwise noted.

CellPress

W.W., H.C.L., A.M.M., M.J., I.S.K., S.S., A.G., P. Singh, S.H., M.W.G., R.C., M.J.E., X.H-F.Z.; software and data curation, I.B., Z.L., Y.W., J.H., L.L., H-H.J., H.W., C.L., and X.H-F.Z.; resources, M.J.E., Z.L., and X.H.-F.Z.; writing—original draft, I.L.B. and X.H.-F.Z.; writing—review and editing, I.B., W.Z., H.W., Z.G., and X.H.-F.Z.; visualization, I.L.B. and X.H.-F.Z.; project administration, I.L.B., W.Z., J.L., and X.H.-F.Z.; supervision and funding acquisition, X.H.-F.Z.

DECLARATION OF INTERESTS

The authors declare no competing interests.

Received: September 12, 2019
Revised: November 30, 2020
Accepted: February 27, 2021
Published: April 19, 2021

REFERENCES

Afgan, E., Baker, D., Batut, B., Van Den Beek, M., Bouvier, D., Cech, M., Chilton, J., Clements, D., Coraor, N., Grüning, B.A., et al. (2018). The Galaxy platform for accessible, reproducible and collaborative biomedical analyses: 2018 update. Nucleic Acids Res. *46*, W537–W544.

Andor, N., Harness, J.V., Müller, S., Mewes, H.W., and Petritsch, C. (2014). Expands: expanding ploidy and allele frequency on nested subpopulations. Bioinformatics *30*, 50–60.

Andrade, K., Fornetti, J., Zhao, L., Miller, S.C., Randall, R.L., Anderson, N., Waltz, S.E., McHale, M., and Welm, A.L. (2017). RON kinase: a target for treatment of cancer-induced bone destruction and osteoporosis. Sci. Transl. Med. *9*, 374.

Bos, P.D., Zhang, X.H.-F., Nadal, C., Shu, W., Gomis, R.R., Nguyen, D.X., Minn, A.J., van de Vijver, M.J., Gerald, W.L., Foekens, J.A., and Massagué, J. (2009). Genes that mediate breast cancer metastasis to the brain. Nature *459*, 1005–1009.

Boyce, B.F., Yoneda, T., and Guise, T.A. (1999). Factors regulating the growth of metastatic cancer in bone. Endocr. Relat. Cancer *6*, 333–347.

Brodie, A., Jelovac, D., Macedo, L., Sabnis, G., Tilghman, S., and Goloubeva, O. (2005). Therapeutic observations in MCF-7 aromatase xenografts. Clin. Cancer Res. *11*, 884s–888s.

Brown, D., Smeets, D., Székely, B., Larsimont, D., Szász, A.M., Adnet, P.Y., Rothé, F., Rouas, G., Nagy, Z.I., Faragó, Z., et al. (2017). Phylogenetic analysis of metastatic progression in breast cancer using somatic mutations and copy number aberrations. Nat. Commun. *8*, 14944.

Buenrostro, J.D., Wu, B., Chang, H.Y., and Greenleaf, W.J. (2015). ATAC-seq: a method for assaying chromatin accessibility genome-wide. Curr. Protoc. Mol. Biol. *109*, 21.29.1–21.29.9.

Campbell, J.E., Kuntz, K.W., Knutson, S.K., Warholic, N.M., Keilhack, H., Wigle, T.J., Raimondi, A., Klaus, C.R., Rioux, N., Yokoi, A., et al. (2015). EPZ011989, A potent, orally-available EZH2 inhibitor with robust in vivo activity. ACS Med. Chem. Lett. *6*, 491–495.

Chang, C.H., Zhang, M., Rajapakshe, K., Coarfa, C., Edwards, D., Huang, S., and Rosen, J.M. (2015). Mammary stem cells and tumor-initiating cells are more resistant to apoptosis and exhibit increased DNA repair activity in response to DNA damage. Stem Cell Rep. *5*, 378–391.

Coleman, R.E. (2001). Metastatic bone disease: clinical features, pathophysiology and treatment strategies. Cancer Treat. Rev. *27*, 165–176.

Derose, Y.S., Wang, G., Lin, Y.C., Bernard, P.S., Buys, S.S., Ebbert, M.T.W., Factor, R., Matsen, C., Milash, B.A., Nelson, E., et al. (2011). Tumor grafts derived from women with breast cancer authentically reflect tumor pathology, growth, metastasis and disease outcomes. Nat. Med. *17*, 1514–1520.

Dravis, C., Chung, C.Y., Lytle, N.K., Herrera-Valdez, J., Luna, G., Trejo, C.L., Reya, T., and Wahl, G.M. (2018). Epigenetic and transcriptomic profiling of mammary gland development and tumor models disclose regulators of cell state plasticity. Cancer Cell *34*, 466–482.e6.

Edgar, R., Domrachev, M., and Lash, A.E. (2002). Gene expression omnibus: NCBI gene expression and hybridization array data repository. Nucleic Acids Res. *30*, 207–210.

Esposito, M., Mondal, N., Greco, T.M., Wei, Y., Spadazzi, C., Lin, S.C., Zheng, H., Cheung, C., Magnani, J.L., Lin, S.-H., et al. (2019). Bone vascular niche E-selectin induces mesenchymal–epithelial transition and Wnt activation in cancer cells to promote bone metastasis. Nat. Cell Biol. *21*, 627–639.

Eyre, R., Alférez, D.G., Santiago-Gómez, A., Spence, K., McConnell, J.C., Hart, C., Simões, B.M., Lefley, D., Tulotta, C., Storer, J., et al. (2019). Microenvironmental IL1β promotes breast cancer metastatic colonisation in the bone via activation of Wnt signalling. Nat. Commun. *10*, 5016.

Fehm, T., Krawczyk, N., Solomayer, E.F., Becker-Pergola, G., Dürr-Störzer, S., Neubauer, H., Seeger, H., Staebler, A., Wallwiener, D., and Becker, S. (2008). ERalpha-status of disseminated tumour cells in bone marrow of primary breast cancer patients. Breast Cancer Res. *10*, R76.

Fillmore, C.M., Gupta, P.B., Rudnick, J.A., Caballero, S., Keller, P.J., Lander, E.S., and Kuperwasser, C. (2010). Estrogen expands breast cancer stem-like cells through paracrine FGF/Tbx3 signaling. Proc. Natl. Acad. Sci. USA *107*, 21737–21742.

Ginestier, C., Hur, M.H., Charafe-Jauffret, E., Monville, F., Dutcher, J., Brown, M., Jacquemier, J., Viens, P., Kleer, C.G., Liu, S., et al. (2007). ALDH1 is a marker of normal and malignant human mammary stem cells and a predictor of poor clinical outcome. Cell Stem Cell *1*, 555–567.

Gonzalez, M.E., Moore, H.M., Li, X., Toy, K.A., Huang, W., Sabel, M.S., Kidwell, K.M., and Kleer, C.G. (2014). EZH2 expands breast stem cells through activation of NOTCH1 signaling. Proc. Natl. Acad. Sci. USA *111*, 3098–3103.

Guo, W., Keckesova, Z., Donaher, J.L., Shibue, T., Tischler, V., Reinhardt, F., Itzkovitz, S., Noske, A., Zürrer-Härdi, U., Bell, G., et al. (2012). Slug and Sox9 cooperatively determine the mammary stem cell state. Cell *148*, 1015–1028.

Gupta, P.B., Pastushenko, I., Skibinski, A., Blanpain, C., and Kuperwasser, C. (2019). Phenotypic plasticity: driver of cancer initiation, progression, and therapy resistance. Cell Stem Cell *24*, 65–78.

Guy, C.T., Cardiff, R.D., and Muller, W.J. (1992). Induction of mammary tumors by expression of polyomavirus middle T oncogene: a transgenic mouse model for metastatic disease. Mol. Cell. Biol. *12*, 954–961.

Hänzelmann, S., Castelo, R., and Guinney, J. (2013). GSVA: gene set variation analysis for microarray and RNA-seq data. BMC Bioinformatics *14*, 7.

Heiman, M., Kulicke, R., Fenster, R.J., Greengard, P., and Heintz, N. (2014). Cell type-specific mRNA purification by translating ribosome affinity purification (TRAP). Nat. Protoc. *9*, 1282–1291.

Heinz, S., Benner, C., Spann, N., Bertolino, E., Lin, Y.C., Laslo, P., Cheng, J.X., Murre, C., Singh, H., and Glass, C.K. (2010). Simple combinations of lineage-determining transcription factors prime cis-regulatory elements required for macrophage and B cell identities. Mol. Cell *38*, 576–589.

Hinohara, K., Wu, H.J., Vigneau, S., McDonald, T.O., Igarashi, K.J., Yamamoto, K.N., Madsen, T., Fassl, A., Egri, S.B., Papanastasiou, M., et al. (2018). KDM5 histone demethylase activity links cellular transcriptomic heterogeneity to therapeutic resistance. Cancer Cell. *34*, 939-953.e9.

Hoefnagel, L.D., van der Groep, P., van de Vijver, M.J., Boers, J.E., Wesseling, P., Wesseling, J., Dutch Distant Breast Cancer Metastases Consortium, van der Wall, E., and van Diest, P.J. (2013). Discordance in ERα, PR and HER2 receptor status across different distant breast cancer metastases within the same patient. Ann. Oncol. *24*, 3017–3023.

Huang, X., Yan, J., Zhang, M., Wang, Y., Chen, Y., Fu, X., Wei, R., Zheng, X.L., Liu, Z., Zhang, X., et al. (2018). Targeting epigenetic crosstalk as a therapeutic strategy for EZH2-aberrant solid tumors. Cell *175*, 186–199.e19.

Italiano, A., Soria, J.C., Toulmonde, M., Michot, J.M., Lucchesi, C., Varga, A., Coindre, J.M., Blakemore, S.J., Clawson, A., Suttle, B., et al. (2018). Tazemetostat, an EZH2 inhibitor, in relapsed or refractory B-cell non-Hodgkin lymphoma and advanced solid tumours: a first-in-human, open-label, phase 1 study. Lancet Oncol *19*, 649–659.

Ithimakin, S., Day, K.C., Malik, F., Zen, Q., Dawsey, S.J., Bersano-Begey, T.F., Quraishi, A.A., Ignatoski, K.W., Daignault, S., Davis, A., et al. (2013). HER2

drives luminal breast cancer stem cells in the absence of HER2 amplification: implications for efficacy of adjuvant trastuzumab. Cancer Res *73*, 1635–1646.

Jäger, B.A.S., Finkenzeller, C., Bock, C., Majunke, L., Jueckstock, J.K., Andergassen, U., Neugebauer, J.K., Pestka, A., Friedl, T.W.P., Jeschke, U., et al. (2015). Estrogen receptor and HER2 status on disseminated tumor cells and primary tumor in patients with early breast cancer. Transl. Oncol. *8*, 509–516.

Johnston, S.R.D. (2010). New strategies in estrogen receptor-positive breast cancer. Clin. Cancer Res. *16*, 1979–1987.

Kalhor, R., Kalhor, K., Mejia, L., Leeper, K., Graveline, A., Mali, P., and Church, G.M. (2018). Developmental barcoding of whole mouse via homing CRISPR. Science *361*, eaat9804.

Kalhor, R., Mali, P., and Church, G.M. (2017). Rapidly evolving homing CRISPR barcodes. Nat. Methods *14*, 195–200.

Kang, Y., Siegel, P.M., Shu, W., Drobnjak, M., Kakonen, S.M., Cordón-Cardo, C., Guise, T.A., and Massagué, J. (2003). A multigenic program mediating breast cancer metastasis to bone. Cancer Cell *3*, 537–549.

Kennecke, H., Yerushalmi, R., Woods, R., Cheang, M.C., Voduc, D., Speers, C.H., Nielsen, T.O., and Gelmon, K. (2010). Metastatic behavior of breast cancer subtypes. J. Clin. Oncol. *28*, 3271–3277.

Kim, K.H., and Roberts, C.W.M. (2016). Targeting EZH2 in cancer. Nat. Med. *22*, 128–134.

Koboldt, D.C., Larson, D.E., and Wilson, R.K. (2013). Using varscan 2 for germline variant calling and somatic mutation detection. Curr. Protoc. Bioinform. *44*, 15.4.1–15.4.17.

Koboldt, D.C., Zhang, Q., Larson, D.E., Shen, D., McLellan, M.D., Lin, L., Miller, C.A., Mardis, E.R., Ding, L., and Wilson, R.K. (2012). VarScan 2: Somatic mutation and copy number alteration discovery in cancer by exome sequencing. Genome Res *22*, 568–576.

Kozlow, W., and Guise, T.A. (2005). Breast cancer metastasis to bone: mechanisms of osteolysis and implications for therapy. J. Mammary Gland Biol. Neoplasia *10*, 169–180.

Kurland, B.F., Peterson, L.M., Lee, J.H., Schubert, E.K., Currin, E.R., Link, J.M., Krohn, K.A., Mankoff, D.A., and Linden, H.M. (2017). Estrogen receptor binding (18F-FES PET) and glycolytic activity (18F-FDG PET) predict progression-free survival on endocrine therapy in patients with ER+ breast cancer. Clin. Cancer Res. *23*, 407–415.

Lambert, A.W., Pattabiraman, D.R., and Weinberg, R.A. (2017). Emerging biological principles of metastasis. Cell *168*, 670–691.

Lehmann, B.D., Bauer, J.A., Chen, X., Sanders, M.E., Chakravarthy, A.B., Shyr, Y., and Pietenpol, J.A. (2011). Identification of human triple-negative breast cancer subtypes and preclinical models for selection of targeted therapies. J. Clin. Invest. *121*, 2750–2767.

Levin-Allerhand, J.A., Sokol, K., and Smith, J.D. (2003). Safe and effective method for chronic 17β-estradiol administration to mice. Contemp. Top. Lab. Anim. Sci. *42*, 33–35.

Li, H., Handsaker, B., Wysoker, A., Fennell, T., Ruan, J., Homer, N., Marth, G., Abecasis, G., and Durbin, R.; 1000 Genome Project Data Processing Subgroup (2009). The sequence alignment/Map format and SAMtools. Bioinformatics *25*, 2078–2079.

Li, S., Shen, D., Shao, J., Crowder, R., Liu, W., Prat, A., He, X., Liu, S., Hoog, J., Lu, C., et al. (2013). Endocrine-therapy-resistant ESR1 variants revealed by genomic characterization of breast-cancer-derived xenografts. Cell Rep. *4*, 1116–1130.

Lim, E., Metzger-Filho, O., and Winer, E.P. (2012). The natural history of hormone receptor-positive breast cancer. Oncol. Williston Park *26*, 688–694, 696.

Lin, E.Y., Jones, J.G., Li, P., Zhu, L., Whitney, K.D., Muller, W.J., and Pollard, J.W. (2003). Progression to malignancy in the polyoma middle T oncoprotein mouse breast cancer model provides a reliable model for human diseases. Am. J. Pathol. *163*, 2113–2126.

Mani, S.A., Guo, W., Liao, M.J., Eaton, E.N., Ayyanan, A., Zhou, A.Y., Brooks, M., Reinhard, F., Zhang, C.C., Shipitsin, M., et al. (2008). The epithelial-mesenchymal transition generates cells with properties of stem cells. Cell *133*, 704–715.

Marotta, L.L.C., Almendro, V., Marusyk, A., Shipitsin, M., Schemme, J., Walker, S.R., Bloushtain-Qimron, N., Kim, J.J., Choudhury, S.A., Maruyama, R., et al. (2011). The JAK2/STAT3 signaling pathway is required for growth of $CD44^+CD24^-$ stem cell-like breast cancer cells in human tumors. J. Clin. Invest. *121*, 2723–2735.

Medina, D., Kittrell, F.S., Shepard, A., Stephens, L.C., Jiang, C., Lu, J., Allred, D.C., McCarthy, M., and Ullrich, R.L. (2002). Biological and genetic properties of the p53 null preneoplastic mammary epithelium. FASEB J. *16*, 881–883.

Minn, A.J., Gupta, G.P., Siegel, P.M., Bos, P.D., Shu, W., Giri, D.D., Viale, A., Olshen, A.B., Gerald, W.L., and Massagué, J. (2005). Genes that mediate breast cancer metastasis to lung. Nature *436*, 518–524.

Nawaz, Z., Lonard, D.M., Dennis, A.P., Smith, C.L., and O'Malley, B.W. (1999). Proteasome-dependent degradation of the human estrogen receptor. Proc. Natl. Acad. Sci. USA *96*, 1858–1862.

Pfefferle, A.D., Spike, B.T., Wahl, G.M., and Perou, C.M. (2015). Luminal progenitor and fetal mammary stem cell expression features predict breast tumor response to neoadjuvant chemotherapy. Breast Cancer Res. Treat. *149*, 425–437.

Priedigkeit, N., Watters, R.J., Lucas, P.C., Basudan, A., Bhargava, R., Horne, W., Kolls, J.K., Fang, Z., Rosenzweig, M.Q., Brufsky, A.M., et al. (2017). Exome-capture RNA sequencing of decade-old breast cancers and matched decalcified bone metastases. JCI Insight *2*, e95703.

Quinlan, A.R., and Hall, I.M. (2010). BEDTools: a flexible suite of utilities for comparing genomic features. Bioinformatics *26*, 841–842.

Rajapaksa, G., Nikolos, F., Bado, I., Clarke, R., Gustafsson, J.Å., and Thomas, C. (2015). ERβ decreases breast cancer cell survival by regulating the IRE1/XBP-1 pathway. Oncogene *34*, 4130–4141.

Ramírez, F., Dündar, F., Diehl, S., Grüning, B.A., and Manke, T. (2014). DeepTools: a flexible platform for exploring deep-sequencing data. Nucleic Acids Res *42*, W187–W191.

Reijm, E.A., Jansen, M.P.H.M., Ruigrok-Ritstier, K., Van Staveren, I.L., Look, M.P., Van Gelder, M.E.M., Sieuwerts, A.M., Sleijfer, S., Foekens, J.A., and Berns, E.M.J.J. (2011). Decreased expression of EZH2 is associated with upregulation of ER and favorable outcome to tamoxifen in advanced breast cancer. Breast Cancer Res. Treat. *125*, 387–394.

Roadmap Epigenomics Consortium, Kundaje, A., Meuleman, W., Ernst, J., Bilenky, M., Yen, A., Heravi-Moussavi, A., Kheradpour, P., Zhang, Z., Wang, J., et al. (2015). Integrative analysis of 111 reference human epigenomes. Nature *518*, 317–330.

Sethi, N., Dai, X., Winter, C.G., and Kang, Y. (2011). Tumor-derived Jagged1 promotes osteolytic bone metastasis of breast cancer by engaging Notch signaling in bone cells. Cancer Cell *19*, 192–205.

Sgroi, D.C., Sestak, I., Cuzick, J., Zhang, Y., Schnabel, C.A., Schroeder, B., Erlander, M.G., Dunbier, A., Sidhu, K., Lopez-Knowles, E., et al. (2013). Prediction of late distant recurrence in patients with oestrogen-receptor-positive breast cancer: a prospective comparison of the breast-cancer index (BCI) assay, 21-gene recurrence score, and IHC4 in the TransATAC study population. Lancet Oncol. *14*, 1067–1076.

Shi, B., Liang, J., Yang, X., Wang, Y., Zhao, Y., Wu, H., Sun, L., Zhang, Y., Chen, Y., Li, R., et al. (2007). Integration of estrogen and Wnt signaling circuits by the polycomb Group protein EZH2 in breast cancer cells. Mol. Cell. Biol. *27*, 5105–5119.

Smid, M., Wang, Y., Zhang, Y., Sieuwerts, A.M., Yu, J., Klijn, J.G., Foekens, J.A., and Martens, J.W. (2008). Subtypes of breast cancer show preferential site of relapse. Cancer Res. *68*, 3108–3114.

Stark, R., and Brown, G. (2011). DiffBind : differential binding analysis of ChIP-Seq peak data. Bioconductor. https://doi.org/10.18129/B9.bioc.DiffBind.

Ström, J.O., Theodorsson, A., Ingberg, E., Isaksson, I.M., and Theodorsson, E. (2012). Ovariectomy and 17β-estradiol replacement in rats and mice: a visual demonstration. J. Vis. Exp. *64*, e4013.

Tam, W.L., Lu, H., Buikhuisen, J., Soh, B.S., Lim, E., Reinhardt, F., Wu, Z.J., Krall, J.A., Bierie, B., Guo, W., et al. (2013). Protein kinase C α is a central signaling node and therapeutic target for breast cancer stem cells. Cancer Cell *24*, 347–364.

Thorvaldsdóttir, H., Robinson, J.T., and Mesirov, J.P. (2013). Integrative Genomics Viewer (IGV): high-performance genomics data visualization and exploration. Brief. Bioinform. *14*, 178–192.

Ullah, I., Karthik, G.M., Alkodsi, A., Kjällquist, U., Stålhammar, G., Lövrot, J., Martinez, N.F., Lagergren, J., Hautaniemi, S., Hartman, J., and Bergh, J. (2018). Evolutionary history of metastatic breast cancer reveals minimal seeding from axillary lymph nodes. J. Clin. Invest. *128*, 1355–1370.

Von Mering, C., Jensen, L.J., Snel, B., Hooper, S.D., Krupp, M., Foglierini, M., Jouffre, N., Huynen, M.A., and Bork, P. (2005). STRING: known and predicted protein-protein associations, integrated and transferred across organisms. Nucleic Acids Res. *33*, D433–D437.

Wang, H., Tian, L., Goldstein, A., Liu, J., Lo, H.C., Sheng, K., Welte, T., Wong, S.T.C., Gugala, Z., Stossi, F., et al. (2017). Bone-in-culture array as a platform to model early-stage bone metastases and discover anti-metastasis therapies. Nat. Commun. *8*, 15045.

Wang, H., Yu, C., Gao, X., Welte, T., Muscarella, A.M., Tian, L., Zhao, H., Zhao, Z., Du, S., Tao, J., et al. (2015). The osteogenic niche promotes early-stage bone colonization of disseminated breast cancer cells. Cancer Cell *27*, 193–210.

Wang, H., Tian, L., Liu, J., Goldstein, A., Bado, I., Zhang, W., Arenkiel, B.R., Li, Z., Yang, M., Du, S., et al. (2018). The osteogenic niche is a calcium reservoir of bone micrometastases and confers unexpected therapeutic vulnerability. Cancer Cell *34*, 823–839.e7.

Weilbaecher, K.N., Guise, T.A., and McCauley, L.K. (2011). Cancer to bone: a fatal attraction. Nat. Rev. Cancer *11*, 411–425.

Welsch, C.W., Swim, E.L., McManus, M.J., White, A.C., and McGrath, C.M. (1981). Estrogen induced growth of human breast cancer cells (MCF-7) in athymic nude mice is enhanced by secretions from a transplantable pituitary tumor. Cancer Lett. *14*, 309–316.

Welte, T., Kim, I.S., Tian, L., Gao, X., Wang, H., Li, J., Holdman, X.B., Herschkowitz, J.I., Pond, A., Xie, G., et al. (2016). Oncogenic mTOR signalling recruits myeloid-derived suppressor cells to promote tumour initiation. Nat. Cell Biol. *18*, 632–644.

Yu, C., Wang, H., Muscarella, A., Goldstein, A., Zeng, H.C., Bae, Y., Lee, B.H.I., and Zhang, X.H.-F. (2016). Intra-iliac artery injection for efficient and selective modeling of microscopic bone metastasis. J. Vis. Exp. *115*, 53982.

Zhang, G.-L., Zhang, Y., Cao, K.-X., and Wang, X.-M. (2019a). Orthotopic injection of breast cancer cells into the mice mammary fat pad. J. Vis. Exp. *143*.

Zhang, W., Bado, I.L., Hu, J., Wan, Y.-W., Wu, L., Wang, H., Gao, Y., Jeong, H.-H., and Zhang, X.H.-F. (2021). The bone microenvironment invigorates metastatic seeds for further dissemination. bioRixv https://www.biorxiv.org/content/10.1101/2020.11.16.383828v2.

Zhang, X.H.F., Giuliano, M., Trivedi, M.V., Schiff, R., and Osborne, C.K. (2013). Metastasis dormancy in estrogen receptor-positive breast cancer. Clin. Cancer Res. *19*, 6389–6397.

Zheng, H., Bae, Y., Kasimir-Bauer, S., Tang, R., Chen, J., Ren, G., Yuan, M., Esposito, M., Li, W., Wei, Y., et al. (2017). Therapeutic antibody targeting tumor- and osteoblastic niche-derived Jagged1 sensitizes bone metastasis to chemotherapy. Cancer Cell *32*, 731–747.e6.

Varambally, S., Dhanasekaran, S.M., Zhou, M., Barrette, T.R., Kumar-Sinha, C., Sanda, M.G., Ghosh, D., Pienta, K.J., Sewalt, R.G., Otte, A.P., et al. (2002). The polycomb group protein EZH2 is involved in progression of prostate cancer. Nature *419*, 624–629.

STAR★METHODS

KEY RESOURCES TABLE

REAGENT or RESOURCE	SOURCE	IDENTIFIER
Antibodies		
Estrogen Receptor alpha (D8H8)	Cell Signaling Technology	Cat# 8644S; RRID: AB_2617128
EZH2 (D2C9)	Cell Signaling Technology	Cat# 5246S; RRID: AB_10694683
Red Fluorescent Protein	Rockland-Fisher	Cat# 600-401-379; RRID: AB_2209751
Beta-actin (8H10D10)	Cell Signaling Technology	Cat# 3700S; RRID: AB_2242334
Cytokeratin 19 (BA-17)	Genetex	Cat# GTX27755; RRID: AB_369536
FGF2 (C-2)	Santa Cruz	Cat# sc-74412; RRID: AB_1122854
Human PDGF R beta Antibody	R&D Systems-Fisher	Cat# AF385-SP; RRID: AB_355339
Fgf Receptor 1 (D8E4) XP	Cell Signaling Technology	Cat# 9740S; RRID: AB_11178519
Human Vimentin (VIM-V9-L-CE)	Leica	Cat# VIM-V9-L-CE; RRID: AB_442141
Vimentin (D21H3)	Cell Signaling Technology	Cat# 5741S; RRID: AB_10695459
PDGF Receptor β (28E1) Rabbit mAb	Cell Signaling Technology	Cat# 3169S; RRID: AB_2162497
Estrogen Receptor alpha Monoclonal (6F11)	Thermo Fisher Scientific	Cat# MA1-80216; RRID: AB_930763
GFP (Htz-GFP19C8)	Sloan-kettering	RRID: AB_2716737
GFP (Htz- GFP19F7)	Sloan-kettering	RRID: AB_2716736
Cytokeratin 8 (k8)	DSHB	Cat# TROMA-I-s; RRID: AB_531826
Donkey Anti-Rat IgG 594	Jackson ImmunoResearch	Cat# 111-585-144; RRID: AB_2307325
Donkey Anti-Mouse IgG 647	Jackson ImmunoResearch	Cat# 715-605-151; RRID: AB_2340863
Goat Anti-Rabbit IgG 488	Jackson ImmunoResearch	Cat# 712-546-153; RRID: AB_2340686
Tri-methyl-Histone H3 (Lys27) Antibody	EMD Millipore	Cat# 07-449; RRID: AB_310624
Tri-methyl-Histone H3 (Lys27) Antibody	Cell Signaling Technology	Cat# C36B11; RRID: AB_11220433
Donkey Anti-Rabbit IgG 488	Jackson ImmunoResearch	Cat# 711-545-152; RRID: AB_2313584
PR Antibody (H-190)	Santa Cruz Biotechnology	Cat# Sc-7208; RRID: AB_2164331
Total Histone 3	Biolegend	Cat# 819412; RRID: AB_2820128
Acetyl-Histone H3 (Lys27) (D5E4) XP	Cell Signaling Technology	Cat# 8173S; RRID: AB_10949503
Alkaline Phosphatase	Abcam	Cat# ab108337; RRID: AB_10862036
Tri-Methyl-Histone H3 (Lys4) (C42D8)	Cell Signaling Technology	Cat# 9751S; RRID: AB_2616028
Tri-Methyl-Histone H4 (Lys20) (D84D2)	Cell Signaling Technology	Cat# 5737S; RRID: AB_10828431
Tri-Methyl-Histone H3 (Lys36) (D5A7) XP	Cell Signaling Technology	Cat# 4909S;RRID: AB_1950412
Tri-Methyl-Histone H3 (Lys9) (D4W1U)	Cell Signaling Technology	Cat# 13969S; RRID: AB_2798355
Bacterial and virus strains		
XL1-Blue	Agilent	Cat# 200236
Stbl3	Thermo Fisher Scientific	C737303
Biological samples		
PDX HCI011	Gift from Dr. Alana L. Welm's Laboratory, University of Utah	N/A
PDX WHIM9	Gift from Dr. Matthew Ellis's Laboratory, Baylor College of Medicine	N/A
Chemicals, peptides, and recombinant proteins		
Human FGF-2	Miltenyi Biotec	Cat# 130093838
Human PDGF-BB	PeproTech-Fisher	Cat# 100-14B
Human PDGF-CC	PeproTech-Fisher	Cat# 100-00CC
Human PDGF-DD	R&D Systems	Cat# 1159-SB-025
β-Estradiol	Sigma-Aldrich	Cat# E2758

(*Continued on next page*)

Continued

REAGENT or RESOURCE	SOURCE	IDENTIFIER
Streptavidin MyOne T1 Dynabeads		N/A
Biotinylated protein L		N/A
Cycloheximide, ultrapure, 98%	Alfa Aesar™-Fisher	Cat# J6690103
1,2-dihexanoyl-sn-glycero-3-phosphocholine (DHPC)	1,2-dihexanoyl-sn-glycero-3-phosphocholine	Cat# 850305P-500 mg
Fulvestrant	Selleck Chemicals	Cat# S1191
4-Hydroxytamoxifen (4-OHT)	Sigma-Aldrich	Cat# H6278-10MG
EPZ-011989-9	Gift from Epizyme	N/A
Anti-Fibroblast MicroBeads, human	Miltenyi Biotec	Cat# 130-050-601
BGJ398 (NVP-BGJ398)	Selleck Chemicals	Cat# S2183
FK506 (Tacrolimis)	ApexBio Technology LLC	Cat# B2143
Carbenoxolone disodium (CBX)	Tocris	Cat# 3096
Sunitinib	Selleckchem-Fisher	S7781
D-Luciferase	Goldbio	Cat# LUCNA-1G
Critical commercial assays		
Nextera XT DNA Library Prep Kit	Illumina	Cat# FC-131-1096
Nextseq 500/500 high output v2 Kit	Illumina	Cat# FC-404-2002
CellTrace™ Far Red Cell Proliferation Kit	Thermo Fisher Scientific	Cat# C34572
iScript™ Reverse Transcription Supermix	Bio-rad	Cat# 1708841
Lipofectamine RNAiMAX Transfection Reagent	Thermo Fisher Scientific	Cat#13778030
iBlot® Transfer Stack, nitrocellulose, mini	Thermo Fisher Scientific	Cat# IB301032
NuPAGE™ Novex™ 4-12% Bis-Tris Protein Gels, 1.5 mm, 15-wel	Thermo Fisher Scientific	Cat# NP0336BOX
Deposited data		
SuperSeries for all sequencing datasets	This Paper	GSE160583
MCF7-MSC TRAP-sequencing dataset	This Paper	GSE137270
Human osteoblast dataset	This Paper	GSE137245
MCF7 bone metastasis evolving barcode dataset	This Paper	GSE160566
Bulk-ATAC-seq SCP2 dataset	This Paper	GSE160582
Whole exome sequencing (WES)	This Paper	GSE161181
Experimental models: cell lines		
Human breast cancer MCF7	ATCC	Cat# HTB-22, RRID:CVCL_0031
Human breast cancer T47D	ATCC	Cat# HTB-133, RRID:CVCL_0553
Human breast cancer ZR75-1	Gift from Dr. Rachel Schiff's Lab, Baylor College of Medicine	Cat# CRL-1500, RRID:CVCL_0588
Human breast cancer ZR75-30	ATCC	Cat# CRL-1504, RRID:CVCL_1661
Human breast cancer MDA-MB-361	ATCC	Cat# HTB-27, RRID:CVCL_0620
Human pre-osteoblast FOB-1.19	ATCC	Cat# CRL-11372, RRID:CVCL_3708
Human mesenchymal stem cell MSC	Gift from Dr. Max Wicha's Laboratory, University of Michigan	N/A
Human Bone Marrow	Lonza	Cat# 2M-125C
Human pre-osteoclast U937	ATCC	Cat# CRL-1593, RRID:CVCL_0007
Mouse pre-osteoblast MC3T3-E1	ATCC	Cat# CRL-2953, RRID:CVCL_0409
Human bone marrow fibroblast Hs5	ATCC	Cat# CRL-11882, RRID:CVCL_3720
Human primary cells HCI011	This paper	N/A
Experimental models: organisms/strains		
Athymic Nude mice [Athymic Nude-Foxn1 nu]	Envigo	N/A

(*Continued on next page*)

Continued

REAGENT or RESOURCE	SOURCE	IDENTIFIER
Scid/Beige mice [C.B-17/IcrHsd-Prkdc scid Lyst bg-J]	Envigo	N/A
Osx1-GFP-cre/iDTR	This paper	N/A
Oligonucleotides		
Silencer™ Negative Control	Thermo Fisher Scientific	AM4611
EZH2 siRNA (human) - ID: s4918	Thermo Fisher Scientific	4392420
EZH2 siRNA (human)- ID: s4916	Thermo Fisher Scientific	4392420
Oligos for qPCR	This paper (Table S1)	N/A
Recombinant DNA		
3X ERE TATA luciferase	A gift from Dr. Donald McDonnell to Addgene, Duke University	Plasmid #11354, RRID_Addgene_11354
GFP-RPL10	Dr. William T. Pu' Laboratory, Harvard Stem Cell Institute	NA
pMD2.G	A gift from Didier Trono to Addgene, EPFL	Plasmid# 12259, RRID_Addgene_12259
psPAX2	A gift from Didier Trono to Addgene, EPFL	plasmid #12260, RRID_Addgene_12260
Pwpt-Fluc/GFP	Wang et al., 2015	N/A
Pwpt-Fluc/RFP	Wang et al., 2015	N/A
ERE-pWPXL/GFP	This paper (modified from Plasmid # 12257; gift from Didier Trono to addgene) EPFL	N/A
hgRNA-A21_pLKO-Puro	A gift from George Church, Harvard (Addgene plasmid # 10057)	Plasmid # 100570. RRID:Addgene 100570
Lenti-iCas9-neo	A gift from Qin Yan, Yale (Addgene plasmid # 85400)	Plasmid # 85400 RRID:Addgene_85400
Software and algorithms		
Expanding Ploidy and Allele-Frequency on Nested Subpopulations	Stanford University	https://CRAN.R-project.org/package=expands
Evolving barcode analysis	This Paper	https://github.com/LiuzLab/ER_positive_breast_cancer_manuscirpt
TraceQC	Baylor College of Medicine	https://github.com/LiuzLab/TraceQC/
Rstudio	Rstudio	http://www.rstudio.com/
Galaxy project	Penn State, Johns Hopkins University, Oregon Health & Science University, and the Galaxy Community	http://galaxyproject.org/
ImageJ	National Institute of Health	https://fiji.sc/
Flow Jo V10.0	FlowJo, LLC	https://www.flowjo.com
LAS AF Lite	Leica Microsystems	*RRID:SCR_013673*
Living Image 4.5.2	PerkinElmer	https://www.perkinelmer.com/lab-products-and-services/resources/in-vivo-imaging-software-downloads.html
Inveon Research Workplace (IRW)	SIEMENS	https://www.siemens-healthineers.com/en-us/molecular-imaging/preclinical-imaging/inveon-workplace/
Graphpad Prism	GraphPad Software, Inc.	https://www.graphpad.com/scientific-software/prism/
Combenefit	Cancer Research UK Cambridge Institute	http://sourceforge.net/projects/combenefit/

RESOURCE AVAILABILITY

Lead contact

Further information and requests for resources and reagents should be directed to and will be fulfilled by the Lead Contac Dr. Xiang H.-F. Zhang at xiangz@bcm.edu

Material availability

Plasmids and cell lines generated in the study will be made available upon request.

Data and code availability

Datasets were deposited in Gene Expression Omnibus (Edgar et al., 2002), with the following GEO accession numbers (GSE137245; GSE137270, GSE160566, GSE160582, and GSE161181). The GEO Reference Series connecting all datasets is GSE160583. Barcode analysis pipeline is accessible at: https://github.com/LiuzLab/ER_positive_breast_cancer-manuscirpt.

EXPERIMENTAL MODEL AND SUBJECT DETAILS

Animal studies

All animal experiments were in compliance with Institutional Animal Care and Use Committee of Baylor College of Medicine. Nude mice [Athymic Nude-Foxn1^{nu}] and SCID/Beige mice [C.B-17/IcrHsd-Prkdc scid Lyst bg-J] were purchased from Envigo. Osx1-GFP-cre/iDTR was generated from Osx1-GFP-cre [B6.Cg-Tg(Sp7-tTA,tetO-EGFP/cre)1Amc/J] and STP-iDTR mice [C57BL/6-Gt(ROSA)26Sortm1(HBEGF) Awai/J] originally obtained from Jackson Laboratory. For all in vivo experiment, 4- to 7-week-old female mice were used.

Patient-derived xenografts (PDXs) and primary cells

ER+ PDX models were kindly provided by Alana L. Welm (HCI011) and Matthew Ellis (WHIM9). All PDXs were maintained in SCID/Beige mice. PDX-HCI011 primary cell line was successfully generated from freshly harvested orthotopic tumors in RPMI medium supplemented with 15–20% FBS, 1X antibiotics Penicillin/Streptomycin and 1X antimycotic Amphotericin (Gibco#15240062). Media was changed every 48 h.

Cell lines

Human estrogen receptor positive (ER+) breast cancer cell lines MCF7, T47D, MDA-MB-361 and ZR75-30, pre-osteoblast cells hFOB-1.19, mesenchymal stem cells MSC, pre-osteoclast U937, and the mouse pre-osteoblast MC3T3-E1 were purchased from *American Type Culture Collection (ATCC)*. *The Human ER+ breast cancer cell line* ZR75-1 was kindly provided by Dr. Rachel Schiff. MCF7 single cell derived populations M7-SCP1, M7-SCP2, M7-SCP3, and M7-SCP4 were generated from single clones of parental MCF7 cells. The mouse cell line AT3 was a kind gift of S.I. Abrams at Roswell Park Cancer Institute.

METHOD DETAILS

Ovariectomy and aromatase inhibition

Mouse ovaries were removed using the previously described surgical procedure (Ström et al., 2012). Briefly, mice were anesthetized with 2% isoflurane, and placed on a temperature-regulated heat pad. The dorsal area covering the lumbar vertebrae was shaved to display a 3x3 cm patch and disinfected. A 1 cm mid incision was performed on the skin and a 0.5 cm incision in the peritoneum allowed access to the ovary. Each ovary was cauterized and removed and each peritoneum was closed using an absorbable suture (Ethicon Vicryl #J497G). Skin closure was completed using EZ clips (Stoelting # 59027) and mice were monitored for recovery. Paracrine estrogen was blocked with oral administration of 0.5 mg/kg Letrozole as previously described (Brodie et al., 2005).

Intra-iliac-artery (IIA) and mammary fat pad (MFP) injections

Intra-iliac-artery (IIA) injection was performed as previously described (Yu et al., 2016). Briefly, breast cancer cells were trypsinized, pelleted, washed twice with PBS, collected in cold PBS and kept on ice. For established breast cancer cell lines such as MCF7 and ZR75, $5x10^5$ cells were injected into the internal iliac artery to generate bone lesions. For PDX models, $2x10^5$ cells were injected except when specified otherwise. For the syngeneic and aggressive model AT3, $1x10^5$ cells were injected. *Mammary fat pad (MFP)* injections were performed as previously described (Zhang et al., 2019a). Cells were prepared as for IIA injection. For all xenograft models except spontaneous metastasis from PDX-HCI011 (Figure 7), estrogen was provided through drinking water to reduce deleterious side effects. Based on previous studies, 8 μg/ml of 17-β-estradiol was added to mouse water bottles and replaced twice a week (Levin-Allerhand et al., 2003; Welsch et al., 1981). In experiments involving dual IIA and MFP injections as in Figure 1D, the same cell number was injected to bone and mammary gland, respectively.

Spontaneous metastasis from PDX models

To evaluate spontaneous metastases from PDX-HCI011, Foxn1^{nu} mice were orthotopically transplanted with 5x10^5 cells from freshly dissociated and purified tumor (Mouse Cell Depletion Kit; miltenyibiotec #130-104-694). Estrogen pellets were subcutaneously implanted to increase the tumor take rate. When tumors reached 1x1 cm, a survival surgery was performed to remove both the primary tumors and the remaining estrogen pellets. A three-week treatment with vehicle or EPZ011989 (125 mg/kg; oral gavage; twice daily) was started two weeks after orthotopic tumor removal. Then, 250 mg/kg of fulvestrant was administered weekly via subcutaneous injection to both EPZ011989 and vehicle pretreated groups for 3 consecutive weeks. Mice were monitored for 3 months before 18F-Fluorodeoxyglucose positron emission tomography (PET) and computed tomography (CT) scans were performed.

Drug treatments

In vivo

The selective estrogen receptor degrader (SERD) fulvestrant (Selleckchem #S1191) was solubilized in 5% DMSO and 95% corn oil and administered subcutaneously at 250 mg/kg per mouse, once a week for 2 consecutive weeks. Letrozole was purchased from Selleckchem (#S1235), diluted in 0.5% sodium carboxymethyl cellulose (NaCMC), and administered at 0.5 mg/kg via oral gavage. EPZ-110989 was kindly provided by Epizyme and stock solutions were prepared following the company's recommendations, using 0.5% sodium carboxymethyl cellulose (NaCMC) and 0.1% Tween-80 as vehicle. A dosage of 125 mg/kg of EPZ-011989 or vehicle was administered twice daily by oral gavage for 3 weeks.

In vitro

Tamoxifen and fulvestrant were used *in vitro* at a concentration of 100 nM and 20 nM per well, respectively. 1-4 uM EPZ011989 was used for coculture experiments. For calcium signaling studies, we used 1 uM of GAP19 (cat#5353) to inhibit gap junction (CX43), and 1 uM of FK506/Tacrolimus (cat#S5003) to block calcineurin. Similarly, 2.5 μM BGJ398 (selleckchem #S2183) and 10 μM Sunitinib (Selleckchem #S7781) were used to inhibit FGF receptors and PDGF receptor B, respectively.

Immunohistochemistry, immunofluorescence, and immunoblotting

IHC/*IF*

Tissues were processed with the help of the Breast Center Pathology Core at Baylor College of Medicine. Immunohistochemistry staining and immunoblotting were performed using antibodies against human ERα (D8H8 and 6F11), Progesterone Receptor (H-190), EZH2 (D2C9), Cytokeratin 8 (TROMA-I), α-Smooth Muscle Actin (D4K9N), Vimentin (D21H3), RANK (64C1385), ALP (ab75635), FGF2 (C2, #sc-74412), CD31 (AF3628), PDGFRβ (28E1), H3K27me3 (C36B11). Western *blot*: Protein extraction was performed using RIPA buffer as previously described (Rajapaksa et al., 2015). Protein electrophoresis and transfer were performed using the XCell SureLock and the iblot system (Invitrogen), respectively. Immunoblotting was performed using antibodies against Estrogen Receptor α (D8H8), Cytokeratin 19 (BA-17), Red Fluorescent Protein (Rockland-Fisher), β-actin (8H10D10), H3K27me3 (Millipore Cat# 07-449), H3K36me3 (D5A7), H3K9me3 (D4W1U), H4K20me3 (D84D2), H3K4me3 (C42D8), and Histone 3 (D1H2). Images were captured using the Odyssey system (Li-cor).

Image acquisition and quantification

Images were acquired with the Leica TCS SP5 or the Zeiss LSM 880 with Airyscan FAST Confocal Microscope. A 40x oil objective lens (Immersion oil refractive index n=1.51) was used to capture images for immunofluorescence quantifications except when specified otherwise. We compared only sets of images that were captured under the same microscopic setting. To further reduce technical biases and batch effects, compared samples were processed and stained in parallel. All images were quantified using ImageJ 1.52i. All statistical analyses represent a two-tailed unpaired Student's t test except when specified otherwise. Whenever applicable (Figures 1E, 1F, 3A–3C, 3E, 3G, 6E, 6K, 6L, 6P, and 7D), single cells from at least 3 biological replicates were used for statistical analysis. Figures 2J, and 6D are representative of at least 3 independent lesions.

Tumor classification

Based on size

metastases were classified based on cell number. On average, small lesions were defined as lesions with fewer than 100 cells. The average maximum cell number common among all models was ~150 for macrometastases (large lesions) and ~90 for micrometastases (small lesions) which gives a fold change superior to >1.5 between the two experimental stages of metastasis. The tumor size in different models (HCI011, WHIM9, MCF7, ZR75-1 and M7-SCP2) of bone metastasis was variable due to differences in tumor aggressiveness. Accordingly, we used a cutoff of median +/- 0.5xS.D. as a more consistent variable to segregate tumors into micrometastasis and macrometastasis. *Based on location*: cancer cells were classified as proximal if they were directly interacting with the bone matrix or separated from it by less than two cells (≤2 cell distance), or classified as distal if separated from the bone matrix by 3 cells or more (≥3 cell distance).

Recombinant protein and calcium treatments

All experiments involving protein recombinants were performed in low serum media (2% serum). Protein recombinants for FGF2 (#130093838), PDGF-BB (100-14B), PDGF-CC (100-00CC), PDGF-DD (1159-SB-025) were diluted in PBS and used at a concentration of 20 or 100ng/ml. To evaluate endocrine resistance after treatment with FGF2 and PDGF recombinants, cells were starved for

48 h in 2% charcoal stripped media before a 20 nM fulvestrant treatment. All experiments involving cells growth were performed in 3D culture and bioluminescence was assessed 72 h post treatment. For western blot, short term treatments were performed for 24 h and long-term ones for up to 72 h. Western blot experiments were performed in 2D in most cases, except when specified otherwise. *Calcium treatment*: 2x10^6 cells (MCF7 or ZR75-1) were cultured in regular medium for 24 hours. Regular medium was replaced with calcium-free minimum essential medium (S-MEM) and treated with vehicle or 2 mM Calcium chloride for 24 h. After collecting all cells, we extracted protein lysates to assess the effect of calcium on ER expression by western blot.

Live imaging

For in vivo experiments, all cells were pre-labelled with Luciferase fused to GFP or RFP as previously described (Wang et al., 2015). 5x10^5 breast cancer cells were injected in bone or mammary fat pad, except when specified otherwise. Tumor growth was monitored using the IVIS Lumina II system. Briefly, mice were anesthetized in an isoflurane chamber (2%) and 100 μl of D-Luciferin was administered through retro-orbital injection to each mouse before image acquisition. For in vitro experiments, 10,000 cells were plated in low attachment 96 well plates to assess cell growth at 72 or 96 h post-treatment. For conditions demanding estrogen depleted media and starvation, 20,000 cells were cultured per well. Images were acquired after adding 1X concentration of D-luciferin containing media to each well.

Reverse phase protein arrays (RPPA)

MCF7 and M7-SCP2 cell lines were injected to bone using intra-iliac artery injection. After 5 weeks of metastasis formation, bones were collected in aseptic conditions and dissociated to generate bone-entrained MCF7-Bo and M7-SCP2-Bo cell lines. Cells were cultured in DMEM 10% FBS supplemented with 1X antibiotics (penicillin, streptomycin) and antimycotics (amphotericin). Bone-educated cells were FACS-sorted and maintained in 2D culture. Approximately 5x10^6 non-entrained and bone-entrained MCF7 and M7-SCP2 cells were harvested in freshly prepared RPPA lysis buffer containing protease and phosphatase inhibitors. Protein lysate was cleared twice via centrifugation (14,000 g for 15 min at 4°C). A BCA assay was adopted for protein quantification (ThermoFisher #23225). All samples were diluted in RPPA solution and SDS to a final concentration of 0.5 mg/ml and heated for 8 min at 100°C for protein denaturation. RPPA was performed as previously described (Welte et al., 2016). In brief, samples and control lysates were spotted onto nitrocellulose-coated slides (Grace Bio-labs; array format of 960 lysates/slide or 2880 spots/slide). The automated slide stainer Autolink 48 (Dako) was used to probe 236 antibodies (against total and phospho-proteins) on slides. Control slides were incubated with antibody diluent. A biotinylated secondary antibody was probed by streptavidin-conjugated IRDye680 fluorophore (LI-COR Biosciences) and total protein was detected with Sypro Ruby Protein Blot Stain according to the manufacturer's instructions (Molecular Probes). All slides were scanned on a GenePix 4400 AL scanner and images were analyzed with GenePix Pro 7.0 (Molecular Devices). Samples were normalized as previously described (Chang et al., 2015). After quality control 233 antibodies remained and were used for subsequent data analysis.

PET/CT imaging and analysis

Radiopharmaceuticals and small-animal PET-CT

Fluorine-18 labeled fluorodeoxyglucose (18F-FDG), fluoroestradiol (18F-FES), and sodium fluoride (18F-NaF) was purchased from (Cyclotope, Houston, TX). All CT and PET images were acquired using an Inveon scanner (Siemens AG, Knoxville, TN). The mice were injected with 9.25 MBq (250 μCi) of FES and 11.1 MBq (300 μCi) of either 18F-FDG or 18F-NaF radiotracers at any given time. To identify skeletal metastases or measure tumor metabolic activities, 18F-NaF or 18F-FDG were injected intraperitoneally, and to measure estrogen activity 18F-FES was injected intravenously via tail vein. Before 18F-FDG administration, the mice were fasted for approximately 12 h. PET and CT were performed 1 h after injection of radioisotopes. During imaging, a respiratory pad was placed under the abdomen of the animal to monitor respiration (Biovet, Newark, NJ). Mice were anesthetized with isoflurane gas (1–3%) mixed with oxygen at a flow rate of 0.5-1 L/minute, and adjusted accordingly during imaging to maintain normal breathing rates. A CT scan was acquired with the following specifications: 220 acquired projections except for the 18F-NaF imaging which was 360 full scan. Each projection was 290 ms with x-ray tube voltage and current set at 60 kVp and 500 μA, respectively. A 30-minute PET scan was immediately acquired afterward. The PET scans were reconstructed using OSEM3D reconstruction method and registered to the CT scan for attenuation correction. *PET Image Analysis*: The PET images were quantified using Inveon Research Workspace IRW (IRW, Siemens AG, Knoxville, TN). Using the reconstructed PET scan, bone (hind limbs) and mammary fat pads were manually selected to form regions of interest (ROI) on the PET-CT images. The data were represented as standardized uptake value (SUV) normalized to body weight. For PDX spontaneous metastasis to bone, a 90% SUVmax thresholding was applied to ROI.

microCT imaging and analysis

A microPET/CT scanner (Siemens Medical Solutions USA, Inc; Malvern, PA; USA) was used to acquire microtomography images. Paired murine hindlimb specimens with bone metastases were imaged with a spatial resolution of 20 microns. Images were converted to Dicom format using Inveon software (version 4.2; Siemens) and bone analyses (volume and mineral density) and three-dimensional reconstruction/visualization performed using Skyscan CTAn and CTVox software packages by Bruker (version 1.19 and 2.3.2; Kontich; Belgium).

Mammosphere and coculture assays

$5x10^5$ cells were plated in low attachment 6 well plates (Greiner) using regular (10% FBS) of serum free DMEM/F12 media supplemented with 2–3% dextran-coated Charcoal stripped. We used a 1/1 ratio for cocultures between cancer cells and stromal cells except when specified otherwise. Cells were collected after 24, 48, or 72 h of culture for downstream analyses. For immunofluorescence, cells were fixed with 2% PFA for 24 h, washed 3 times with PBS, embedded in paraffin, and sectioned for imaging.

Quantitative real-time PCR

Total RNA was extracted using the Direct-zol Zymo according to the manufacturer protocol. Copy DNA was synthesized using the iScript cDNA Synthesis Kit (Biorad). All primers are indicated in Table S1. Real-time PCR was performed on the CFX connect system (Biorad) using PowerUP SYBR Green master mix (Thermo Fisher, #A25780) for amplification.

Bulk ATAC sequencing (ATAC-seq) and analysis

ATAC-seq assay

ATAC-seq was performed as previously described (Buenrostro et al., 2015). Here, we collected 50,000 cells from parental (M7-SCP2) and bone-entrained (M7-SCP2-Bo) cells at different passages (#2, #4, #6 and #12). DNA transposition was performed on freshly collected cells using the Nextera Tn5 Transposase from Illumina. Purified DNA was stored at -80 ^{o}C for each passage before library preparation. All experiments were performed in parallel in both parental and bone-entrained cells.

ATAC-seq analysis

Peak generation pipeline

Analysis was conducted with a modified version of the Encode Consortium's ATAC-Seq Pipeline. Adapters were trimmed from input FASTQ files using cutadapt. Alignment was performed using Bowtie2. Samtools and Picard were used for post alignment filtering to remove duplicate, unmapped, and mitochondrial reads. Pseudo-replicates were generated for both individual replicates and pooled replicates by randomly dividing the input into two equal length files. The MACS2 peak caller was utilized to generate peaksets for all true replicates and pseudo-replicates. Peaks with p value < 10^{-5} were retained for further analysis. Peaks in the Encode DCC consensus blacklist regions were also removed. Then, pairwise comparisons between each pair of biological replicates, the two pseudo-replicates generated from the pooled replicate file, and pseudo-replicates generated from each replicate were conducted. The Encode IDR (irreproducible discovery rate) was used to rank the consistency of each peak region; only peaks with IDR<0.05 were retained. Further analysis was conducted using the overlap IDR thresholded peaks between pooled pseudo-replicates.

Post-peak analysis

A consensus peakset was then generated by merging all the peak regions for the samples of interest using BedTools (Quinlan and Hall, 2010). Promoter regions were retrieved from the UCSC genome browser and were defined as 5000 bases up and 1000 bases down from the TSS. Heatmaps and profile plots for the peak and promoter regions were generated using the DeepTools (Ramírez et al., 2014) utility. The IGV (Thorvaldsdóttir et al., 2013) utility was utilized to generate visualizations for specific gene regions. Further analysis utilized the DiffBind (Stark and Brown, 2011) suite to identify differentially accessible regions (DAR). Both promoter and consensus peak regions were used as peaksets for occupancy and differential binding affinity analysis. DiffBind utilizes DeSeq2 to identify and calculate log fold change and p values for DAR. Contrasts were established between the MCF7 parental and MCF7-Bo samples and the M7-SCP2 and M7-SCP2-Bo samples while controlling for passage number as a confounding factor. DiffBind was also used to generate the PCA and Volcano Plots. DAR generated from Diffbind were then labelled with genes based on the nearest TSS using HOMER (Heinz et al., 2010). HOMER's findMotifGenome module was also utilized to conduct motif analysis. The input file consisted of regions with lower binding in M7-SCP2-Bo compared to M7-SCP2 with an FDR cutoff of <0.05. A region size of 200 and the masked genome setting were used. All other settings used the default HOMER options.

Whole-exome sequencing (WES)

WES library was prepared using the Nextera DNA exome kit (Illumina # 20020616) per manufacturer's instructions and sequenced on a Novaseq 6000 platform at ~100x depth (paired end 100bp, 50 million reads per sample). FastQC and mulitQc were used for quality control. After adaptor removal using cutadapt and trim galore, reads were aligned to reference genome (hg19) using BWA-MEM. BAM files were filtered, and duplicate reads removed using samtools (Li et al., 2009) and Picard. A normal whole exome sequencing sample was downloaded for 1000-Genomes (ERR031938), aligned to the reference genome (hg19), and downsampled (http://broadinstitute.github.io/picard/). We generated pileups from BAM files using samtools mpileup. Varscan 2 was used to call copy numbers and somatic mutations (Koboldt et al., 2012, 2013). Only variant calls with p value < 10^{-2} were used for downstream analyses. Data processing was performed on public server (Afgan et al., 2018). To evaluate the heterogeneity and subclonality of all M7-SCP cells, we used the Expands package (http://cran.r-project.org/web/packages/expands). For each sample, a Z-score analysis was performed using the matrix of predicted subpopulation. Dominant subpopulations with a positive Z-score were used to assess tumor heterogeneity represented by pie charts. Tumor purity was estimated based on cellular frequencies of the largest subpopulation as previously described (Andor et al., 2014).

Histone protein post-translational modification (PTM) analysis

Un-entrained (MCF7 and M7-SCP2) cells were either directly purified from bone (Passage 0: P0) or purified from bone and cultured in vitro for 10 passages (P10). Each sample was washed 3 times with PBS and snap frozen pellets were shipped to Active Motif for PTM quantitation (www.activemotif.com). Briefly, a pilot study was performed to determine the optimal histone extraction method for the samples. Using the additional 6 samples, three lysis methods were evaluated: 1) A one-step method wherein histones are acid extracted directly from the frozen cell pellet, 2) A two-step method wherein a sucrose-based hypotonic buffer is used to lyse the cells and histones are acid extracted from isolated nuclei, or 3) A two-step method wherein an IGEPAL-containing hypotonic buffer is used to lyse the cells and histones are acid extracted from isolated nuclei. Acid extraction was performed for 2 h at 4 °C, cellular debris was pelleted, and lysate aliquots were frozen in a methanol-dry ice bath and stored at -80 °C until testing. Histone yields for the three methods were evaluated using the Histone H3 Total bead and a two-fold five-point dilution series of the samples. The IGEPAL-containing hypotonic lysis buffer method gave the highest yield and was selected for use with the experimental samples. *Lysate Preparation*: Histones were extracted from the experimental samples using the method described above. Cellular debris was pelleted, and lysate aliquots were frozen in a methanol-dry ice bath and stored at -80°C until testing. Next, relative histone H3 concentrations in the samples were determined using the H3 Total bead. Multiplex assays were performed with the beads of interest using sample volumes normalized for histone H3 concentration. *Assay protocol*: (1) Beads were added to wells in 25 μl Assay Buffer supplemented with Inhibitor Cocktails (ABIC) for proteases, phosphatases and HDACs. (2) Samples as a four-point 1.4 dilution series were added to wells in 25 μl ABIC in duplicate and incubated for 1 h at room temperature. (3) Three 100 μl washes with 1X Wash Buffer (PBS containing 0.05% Tween-20) were performed using plate magnet to retain beads. (4) 50 μl biotinylated Histone H3 antibody diluted 1:500 in Assay Buffer was added for the high abundance PTM multiplex assay for 1 h with agitation. 50 μl biotinylated Histone H3 antibody diluted 1:250 in Assay Buffer was added for the low abundance PTM multiplex assay for 1 h with agitation. (5) Washes were performed as above. (6) 50 μl of SAPE diluted 1:100 in Assay Buffer was added to each well and incubated for 30 min with agitation. 7) Beads were collected on a plate magnet and the SAPE solution discarded. 8) The assay plate was removed from the plate magnet and beads resuspended in 100 μl 1X Wash Buffer and read on the Luminex LX100 Instrument. *Data analysis*: Histone H3 Total matched data sets were used to determine PTM/H3 ratios, the PTM percent change relative to each other and Student's t test p values.

Translating ribosome affinity purification (TRAP) sequencing (TRAP-seq)

TRAP assay was adopted from previous studies (Heiman et al., 2014). Here, we performed all experiments in 3D. We stably labeled MCF7 cells with GFP-RPL10a plasmids kindly provided by Dr. William Pu from Harvard. Cells were sorted using FACSAria II to enrich for GFP-positive cells. GFP-RPL10a-expressing MCF7 cells were maintained in 2% charcoal stripped medium for 48 h from which 1 million cells were seeded in 100 mm low attachment plates (Corning, cat #05-539-101) either alone or in coculture with human mesenchymal stem cells (MSCs). These cultures were incubated overnight and treated with 10 nM 17β-estradiol, fulvestrant or 100 nM Tamoxifen for 24 h. Cells were collected for TRAP sequencing. Library was prepared using illumina Nextera XT Kit and paired-end sequencing was performed on a Nextseq 550 System. All sequencing experiments were performed at the Genomic and RNA Profiling core (GARP) at Baylor College of Medicine.

Tracing metastasis expansion in bone using CRISPR-Cas9/hgRNA system

CRISPR-Cas9 barcoding

The hgRNA A21 vector was previously characterized and published (Kalhor et al., 2017). MCF7 cells were stably infected with Lenti-iCas9-neo (Addgene #85400) and hgRNA-A21 (Addgene #100570) using Neomycin/puromycin antibiotic selection before intra-iliac artery injection (IIA). To activate cas9 expression, mice were administered 2 mg/kg of doxycycline via intraperitoneal injection at day 1 post-IIA. Doxycycline treatment was repeated once a week for 3 more weeks (see experimental design Figure 1A).

Laser capture micro-dissection (LCM) and barcode sequencing

Tumor bearing limbs (femur and tibia) were isolated, embedded in Tissue-Tek O.C.T., snap-frozen in liquid nitrogen, and stored at -80°C until sectioning. 10 μm cryosections of each bone were generated using Leica CM3050S cryotome equipped with a low-profile microtome blade. The chamber temperature was set at -26°C. Sectioning was facilitated with the CryoJane Tape Transfer System and then placed on the PET membrane slides (MMI, Prod. No. 50103). Sections were fixed in ethanol and stained with DAPI and ArcturusTM HistoGeneTM solution (Applied Biosystems) according to the instruction manual. Microdissection was performed using the Leica LMD7000 instrument. DNA was purified from each LCM-derived lesion using the Quick-DNA/RNA Microprep Plus Kit from Zymo (D7005). The evolving barcode library was generated as previously described (Kalhor et al., 2017). A paired-end sequencing was performed using the Hiseq 4000 system.

Bioinformatic analysis of the evolving barcode system

The R1 sequences were aligned and annotated using the TraceQC package (https://github.com/LiuzLab/TraceQC). First, the CRISPR barcode sequences were aligned to the hgRNA_A21 reference construct using the following score system: match +2, mismatch -2, gap opening -6, gap extension -0.1. After annotating the aligned sequences, the adapters were trimmed off and sequences with low alignment scores (<200) were filtered out. Sequences with less than 10 count were subsequently filtered out. TraceQC extracted mutation events from the sequence into 4 attributes: 1) the mutation type (insertion, deletion or point mutation), 2) the starting position of mutation, 3) the length of mutation, and 4) the altered sequence. We combined the mutation events for all the samples into a mutation count matrix and normalized samples using the read count per million (RPM) approach. The hierarchical

clustering based on mutations revealed 3 major modules. Within each module, the mutation count matrix was binarized into whether each mutation event exists in the samples or not: TRUE (mutation present) or FALSE (mutation absent). Then, we used maximum parsimony to establish the lineage relations within each module. To build the cell lineage network, we performed graphic LASSO using the Huge package. First, the mutation count matrix was Gaussianized using non-paranormal transformation provided by Huge package. Then, the graphic LASSO was applied to the Gaussianized mutation count matrix. We selected lambda = 0.52 to make the graph have the maximum sparsity while remaining fully connected. Next, we applied a random walk-based community detection algorithm to detect the 3 modules in the graph. The algorithm is provided by the iGraph package. Detailed analysis pipeline is accessible at: https://github.com/LiuzLab/ER_positive_breast_cancer-manuscirpt.

QUANTIFICATION AND STATISTICAL ANALYSIS

Data analysis was conducted in GraphPad Prism (v8.0.1) and R (version 3.4 R). Specific statistical approaches are indicated for each figure in the figure legend. For PET imaging, Mann Whitney *U*-test was used for statistical analysis. Pearson correlation was used for correlation studies.

CANCER

Harnessing the power of antibodies to fight bone metastasis

Zeru Tian[1†], Ling Wu[2†], Chenfei Yu[1], Yuda Chen[1], Zhan Xu[2], Igor Bado[2], Axel Loredo[1], Lushun Wang[1], Hai Wang[2], Kuan-Lin Wu[1], Weijie Zhang[2], Xiang H.-F. Zhang[2]*, Han Xiao[1,3,4]*

Antibody-based therapies have proved to be of great value in cancer treatment. Despite the clinical success of these biopharmaceuticals, reaching targets in the bone microenvironment has proved to be difficult due to the relatively low vascularization of bone tissue and the presence of physical barriers. Here, we have used an innovative bone-targeting (BonTarg) technology to generate a first-in-class bone-targeting antibody. Our strategy involves the use of pClick antibody conjugation technology to chemically couple the bone-targeting moiety bisphosphonate to therapeutic antibodies. Bisphosphonate modification of these antibodies results in the delivery of higher conjugate concentrations to the bone metastatic niche, relative to other tissues. In xenograft mice models, this strategy provides enhanced inhibition of bone metastases and multiorgan secondary metastases that arise from bone lesions. Specific delivery of therapeutic antibodies to the bone, therefore, represents a promising strategy for the treatment of bone metastatic cancers and other bone diseases.

INTRODUCTION

Antibody-based therapies, including those using monoclonal antibodies, antibody-drug conjugates, bispecific antibodies, checkpoint inhibitors, and others, have realized their clinical potential in terms of their power to treat a variety of cancers (*1*–*4*). Nevertheless, despite the fact that most therapeutic antibodies have high affinities for their targets, the presence of these same targets in normal tissues can markedly limit the ability of therapeutic agents to hit their targets without inducing unacceptable "on-target" toxicity in healthy cells (*5*–*7*). Furthermore, low levels of delivery of therapeutic antibodies to some tissues such as brain or bone can significantly limit their efficacy in treating diseases in these tissues (*8*). Thus, it is likely that enhancing both the antigen and tissue specificity of antibodies will ultimately transform the efficacy of antibody therapy for clinical treatment of cancer.

Half of patients with an initial diagnosis of metastatic breast cancer (BCa) will develop bone metastases (*9*). Patients having only skeletal metastases usually have a better prognosis than patients with vital organ metastases (*9*, *10*). Furthermore, bone metastasis is associated with severe symptoms such as spinal cord compression, pathological fractures, and hypercalcemia (*11*). Despite our deep understanding of molecular mechanisms (*12*, *13*), effective therapies that can eliminate cancer cells in the bone niche are still lacking (*14*). The bone is also not the final destination of metastatic dissemination. Recent genomic analyses have revealed frequent "metastasis-to-metastasis" seeding (*15*–*17*). More than two-thirds of bone-only metastases subsequently develop secondary metastases to other organs, ultimately leading to the death of patients (*9*, *10*). Some metastases initially identified in non-bone organs are actually the result of seeding from subclinical bone micrometastases (BMMs). This apparently is the result of cancer cells initially arriving in the bone and then acquiring more aggressive phenotypes that allow them to establish more overt metastases in both bone and other sites (*18*). It should therefore be useful to develop strategies for preventing BMMs from establishing more overt metastases in both bone and non-bone tissues.

While targeted antibody therapy and immunotherapy are now emerging as new avenues for treating metastatic BCa, the performance of these agents in patients with bone metastases has been disappointing. For example, trastuzumab (Tras; Herceptin) and pertuzumab (Perjeta) antibodies targeting human epidermal growth factor receptor 2 (HER2) have been used to treat patients in adjuvant and metastatic settings. Although many BCa patients benefit from these treatments, in large numbers of BCa patients with bone metastasis, the disease progresses within 1 year, and few patients experience prolonged remission (*19*–*22*). In another phase 3 clinical trial testing atezolizumab in patients with metastatic triple-negative BCa, progression-free survival was significantly longer in the atezolizumab group than in the placebo group. However, among BCa patients with bone metastases, no significant difference was observed between the atezolizumab-treated and placebo groups for risk of progression or death (*23*). Therapies with improved outcomes for BCa patients with bone metastases are therefore highly desired.

Attempts to ensure effective concentrations of a therapeutic drug in the bone unavoidably lead to high concentrations in other tissues as well, often resulting in adverse systemic effects or side effects that may limit or exclude the use of the drug (*24*, *25*). In this case, the potential benefit of passive targeting is lost. Here, we describe an innovative bone-targeting (BonTarg) technology that enables the tissue-specific delivery of therapeutic antibodies to the bone via conjugation of bone-targeting moieties. The resulting bone-targeting antibodies can specifically target the bone metastatic niche to eliminate BMMs and also prevent seeding of multiorgan metastases from bone lesions. Taking advantage of the high mineral concentration unique to the bone hydroxyapatite (HA) matrix, bisphosphonate (BP) conjugation has been used for selective delivery of small molecule drugs, imaging probes, nuclear medicines, and nanoparticles to the bone as a means of treating osteoporosis, primary and metastatic bone neoplasms, and other bone disorders (*24*, *26*–*30*). Negatively charged BP has a high affinity for HA, which

[1]Department of Chemistry, Rice University, 6100 Main Street, Houston, TX 77005, USA. [2]Department of Molecular and Cellular Biology, Baylor College of Medicine, 1 Baylor Plaza, Houston, TX 77030, USA. [3]Department of Biosciences, Rice University, 6100 Main Street, Houston, TX 77005, USA. [4]Department of Bioengineering, Rice University, 6100 Main Street, Houston, TX 77005, USA.
*Corresponding author. Email: han.xiao@rice.edu (H.X.); xiangz@bcm.edu (X.H.-F.Z.)
†These authors contributed equally to this work.

is the main component of hard bone, resulting in preferential binding to the bone. However, the potential benefit of bone-specific delivery of large therapeutic proteins to the bone by modifying BP has not yet been explored. We have used pClick conjugation technology to site-specifically couple the BP drug Alendronate (ALN) to the HER2-targeting monoclonal antibody Tras. In two xenograft models based on intra-iliac artery (IIA) injection, the resulting Tras-ALN conjugate significantly enhances the concentration of therapeutic antibody in the bone metastatic niche, inhibits cancer development in the bone, and limits secondary metastases to other organs. This type of specific delivery of therapeutic antibodies to the bone has the potential to enhance both the breadth and potency of antibody therapy for bone-related diseases.

RESULTS

Development of the first bone-targeting antibody using BonTarg technology

To explore the possibility of specifically delivering therapeutic antibodies to the bone via conjugation to BP molecules, we designed a model using the HER2-targeting antibody Tras and the BP drug ALN. ALN is a second-generation BP drug that is used as a bone-targeting agent as well as a regimen for treating osteoporosis and bone metastasis (*31*). To ensure that ALN conjugation does not impair the therapeutic efficacy of the antibody, we have used a novel proximity-induced antibody conjugation strategy named pClick. pClick technology enables the site-specific attachment of payloads to native antibodies under mild conditions, thus minimizing the disruption of binding to the antigen receptor or the FcγRIII receptor, the receptor responsible for activating antibody-dependent cell-mediated cytotoxicity. The pClick technology does not rely on antibody engineering or on the ultraviolet/chemical/enzymatic treatments that characterize the generation of most therapeutic antibodies. To prepare the Tras-ALN conjugate, we first used pClick to generate Tras containing an azide functional moiety, followed by reaction with bicyclo[6.1.0]nonyne (BCN)–functionalized ALN (Fig. 1A and figs. S1 to S3). The resulting Tras-ALN was further purified on a desalting column and fully characterized by SDS–polyacrylamide gel electrophoresis (PAGE) and electrospray ionization mass spectrometry (ESI-MS) (Fig. 1, B and C). To our delight, no unconjugated heavy chain or degradation products were revealed by SDS-PAGE, indicating a more than 95% coupling efficiency. ESI-MS analysis also revealed that more than 95% of the heavy chain was conjugated with the ALN molecule.

Antibody conjugation to ALN retains antigen binding and specificity

To investigate the effect of ALN conjugation on antigen-binding affinity and specificity, binding affinities of Tras and Tras-ALN were assessed by flow cytometry analysis of HER2-positive and HER2-negative cell lines. Figure 1D reveals that both Tras and Tras-ALN have strong binding affinities for the HER2-expressing cell lines BT474, SK-BR-3, and MDA-MB-361, but not for the HER2-negative cell line MDA-MB-468, suggesting that the antibody specificity was not altered by ALN conjugation (table S1). The dissociation constant (K_d) values for binding to HER2-positive cells are within a similar range for Tras and Tras-ALN (BT474, 3.0 versus 3.8 nM and SK-BR-3, 2.3 versus 3.0 nM, respectively), indicating that ALN conjugation does not affect the strength of antigen binding (figs. S4 to S7). Confocal fluorescent imaging further confirms that Tras-ALN retains antigen binding and specificity (fig. S8). HER2-positive BT474 and SK-BR-3 cells, and HER2-negative MDA-MB-468 cells were incubated for 30 mins with fluorescein isothiocyanate (FITC)–labeled Tras-ALN. Confocal imaging indicates that cell surface–associated fluorescence is only exhibited for HER2-positive BT474 and SK-BR-3 cells and not for HER2-negative MDA-MB-468 cells (fig. S8). Thus, ALN modification of Tras does not affect its antigen-binding affinity and specificity. Next, the Tras-ALN conjugate was tested for selective cytotoxicity against HER2-expressing and HER2-negative BCa cells. As shown in Fig. 1 (E and F) and table S1, the Tras-ALN conjugate exhibits cytotoxic activity against HER2-positive BT-474 cells [median effective concentration (EC_{50}) of 2.3 ± 0.7 μg/ml] and MDA-MB-361 (EC_{50} of 78 ± 21 μg/ml) that is indistinguishable from that of Tras (EC_{50} of 1.4 ± 0.9 μg/ml and EC_{50} of 57 ± 10 μg/ml). Neither antibody kills HER2-negative MDA-MB-468 cells (EC_{50} > 500 μg/ml). These results indicate that the conjugation of the negatively charged moiety ALN preserves the antigen binding and in vitro antitumor cell activity of the Tras antibody.

Enhanced targeting of the bone metastatic niche by Tras-ALN in vitro and in vivo

We next explored the ability of the Tras-ALN conjugate to target bone tissue. Nondecalcified bone sections from C57BL/6 mice were incubated overnight at 4°C with Tras or Tras-ALN conjugate (50 μg/ml), followed by labeling with FITC-labeled anti-human immunoglobulin G (IgG). Before imaging via confocal laser scanning microscopy, these bone sections were further stained for 30 min with xylenol orange (XO, 4 μg/ml; known to label bone). We observed an FITC signal in sections stained with the Tras-ALN conjugate but not in sections stained with unmodified Tras (Fig. 1G). Furthermore, localization of the Tras-ALN signal correlated well with the XO signal, confirming the specific targeting of the bone by Tras-ALN. To quantify the difference in affinity between binding of the Tras-ALN conjugate and unmodified Tras, we incubated Tras-ALN and Tras with HA or native bone. As shown in Fig. 1 (H and I), unmodified Tras exhibited only slight binding to HA or native bone. Even with an increase in the incubation time, the binding affinity of Tras did not change significantly. In contrast, approximately 80 to 90% of Tras-ALN was bound to HA and the native bone after 2 and 10 hours, respectively.

Encouraged by the in vitro bone-targeting ability of ALN-conjugated Tras, we carried out an in vivo biodistribution study with the Tras-ALN conjugate using a tumor xenograft model. To facilitate the detection of antibodies in vivo, we first conjugated Tras and Tras-ALN with Cyanine 7.5 (Cy7.5)–*N*-hydroxysuccinimide ester. The resulting Cy7.5-labeled conjugates were analyzed using SDS-PAGE. As expected, fluorescence was associated only with the Cy7.5-labeled conjugates (Fig. 1B). An important feature of BP is that the uptake into bone metastases is much higher than in healthy bone tissue due to the relatively low pH of the bone metastatic microenvironment (*32*–*35*). To investigate whether Tras-ALN can specifically target bone metastases, thus minimizing on-target toxicity to normal bone tissue, we evaluated the targeting properties of Tras-ALN in a bone tumor model. We created a BMM model by using IIA injection of MDA-MB-361 cells labeled with luciferase and red fluorescent protein (RFP) into the right hindlimbs of nude mice. IIA injection is a novel technology recently developed in our laboratory for establishing BMMs. Our method allows for selective

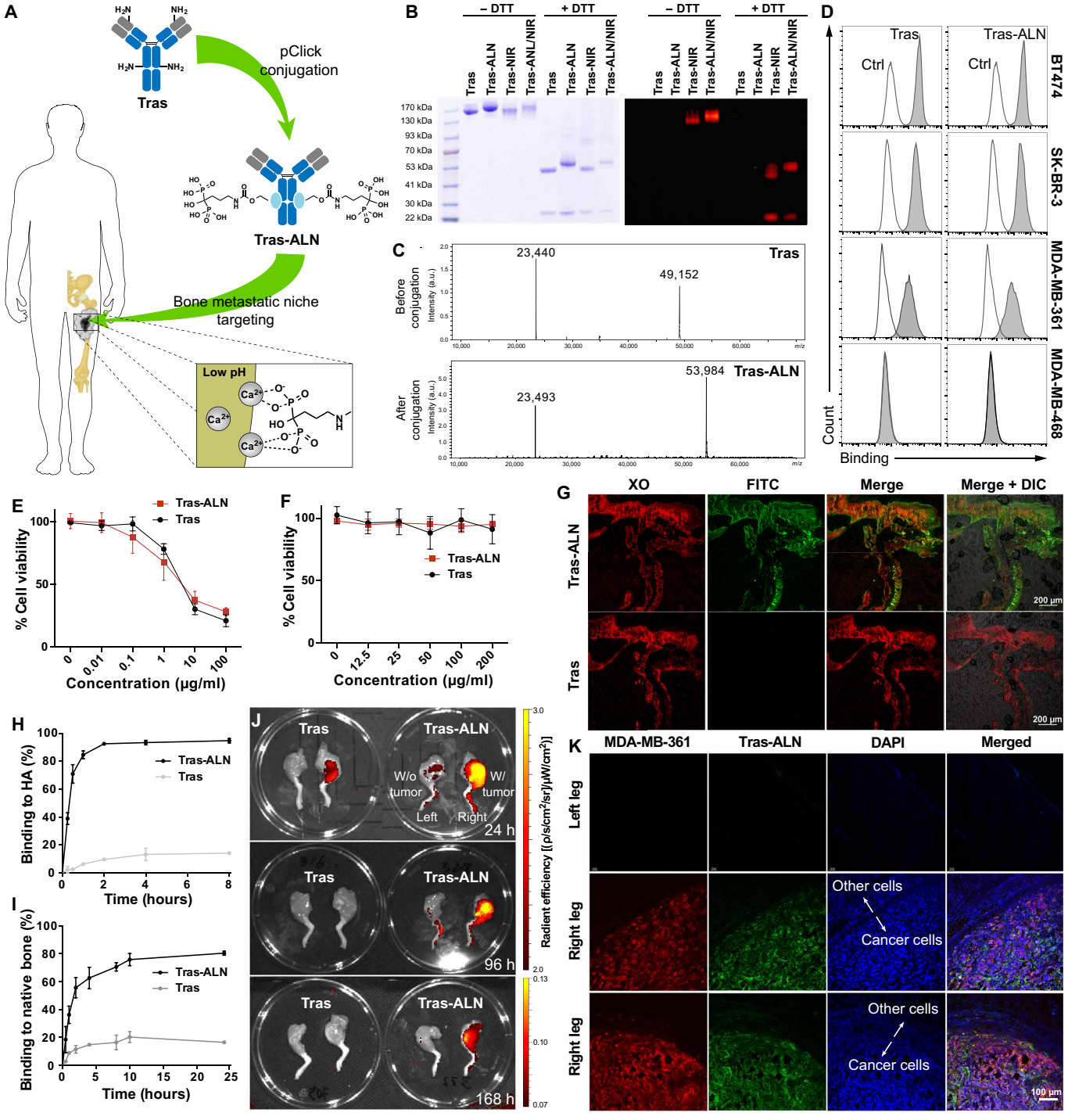

Fig. 1. Preparation and characterization of bone-targeting antibodies. (**A**) Therapeutic antibodies can be site-specifically delivered to the bone by pClick conjugation of BP molecules that bind to the bone HA matrix. (**B**) SDS–polyacrylamide gel electrophoresis (PAGE) analysis of Tras, Tras-ALN, and their near-infrared (NIR) fluorophore conjugates under reducing and nonreducing conditions, visualized by Coomassie blue staining (left) and a fluorescence scanner (right) (**C**) Mass spectrometry analysis of Tras and Tras-ALN. a.u., arbitrary units; *m/z*, mass/charge ratio. (**D**) Flow cytometric profiles of Tras and Tras-ALN binding to BT474 (HER2^{+++}), SK-BR-3 (HER2^{+++}), MDA-MB-361 (HER2^{++}), and MDA-MB-468 (HER2^{-}) cells. (**E** and **F**) In vitro cytotoxicity of Tras and Tras-ALN against BT474 and MDA-MB-468 cells (data represent the means ± SD for three independent repeats). (**G**) Differential bone-targeting ability of unmodified Tras and Tras-ALN conjugate. Nondecalcified bone sections from C57/BL6 mice were incubated with Tras or Tras-ALN (50 μg/ml) overnight, followed by staining with fluorescein isothiocyanate (FITC)–labeled anti-human IgG and XO (4 μg/ml) (known to label bone). Differential interference contrast (DIC). Scale bars, 200 μm. (**H** and **I**) Binding kinetics of Tras and Tras-ALN to HA and native bone. (**J**) Ex vivo fluorescence images of lower limbs of athymic nude mice bearing MDA-MB-361 tumors 24, 96, or 168 hours after the retro-orbital injection of Cy7.5-labeled Tras and Tras-ALN. Tumor cells were inoculated into the right limbs of nude mice via IIA injection. **(K)** Nondecalcified bone sections from the biodistribution study were stained with FITC-labeled anti-human IgG (green), RFP (red), and DAPI (blue), Scale bar, 100 μm.

delivery of cancer cells into hindlimb bones without causing tissue damage (*36*–*38*). This technology allows sufficient time for some indolent cells to eventually colonize the bone and a large number of cancer cells to specifically colonize the bone, thereby enriching micrometastases in early stages. This allows for swift detection and robust quantification of micrometastases. The establishment of micrometastases was followed by treatment with Tras or Tras-ALN (1 mg/kg). Twenty-four, 96, or 168 hours after administration of antibody or antibody conjugate, the major organs, including the heart, liver, spleen, kidney, lung, and bone, were removed and analyzed using the Caliper IVIS Lumina II imager (Fig. 1J and fig. S9). Significantly, ex vivo fluorescence images at 96 hours after injection of antibody confirmed clear accumulation of Cy7.5-labeled Tras-ALN in the bone compared with Cy7.5-labeled Tras (Fig. 1J and fig. S10). Furthermore, the uptake of Tras-ALN into cancer-bearing bones is significantly higher than into healthy bone tissue. To evaluate the distribution of Tras-ALN to other bone tissues, such as the backbone, breastbone, harnpan, and nontumor-bearing limbs, Cy7.5-labeled Tras (1 mg/kg) or Tras-ALN (1 mg/kg) were administrated to tumor-bearing mice by retro-orbital injection. Seventy-two hours after the administration, the major organs and bones were isolated and imaged using Caliper IVIS Lumina II imager (fig. S11). Comparing with other bones, Tras-ALN preferred to target the tumor-bearing limbs, which was consistent with the previous results that BPs preferred to target acidic bone metastatic sites comparing with healthy bone (*34*). In a separate study, unlabeled Tras-ALN (1 mg/kg) was administered into the nude mice bearing MDA-MB-361 tumor in the right hindlimb. Bone sections from this study were also stained with FITC-labeled anti-human IgG, RFP, and 4′,6-diamidino-2-phenylindole (DAPI). We only observed FITC signals in sections from the right leg harboring MDA-MB-361 tumors. No FITC signals were detected in the left leg without tumors (Fig. 1K). Significantly, the FITC signal correlated well with the red fluorescence of MDA-MB-361 cells, suggesting that Tras-ALN conjugate selectively targets the bone metastatic site but not the healthy bone. These results demonstrate that ALN conjugation can significantly enhance the delivery and concentration of therapeutic antibodies in bone metastatic sites.

Next, we evaluated the effect of ALN-conjugation on the pharmacokinetics and neonatal Fc receptor (FcRn) binding of antibodies. A single dose of Tras and Tras-ALN (1 mg/kg) in phosphate-buffered saline (PBS) were injected retro-orbitally, and serum was collected at regular intervals for 7 days and analyzed by the Trastuzumab enzyme-linked immunosorbent assay (ELISA) Kit. The serum concentration of both Tras and Tras-ALN decreased and did not show significant differences (fig. S12). Next, we determined the effect of ALN conjugation on FcRn binding. We found that the ALN conjugation does not have an obvious effect on the FcRn binding at pH 6.0 (table S2).

Enhanced therapeutic efficacy of Tras-ALN against BMMs

To determine whether bone-targeting Tras represents a novel therapeutic approach for treating micrometastases of BCa in the bone, we carried out a xenograft study using MDA-MB-361 cells in nude mice. MDA-MB-361 cells that endogenously overexpress HER2 are known to metastasize to bones (*39*). Using IIA injection, we inoculated the right hindlimbs of nude mice with 5×10^5 MDA-MB-361 cells labeled with firefly luciferase. Five days after the IIA injections, mice were treated with PBS, ALN (10 μg/kg), Tras (1 mg/kg), or Tras-ALN (1 mg/kg) via retro-orbital injection. As shown in Fig. 2A and fig. S13, micrometastases in PBS- and ALN-treated mice accumulated rapidly, while the development of lesions in Tras- and Tras-ALN–treated mice was delayed. Whole-body bioluminescence imaging (BLI) signals suggested that treatment with Tras-ALN resulted in more significant inhibition of micrometastasis progression, compared to that seen in Tras-treated mice (fig. S14, A and B). The increases in BLI from days 6 to 87 showed that the Tras-ALN–treated group had fewer fold increases in the tumor sizes compared to Tras-treated group (Tras versus Tras-ALN: 1965.1 ± 798.3 versus 42.6 ± 23.4; Fig. 2, B and C). As we built the bone metastasis in the hindlimbs, the effect of Tras-ALN on the BLI signal in the hindlimbs was also quantified. Similar to whole-body BLI signal, Tras-ALN–treated group had less BLI signal intensity and fewer fold increase in the hindlimbs (fig. S15). Moreover, survival of Tras-ALN–treated mice was notably enhanced compared to that of PBS-, ALN-, and Tras-treated mice, demonstrating the efficacy of Tras-ALN against HER2-positive cells in vivo (Fig. 2D). Furthermore, no weight loss as a sign of ill health was observed in any of the treated mice, suggesting the absence of toxicity associated with the bone-targeting antibodies (Fig. 2E).

These results were further confirmed by micro–computed tomography (microCT) data and histology, emphasizing the finding that bone-targeting antibodies can decrease both the number and the extent of osteolytic lesions. As shown in Fig. 2F and fig. S16, femurs from PBS-, ALN-, and Tras-treated groups exhibited significant losses of bone mass, while bone loss in the Tras-ALN–treated group was much reduced. Quantitative analysis revealed that the Tras-ALN–treated group had significantly higher bone volume fraction [6B: BV/TV (%), 35.08 ± 2.65 versus 56.67 ± 1.02, $P = 0.0005$; Fig. 2G], trabecular thickness [Tb.Th (mm), 0.061 ± 0.003 versus 0.094 ± 0.002, $P = 0.003$; Fig. 2H], and higher trabecular bone mineral density (BMD; mg/mm^3), 101.16 ± 12.24 versus 165.94 ± 12.84, $P = 0.035$; Fig. 2I] compared to the Tras-treated group.

Tumor size was also analyzed by histomorphometric analysis of the bone sections. Tibiae and femurs from the PBS- and ALN-treated groups had high tumor burdens (Fig. 2J). Tras treatment slightly reduced the tumor burden, but the reduction was not statistically significant. In contrast, a significant reduction of tumor burden was observed in the Tras-ALN–treated group. Histological examination of the bone samples from various treatment groups reveals that bone matrix is generally destroyed in bones with high tumor burden, whereas bones with less tumor burden in the Tras-ALN–treated group exhibit intact bone matrix. The reduction of tumor burden was also confirmed by HER2 immunohistochemistry (IHC). As shown in Fig. 2K, the number of HER2-positive BCa cells is markedly decreased in Tras-ALN–treated mice, although HER2 expression by individual tumor cells is unchanged. This suggests that extended treatment with Tras-ALN has no effect on HER2 expression by MDA-MB-361 cells.

To examine Tras-ALN inhibition of tumor-induced osteolytic bone destruction, we examined the bone-resorbing, tartrate-resistant, acid phosphatase–positive multinucleated osteoclasts in bone samples (Fig. 2K). Tartrate-resistant acid phosphatase (TRAP) staining identified reduced numbers of osteoclasts (pink cells) lining the eroded bone surface in Tras-ALN–treated mice, compared to Tras-treated mice (Fig. 2, K and L, and fig. S17). Serum TRAcP 5b and calcium levels, indicators of bone resorption, were also measured at the experimental endpoint. Significantly higher reductions in bone resorption were observed in the Tras-ALN–treated group (Fig. 2, M and N).

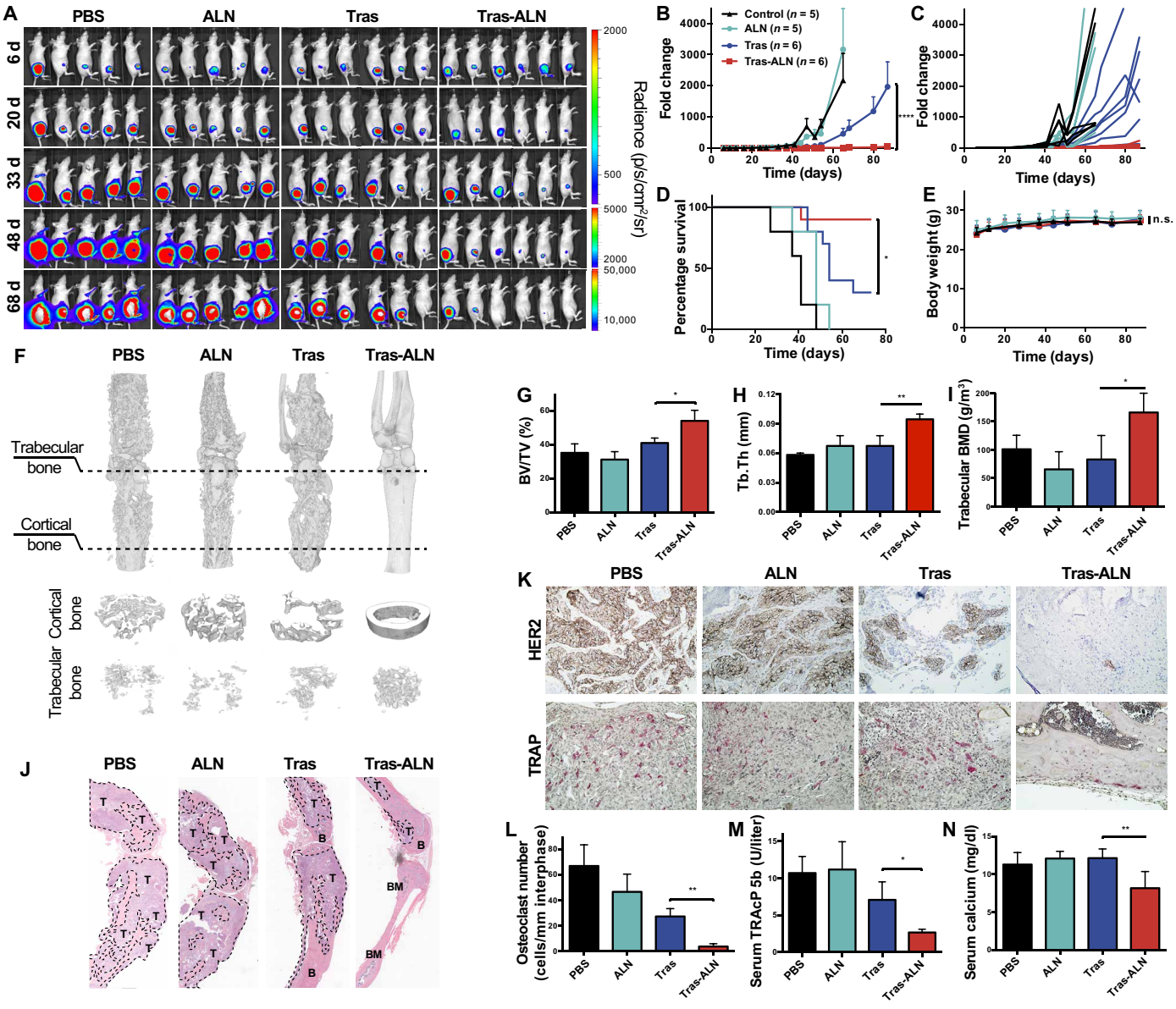

Fig. 2. Tras-ALN inhibits BCa metastases in the bone. (**A**) MDA-MB-361 cells were IIA injected into the right hindlimb of nude mice, followed by treatment with PBS ($n = 5$), ALN (10 μg/kg retro-orbital injection in PBS twice a week, $n = 5$), Tras (1 mg/kg retro-orbital injection in sterile PBS twice a week, $n = 10$), and Tras-ALN conjugate (the same as Tras, $n = 10$). Tumor burden was monitored by weekly bioluminescence imaging (BLI). (**B**) Fold change in mean luminescent intensity of MDA-MB-361 tumors in mice treated as described in (A), two-way ANOVA comparing Tras to Tras-ALN. (**C**) Fold change in individual luminescent intensity of HER2-positive MDA-MB-361 tumors in mice treated as described in (A). (**D**) Kaplan-Meier plot of the time-to-euthanasia of mice treated as described in (A). For each individual mouse, the BLI signal in the whole body reached 10^7 photons s^{-1} was considered as the endpoint. (**E**) Body weight change of tumor-bearing mice over time. (**F**) MicroCT scanning in the supine position for groups treated with PBS, ALN, Tras, or Tras-ALN 82 days after tumor implantation. (**G**) Quantitative analysis of bone volume fraction (BV/TV). (**H**) Quantitative analysis of trabecular thickness (Tb.Th). (**I**) Quantitative analysis of trabecular bone mineral density (BMD). (**J**) Representative longitudinal, midsagittal hematoxylin and eosin (H&E)–stained sections of tibia/femur from each group. T, tumor; B, bone; BM, bone marrow. (**K**) Representative images of HER2 and TRAP staining of bone sections from each group. (**L**) Osteoclast number per image calculated at the tumor-bone interface in each group [pink cells in (K) were considered as osteoclast positive cells]. (**M**) Serum TRAcP 5b levels of mice treated as described in (A). (**N**) Serum calcium levels of mice treated as described in (A). $P > 0.05$ [not significant (n.s.)], $^*P < 0.05$, $^{**}P < 0.01$, and $^{****}P < 0.0001$.

Together, these results indicate that BP modification of therapeutic antibodies significantly enhanced their ability to retard the development of micrometastasis-induced osteolytic lesions (table S3).

To further evaluate the therapeutic efficacy of Tras-ALN in the presence of both primary and secondary tumors, we carried out a xenograft study in nude mice using both mammary fat pad and IIA injections. For the cells inoculated in the right hindlimbs, we used luciferase-labeled MDA-MB-361 cells (2×10^5). For the mammary fat pad injection, we injected with nonlabeled MDA-MB-361 cells (1×10^6). Six days after injection, mice were treated with Tras (1 mg/kg)

and Tras-ALN (1 mg/kg). The tumor progressions of primary and bone metastasis were monitored by tumor size measurement and bioluminescence, respectively. Compared with the Tras-treated group, Tras-ALN had a significant effect in preventing tumor growth in the hindlimb (fig. S18, A and B). However, there was no significant growth difference for the mammary fat pad tumor (fig. S18C). These results suggested that Tras-ALN has a better therapeutic effect on bone metastases but a similar effect on primary tumor compared with wild type Tras.

Tras-ALN inhibits multiorgan metastases from bone lesions

In more than two-thirds of cases, bone metastases are not confined to the skeleton but rather give rise to subsequent metastases to other organs (*9*, *10*, *40*). While we have used IIA injection to investigate early-stage bone colonization, as these bone lesions progress over an 8- to 12-week period, metastases begin to appear in other organs, including additional bones, lungs, liver, kidney, and brain. Hence, we investigated the ability of Tras-ALN to reduce the metastasis of HER2-positive MDA-MB-361 cancer cells to other organs. As before, 5×10^5 MDA-MB-361 cells labeled with firefly luciferase were introduced into the right hindlimbs of nude mice via IIA injection, followed by treatment with Tras (1 mg/kg) and Tras-ALN (1 mg/kg). Then, mice were subjected to whole-body BLI twice a week following tumor-cell injection. The whole-body and hindlimbs BLI signals were quantified and shown in fig. S19A. Secondary metastases in various organs were calculated as follows: BLI signal in whole body − BLI signal in hindlimbs. As shown in fig. S19, there was a time-dependent increase in the organs BLI signal to 10^6 photons s^{-1} in the Tras-treated group. Furthermore, there was significant inhibition of BLI signal accumulation in organs of Tras-ALN–treated group ($P < 0.0001$). At the endpoint of the study, mice were euthanized, and the organs were harvested for BLI. Much higher levels of the right hindlimb (100%), heart (20%), liver (80%), spleen (40%), lung (60%), kidney (60%), and brain metastasis (40%) were observed in the Tras-treated group, compared to the right hindlimb (42.9%) and liver (14.3%) (Fig. 3, A and B, and fig. S20) in the Tras-ALN group. Other organs such as the lungs, spleen, kidney, and brain were devoid of metastases in Tras-ALN–treated mice. Our data indicated that bone-targeting antibodies, compared to unmodified antibodies, can significantly inhibit multiorgan metastases resulting from the dissemination of initial BMMs. Mice treated with Tras-ALN exhibited fewer metastases to other organs than mice in the other treatment groups, establishing the ability of bone-targeting antibodies to inhibit "metastasis-to-metastasis seeding."

Enhanced therapeutic efficacy of Tras-ALN in an HER2-negative model

Previous reports indicate that a substantial portion of the minimal residual disease seen in HER2-negative patients may nevertheless be due to HER2 signaling (*41*, *42*). It was also reported that HER2 signaling may mediate stem cell properties in a subpopulation of HER2-negative cells, and this raises the possibility that anti-HER2 treatment may be able to eradicate bone metastases of both HER2-positive and HER2-negative BCa (*43*). Our recent study suggested that tumor cells exhibit phenotypic reprogramming when inoculated in the bone microenvironment. Specifically, the expression level of HER2 protein of HER2-negative BCa cells, such as MCF-7, was significantly up-regulated in the early stage of bone metastasis (*44*). We therefore evaluated the therapeutic effects of Tras-ALN using BCa cells that are not HER2-positive but exhibit HER2 up-regulation specifically in bones. We used IIA injection to deliver MCF-7 [$HER2^-$, Estrogen Receptor $(ER)^+$] cancer cells into hindlimb bones (*36*, *38*), followed by treatment with Tras or Tras-ALN (seven mice per group, 1 mg/kg). Mice were imaged twice a week, and signal intensity of whole-body and hindlimbs were quantified. As shown in Fig. 4 and figs. S21 and S22, treatment with Tras-ALN resulted in more significant inhibition of tumor growth than seen in Tras-treated mice, demonstrating the efficacy of Tras-ALN against HER2-negative cells in vivo ($P < 0.005$). Meanwhile, significant reductions of serum TRAcP 5b (4.41 ± 1.12 U/liter, $P < 0.05$) and serum calcium (10.36 ± 0.53 mg/dl, $P < 0.05$) levels were observed in Tras-ALN–treated group (fig. S23). Similar to $HER2^+$ model, secondary metastases in various organs were also exhibited significant reductions in BLI signal ($P < 0.0001$) over the course of the study (fig. S24). Next, we also evaluated the ability of Tras-ALN to inhibit multiorgan metastases from bone lesions ex vivo. At day 68, metastatic cells were observed in the right hindlimb (83.4%), liver (33.4%), lung (83.4%), and brain (66.7%) in the Tras-treated group, compared to values found in the right hindlimb (50%), lung (50%), and brain (50%) (fig. S25) of Tras-ALN–treated mice. These data suggest that the bone-targeting Tras-ALN conjugate may be useful in preventing the progression of HER2-negative BMMs to overt bone metastases and blocking the secondary metastasis of HER2-negative cells to other organs (table S4).

DISCUSSION

Despite the fact that BCa patients have an extremely good chance of recovery from the disease, 20 to 40% of BCa survivors will eventually suffer metastases to distant organs (*45*). Metastasis to the bone occurs in about 70% of these cases (*46*, *47*). BCa patients with bone metastases suffer from pain and immobility, along with susceptibility to skeletal-related events (SREs) such as fracture, bone pain, spinal cord compression, and hypercalcemia. SREs significantly reduce the quality of life and increase mortality. The 1-year survival rate of BCa patients with bone metastases is 51%, but the 5-year survival rate drops to 13% (*48*, *49*). In cases where the skeleton is the only site of metastasis, patients usually have better prognoses than patients with visceral organ metastases (*9*, *10*). In more than two-thirds of cases, bone metastases will not remain confined to the skeleton but instead are responsible for subsequent metastases to other organs and eventually to the death of patients (*9*, *10*). Recent genomic analyses suggest that most metastases are the result of seeding from other metastases rather than from primary tumors (*15*–*17*). Some metastases initially found in nonskeletal organs also appear to be seeded from subclinical BMMs, as suggested by the finding that, subsequent to colonization of bone, metastatic cancer cells in BMMs can acquire more aggressive phenotypes even before establishing overt bone metastases (*18*). Thus, strategies for inhibiting progression of BMMs can prevent further BCa metastasis within the bone and secondary metastases from the bone to other organs.

Chemotherapy, hormone therapy, and radiation therapy are now used to treat women with bone metastatic BCa. While these treatments often shrink or slow the growth of bone metastases and can help alleviate symptoms associated with bone metastasis, they usually do not eliminate the metastases completely. Targeted antibody therapies, including Tras and pertuzumab, are established standards of care for HER2-positive adjuvant and metastatic BCa. However, the poor bioavailability of these agents within bone tissues has

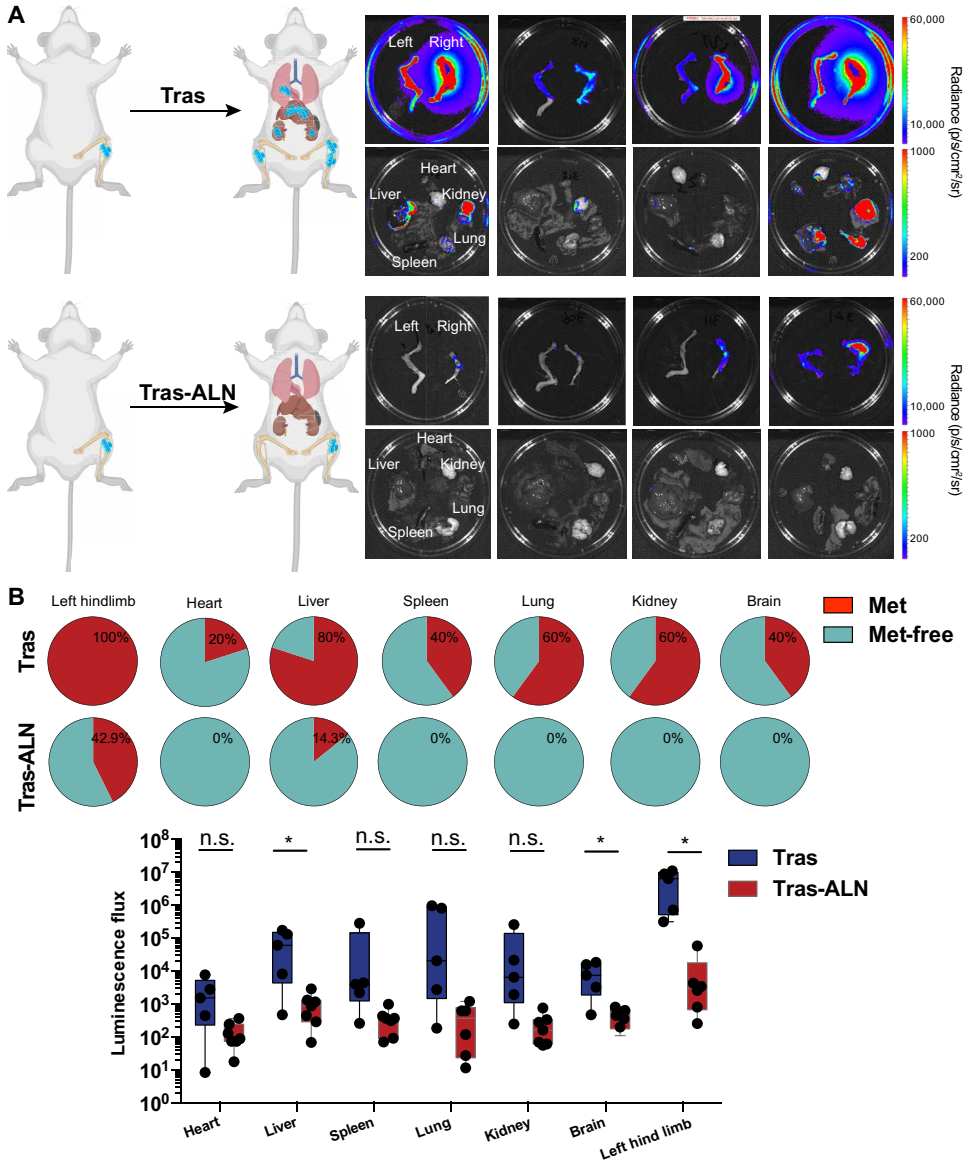

Fig. 3. The therapeutic efficacy of Tras-ALN to inhibit multiorgan metastases. (**A**) Secondary metastases observed in various organs in mice treated with Tras (top, $n = 5$) or Tras-ALN (bottom, $n = 7$). (**B**) Pie charts (top) show the frequencies of metastasis observed in various organs in mice treated with Tras (1 mg/kg retro-orbital injection in sterile PBS twice a week), and Tras-ALN conjugate (the same as Tras). Quantification of bioluminescence signal intensity (bottom) in different organs, including other bones, as measurement of metastases resulted from Tras and Tras-ALN–treated mice. *P* values are based on one-way ANOVA test. $P > 0.05$ (n.s.) and $^*P < 0.05$.

limited their efficacy in dealing with HER2-positive bone metastases (*19*–*22*). In a recent long-term follow-up study of patients with HER2-positive metastatic BCas who received chemotherapy and Tras, only 17% of patients with bone metastatic BCa experienced a complete response, and none experienced a durable complete response. By comparison, a 40% complete response and 30% durable complete response was achieved in BCa patients with liver metastases (*22*). Thus, therapies with improved outcomes for BCa patients with bone metastases are highly desired.

In this study, we have used conjugation of bone-targeting moieties to develop an innovative BonTarg technology that enables the preparation of antibodies with both antigen and bone specificity. Our data suggest that modification of the therapeutic HER2 antibody Tras with the bone-targeting BP molecule, ALN, results in enhanced conjugate localization within the bone metastatic niche, relative to other tissues, raising the intriguing possibility that the bone-targeting antibody represents an enhanced targeted therapy for patients with bone metastases. We have tested this hypothesis using two BCa BMM models. The bone-targeting antibody conjugate, Tras-ALN, retains all the mechanistic properties of unmodified Tras but exhibits enhanced ability to inhibit further BCa metastasis within the bone and metastasis-to-metastasis seeding from bone lesions. We find that, compared to either ALN or Tras separately, the Tras-ALN conjugate represents a superior treatment for HER2-positive tumor cell–derived BMMs. BMMs in BCa patients with HER2-negative tumors can actually express HER2 and may rely on HER2 signaling

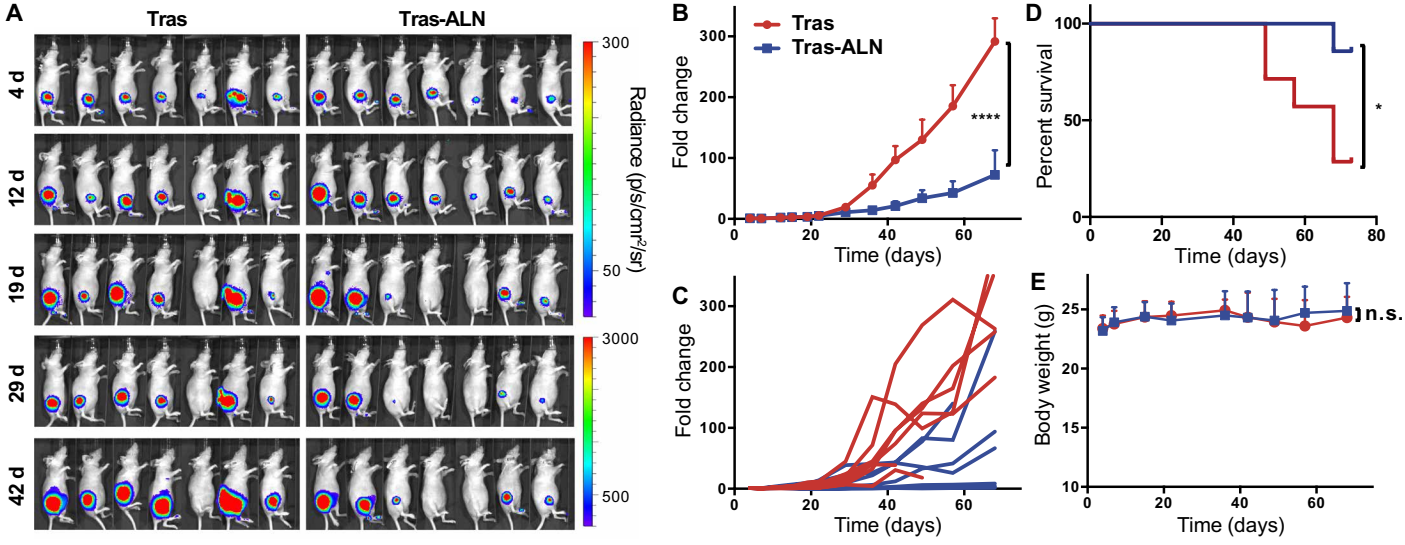

Fig. 4. In vivo comparison of Tras and Tras-ALN in HER2-negative model. (**A**) Tumor burden was monitored by weekly BLI (Tras, $n = 7$; Tras-ALN, $n = 7$), and (**B**) quantified by the radiance detected in the ROI. **(C)** Fold change in individual luminescent intensity of HER2-negative MCF-7 tumors in mice treated as described in (A). (**D**) Kaplan-Meier plot of the time to sacrifice of mice treated as described in (A). For each individual mouse, the BLI signal in the whole body reached 10^7 photons s^{-1} was considered as the endpoint. (**E**) Body weight change of tumor-bearing mice over time. $P > 0.05$ (n.s.), $^*P < 0.05$, and $^{****}P < 0.0001$.

for progression (*41*, *42*). Similarly, we also find that Tras-ALN is effective in treating BMMs in a model of HER2-negative bone metastasis, providing a new therapeutic strategy using Tras-ALN to reduce latent metastases that occur in some HER2-negative BCa patients. The affinity of ALN for bone tissue helps overcome physical and biological barriers in the bone microenvironment that impede delivery of therapeutic antibodies, thereby enriching and retaining Tras in the bone. The Tras-ALN conjugate also reaches higher concentrations in the bone metastatic niche, relative to healthy bone tissues, due to the low pH of bone tumor sites (*12*). This is consistent with previous observations that BP molecules prefer to bind to the bone matrix in an acidic tumor environment (*32*–*35*).

The evolution of current antibody therapy has been focused on targeting new biomarkers and functionalizing it with novel cytotoxic payloads. In this study, we explore the potential benefits of adding tissue specificity to antibody therapy. Using the novel BonTarg technology, we have prepared the first bone-targeting antibodies by site-specifically modifying with bone-targeting moieties. The resulting bone-targeting antibodies exhibit improved in vivo therapeutic efficacy in the treatment of BCa micrometastasis and in the prevention of secondary metastatic dissemination from the initial bone lesions. This type of precision delivery of biological medicines to the bone niche represents a promising avenue for treating bone-related diseases. The enhanced therapeutic profile of our bone-targeted HER2 antibody in treating microscopic BCa bone metastases will inform the potential benefit of adding tissue specificity to traditional therapeutic antibodies.

MATERIALS AND METHODS

Construction of Tras-ALN conjugates

The noncanonical amino acid azide-Lys was incorporated at the C terminus of the ssFB-FPheK peptide via solid-phase peptide synthesis (fig. S2). After high-performance liquid chromatography purification, the peptide was denatured with 6 M urea and stepwise dialyzed to remove the urea and allow peptide refolding. After buffer exchange into PBS (pH 8.5), 32 equivalent of ssFB-azide peptide was coincubated with Tras (BS046D from Syd labs) in PBS (pH 8.5) buffer at 37°C for 2 days. The Tras-azide conjugate was then purified via a PD-10 desalting column to remove excess ssFB-azide. The Tras-azide conjugate was characterized by ESI-MS. ESI-MS: expected, 53,564; found: 53,558 (fig. S3). Ten equivalent of BCN-ALN was added to the solution at room temperature (RT) overnight to selectively react with the azide group on the conjugate. Last, the ALN-labeled antibody conjugate was purified via a PD-10 desalting column to remove excess ALN-BCN. The conjugate was characterized by ESI-MS. ESI-MS: expected, 53,988; found: 53,984 (Fig. 1C).

Cell lines

MDA-MB-361, MCF-7, BT474, SK-BR-3, and MDA-MB-468 cell lines were cultured according to the American Type Culture Collection instructions. Firefly luciferase– and RFP-labeled MDA-MB-361 and MCF 7 cell lines were generated as previously described (*50*).

HA binding assay

Briefly, Tras or Tras-ALN was diluted in 1 ml of PBS in an Eppendorf tube. HA (15 equiv, 15 mg) was added, and the resulting suspension was shaken at 220 rpm at 37°C. Samples without HA were used as controls. After 0.25, 0.5, 1, 2, 4, and 8 hours, the suspension was centrifuged (3000 rpm, 3 min), and the absorbance of the supernatant at 280 nm was measured by NanoDrop. The percent binding to HA was calculated as follows, where OD represents optical density

$$[(OD_{\text{without HA}} - OD_{\text{with HA}})/(OD_{\text{without HA}})] \times 100\%$$

Native bone–binding assay

Long bones of mice were cut into small fragments, washed with distilled H_2O and anhydrous ethanol, and then dried at RT overnight.

For binding studies, Tras or Tras-ALN was diluted in 1 ml of PBS in an Eppendorf tube. Dried bone fragments (30 mg) were added to the tube, and the resulting suspension was shaken at 220 rpm at 37°C. Samples without bone fragments were used as controls. After 0.25, 0.5, 1.0, 2.0, 4.0, and 8.0 hours, the suspensions were centrifuged (3000 rpm, 5 min), and the absorbance at 280 nm of the supernatant was measured by Nanodrop. The percent binding to native bone was calculated according to the following formula, where OD represents optical density

$$[(OD_{\text{without native bone}} - OD_{\text{with native bone}}) / (OD_{\text{without native bone}})] \times 100\%$$

In vitro cytotoxicity of Tras and Tras-ALN

SK-BR-3, BT474, and MDA-MB-468 cells were seeded in 200 μl of culture medium into 96-well plates at a density of 2×10^3 cells per well and incubated overnight to allow attachment. The culture medium was then removed, replaced by different concentrations of Tras and Tras-ALN dissolved in culture medium, and then incubated for 4 days. Twenty microliters of MTT solution (5 mg/ml) was then added to each well and incubated for another 4 hours. The medium was aspirated, and 150 μl of dimethyl sulfoxide was added to each well. The absorbance at 570 nm was measured by microplate reader (Infinite M Plex by Tecan) to quantify living cells.

Flow cytometry

Cancer cells (3×10^3) were resuspended in 96-well plates and stained with Tras and Tras-ALN (30 μg/ml) for 30 min at 4°C. After staining, the cells were washed twice with PBS and then further incubated with Fluorescein (FITC) AffiniPure Goat Anti-Human IgG (H+L) (code: 109-095-003, Jackson ImmunoResearch) for 30 min at 4°C. Fluorescence intensity was determined using a BD FACSVerse (BD Biosciences).

Determination of K_d values

The functional affinity of Tras-ALN for HER2 was determined as reported (*51*). Briefly, 2×10^5 SK-BR-3, BT474, MDA-MB-361, or MDA-MB-468 cells were incubated with increasing concentrations of Tras and Tras-ALN for 4 hours on ice. After washing away unbound material, bound antibody was detected using Fluorescein (FITC) AffiniPure Goat Anti-Human IgG (H+L) (Jackson Immunology). The cells were analyzed for fluorescence intensity after propidium iodide (Molecular Probes, Eugene, OR) staining. The linear portion of the saturation curve was used to calculate the K_d, using the Lineweaver-Burk method of plotting the inverse of the median fluorescence as a function of the inverse of the antibody concentration. The K_d was determined as follows: $1/F = 1/F_{max} + (K_d/F_{max})(1/[Ab])$, where F corresponds to the background subtracted median fluorescence and F_{max} was calculated from the plot.

Confocal imaging

Cancer cells were grown to about 80% confluency in eight-well confocal imaging chamber plates. The cells were incubated with 30 nM Tras-FITC for 30 min and then fixed by 4% paraformaldehyde for 15 min. The cells were washed three times with PBS (pH 7.4) and then incubated with DiIC18(3) (Marker Gene Technologies Inc.) for 20 min and Hoechst 33342 (catalog number H1399, Life Technologies) for 5 min. The cells were then washed three times with PBS (pH 7.4) and used for confocal imaging. Confocal fluorescence images of cells were obtained using a Nikon A1R-si Laser Scanning Confocal Microscope (Japan), equipped with lasers of 405/488/561/638 nm.

Binding to bone cryosections

Nondecalcified long bone sections from C57BL/6 mice were incubated with Tras or Tras-ALN (50 μg/ml), conjugated overnight at 4°C, followed by staining with FITC-labeled anti-human IgG for 60 min at RT. After washing three times with PBS, specimens were incubated for 30 min at 37°C with XO [stock: 2 mg/ml, dilute 1:500; dilute buffer: PBS (pH 6.5)]. After three washes with PBS, specimens were stained with Hoechst 33342 (stock: 10 mg/ml, dilute 1:2000) for 10 min. Slides were then washed with PBS, air dried, and sealed with ProLong Gold Antifade Mountant (from Thermo Fisher Scientific).

In vivo evaluation of Tras-ALN

IIA injections and in vivo imaging system (IVIS) imaging were performed as previously described (*37*). Five days after injection, the animals were randomized into four groups: PBS-treated control, ALN (a representative of free BP, 10 μg/kg retro-orbital injection in PBS twice a week for 16 weeks), Tras (1.0 mg/kg retro-orbital injection in sterile PBS twice a week), and Tras-ALN conjugate (the same as Tras). After injection, the animals were imaged twice a week using IVIS Lumina II (Advanced Molecular Vision), following the recommended procedures and manufacturer's settings. On day 110, mice were anesthetized and blood was collected by cardiac puncture before euthanasia. Tumor-bearing tibia, heart, liver, spleen, lung, brain, and kidney were collected for further tests. All experimental procedures were approved by the Institutional Animal Care and Use Committee at the Rice University and the Baylor College of Medicine.

Ex vivo metastasis-to-metastasis analysis

Mice were anesthetized with 2.5% isoflurane in oxygen and injected with luciferin retro-orbitally. Mice were then euthanized, and their hearts, livers, spleens, lungs, kidneys, brain, and tibia bones were collected. Ex vivo bioluminescence and fluorescence imaging of these organs were immediately performed on the IVIS Lumina.

Bone histology and IHC

Harvested long bones were fixed for 1 week in 10% formalin and then decalcified in 12% EDTA at 4°C for 2 weeks. Specimens were embedded in paraffin using the standard procedure. From these blocks, 5-μm sections were cut and collected on glass slides. The sections were dried in an oven overnight (37°C) and then deparaffinized in xylene solution for 10 min. Hematoxylin and eosin (H&E) staining were performed via the conventional method. IHC analysis was performed on decalcified paraffin–embedded tissue sections using the HRP/DAB ABC IHC Kit (Abcam) following the manufacturer's protocol.

Radiographic analysis

Tibiae were dissected, fixed, and scanned by microCT (SkyScan 1272, Aartselaar, Belgium) at a resolution of 6.64 μm per pixel. Raw images were reconstructed in NReconn and analyzed in CTAn (SkyScan, Aartselaar, Belgium) using a region of interest. Bone parameters analyzed included trabecular thickness (Tb.Th), bone volume fraction (BV/TV), BMD, and bone surface/bone volume ratio.

Biodistribution

MDA-MB-361 cells were introduced into female athymic nude mice (body weight, 13 to 15 g) via IIA injections. After 3 months,

Cy7.5-labeled Tras and Tras-ALN (1 mg/kg) were administrated to tumor-bearing nude mice by retro-orbital injection. At 24, 96, or 168 hours after injection, major organs including the heart, liver, spleen, kidney, lung, and bone tumor tissue were removed. The fluorescence intensity in organs and bone tumor tissues was determined semiquantitatively by using the Caliper IVIS Lumina in vivo imager (Caliper Life Science, Boston, MA, USA). Bones from Tras-ALN–treated mice were fixed and sectioned to further evaluate biodistribution. For the distribution at other bones, Cy7.5-labeled Tras (1 mg/kg) or Tras-ALN (1 mg/kg) were administrated to tumor-bearing mice by retro-orbital injection. Seventy-two hours after the administration, the major organs and bones were isolated and imaged using Caliper IVIS Lumina II imager.

In a separate study, unlabeled Tras-ALN (1 mg/kg) was administered via retro-orbital injection to nude mice bearing MDA-MB-361 tumors in their right hindlimbs. After 48 hours, long bones from Tras-ALN–treated mice were isolated and immediately sectioned without decalcification. Bone sections were then fixed and incubated with anti-RFP (rabbit) antibody (1:200, purchased from Rockland) overnight at 4°C, followed by staining with FITC-labeled anti-human IgG (1:100, purchased from Jackson Immunology) and Alexa Fluor 555 AffiniPure Donkey Anti-Rabbit IgG (H+L) (1:200, purchased from Thermo Fisher Scientific) for 120 min at RT. Sections were mounted with Prolong gold anti-fade mountant with DAPI (from Thermo Fisher Scientific), sealed with a coverslip, and then used for confocal imaging.

Pharmacokinetic analysis and FcRn binding assay

Athymic nude mice were injected retro-orbitally with a single dose of Tras and Tras-ALN (1 mg/kg) in PBS, and serum was collected at regular intervals for 7 days and analyzed by the Trastuzumab ELISA Kit (Lab Bioreagents). FcRn binding was determined using Lumit FcRn Binding Immunoassay kit (Promega) according to the manual.

Quantification of TRAP and calcium levels in serum

At terminal time points, blood was collected by cardiac puncture and centrifuged for 15 min at 3000 rpm to obtain the serum. The concentration of osteoclast-derived TRAcP 5b was measured by using the Mouse ACP5/TRAP ELISA Kit (catalog number IT5180, G-Biosciences). Serum calcium levels were determined colorimetrically using a calcium detection kit (catalog number DICA-500, Bioassays).

Statistical methods

Data are presented as means ± SEM and statistically analyzed using GraphPad Prism software version 6 (GraphPad software, San Diego, CA). Two-way analysis of variance (ANOVA) followed by Sidak's multiple comparisons was used for all data collected over a time course. One-way ANOVA followed by Tukey's multiple comparisons was used for microCT data. Unpaired Student's t test was used for multiorgan metastasis data. $P < 0.05$ was considered to represent statistical significance.

SUPPLEMENTARY MATERIALS

Supplementary material for this article is available at http://advances.sciencemag.org/cgi/content/full/7/26/eabf2051/DC1

View/request a protocol for this paper from *Bio-protocol*.

REFERENCES AND NOTES

1. A. M. Scott, J. D. Wolchok, L. J. Old, Antibody therapy of cancer. *Nat. Rev. Cancer* **12**, 278–287 (2012).
2. E. L. Sievers, P. D. Senter, Antibody-drug conjugates in cancer therapy. *Annu. Rev. Med.* **64**, 15–29 (2013).
3. D. M. Pardoll, The blockade of immune checkpoints in cancer immunotherapy. *Nat. Rev. Cancer* **12**, 252–264 (2012).
4. A. F. Labrijn, M. L. Janmaat, J. M. Reichert, P. W. H. I. Parren, Bispecific antibodies: A mechanistic review of the pipeline. *Nat. Rev. Drug Discov.* **18**, 585–608 (2019).
5. A. W. Tolcher, Antibody drug conjugates: Lessons from 20 years of clinical experience. *Ann. Oncol.* **27**, 2168–2172 (2016).
6. T. T. Hansel, H. Kropshofer, T. Singer, J. A. Mitchell, A. J. T. George, The safety and side effects of monoclonal antibodies. *Nat. Rev. Drug Discov.* **9**, 325–338 (2010).
7. J. Descotes, Immunotoxicity of monoclonal antibodies. *MAbs* **1**, 104–111 (2009).
8. L. T. Baxter, H. Zhu, D. G. Mackensen, W. F. Butler, R. K. Jain, Biodistribution of monoclonal antibodies: Scale-up from mouse to human using a physiologically based pharmacokinetic model. *Cancer Res.* **55**, 4611–4622 (1995).
9. R. E. Coleman, R. D. Rubens, The clinical course of bone metastases from breast cancer. *Br. J. Cancer* **55**, 61–66 (1987).
10. R. E. Coleman, P. Smith, R. D. Rubens, Clinical course and prognostic factors following bone recurrence from breast cancer. *Br. J. Cancer* **77**, 336–340 (1998).
11. G. R. Mundy, Metastasis to bone: Causes, consequences and therapeutic opportunities. *Nat. Rev. Cancer* **2**, 584–593 (2002).
12. L. A. Kingsley, P. G. J. Fournier, J. M. Chirgwin, T. A. Guise, Molecular biology of bone metastasis. *Mol. Cancer Ther.* **6**, 2609–2617 (2007).
13. B. Ell, Y. Kang, SnapShot: Bone metastasis. *Cell* **151**, 690–690.e1 (2012).
14. J. Fornetti, A. L. Welm, S. A. Stewart, Understanding the bone in cancer metastasis. *J. Bone Miner. Res. Off. J. Am. Soc. Bone Miner. Res.* **33**, 2099–2113 (2018).
15. D. Brown, D. Smeets, B. Székely, D. Larsimont, A. M. Szász, P.-Y. Adnet, F. Rothé, G. Rouas, Z. I. Nagy, Z. Faragó, A.-M. Tőkés, M. Dank, G. Szentmártoni, N. Udvarhelyi, G. Zoppoli, L. Pusztai, M. Piccart, J. Kulka, D. Lambrechts, C. Sotiriou, C. Desmedt, Phylogenetic analysis of metastatic progression in breast cancer using somatic mutations and copy number aberrations. *Nat. Commun.* **8**, 14944 (2017).
16. M. B. Siegel, X. He, K. A. Hoadley, A. Hoyle, J. B. Pearce, A. L. Garrett, S. Kumar, V. J. Moylan, C. M. Brady, A. E. Van Swearingen, D. Marron, G. P. Gupta, L. B. Thorne, N. Kieran, C. Livasy, E. R. Mardis, J. S. Parker, M. Chen, C. K. Anders, L. A. Carey, C. M. Perou, Integrated RNA and DNA sequencing reveals early drivers of metastatic breast cancer. *J. Clin. Invest.* **128**, 1371–1383 (2018).
17. I. Ullah, G.-M. Karthik, A. Alkodsi, U. Kjällquist, G. Stålhammar, J. Lövrot, N.-F. Martinez, J. Lagergren, S. Hautaniemi, J. Hartman, J. Bergh, Evolutionary history of metastatic breast cancer reveals minimal seeding from axillary lymph nodes. *J. Clin. Invest.* **128**, 1355–1370 (2018).
18. M. Balic, H. Lin, L. Young, D. Hawes, A. Giuliano, G. McNamara, R. H. Datar, R. J. Cote, Most early disseminated cancer cells detected in bone marrow of breast cancer patients have a putative breast cancer stem cell phenotype. *Clin. Cancer Res.* **12**, 5615–5621 (2006).
19. M. Marty, F. Cognetti, D. Maraninchi, R. Snyder, L. Mauriac, M. Tubiana-Hulin, S. Chan, D. Grimes, A. Antón, A. Lluch, J. Kennedy, K. O'Byrne, P. Conte, M. Green, C. Ward, K. Mayne, J.-M. Extra, Randomized phase II trial of the efficacy and safety of trastuzumab combined with docetaxel in patients with human epidermal growth factor receptor 2-positive metastatic breast cancer administered as first-line treatment: The M77001 study group. *J. Clin. Oncol. Off. J. Am. Soc. Clin. Oncol.* **23**, 4265–4274 (2005).
20. V. Valero, J. Forbes, M. D. Pegram, T. Pienkowski, W. Eiermann, G. von Minckwitz, H. Roche, M. Martin, J. Crown, J. R. Mackey, P. Fumoleau, J. Rolski, Z. Mrsic-Krmpotic, A. Jagiello-Gruszfeld, A. Riva, M. Buyse, H. Taupin, G. Sauter, M. F. Press, D. J. Slamon, Multicenter phase III randomized trial comparing docetaxel and trastuzumab with docetaxel, carboplatin, and trastuzumab as first-line chemotherapy for patients with HER2-gene-amplified metastatic breast cancer (BCIRG 007 study): Two highly active therapeutic regimens. *J. Clin. Oncol. Off. J. Am. Soc. Clin. Oncol.* **29**, 149–156 (2011).
21. R. Nahta, D. Yu, M.-C. Hung, G. N. Hortobagyi, F. J. Esteva, Mechanisms of disease: Understanding resistance to HER2-targeted therapy in human breast cancer. *Nat. Clin. Pract. Oncol.* **3**, 269–280 (2006).
22. G. Gullo, M. Zuradelli, F. Sclafani, A. Santoro, J. Crown, Durable complete response following chemotherapy and trastuzumab for metastatic HER2-positive breast cancer. *Ann. Oncol.* **23**, 2204–2205 (2012).
23. P. Schmid, S. Adams, H. S. Rugo, A. Schneeweiss, C. H. Barrios, H. Iwata, V. Diéras, R. Hegg, S.-A. Im, G. Shaw Wright, V. Henschel, L. Molinero, S. Y. Chui, R. Funke, A. Husain, E. P. Winer, S. Loi, L. A. Emens; IMpassion130 Trial Investigators, Atezolizumab and nab-paclitaxel in advanced triple-negative breast cancer. *N. Engl. J. Med.* **379**, 2108–2121 (2018).
24. L. E. Cole, T. Vargo-Gogola, R. K. Roeder, Targeted delivery to bone and mineral deposits using bisphosphonate ligands. *Adv. Drug Deliv. Rev.* **99**, 12–27 (2016).

25. L. Dang, J. Liu, F. Li, L. Wang, D. Li, B. Guo, X. He, F. Jiang, C. Liang, B. Liu, S. A. Badshah, B. He, J. Lu, C. Lu, A. Lu, G. Zhang, Targeted delivery systems for molecular therapy in skeletal disorders. *Int. J. Mol. Sci.* **17**, 428 (2016).
26. M. Stapleton, K. Sawamoto, C. J. Alméciga-Díaz, W. G. Mackenzie, R. W. Mason, T. Orii, S. Tomatsu, Development of bone targeting drugs. *Int. J. Mol. Sci.* **18**, 1345 (2017).
27. T. Singh, V. Kaur, M. Kumar, P. Kaur, R. S. R. Murthy, R. K. Rawal, The critical role of bisphosphonates to target bone cancer metastasis: An overview. *J. Drug Target.* **23**, 1–15 (2015).
28. F. H. Ebetino, A.-M. L. Hogan, S. Sun, M. K. Tsoumpra, X. Duan, J. T. Triffitt, A. A. Kwaasi, J. E. Dunford, B. L. Barnett, U. Oppermann, M. W. Lundy, A. Boyde, B. A. Kashemirov, C. E. McKenna, R. G. G. Russell, The relationship between the chemistry and biological activity of the bisphosphonates. *Bone* **49**, 20–33 (2011).
29. K. B. Farrell, A. Karpeisky, D. H. Thamm, S. Zinnen, Bisphosphonate conjugation for bone specific drug targeting. *Bone Rep.* **9**, 47–60 (2018).
30. R. N. Young, M. D. Grynpas, Targeting therapeutics to bone by conjugation with bisphosphonates. *Curr. Opin. Pharmacol.* **40**, 87–94 (2018).
31. H. Fleisch, *Bisphosphonates in Bone Disease: From the Laboratory to the Patient* (Elsevier, 2000).
32. J. E. Bayouth, D. J. Macey, L. P. Kasi, F. V. Fossella, Dosimetry and toxicity of samarium-153-EDTMP administered for bone pain due to skeletal metastases. *J. Nucl. Med.* **35**, 63–69 (1994).
33. H. Hirabayashi, T. Sawamoto, J. Fujisaki, Y. Tokunaga, S. Kimura, T. Hata, Relationship between physicochemical and osteotropic properties of bisphosphonic derivatives: Rational design for osteotropic drug delivery system (ODDS). *Pharm. Res.* **18**, 646–651 (2001).
34. K. Hochdörffer, K. Abu Ajaj, C. Schäfer-Obodozie, F. Kratz, Development of novel bisphosphonate prodrugs of doxorubicin for targeting bone metastases that are cleaved pH dependently or by cathepsin B: Synthesis, cleavage properties, and binding properties to hydroxyapatite as well as bone matrix. *J. Med. Chem.* **55**, 7502–7515 (2012).
35. W. F. Goeckeler, B. Edwards, W. A. Volkert, R. A. Holmes, J. Simon, D. Wilson, Skeletal localization of samarium-153 chelates: Potential therapeutic bone agents. *J. Nucl. Med.* **28**, 495–504 (1987).
36. C. Yu, H. Wang, A. Muscarella, A. Goldstein, H.-C. Zeng, Y. Bae, B. H. I. Lee, X. H.-F. Zhang, Intra-iliac artery injection for efficient and selective modeling of microscopic bone metastasis. *J. Vis. Exp.* **26**, 53982 (2016).
37. H. Wang, C. Yu, X. Gao, T. Welte, A. M. Muscarella, L. Tian, H. Zhao, Z. Zhao, S. Du, J. Tao, B. Lee, T. F. Westbrook, S. T. C. Wong, X. Jin, J. M. Rosen, C. K. Osborne, X. H.-F. Zhang, The osteogenic niche promotes early-stage bone colonization of disseminated breast cancer cells. *Cancer Cell* **27**, 193–210 (2015).
38. H. Wang, L. Tian, J. Liu, A. Goldstein, I. Bado, W. Zhang, B. R. Arenkiel, Z. Li, M. Yang, S. Du, H. Zhao, D. R. Rowley, S. T. C. Wong, Z. Gugala, X. H.-F. Zhang, The osteogenic niche is a calcium reservoir of bone micrometastases and confers unexpected therapeutic vulnerability. *Cancer Cell* **34**, 823–839.e7 (2018).
39. L. E. Barney, E. C. Dandley, L. E. Jansen, N. G. Reich, A. M. Mercurio, S. R. Peyton, A cell–ECM screening method to predict breast cancer metastasis. *Integr. Biol.* **7**, 198–212 (2015).
40. W. Zhang, I. L. Bado, J. Hu, Y.-W. Wan, L. Wu, H. Wang, Y. Gao, H.-H. Jeong, Z. Xu, X. Hao, B. M. Lege, R. Al-Ouran, L. Li, J. Li, L. Yu, S. Singh, H. C. Lo, M. Niu, J. Liu, W. Jiang, Y. Li, S. T. C. Wong, C. Cheng, Z. Liu, X. H.-F. Zhang, The bone microenvironment invigorates metastatic seeds for further dissemination. *Cell* **184**, 2471–2486.e20 (2021).
41. M. J. M. Magbanua, H. S. Rugo, L. Hauranieh, R. Roy, J. H. Scott, J. C. Lee, F. Hsiao, E. V. Sosa, L. van't Veer, L. J. Esserman, J. W. Park, Genomic and expression profiling reveal molecular heterogeneity of disseminated tumor cells in bone marrow of early breast cancer. *Npj Breast Cancer.* **4**, 31 (2018).
42. E. F. Solomayer, S. Becker, G. Pergola-Becker, R. Bachmann, B. Krämer, U. Vogel, H. Neubauer, D. Wallwiener, J. Huober, T. N. Fehm, Comparison of HER2 status between primary tumor and disseminated tumor cells in primary breast cancer patients. *Breast Cancer Res. Treat.* **98**, 179–184 (2006).
43. S. Ithimakin, K. C. Day, F. Malik, Q. Zen, S. J. Dawsey, T. F. Bersano-Begey, A. A. Quraishi, K. W. Ignatoski, S. Daignault, A. Davis, C. L. Hall, N. Palanisamy, A. N. Heath, N. Tawakkol, T. K. Luther, S. G. Clouthier, W. A. Chadwick, M. L. Day, C. G. Kleer, D. G. Thomas, D. F. Hayes, H. Korkaya, M. S. Wicha, HER2 drives luminal breast cancer stem cells in the absence of HER2 amplification: Implications for efficacy of adjuvant trastuzumab. *Cancer Res.* **73**, 1635–1646 (2013).
44. I. L. Bado, W. Zhang, J. Hu, Z. Xu, H. Wang, P. Sarkar, L. Li, Y.-W. Wan, J. Liu, W. Wu, H. C. Lo, I. S. Kim, S. Singh, M. Janghorban, A. M. Muscarella, A. Goldstein, P. Singh, H.-H. Jeong, C. Liu, R. Schiff, S. Huang, M. J. Ellis, M. W. Gaber, Z. Gugala, Z. Liu, X. H.-F. Zhang, The bone microenvironment increases phenotypic plasticity of ER^+ breast cancer cells. *Dev. Cell* **56**, 1100–1117.e9 (2021).
45. H. Kennecke, R. Yerushalmi, R. Woods, M. C. U. Cheang, D. Voduc, C. H. Speers, T. O. Nielsen, K. Gelmon, Metastatic behavior of breast cancer subtypes. *J. Clin. Oncol.* **28**, 3271–3277 (2010).
46. K. Manders, L. V. van de Poll-Franse, G.-J. Creemers, G. Vreugdenhil, M. J. van der Sangen, G. A. Nieuwenhuijzen, R. M. Roumen, A. C. Voogd, Clinical management of women with metastatic breast cancer: A descriptive study according to age group. *BMC Cancer* **6**, 179 (2006).
47. I. Kuchuk, B. Hutton, P. Moretto, T. Ng, C. L. Addison, M. Clemons, Incidence, consequences and treatment of bone metastases in breast cancer patients-Experience from a single cancer centre. *J. Bone Oncol.* **2**, 137–144 (2013).
48. E. Svensson, C. F. Christiansen, S. P. Ulrichsen, M. R. Rørth, H. T. Sørensen, Survival after bone metastasis by primary cancer type: A Danish population-based cohort study. *BMJ Open* **7**, e016022 (2017).
49. A. Parkes, C. L. Warneke, K. Clifton, A. Al-Awadhi, O. Oke, R. C. Pestana, O. Alhalabi, J. K. Litton, G. N. Hortobagyi, Prognostic factors in patients with metastatic breast cancer with bone-only metastases. *Oncologist* **23**, 1282–1288 (2018).
50. H. Wang, L. Tian, A. Goldstein, J. Liu, H.-C. Lo, K. Sheng, T. Welte, S. T. C. Wong, Z. Gugala, F. Stossi, C. Zong, Z. Li, M. A. Mancini, X. H.-F. Zhang, Bone-in-culture array as a platform to model early-stage bone metastases and discover anti-metastasis therapies. *Nat. Commun.* **8**, 15045 (2017).
51. R. L. Dillon, S. Chooniedass, A. Premsukh, G. P. Adams, J. Entwistle, G. C. MacDonald, J. Cizeau, Trastuzumab-deBouganin conjugate overcomes multiple mechanisms of T-DM1 drug resistance. *J. Immunother.* **39**, 117–126 (2016).

Acknowledgments: We thank Xiao and Zhang laboratory members for insightful comments. **Funding:** This work was supported by the Cancer Prevention Research Institute of Texas (CPRIT RR170014 to H.X.), NIH (GM133706, AI165079, and CA255894 to H.X. and CA183878, CA251950, and CA221946 to X.H.-F.Z.), the Robert A. Welch Foundation (C-1970 to H.X.), U.S. Department of Defense (BC201371 to H.X. and X.H.-F.Z., and DAMD W81XWH-16-1-0073 and Era of Hope Scholarship to X.H.-F.Z.), the John S. Dunn Foundation Collaborative Research Award (to H.X.), and the Hamill Innovation Award (to H.X.). X.H.-F.Z. is also supported by the Breast Cancer Research Foundation and McNair Medical Institute. H.X. is a Cancer Prevention and Research Institute of Texas (CPRIT) scholar in cancer research. **Author contributions:** Z.T., L.W., X.H.-F.Z., and H.X. developed the hypothesis, designed experiments, analyzed the data, and wrote the manuscript. Z.T., L.W., C.Y., Z.X., I.B., H.W., and W.Z. performed experiments. Y.C., A.L., Lu. W., K.-L.W., X.H.-F.Z., and H.X. contributed to experimental design, generation of the reagents, and manuscript editing. X.H.-F.Z. and H.X. conceived and supervised the project. **Competing interests:** The authors declare that they have no competing interests. **Data and materials availability:** All data needed to evaluate the conclusions in the paper are present in the paper and/or the Supplementary Materials. Additional data related to this paper may be requested from the authors.

Submitted 10 October 2020
Accepted 10 May 2021
Published 23 June 2021
10.1126/sciadv.abf2051

Citation: Z. Tian, L. Wu, C. Yu, Y. Chen, Z. Xu, I. Bado, A. Loredo, L. Wang, H. Wang, K.-L. Wu, W. Zhang, X. H.-F. Zhang, H. Xiao, Harnessing the power of antibodies to fight bone metastasis. *Sci. Adv.* **7**, eabf2051 (2021).

Harnessing the power of antibodies to fight bone metastasis

Zeru Tian, Ling Wu, Chenfei Yu, Yuda Chen, Zhan Xu, Igor Bado, Axel Loredo, Lushun Wang, Hai Wang, Kuan-Lin Wu, Weijie Zhang, Xiang H.-F. Zhang and Han Xiao

Sci Adv **7** (26), eabf2051.
DOI: 10.1126/sciadv.abf2051

Evolving cancer–niche interactions and therapeutic targets during bone metastasis

Robert L. Satcher[1] *and Xiang H.-F. Zhang*[2,3,4]✉

Abstract | Many cancer types metastasize to bone. This propensity may be a product of genetic traits of the primary tumour in some cancers. Upon arrival, cancer cells establish interactions with various bone-resident cells during the process of colonization. These interactions, to a large degree, dictate cancer cell fates at multiple steps of the metastatic cascade, from single cells to overt metastases. The bone microenvironment may even influence cancer cells to subsequently spread to multiple other organs. Therefore, it is imperative to spatiotemporally delineate the evolving cancer–bone crosstalk during bone colonization. In this Review, we provide a summary of the bone microenvironment and its impact on bone metastasis. On the basis of the microscopic anatomy, we tentatively define a roadmap of the journey of cancer cells through bone relative to various microenvironment components, including the potential of bone to function as a launch pad for secondary metastasis. Finally, we examine common and distinct features of bone metastasis from various cancer types. Our goal is to stimulate future studies leading to the development of a broader scope of potent therapies.

Osteoblasts
Cells that are responsible for synthesis and mineralization of new bones during development and bone remodelling. They are derived from mesenchymal linage, usually localize at the surface of bone matrix and can differentiate into osteocytes.

[1]*Department of Orthopedic Oncology, The University of Texas MD Anderson Cancer Center, Houston, TX, USA.*

[2]*Lester and Sue Smith Breast Center, Baylor College of Medicine, Houston, TX, USA.*

[3]*Dan L. Duncan Cancer Center, Baylor College of Medicine, Houston, TX, USA.*

[4]*Department of Molecular and Cellular Biology, Baylor College of Medicine, Houston, TX, USA.*

✉*e-mail: xiangz@bcm.edu*

https://doi.org/10.1038/s41568-021-00406-5

Bone and bone marrow together represent a highly complex environment. This complexity results from the intricate spatial organization of many different resident cell types and their agile temporal dynamics. The major functions of bone include mechanical support and haematopoiesis. The former function is carried out by the mineral part of bone, which is built and maintained primarily by osteoblasts, osteocytes, osteoclasts, their precursors and mesenchymal stem cells (MSCs). The latter function involves a hierarchy of cells, including haematopoietic stem cells (HSCs), various intermediate progenitor cells, as well as matured blood cells. MSCs and their descendent cells cooperate with the haematopoietic cells at different levels of the hierarchy and have important roles in regulating haematopoiesis. In addition, bone and bone marrow are highly vascularized. Arteries enter long bones from the periosteum, branch into smaller arterioles and form capillaries — type H capillaries — at the metaphyseal and epiphyseal regions (FIG. 1). The blood then drains into the sinusoidal network — type L capillaries, which extend in the reverse direction — converges into a central vein and eventually exits the medullary cavity[1]. Furthermore, different blood vessels are also accompanied by different mural or perivascular cells. Arteries, arterioles, type H and type L capillaries are covered by perivascular cells that are αSMA^{+}NG2^{+}, PDGFRβ^{+}nestin–GFP^{high}NG2^{+}, PDGFRβ^{+}NG2^{+} and LEPR^{+}nestin–GFP^{low}PDGFRα^{+}, respectively[2–6]. Therefore, the vasculature in the bone is heterogeneous. Nerves, including sensory and sympathetic neurons and their supportive cells[7], usually accompany blood vessels. Together, this miscellany of cells constitutes the bone microenvironment (BME) and functions in a delicate balance to maintain bone mass and integrity (BOX 1).

Bone and bone marrow are frequently affected by metastasis from cancers in multiple organs, including breast, prostate, colon, lung, bladder, kidney and head and neck. The proclivity of these cancer types to colonize bone remains poorly understood and may be related to the fact that the BME is enriched with factors and niches that nurture stem cells.

Fully developed metastatic disease has devastating consequences for the function of bone and accelerates cancer progression. Current standard-of-care therapies target the ability of cancer cells to resorb bone, which presumably does not occur until a late stage of bone colonization in most cancer types. Although such therapies undeniably improve quality of life, patient survival is not significantly elongated. Additional therapeutic strategies may be revealed with a deeper understanding of the process of early bone colonization, including the initial interactions between disseminated tumour cells (DTCs) and the various microenvironment niches, and the

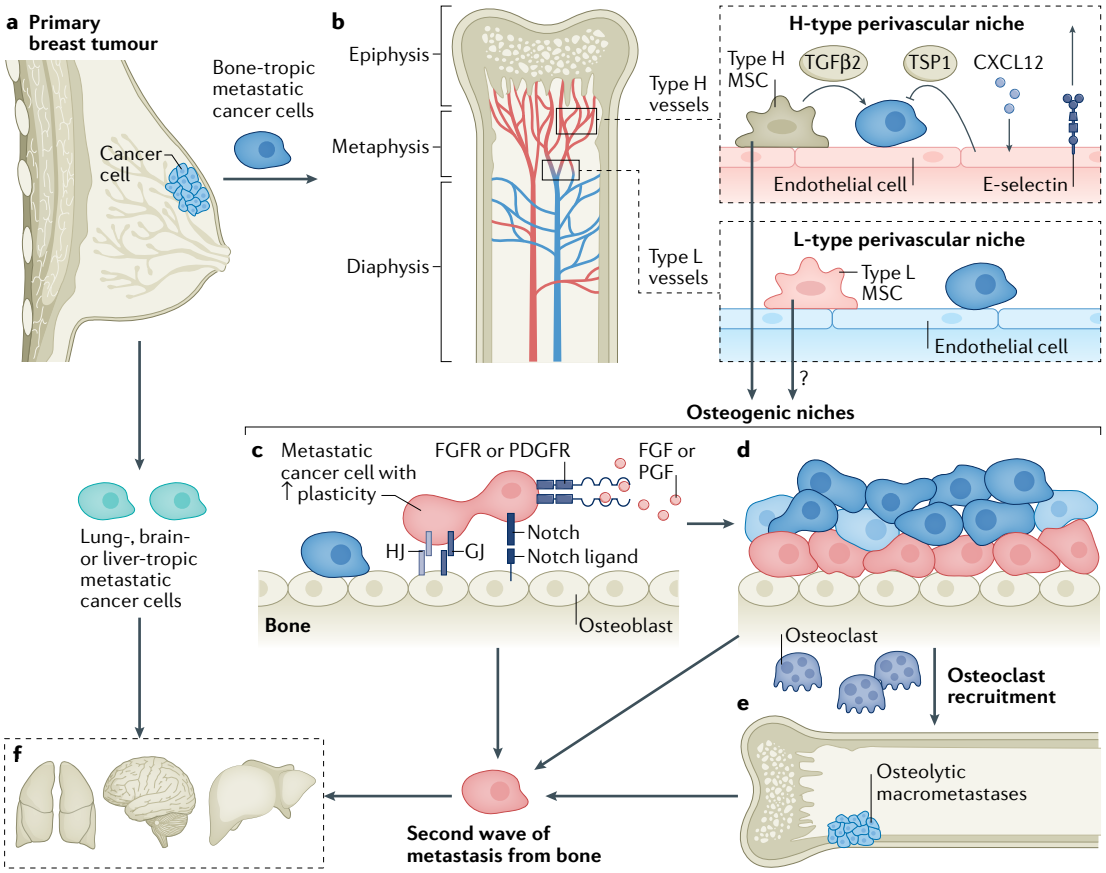

Fig. 1 | **The journey of DTCs towards bone metastasis and beyond. a** | Metastatic organotropism may be encoded by genetic traits and arise in primary tumours by various mechanisms. **b** | Blood vessels may provide the first foothold for disseminated tumour cells (DTCs). The vasculature in the bone marrow is highly heterogeneous. Most notably, the capillaries can be classified into type H, which connect to arterioles, and type L, which connect to veins. Type H capillaries are localized to metaphyseal regions as well as in parallel to the endosteal surface. By contrast, type L capillaries are mostly within diaphysis and are sinusoidal. Endothelial cells in type H and type L capillaries express high and low levels of CD31 and endomucin, respectively. The perivascular niches harbour dormant DTCs. Type H and type L vessels may represent different niches with endothelial and perivascular cells differing from one another. TGFβ2 produced by perivascular mesenchymal cells and thrombospondin 1 (TSP1) produced by endothelial cells may mediate cellular quiescence of cancer cells. The counteraction between CXCL12 and E-selectin may also determine the fate and positioning of cancer cells relative to the niche. The perivascular mesenchymal cells possess mesenchymal stem cell (MSC) activities and may contribute to osteogenesis. **c** | The osteogenic niche promotes progression of DTCs towards micrometastases through multiple mechanisms, including direct interaction by heterotypic adherens junctions (HJs), gap junctions (GJs) and Notch signalling. The osteogenic cells may also secrete TSC, which activates integrin signalling. Furthermore, paracrine signalling of FGF2 and PDGF-DD produced by the bone microenvironment enhances the phenotypic plasticity of cancer cells. **d** | As micrometastases grow, cancer cells that remain adjacent to osteogenic cells may maintain their plasticity whereas those that are pushed away may revert to a more differentiated status. **e** | Recruitment and activation of osteoclasts start the vicious cycle and drive progression towards osteolytic macrometastases. This is the phase that causes symptoms and leads to diagnosis in the clinic. **f** | The interaction with osteogenic cells leads to increased cancer cell stemness and phenotypic plasticity, which may fuel further dissemination to multiple other organs. The second wave of metastasis from bone may be less organotropic, which is distinct from the initial wave of metastasis.

Osteocytes
Cells that are derived from osteoblasts and become embedded in the bone matrix.

Osteoclasts
Cells that are responsible for resorption of bones. They are derived from myeloid cell lineage. Matured osteoclasts are multinuclear and function in close coordination with osteoblasts.

Mesenchymal stem cells
(MSCs). Cells that are multipotent and responsible for the production of mesenchymal cells, including osteoblasts, chondrocytes, adipocytes and fibroblasts.

Haematopoietic stem cells
(HSCs). Cells that are multipotent and responsible for production of all blood cells.

Type H capillaries
Vascular networks in the bone marrow that continue from arterioles and precede sinusoid vein vessels. They are surrounded by osteoprogenitor cells and couple osteogenesis and angiogenesis.

Type L capillaries
Sinusoid veins that continue from the H-type capillaries and converge on central vein in the medullar cavity of bone marrow.

subsequent progression towards bone-deconstructing overt bone metastases.

Here, we present a Review on the topic of bone metastatic diseases, focusing on tumour cell interactions with the microenvironment during the journey from primary tumour to bone and, as more recently unveiled, from bone to additional target organs. We summarize our knowledge of bone metastasis as a sequence of connected steps using the example of breast cancer and other representative cancer types to highlight the spectrum of tumour-driven interactions in the BME that uniquely describe the metastatic journey. Specifically, we compare the metastatic journey of disseminated cells from breast cancer, which is the most studied tumour type with the highest incidence of bone metastasis among the cancers we discuss, with those of other selected solid tumours that differ mechanistically according to their phenotype (prostate — osteoblastic), treatment resistance (renal — osteolytic) and their immunological properties (multiple myeloma (MM) — osteolytic). Finally, we review newly emerging therapeutic targets that may mediate the various steps of bone colonization.

Premetastatic niche
Potential destination of metastasis in distant organs before the actual arrival of metastatic cells. It is different from normal tissue because of interactions with bone marrow-derived cells stimulated by primary tumours.

Endosteal niche
The microenvironmental location at the endosteal surface. It is enriched with osteoblasts and osteoprogenitors as well as osteoclasts. Transplanted haematopoietic stem cells often adhere to this niche.

The metastatic journey from breast to bone

To obtain a relatively integrated view, we use mostly breast cancer studies as examples for the discussion of the metastatic journey to bone, as there are more experimental models available compared with other cancers (TABLE 1; BOX 2) and, as a result, a larger number of published studies exist for analysis. However, insights from other cancers can sometimes facilitate deeper understanding and broader discussion, and therefore, are mentioned with cancer type specified. Briefly, we summarize the process through which cancer cells disseminate from primary tumours, establish the initial foothold that facilitates dormancy, begin proliferation under the influence of the (altering) BME, recruit osteoclasts to trigger a vicious osteolytic cycle and, finally, further metastasize to multiple other organs.

Premetastatic alterations in bone. Breast tumours may systemically affect distant organs even before metastasis occurs[8]. The development of a 'premetastatic niche' was first characterized in lungs and implicated changes in the bone marrow. Specifically, bone marrow-derived VEGFR1$^+$ cells can be mobilized by primary tumours and recruited to the lungs before the arrival of metastatic cancer cells[9]. These cells can prepare the lung tissues and make them more amenable to metastatic seeding. Subsequent studies provided further details of this process and expanded our knowledge of the mechanisms of premetastatic niche development (see, for example, REFS[10–12]). In some cases this niche was shown to suppress, rather than promote, metastatic seeding[13,14]. Overall, these studies also confirmed that the bone marrow acts as a remote responder to primary tumours and as a source of cells recruited to other organs for premetastatic niche formation. However, these studies did not address the questions of how the BME is altered in this process and whether such alterations affect potential metastatic seeding to bone itself.

Independently of the above studies, it has long been observed that breast tumours skew haematopoiesis towards the myeloid lineage with cells of abnormal functionality[15–17]. We and other groups have shown that some breast tumours can induce systemic accumulation of immature myeloid cells that are immunosuppressive, known as myeloid-derived suppressor cells (MDSCs)[18,19]. However, the level of MDSC accumulation varies between different tumours and may be dictated by tumour-intrinsic characteristics such as epithelial-to-mesenchymal transition (EMT) status and levels of mTOR signalling in cancer cells[20,21]. Although the systemic roles of MDSCs in tumour progression have been intensively investigated, their local impact on bone metastasis remains poorly defined.

The rise of bone-tropic metastatic seeds in primary tumours. Before cancer cells embark on the metastatic journey, their fate and destination may already be partly determined. The nonrandom distribution of metastases to specific organs is referred to as metastatic organotropism and is a long-standing clinical observation[22]. The organs frequently affected by breast cancer metastasis include bone, lung, brain and liver. Different breast cancer subtypes exhibit largely different organ preferences: whereas luminal-like tumours (mostly oestrogen receptor positive (ER$^+$)) tend to metastasize first to bone, basal-like tumours (mostly ER$^-$, progesterone receptor negative (PR$^-$) and HER2$^-$, also known as triple negative breast cancer (TNBC)) aggressively disseminate initially to visceral organs, including the lungs[23,24]. Moreover, visceral metastases usually occur within 5 years after surgical removal of primary tumours. By contrast, ER$^+$ bone metastases are often diagnosed after a much longer latency, and the risk of late-onset bone metastases persists for years to decades[25,26]. This inter-subtype discrepancy remains largely unexplained.

Although at a lower frequency than in ER$^+$ breast cancer, bone metastases still occur in TNBC. Our previous work (X.H.-F.Z.) based on experimental metastasis models (TABLE 1; BOX 2) suggests that SRC activity in TNBC cells may be linked to proclivity for bone metastasis mainly through potentiating CXCR4 and/or IGFR–AKT signalling cascades in cancer cells. The bone-specific role of SRC results from abundant expression of the cognate ligands of CXCR4 and IGF1R, which are CXCL12 and IGF1, respectively, secreted by stromal cells in the BME[26]. Interestingly, cancer cells with higher

Box 1 | The multidimensional view of bone microenvironment

Spatial organization of bone

In long bones, osteoclasts, osteoblasts and their precursors are predominantly localized at the surface of cortical bones (termed endosteum) and trabecular bones, which constitute the 'endosteal' or 'osteogenic' niche[1]. Differentiated osteocytes are embedded into the bone matrix. Mesenchymal stem cells (MSCs), the multipotent stem cells of osteoblasts, chondrocytes and adipocytes, are usually found adjacent to blood vessels, in the perivascular niche. Haematopoietic stem cells (HSCs), on the other hand, were found to be in both the osteogenic and perivascular niches[225–227].

The blood capillaries can be divided into two types: H and L. Type H capillaries are localized to metaphyseal regions as well as in parallel with the endosteal surface. By contrast, type L capillaries are mostly within diaphysis and are sinusoidal[228,229].

Furthermore, arteries, arterioles, type H and L capillaries are surrounded by perivascular cells that express different markers[3,230,231]. Besides MSCs, there is a distinct class of perivascular cells in the bone marrow, namely CXCL12-abundant reticular cells[232–234]. Single cell RNA-seq defined subsets of CXCL12-abundant reticular cells with a transcriptomic profile characteristic of osteogenic cells or adipocytes. They preferentially localize to arteriolar and sinusoidal vessels, respectively, and can shape the local microenvironment through cytokine secretion[235].

Although most studies implicate the perivascular niche as the major location of HSCs, there is debate as to whether the adjacent vasculature is arteriolar or sinusoidal[4,226,236]. The endosteal niche was also suggested to host engrafted HSCs[40]. Perivascular and endothelial niches may be physically close to one another and even share some niche components owing to the coupling between angiogenesis and osteogenesis[229]. Furthermore, megakaryocytes may also provide a unique HSC niche and maintain HSC quiescience[237–240].

Temporal dynamics of bone

In addition to the daily production of blood cells by the bone marrow, it is estimated that 5–25% of all skeleton is replenished every year in healthy adults[241] with osteoclasts absorbing old bone and osteoblasts depositing new bone[242]. Pathological conditions can significantly affect bone turnover. For instance, diabetes and obesity both increase resorption of old bones and decrease formation of new bones[243–245]. In particular, bone fracture induces a healing process involving development of haematoma, acute inflammation, resolution of inflammation, formation of soft callus in association with neoangiogenesis, growth of woven bones (newly formed bone) and finally remodelling of woven bones to healed bones[246,247].

Taken together, bone is exquisitely organized and agilely dynamic. Therefore, the bone microenvironment needs to be investigated in a well-defined spatiotemporal context.

Epithelial-to-mesenchymal transition
(EMT). A process through which epithelial cells lose cell–cell adhesions and other epithelial traits but acquire mesenchymal characteristics, including migration and invasion. Recent studies demonstrate that EMT is a continuum and there exists a hybrid status with both epithelial and mesenchymal features. The hybrid EMT phenotype has been linked to cancer stemness, or the ability to regenerate a tumour.

Metastatic organotropism
The observations that metastasis does not occur randomly to all organs but rather preferentially affects a specific set of distant organs.

SRC activity can be enriched in primary tumours by Darwinian selection (the major conceptual framework of our understanding of the metastatic cascade[27]), when there is a similar enrichment of CXCL12 and IGF1 (REF.[28]). Therefore, the mimicry of bone cytokine milieu in the primary tumour may pre-select metastatic seeds that might be 'primed' to survive and grow in the BME.

Cancer cells may also demonstrate 'osteomimicry', which refers to the evolution of cancer cells to exhibit bone-resident cell phenotypes[29,30]. Osteomimicry mostly occurs in cancer cells that have already metastasized to bone, and therefore represents a later step in the journey. Of note, in orthotopic or subcutaneous tumours in mice, ectopic bone tissues were occasionally observed[31], which suggests an osteomimicry-like process in non-bone tissues seemingly independent of the presence of bone metastasis. How such a process in primary tumours relates to later bone metastasis remains unknown. It is reasonable to hypothesize that cancer cells undergoing osteomimicry and thus assuming bone cell phenotypes may confer selective advantages on DTCs and drive bone-tropic metastasis.

Of note, genes and pathways that mediate bone metastasis are not expected to confer selective advantages in primary tumours as the interactions with bone have not yet occurred. The microenvironmental pressure is not yet available at this point to drive bone-tropic genetic selection or reactive adaptation. This is especially true for late-onset bone recurrences, during which metastases must undergo prolonged parallel evolution in bone, thereby allowing them to become distinct from primary tumours. However, resemblance of the microenvironment between primary and metastatic tumours may drive convergent evolution and result in overlapping phenotypic profiles. Therefore, both seed pre-selection and osteomimicry are plausible hypotheses to explain the paradox that bone tropism is predictable in primary tumours (FIG. 1a).

The perivascular niche and metastasis dormancy. The first niche that DTCs encounter upon arrival in the BME may have important roles in determining the subsequent metastatic process. A study in prostate cancer showed that inoculation of cancer cells into peripheral blood induced egress of HSCs from the bone marrow[32], which led to the hypothesis that DTCs and HSCs both share and compete for the same niches. This hypothesis gained support from recent studies in experimental metastasis models (TABLE 1) of breast cancer. Ghajar et al.[33] demonstrated that DTCs (introduced by intra-cardiac injection; see TABLE 1) stay close to blood vessels after extravasation. Moreover, thrombospondin 1 (TSP1) produced by endothelial cells induced dormancy in DTCs. Using the same approach, Price et al.[34] corroborated this conclusion and elucidated that endothelial cell-derived E-selectin and CXCL12 induced the migration of DTCs

Table 1 | **Experimental models of bone metastasis**

Transplantation route	Cancer types	Pros	Cons
Direct injection into circulation (experimental metastasis models)			
Left ventrical[85,214]	Breast, prostate, renal, colorectal, lung, head and neck, multiple myeloma	Non-invasive procedures; cancer cells distributed to multiple bones	Bypasses the early steps of metastasis cascade; introduction of non-bone metastases that often shorten animal survival; high experimental variability; incapable of delineating further metastasis from bone
Tibia or femur bones[215]	Breast, prostate, renal, colorectal, lung, head and neck, multiple myeloma	Robust delivery of cancer cells; restriction of cancers relatively specifically to tibia or femur bones	Bypasses the early steps of metastasis cascade; highly invasive procedures that introduce confounding tissue injuries; many cancer cells escape to veins
Illiac artery[42,216]	Breast and prostate	Precise delivery of cancer cells to one hindlimb; amenable to quantitative studies of early-stage bone colonization events; amenable to tracking further dissemination from the hindlimb to other organs including the contralateral hindlimb	Bypasses the early steps of metastasis cascade; difficult to learn; low throughput
Caudal artery[217]	Breast, prostate, renal, lung, osteosarcoma	Precise delivery of cancer cells to both hindlimbs; amenable to quantitative studies of early-stage bone colonization events; easy to learn	Bypasses the early steps of metastasis cascade
Orthotopic injection (spontaneous metastasis)			
Mammary fat pad[218]	Breast	Complete metastasis cascade	Extremely high experimental variability; nonsynchronous metastasis — difficult to delineate and quantitatively study different temporal steps in metastasis; animals often die of metastases in other organs before bone metasases fully develop; difficult to track further metastasis from bone
Nipple[219]	Breast		
Prostate[220]	Prostate		
Renal capsule[221]	Renal		
Rectal[222]	Colorectal		
Lung[223,224]	Lung		
Perimaxillary gingival submucosa	Head and neck		

Box 2 | **Limitations of current models will need to be overcome with innovation of new models**

Immunocompetent versus immunocompromised models
Findings in the current literature are predominantly based on transplantation of human cell lines into immunocompromised hosts, which severely limits our ability to investigate the roles of immune cells in bone colonization. Only a couple of available murine cell lines spontaneously metastasize to bones, AT3 (REF.[78]) and 4T1.2 (REF.[248]). Considering the unique immune milieu provided by the bone marrow, it is imperative to develop more syngeneic models to allow systematic characterization of the mutual impact of cancer cells and the bone microenvironment (BME). This need is especially urgent for certain tumour types or subtypes exhibiting stronger bone tropism, for example, prostate cancer and ER^+ breast cancer.

Patient-derived xenograft versus cell lines
Cell lines maintained in culture are subject to artificial selective pressures and may genetically drift to lose pathologically relevant heterogeneity. Patient-derived xenografts (PDXs) can overcome this caveat to some extent[249]. A challenge for establishing PDX models of bone metastasis, aside from the rareness of metastatic tissues, is the need for orthotopic transplantation, which in this case is to bone rather than breast. This is presumably important for the maintenance of the crucial cancer–microenvironment interaction[250]. A robust and efficient pipeline will need to be developed towards this end in future research.

In vivo versus ex vivo models
The BME can be partially recapitulated ex vivo. In the simplest case, osteogenic cells can be co-cultured with cancer cells in 3D suspension medium[42]. Interestingly, this admixture forms heterotypic organoids with the two cell types either well intermixed or organized into a shell–core structure. Cell–cell interactions can be dissected using the 3D organoids. Bone fragments can also be used ex vivo to host cancer cells[192]. When seeded to appropriate scaffolds and stimulated by specific cytokines, osteocytes can differentiate into osteoblasts and become minimized to mimic the BME[48,251,252], which can provide cancer cells with a representative environment. The ideal ex vivo models will need to be scalable and inclusive of major bone and bone marrow components, including the mesenchymal lineage, haematopoietic lineage and endothelial cells. Compared with in vivo models, the ex vivo platforms are more amenable to molecular manipulation and high-throughput screening. Importantly, the ex vivo setting will also allow use of human cells so that cancer–niche interactions can be studied in a human–human setting.

towards the endosteal surface and the retention of DTCs at the perivascular niche, respectively. More recently, it was suggested that the perivascular niche renders cancer cells resistant to chemotherapies through integrin signalling[35]. Furthermore, perivascular $NG2^+$ cells were also shown to reinforce dormancy through secretion of TGFβ2 (REF.[36]). Taken together, it has become increasingly clear that the perivascular niche is the first foothold of DTCs in the bone marrow and has an important role in determining cancer cell fate (FIG. 1b).

Much remains to be discovered about cancer cell dormancy and the perivascular niche. Additional pathways in cancer cells may induce dormancy, including those involving LIFR and MSK1 through regulating STAT3 activities and cell differentiation status, respectively[37,38]. Blood vessels and perivascular cells are highly heterogeneous in the bone marrow as previously discussed. It will be important to determine what specific type of blood vessels (that is, arteriolar, type H capillaries or type L capillaries) preferentially constitute the niche of dormancy (FIG. 1b). This information may reconcile the seemingly conflicting finding that vascular E-selectin stimulates mesenchymal-to-epithelial transition and promotes proliferation of DTCs through WNT signalling[39]. Thus, the understanding of cancer–niche interactions will likely benefit from a deeper and more precise characterization of the normal bone marrow microenvironment.

The osteogenic niche and metastasis outgrowth. In addition to the perivascular niche, other microenvironment niches may also regulate the fate of DTCs. The endosteal surface of cortical bones and the surface of trabecular bones harbour osteoblasts and represent sources of new bone. This region is termed the 'endosteal' niche and also hosts HSCs and other haematopoietic progenitor cells[40,41]. We (X.H.-F.Z.) and others observed that bone micrometastases (BMMs) are usually in close contact with cells that have osteogenic potential, including MSCs, osteoprogenitors, pre-osteoblasts and osteoblasts, but not osteoclasts[42–44]. Thus, we used the term the 'osteogenic niche' in this Review to collectively refer to these cell types. Using the intra-iliac injection-based experimental metastasis model (TABLE 1), we (X.H.-F.Z.) showed that the cancer–osteogenic niche interaction was mediated by heterotypic adherens and gap junctions and stimulated multiple pathways inside BMMs, including mTOR and calcium signalling, which can drive proliferation of cancer cells[42,43,45] (FIG. 1c,d). Also, osteoblast-produced cytokines (for example, FGF2 and PDGF-DD) can induce epigenomic reprogramming via activation of EZH2, which in turn confers stemness on BMMs in the context of ER^+ breast cancer xenograft models. Here, epigenetic changes were in part reflected by a transient and reversible loss of ER expression and the emergence of a hybrid EMT phenotype, particularly in cancer cells that directly interact with the osteogenic cells[46] (FIG. 1c,d). Multiple other crosstalk mechanisms between cancer cells and osteogenic cells were discovered, including tumour-derived JAGGED1-induced Notch signalling in osteoblasts, which activated production of TGFβ and led to activation of osteoclasts (see later sections for more discussions)[47]. Interestingly, activation of the Notch pathway in cancer cells conferred resistance of experimental bone metastasis to chemotherapies in multiple xenograft models[43] (FIG. 1c). In addition, in an MSC-derived ex vivo model (TABLE 1; BOX 2), MSCs produced tenascin (TNC) upon interaction with cancer cells[48]. TNC is a well-described stem cell niche component[49] that signals through integrins to promote tumour progression[48,50]. Taken together, it has become increasingly clear that the osteogenic niche may foster metastasis outgrowth, which represents one mechanism for activation of proliferation or the termination of dormancy (FIG. 1d).

Many aspects of the osteogenic niche need to be better understood. Conditioned medium of breast cancer-educated osteoblasts was shown to suppress tumour growth and osteoclastogenesis in vitro[51], suggesting that the secretome of osteoblasts in culture produces the opposite effect to the observations in vivo discussed above. Moreover, in MM bone metastasis, the osteogenic niche was shown to induce dormancy instead of terminating it[52]. Again, these seemingly conflicting observations may be explained by differences in experimental models and/or the diversity of bone niches and the exquisite spatiotemporal arrangement of the BME. In this regard, accurately mapping cancer–niche

Darwinian selection
A process of evolution whereby individuals with greatest fitness among a population survive the selective pressure exerted by the environment. In cancer biology, it was adopted to understand how cancer cells with the most enabling genetic traits progress and expand over other cancer cells under the selective pressure from the microenvironment.

Perivascular niche
The microenvironmental location adjacent to a blood vessel. The components include endothelial cells, pericytes and haematopoietic stem cells. The pericytes exhibit mesenchymal stem cell activities.

Osteogenic niche
The microenvironmental locations including endosteum and trabecular bones, where osteogenesis occurs. It is enriched with osteoblasts and precursor cells. It overlaps with the endosteal niche, but also includes trabecular bones while lacking the osteoclast component by definition.

Phenotypic plasticity
The potential of a cell to alter its phenotypic characteristics in response to environmental stimuli. The ability to switch between epithelial and mesenchymal phenotypes is considered one example of phenotypic plasticity.

interactions to a single-cell resolution will significantly benefit bone metastasis research.

The vicious cycle and osteolytic bone metastasis. The hallmark of overt bone metastasis in breast cancer is the recruitment and activation of osteoclasts through paracrine relay between cancer cells and osteoblasts. Specifically, cancer cells can produce PTHrP, which induces osteoblasts to secrete RANKL[53,54]. The RANKL–RANK pathway is a master regulator of osteoclastogenesis[55]. Resorption of bone matrix by osteoclasts leads to the release of TGFβ and IGFs, which reciprocally act on cancer cells to stimulate further progression[56–58]. Altogether, these processes form an osteolytic vicious cycle (FIG. 1e). Many recently discovered pathways converge to regulate this cycle and promote bone metastasis, including VCAM1 (REF.[59]) generated by tumours, which recruits osteoclasts; integrin signalling activated in cancer cells[60]; RON signalling activated by MSP in both cancer cells[61] and osteoclasts[62]; Notch signalling activated mutually between cancer cells[47] and osteoblasts[43]; and IL-6 released by osteoblasts or senescent stromal cells that activates osteoclasts[47,63]. The osteolysis caused by metastasis leads to skeletal related events (SREs), including bone pain, spinal cord compression, hypercalcaemia and pathological fractures. Therapies that target osteoclasts significantly improve patient quality of life, thereby confirming the vicious cycle as a paradigm of late-stage bone metastasis[64] (FIG. 1e,f). The molecular details of this paradigm have been increasingly elucidated in the past few decades and have been summarized by excellent recent reviews[65,66].

Further dissemination from bone to other organs. Establishment of bone metastasis may not be the final step of the journey. In recent studies collectively surveying more than 4,000 patients with breast cancer, the first metastasis diagnosed was found in a single organ rather than multiple organs in 74% of patients[23,24,67]. However, although breast cancers of patients with different subtypes exhibit distinct metastatic distributions[23,24], autopsies of patients with breast cancer revealed a high percentage of metastases in multiple organs[68–70]. In fact, only 6% of patients had single-organ metastases[68], which led to the previous conclusion that "breast cancer was nonselective in its metastatic targets"[69]. These seemingly contradictory observations may be reconciled by the function of the BME in invigorating a second wave of metastasis with reduced organotropism (FIG. 1f).

The notion that cancer cells in bone can further disseminate has been indirectly suggested by a few observations. First, the presence of DTCs in the bone marrow of patients with breast cancer was associated with recurrences that are not restricted to bone[71,72]. Second, roughly two-thirds of patients with bone-only metastases later developed other metastases[73,74]. Third, in patients who are postmenopausal, adjuvant treatment with bisphosphonate, a bone-targeting agent, was associated with a reduction of all distant metastases and improved overall survival[75], especially in DTC$^+$ patients[76,77]. Although each of these observations could have an alternative explanation (for example, bisphosphonates might have direct inhibitory effects on metastatic cells in other organs), they collectively suggest that DTC and bone metastasis are tightly associated with metastases in other organs, and therefore, might be the source of further dissemination.

We recently demonstrated that the interaction with osteogenic cells can invigorate cancer cells for further dissemination[78] Breast cancer-derived circulating tumour cells (CTCs) in bone metastasis-carrying animals exhibited a stronger stem cell-like phenotype than those in mice with orthotopic breast tumours or lung metastases. An evolving barcode system[79,80] was used to delineate the phylogenetic relationship between spontaneous metastatic lesions in various organs, showing that at least a proportion of metastases in visceral organs were closely related to bone metastases[78]. Mechanistically, the BME induced transient epigenomic reprogramming driven by EZH2 and increased phenotypic plasticity of BMMs compared with primary tumours and macrometastases in breast cancer models[46]. Remarkably, inducible knockdown of EZH2 in cancer cells did not alter the growth of the initial bone metastasis but abolished further metastasis from bone[78]. Together, this suggests that bone can serve as a robust 'launch pad' for secondary metastasis, as opposed to a terminal destination, in the metastatic cascade (FIG. 1g,h).

Of note, further metastasis from bone is a different process from tumour self-seeding or cross-seeding. Self-seeding refers to the observation that CTCs may return to seed their tumours of origin, whereas during cross-seeding, CTCs infiltrate other pre-existing tumours in the same host[81]. By contrast, bone metastases provide an environment that enables cancer cells to seed other organs and establish secondary metastases de novo.

The specific epigenomic reprogramming process behind secondary metastasis from bone appears fundamentally different from the Darwinian selection known to drive tumour progression. The latter usually operates on stable genetic traits and results in irreversible changes in tumour clonal structures[82]. By contrast, the reprogramming induced by BME appears to be transient and reversible as shown using experimental bone metastasis models of ER$^+$ breast cancer[46]. Numerous previous studies, including many referenced earlier in this Review, suggested that Darwinian selection is the basis of organotropic metastasis[26,28,83–85]. This concept may be accurate for the first wave of metastasis directly from primary tumours. However, in recent studies we demonstrated a fundamentally different metastasis process from bone[46,78]. Specifically, mice carrying established bone lesions of breast and prostate cancers subsequently developed further metastases in multiple organs. Interaction with the BME enabled multi-organ metastasis of cells that were initially non-metastatic and genetically homogeneous (immediately expanded from a single cell), thereby ruling out Darwinian selection as the major driving mechanism. An evolving barcode system facilitates the dissection of metastatic evolution and supports that many metastases in non-bone organs may result from further spread of spontaneous bone metastases. Significantly, targeting EZH2,

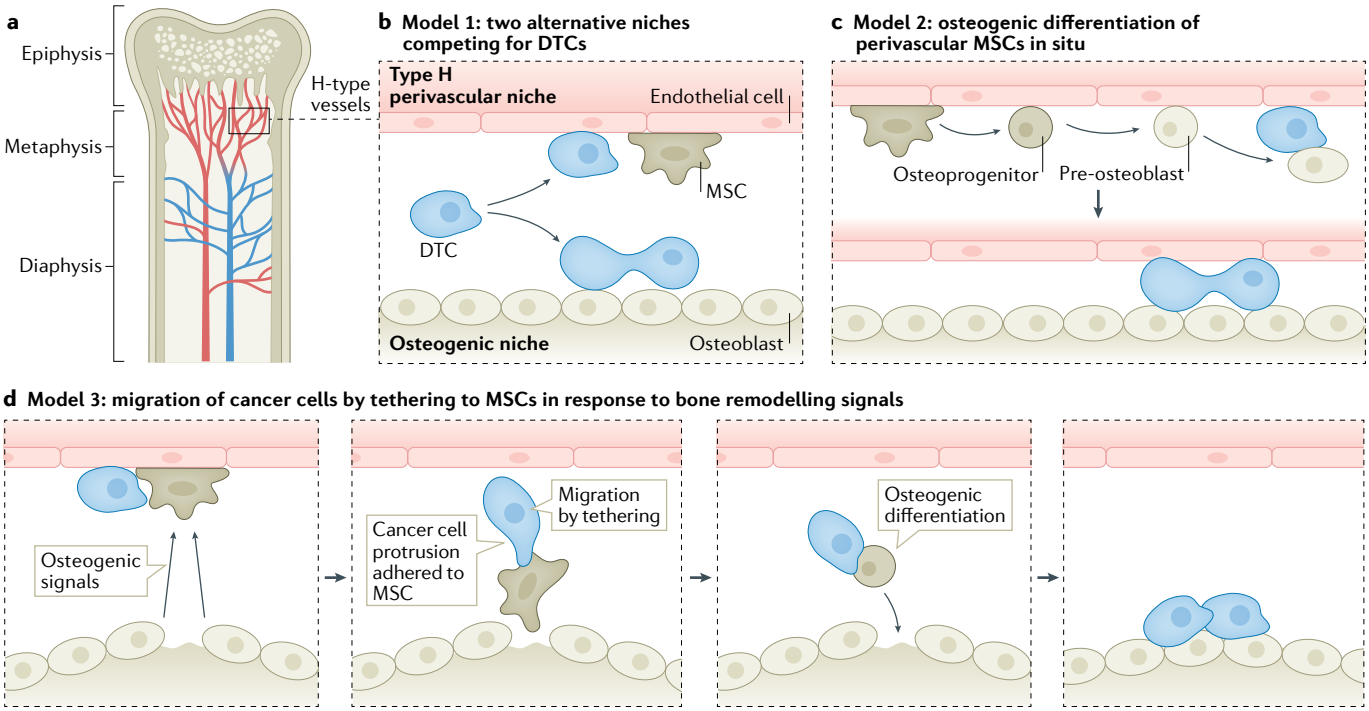

Fig. 2 | **The possible relationship between different microenvironment niches during early-stage bone metastasis. a** | The vascular network in the bone marrow is in close proximity to trabecular bones and endosteum, where osteogenic cells localize. The perivascular niche and osteogenic niche may have a few possible relationships during bone metastasis. **b** | Model 1: the two niches may compete for disseminated tumour cells (DTCs). DTCs localize to the perivascular niche and osteogenic niche, after which they may enter dormancy or begin proliferation, respectively. **c** | Model 2: the perivascular mesenchymal cells of type H vessels possess mesenchymal stem cell (MSC) activities and may differentiate into osteogenic cells. Therefore, in situ differentiation may create a new osteogenic niche adjacent to the perivascular niche, and may terminate dormancy and trigger proliferation of cancer cells. **d** | Model 3: dormant DTCs and quiescent MSCs colocalize in the perivascular niche. Bone homeostasis or pathological bone injuries release osteogenic signals to mobilize MSCs. Cancer cells may form specialized protrusions to attach to MSCs that are undergoing chemotaxis towards the source of osteogenic signals. Upon arrival, the MSCs differentiate into osteoblasts. The associated cancer cells remain in the newly formed osteogenic niche and begin proliferation.

an epigenomic modifying enzyme, in cancer cells abolished the secondary metastasis from bone. Together, these findings suggest that the adaptive epigenomic alterations induced in metastatic cancer cells in the bone marrow may enable the second wave of metastasis with reduced organotropism as compared with the first wave. Taken together, coordination of genetic and epigenetic mechanisms may provide a more complete view of the metastatic cascade from localized primary tumours to terminal-stage multi-organ metastases and may also reconcile two seemingly contradictory observations in breast cancer care: strong organotropism of first-site metastasis[23,24] versus multi-organ distribution of metastases towards the terminal stage of diseases[68–70].

Missing links in the journey. Our knowledge of the bone metastasis journey is far from complete. A few key questions need to be addressed to strengthen our understanding of the spatiotemporal evolution of breast cancer cells in bone.

First, the relationship between different microenvironment niches needs to be better defined. In particular, the perivascular and osteogenic niches both harbour cancer cells, raising the question of how these niches are related to one another. There is considerable evidence suggesting that they enforce different cellular fates of cancer cells (FIG. 2a,b). In particular, the perivascular and osteogenic niches seem to be associated with cellular quiescence and proliferation, respectively, in breast cancer models[33,34,42,45]. However, there is a lack of consensus as to the general roles of these niches in dormancy in different cancer types. For instance, when murine and human MM cells were intravenously transplanted into mice, osteoblasts in the osteogenic niche were observed to turn on the dormancy programme, whereas osteoclast activity could wake the dormant cells[52,86]. Thus, the exact roles of different niches may be cancer type specific. A further question is whether these different types of niche may be interconvertible. For instance, the perivascular MSCs may undergo osteogenic differentiation[87,88], thereby creating an adjacent osteogenic niche and altering DTC fate[42,45] (FIG. 2c). In the case of breast cancer, the generation of a new osteogenic niche from perivascular MSCs may terminate DTC dormancy and initiate metastatic colonization[42,45]. Finally, DTC fate may be altered through DTC relocation from one type of niche to another. In breast cancer mouse models, perivascular MSCs colocalized with dormant DTCs[36]. These MSCs may be activated by osteogenic signals released from sites of bone turnover or injury and migrate to the site through chemotaxis[36]. Indeed, DTCs can form unique protrusions that tether to the migrating MSCs[89].

This co-migration mechanism may allow DTCs to relocate from the perivascular niche to the osteogenic niche (FIG. 2d). Taken together, the dynamics of various types of niche may profoundly affect the course of bone colonization. The application of high-resolution, spatiotemporal mapping of cancer–niche interactions will help to distinguish the above-mentioned possibilities and reconcile many seemingly contradictory observations.

Second, the transition from asymptomatic to osteolytic bone metastasis needs to be characterized. In breast cancer, bone metastasis often occurs late, as long as years to even decades after primary tumour removal[25]. The prolonged asymptomatic phase is poorly understood. This phase likely occurs before the vicious cycle, which would otherwise lead to severe symptoms. We know very little about the initiation of the vicious cycle. It has been suggested that cancer cells can produce the soluble form of VCAM1, thereby recruiting osteoclast progenitors[59]. Interestingly, *VCAM1* is a target gene of HIF1α in endothelial cells[90]. Thus, the accumulation of tumour mass in asymptomatic metastasis may exacerbate hypoxia and activate HIF1α–VCAM1 signalling[90]. Whether this signalling axis in cancer cells and/or endothelial cells contributes to the initiation of the vicious cycle will need to be tested in future investigations. In general, onset of the vicious cycle may represent termination of dormancy. Therefore, any physiological or pathological cues that induce osteoclastogenesis could potentially awaken dormant cancer cells. These cues and their underlying molecular mechanisms need to be identified and therapeutically targeted.

Finally, the observation of further dissemination of bone metastases raises many questions. Among these, the timing of dissemination may be the most urgent to address. Hypothetically, dissemination could occur early, when source bone metastases are still microscopic. As a result, metastases diagnosed in other organs may be seeded from bone rather than from the primary tumour even if there are no overt bone metastases. Related to this point, our data suggest that the size of metastases does not necessarily correlate with their position in the phylogenetic hierarchy as indicated by evolving barcodes[78]. This is consistent with the notion that small bone lesions may already begin to spur metastatic seeds to other organs. One provocative little-understood association is the relationship between dormancy and the second wave of metastasis. Like HSCs, cancer cells with stem cell properties are often more quiescent but persistent[91]. Although requiring further validation, it is conceivable that interaction with the BME may confer stemness on DTCs[46,78,92], which may be accompanied by dormancy. Thus, the potential for further metastasis may be harboured in cancer cells that appear indolent. Further studies will be needed to reveal the trigger for further dissemination and to determine how this event is related to the initiation of local bone colonization. It also remains unclear whether the ability to empower further metastasis is unique to bone. Recent genomic analyses revealed frequent metastasis-to-metastasis seeding[93,94]. Future studies and analyses with deeper sequencing and larger sample size may help to elucidate preferred sources of metastatic seeds.

Osteogenesis
The process of osteoblast and osteocyte differentiation and formation of new bones.

Bone metastasis of different cancer types

In what follows, we summarize the bone metastatic cascade for prostate cancer, kidney cancer and MM. These cancers were selected to highlight significant mechanistic and/or phenotypic differences. The role of bone-specific adaptation is suggested by cancer type-specific differences in phenotypes of bone metastases (osteolytic, osteoblastic or mixed) and, as more recently observed, differences in resistance mechanisms to bone-targeted therapies. Prostate cancer is included because of its propensity for creating sclerotic metastases. MM, as a marrow-based malignancy, introduces unique immunological factors, although sharing features with kidney cancer in creating almost exclusively osteolytic bone metastases.

Prostate cancer. Prostate cancer metastasizes predominantly to bone usually after the development of castration resistance[95]. Bone metastases of prostate cancer have many commonalities with those of breast cancer, including clinical treatments[95] and key roles of certain molecular pathways (for example, TGFβ and IGF1)[96–98] (FIG. 3a). This is largely because the vicious cycle between osteoclasts and prostate cancer cells, similar to breast cancer cells, is a major driver of bone colonization[56]. Moreover, we recently showed that disseminated prostate cancer cells, like breast cancer cells, adhere to osteogenic cells and form heterotypic gap junctions when inoculated into bone in mice. Interaction with the BME similarly invigorated further metastasis to multiple organs[78]. Despite these shared properties, bone metastases of prostate cancer are predominantly osteosclerotic, with excessive bone formation outperforming the excessive bone resorption[99,100]. Although our knowledge is still scarce, a few aspects of prostate cancer biology have been uncovered to explain this uniqueness.

After prostate cancer cells reach the BME, they increasingly exhibit properties of osteoblasts, including the secretion of osteoblast-characteristic molecules such as alkaline phosphatase, osteocalcin, osteopontin and bone morphogenetic proteins (BMPs)[101,102]. The acquisition of these properties is referred to as 'osteomimicry' and is often stimulated by osteoblasts. Osteomimicry of prostate cancer can be driven by cancer cell expression of RUNX2, a transcription factor that regulates osteoblast differentiation[103]. RUNX2 expression is negatively regulated by the PTEN–FOXO1 signalling axis[104,105]. In addition, prostate cancer cells in the BME express cytokines, including WNTs[106], PTHrP[107], ET1 (REF.[108]) and FGFs[109], which are known to favour osteoblast proliferation and differentiation (FIG. 3b). In particular, the WNT pathway has important roles in regulating osteoblast differentiation and function[110]. Prostate cancer cells can secrete WNT ligands to induce osteogenesis[106] and may also activate intrinsic WNT signalling to promote invasion[111]. Thus, prostate cancer cells 'blend' into the osteogenic environment, and seem to evolve to reinforce and benefit from this environment. It was also recently shown in the C4-2B cell-based intrafemoral injection model (TABLE 1; BOX 2) that prostate cancer cells can stimulate osteogenesis in vivo by secreting BMP4, which induces endothelial cells to become osteoblasts[112].

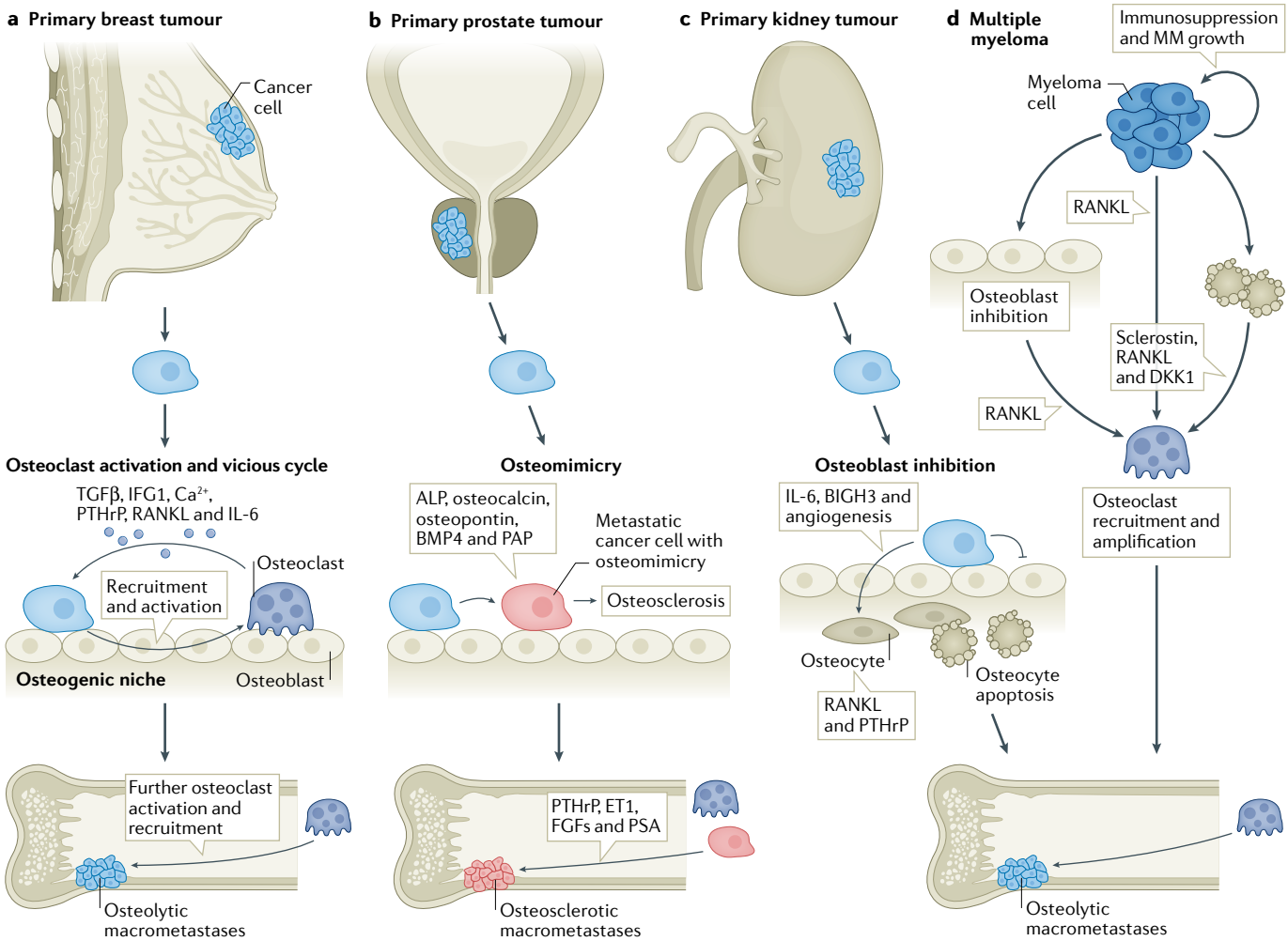

Fig. 3 | **The relationship between primary tumour and the vicious cycle of late-stage bone metastasis in various cancer types. a** | For breast cancer, disseminated tumour cells (DTCs) awaken from dormancy to create osteolytic macrometatases by both paracrine and heterotypic heterotypic adherens junction and gap junction interactions in the osteogenic niche, which directly and indirectly stimulate osteoclast recruitment and activation. Osteoclast activity, in turn, releases TGFβ, IGF1, Ca^{2+} and other growth factors from bone that further stimulate tumour proliferation. This is the classic 'vicious cycle'. **b** | For prostate cancer, osteomimicry of DTCs in the osteogenic niche harnesses both the anabolic and lytic components of normal bone homeostasis, leading to osteolysis (PSA) and/or osteosclerosis (PAP). Tumour cells induce osteosclerosis via secretion of osteogenic factors such as ALP, osteocalcin, osteopontin and bone morphogenic protein 4 (BMP4). Osteolysis is induced via secretion of PTHrP, ET1 and IGF1. This global alteration towards bone-like phenotypes may be driven by RUNX2. The underlying genomics of osteomimicry and why it is not as predominant in other tumour types are not known. **c** | For kidney cancer, the road to bone destruction is more indirect than for breast or prostate cancer, and resembles that for multiple myeloma (MM). DTCs create a vicious cycle via paracrine inhibition of osteoblast function and osteocyte apoptosis. Consequently, the adverse impact on the anabolic component of the osteogenic niche creates an environment that increases the RANKL to OPG ratio, promoting osteoclast recruitment and activity that creates predominantly lytic macrometastases. The details of interactions in the perivascular and osteogenic niches are likely tightly linked, as neovascular induction is a prominent component of kidney cancer bone metastasis. **d** | MM is almost exclusively bone organotropic. Interactions in the osteogenic niche are driven by crosstalk between MM cells and osteocytes, osteoblasts and osteoclasts. Osteolysis is induced via secretion of RANKL by MM cells, and amplified by RANKL from apoptotic osteocytes and inhibited osteoblasts. Immunosuppression enabling MM proliferation and progression is provoked by immune dysregulation, influencing T cell immunity, natural killer cell function and the antigen-presenting capacity of dendritic cells; and via myeloid derived suppressor cell amplification by osteoclasts. DKK1, Dickkopf-related protein 1.

Reciprocally, a recent study has shown that calvariae of newborn mice (enriched with osteoblasts) can secrete into conditioned medium multiple dormancy-inducing factors that employ distinct signalling pathways in prostate cancer cells, including the p38 MAPK signalling pathway[113]. What remains to be elucidated, however, is how the osteogenic transcriptional programme is activated inside prostate cancer cells in the bone milieu, whether driven by genetic selection or epigenetic adaptation. Similarly notable is why the osteomimicry phenomenon is so pronounced in prostate cancer and whether this phenomenon may underlie the strong bone tropism of prostate cancer metastasis. Further research will be required to address these questions.

Compared with other cancer types, prostate cancer cells uniquely express several genes such as those encoding prostate-specific antigen (PSA) and prostatic acid phosphatase (PAP). PSA has been widely used as a biomarker to monitor tumour burden in patients[114]. Interestingly, PSA is a serine protease. Its activities lead

to activation of PTHrP[115], TGFβ[116] and IGF1 (REF.[117]), all of which have important roles in driving the osteolytic vicious cycle. Conversely, PAP stimulates osteoblast differentiation, increases collagen synthesis and enhances expression of ALP[118,119]. The coordinated action of these prostate-specific enzymes may further enhance abnormal osteogenesis and lead to osteomimicry (FIG. 3b).

Kidney cancer. Renal cell carcinoma bone metastases (RCCBMs) have unique phenotypic aspects that distinguish them from bone metastases of breast and prostate cancer. Bone metastases from kidney cancer are almost exclusively osteolytic[120–123]. Our knowledge of the premetastatic niche that leads to this phenotype is more limited than with breast and prostate cancer and is the focus of current work by our group and others[124–127]. Moreover, little is understood about dormancy and the relative influences of the perivascular versus osteogenic niches on metastatic progression. The interactions between kidney cancer and bone-resident cells during the end stage of the vicious cycle promote bone destruction that is more resistant to treatment with bone-targeting agents, such as bisphosphonates and denosumab[120,128,129]. Whether this resistance results from Darwinian selection and/or epigenomic reprogramming is unknown. Defining interactions between kidney cancer and the microenvironment will be important for identifying targeted therapeutic strategies that are more effective.

Similar to other cancers, kidney cancers express high levels of cadherin 11 and CXCR4, which confer a predisposition for homing to the osteogenic niche[130–132]. However, it is unclear whether disseminated kidney cancer cells form heterotypic adherens junctions and/or heterotypic gap junctions with osteogenic cells, as is seen in breast cancer[45]. Interestingly, the pathological mechanism emerging for kidney cancer (FIG. 3c) appears to share more commonalities with MM, in which osteocyte apoptosis and osteoblast inhibition have been observed in patients with lytic bone lesions[133–135]. The kidney cancer vicious cycle in bone appears to be driven by interactions between kidney cancer cells and osteoblasts as well as osteocytes, instead of osteoclasts[124] (FIG. 3c). In the course of investigating these unique aspects of kidney cancer bone metastasis progression, our group (R.L.S.) showed that cabozantinib, which has osteoanabolic activity, reversed osteoblast inhibition and reduced SREs in a preclinical model[136]. This mechanism is consistent with clinical observations of improved survival in patients with kidney cancer and bone metastases treated with cabozantinib[137–139]. There are likely to be new treatment strategies discovered as the kidney cancer vicious cycle in the osteogenic niche is further defined.

Recent findings point to the osteogenic niche as an essential driver of treatment-resistant bone destruction in RCC. Both preclinical studies and patient samples have demonstrated increased osteocyte apoptosis (R.L.S. unpublished data) near lytic bone lesions promoted by tumour secretion of BIGH3, a TGFβ-induced protein[124]. Until recently, BIGH3 was mostly known for causing apoptosis in human retinal pericytes[140] and for being downregulated in melorheostosis[141], a rare bone disease characterized by linear hyperostosis (excessive osteogenesis). BIGH3 is not structurally related to the TGFβ family, and is known to bind to integrins and other extracellular matrix proteins in the BME that mediate cell adhesion and migration[142]. BIGH3 is upregulated in kidney and colorectal cancer cells[143]. In addition, BIGH3 inhibits differentiation of mature osteoblasts in vitro and in vivo[144]. In normal bone biology, an osteolytic response is counterbalanced by bone formation[110,145]. Pathological osteolysis is thus promoted by impaired bone formation. In MM, inhibition of bone formation by Dickkopf-related protein 1 (DKK1) secreted by myeloma cells in the BME was found to contribute to induced osteolysis[146]. Studies by our group have highlighted the pro-osteolytic properties of BIGH3 in RCCBM. BIGH3 and IL-6 (similarly to breast cancer) secreted from tumour cells both inhibit osteoblast differentiation, thereby reducing anabolic activity and the healing of osteolytic lesions, and induce osteocyte apoptosis, creating a premetastatic niche that is pro-osteolytic and potentially associated with increased disease burden[131,136]. The osteolytic environment is further promoted by secretion of RANKL and PTHrP by both invading tumour cells and apoptotic osteocytes[131] (FIG. 3c).

In the perivascular niche, kidney cancer cells are likely spurred towards other organs. Metastatic kidney cancer cells express high levels of CXCR4, a chemokine receptor, indicative of an affinity for the perivascular niche and bone marrow space[147–149]. And although events are not well characterized, the response is a defining characteristic of metastatic disease. Kidney cancer metastases in most organs are hypervascular, thereby inducing an angiogenic response during progression[150,151]. For bone, this angiogenesis appears to be essential for tumour growth. Indeed, treatments that target neovascularization, such as embolization, are frequently used in conjunction with surgical intervention[123,152]. In patients, hypervascularity has been attributed to a common mutation in the gene encoding the von Hippel–Lindau (VHL) E3 ubiquitin ligase, which normally interacts with and targets HIF1α for proteasomal degradation[153]. Mutation in the VHL tumour suppressor gene leads to the stabilization of HIF1α and initiates gene transcription of its target genes, leading to upregulation of several angiogenic factors and growth factors[154,155]. Angiogenic factors that are highly expressed by kidney cancer bone metastases include HIF1α, VEGF and angiopoietin 1 (REFS[122,131,156–158]). The impact of VHL–HIF signalling is not restricted to the initial tumorigenesis, but gets expanded to drive further metastasis via epigenetic mechanisms[159]. Further research is needed to determine the role of the neovascular response in awakening dormant kidney cancer cells and/or promoting their propagation to other distant organs.

Multiple myeloma. MM causes almost exclusively osteolytic lesions that frequently lead to SREs such as pathological fractures, spinal cord compression and the need for radiotherapeutic or surgical intervention[135]. The hallmarks of MM bone disease include both homotypic and heterotypic interactions in the BME that promote bone

Cabozantinib
A small-molecule inhibitor of the tyrosine kinases Met, VEGFR2, AXL and RET. It is approved to treat medullary thyroid cancer, renal cell carcinoma and hepatocellular carcinoma.

Embolization
Blockade of blood vessels by an agglomeration of cancer cells or other substance.

destruction by dysregulating the normal homeostatic balance[160,161]. Exclusive bone organotropism distinguishes MM, with both regional and vascular spread to other bones, but rarely to other organs. Further elucidation of the bone specificity of MM will help in understanding why MM differs in secondary organotropism from other tumours, such as breast cancer, that produce a second wave of metastasis to other organs from bone.

Like kidney cancer cells (FIG. 3d), myeloma cells are able to suppress osteoblast function and induce osteocyte apoptosis[133,135]. During the progression of MM, osteocytes directly interact with MM cells that adhere to cells in the osteogenic niche via the VLA4–VCAM1 integrin system[135,160]. Such interactions stimulate osteocytes to produce sclerostin, DKK1 and RANKL[160]. This stimulates the recruitment of osteoclast precursors and decreases WNT signalling, thereby leading to the inhibition of osteoblast differentiation[134]. Sclerostin is a protein secreted by osteocytes that impedes activation of the canonical WNT pathway, inhibits osteoblast differentiation and mineralization, and induces osteoblast apoptosis[162]. Direct interactions with myeloma cells also induce osteocyte apoptosis, leading to the creation of a premetastatic niche for myeloma cells[134,162]. This has been demonstrated in patients with MM who have reduced numbers of viable osteocytes and suppressed osteoblast activity[133,135]. In addition, other factors such as BIGH3 and its transactivator, KLF10 (Kruppel-like transcriptional factor induced by TGFβ), which are overexpressed in the BME in RCC[143], are less well studied in the BME with MM. Most evidence indicates that KLF10 is a tumour suppressor in MM and is downregulated in both MM cell lines and patient samples[163]. Overexpression of KLF10 causes myeloma apoptosis via the β-catenin pathway[163]. Further work is needed to identify whether KLF10 and BIGH3 are significant factors in osteolysis induced by MM.

A multilayered pathophysiological mechanism creates the characteristic destructive bone process. Notch signalling is induced by myeloma cells, which express Notch family and Jagged[135] ligands in their membranes. The resulting pathway activation increases RANKL production by myeloma cells[164]. In addition, osteocyte and osteoblast production of RANKL amplifies osteoclast activity and synergizes with osteoblast inhibition. MM cells also induce release of pro-osteoclastogenic factors, including IL-6 (REF.[135]), IL-11 (REF.[162]), activan A[165] and MIP1α[166]. Overall, crosstalk between the bone-resident cells and myeloma cells, driven by bidirectional Notch signalling, promotes bone deconstruction and MM proliferation.

Because MM is not a solid tumour and arises in the bone marrow as a malignancy from cells of immune origin, it has unique immunological properties that distinguish its progression. Immunosuppression in the BME contributes to MM growth[161,167]. In the presence of MM, the BME is altered from the interplay between MM cells, mature osteoblasts and osteoclasts[52,86]. Interactions with osteoclasts potentiate immune dysregulation, influencing T cell immunity, natural killer cell function and the antigen-presenting capacity of dendritic cells[168]. Osteoclasts promote the expansion of T helper 17 (T_H17) lymphocytes and MDSCs, thereby inhibiting cytotoxic T and natural killer cells that target MM cells[161]. Taken together, there is a loss of tumour-specific lymphocytes ($CD4^+$ T helper cells and $CD8^+$ cytotoxic T cells) and a rise in immune suppressor cells in the MM cell-containing BME. As a consequence, osteolytic lesions that arise in MM are treated with strategies that differ from those used in kidney cancer and other solid tumours, in that treatment options include immunotherapy that enhances the host anti-myeloma immunity[169,170]. In the past 5–10 years, treatment options introduced include immunomodulatory agents, proteasome inhibitors, duratumumab (an anti-CD38 antibody), newer generations of monoclonal antibodies and CAR (chimeric antigen receptor)-T cells. The result has been substantial, with a near doubling of the 5-year relative survival range in the past 20 years (increased from 32% in 1996 to 55% in 2016)[171,172].

New therapeutic targets

Bone-targeting therapies, such as bisphosphonates, were introduced in the late 1990s for the purpose of improving clinical outcomes for patients with metastatic bone disease. Their effectiveness is related to their ability to inhibit bone resorption. Accordingly, the results of bisphosphonate therapy of patients with bone metastasis from breast, lung and prostate cancers, and MM, have been positive, including reducing the risk of fracture and bone pain[75,173–176], as well as prolonging progression-free survival and reducing mortality[173,177–179]. There is mixed evidence regarding whether bisphosphonates extend overall survival[75,128,157,175,178,180]. By contrast, RCCBM has been relatively resistant to bisphosphonate treatment[128,157,180]. In recent years RCCBM has become the most common solid tumour bone metastasis requiring surgical intervention for treatment and/or palliation despite patients with RCC having a lower incidence of bone metastasis than patients with breast, prostate or lung cancer[181,182]. Because of the inconsistent treatment response of RCCBM to bone-targeted therapy such as bisphosphonates and denosumab[121,183], additional interventions for the purposes of palliation (rather than cure) are often the only remaining option. Most often, these treatments include radiation for bone pain (in nearly 80% of patients), and surgical intervention to treat or prevent an impending fracture (28%)[183,184].

Anti-resorption treatments can stabilize bone metastases by mitigating the vicious cycle[185]. Two major classes of drugs, namely bisphosphonates and denosumab, are used to target osteoclasts by inducing apoptosis[186,187] and preventing activation[188], respectively. Despite their effectiveness at strengthening the bone and improving quality of life, they do not significantly prolong overall survival of patients with bone metastases[185], and about two-thirds of patients with breast cancer and bone metastases later develop metastases in other organs[73,74]. Thus, additional therapies are urgently needed. In this section, we discuss novel potential therapeutic targets emerging from recent research.

Targeting dormant DTCs, asymptomatic BMMs and their niches. It has become increasingly clear that the vicious cycle is not initiated immediately upon DTC arrival in the bone marrow. The asymptomatic stage

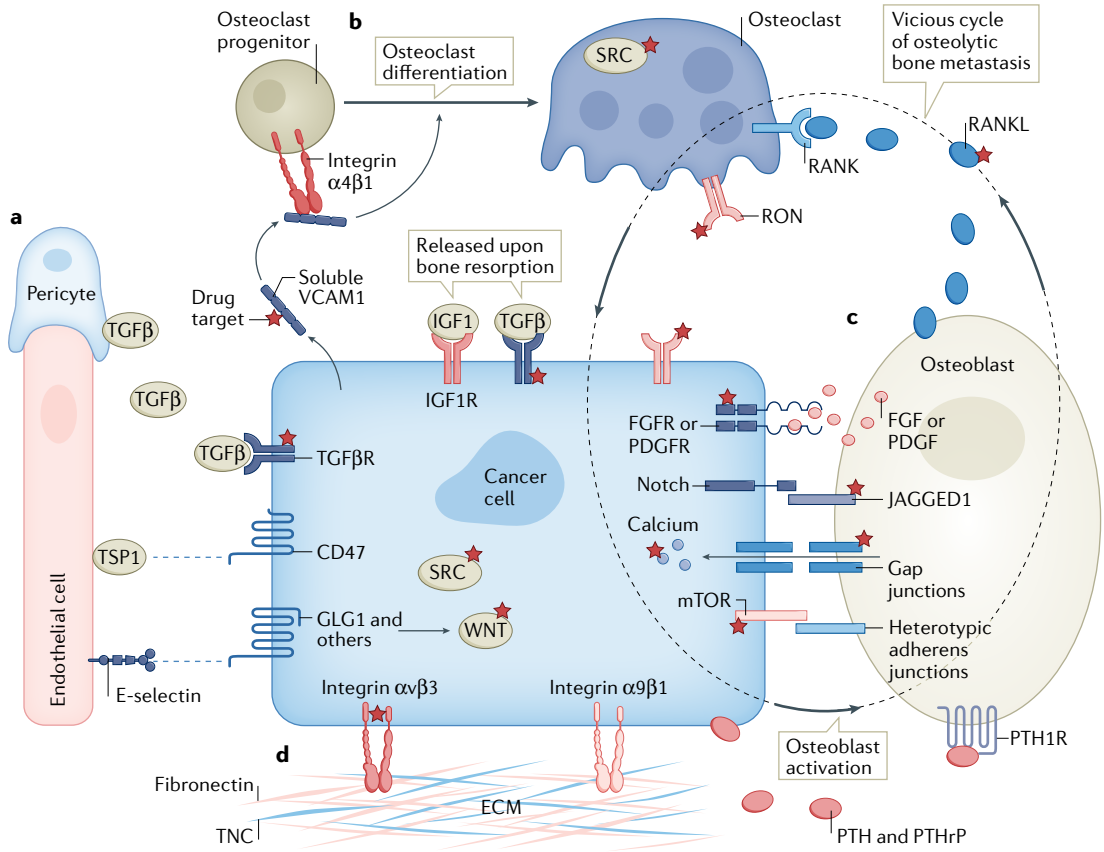

Fig. 4 | **Emerging therapeutic targets in bone metastasis. a** | Molecular crosstalk between cancer cells and perivascular niche cells including endothelial cells and pericytes. **b** | Therapeutic targets in differentiation of osteoclast progenitor cells into mature osteoclasts. **c** | Direct cell–cell interactions and paracrine between cancer cells and osteogenic cells. **d** | The integrin pathways mediating interaction between cancer cells with extracellular matrix (ECM) during bone metastasis. The dotted circle indicates the paradigm of vicious cycle that includes secretion of PTH and PTHrP by cancer cells that activates osteoblasts, the secretion of RANKL by osteoblasts that drives osteoclast differentiation and the release of TGFβ and IGF1 from bone matrix upon bone resorption that reciprocally promotes cancer cell progression. Molecules with targeted therapies available are highlighted with red stars. TNC, tenascin.

of bone colonization may persist for years or even decades in different cancer types[25,189]. This stage may be divided into two phases characterized by the presence of quiescent DTCs and proliferative BMMs, respectively. As previously discussed, the cellular and molecular status of these early-stage lesions is determined by their interactions with various microenvironment niches.

There are two challenges in targeting DTCs and BMMs. First, clinical information from corresponding primary tumours may not be applicable to these populations. DTCs and BMMs represent only a small fraction of cells residing in primary tumours. Moreover, cancer–niche interactions provide therapeutic resistance and vulnerability not seen in primary tumours. For instance, gap junctions between cancer cells and osteogenic cells provide a channel for calcium flux into the former and result in activation of calcium signalling and unexpected therapeutic sensitivity to arsenic trioxide[45]. ER^+ breast cancer cells may transiently lose their ER expression and acquire endocrine resistance under the influence of the osteogenic cells[46]. The integrin-mediated signalling between the perivascular niche and DTCs causes resistance to chemotherapies[35]. These findings implicate new targets to disrupt cancer–niche interactions, and treating these targets may eliminate DTCs and BMMs either directly or through sensitization to traditional therapies. The second challenge in targeting DTCs and BMMs is their 'invisibility' to current diagnostic technologies, which makes it difficult to define clinical end points in adjuvant settings other than overt recurrence[190]. As recurrences often occur years later and in only 20–40% of patients[25], clinical trials would need to recruit many patients with long follow-up times to capture enough events. To overcome this challenge, biomarkers that distinguish patients with high recurrence risk are urgently needed.

Recent studies have started to reveal potential therapeutic targets to abolish the tumorigenic capacity of DTCs and BMMs. For example, E-selectin might serve as a potential target on the basis of its role in inducing phenotype plasticity in cancer cells as discussed above[39]. Blockade of E-selectin activity might force DTCs to remain dormant. Notably, a small-molecule inhibitor of E-selectin is being investigated for treatment of leukaemia[191] (FIG. 4a). As previously mentioned, osteoblasts and their progenitor cells provide several targetable mechanisms to drive metastasis progression, including the activation of mTOR by heterotypic adherens junctions, calcium signalling by gap junctions,

Notch signalling by JAGGED1, and EZH2 by FGFR and PDGFR signalling. Indeed, pharmacological inhibition of mTOR, adherens junctions, calcium signalling and gap junctions impeded bone colonization in experimental models of metastasis[42,43,45–47,78,192] (FIG. 3b).

Another therapeutic strategy is to reinforce dormancy without necessarily killing DTCs and/or BMMs. Towards this end, agonists of TSP1 signalling are compelling potential therapies. In fact, TSP1-agonist mimetic peptides have been available, but have not been exploited in metastatic models[193] (FIG. 4a). As discussed earlier, the conversion or alteration from perivascular to osteogenic niche may terminate dormancy and initiate proliferation (FIG. 2). Osteogenesis may be a major driving force of the initiation of proliferation upon dormancy termination, as part of either normal bone turnover or bone repair/remodelling. Therefore, it is conceivable that perturbation of osteogenesis may affect outgrowth of DTCs and/or BMMs. Indeed, this notion is consistent with the observation that bisphosphonates (which inhibit bone turnover[194]) reduce breast cancer metastases specifically in postmenopausal women[75], in whom bone turnover is increased[195]. The termination of dormancy may also be mediated by several signals, including soluble VCAM1 produced by cancer cells[59] (FIG. 4b) and periostin produced by endothelial tip cells[33]. These molecules represent potential targets to keep DTCs dormant. Specifically, VCAM1 signals through integrin α4, which can be blocked by monoclonal antibodies or small-molecule inhibitors[196]. For periostin, a monoclonal antibody targeting the cancer-specific isoform has recently been applied to xenograft models of breast cancer and exhibited efficacies in combatting chemoresistance[197]. Although promising, the above agents have not been tested in models of metastasis dormancy. Moreover, the metastasis preventive strategy entails persistent long-term treatment, which may be challenging in the clinical setting.

Finally, dormant DTCs may be eradicated after being mobilized through perturbation of important niche components. As DTCs and HSCs share common niches, strategies to mobilize HSCs can also stimulate DTCs to leave their niches. Administration of G-CSF, which can mobilize HSCs, increased leukaemic stem cells (LSCs) in the circulation of acute myeloid leukaemia[198] and in patients with breast cancer[199]. Similarly, both HSCs and DTCs express CXCR4, which mediates their homing and retention to the niche. The cognate ligand of CXCR4, CXCL12, is highly expressed by niche cells. Consistent with this roles in HSCs, perturbation of the CXCR12–CXCR4 axis by a CXCR4 inhibitor (AMD3100) and in prostate cancer and lymphoblastic leukaemia models resulted in release of cancer cells into circulation[32,200]. In combination with other therapies, this mobilization can lead to effective elimination of dormant and therapy-resistant cancer cells[201].

Targeting the vicious cycle. Several pathways were recently discovered to participate in the vicious cycle mainly through driving osteoclast differentiation and functions. The RON kinase is expressed by both bone metastatic cells of breast cancer and osteoclasts. A specific RON inhibitor is currently being tested in clinical trials[62,202] (FIG. 4c). Inside osteoclasts, the SRC kinase promotes the transduction of signals towards differentiation[203] and production of bone-degrading enzymes[204]. As a result, inhibition of SRC may achieve dual inhibitory effects on both cancer cells and osteoclasts, thereby representing a possible strategy to impede the vicious cycle. This hypothesis has been validated in preclinical models of breast cancer metastasis (both experimental metastases based on intra-cardiac injection and spontaneous metastases from orthotopic tumours, see TABLE 1 and BOX 2) via genetic knockdown of SRC[178] or application of a SRC inhibitor, dasatinib[26]. Notch signalling mediates crosstalk between cancer cells and osteoblasts and renders cancer cells resistant to chemotherapies as part of the vicious cycle[47,58]. A therapeutic antibody to JAGGED1, the pertinent Notch ligand, represents a promising agent to block bone metastasis[43]. Likewise, integrin β3 is induced in cancer cells by the BME, mediates chemoresistance and may be targeted by nanotherapy[60], possibly through interaction with fibronectin (FIG. 4d). Senescent osteoblasts produce IL-6 to promote osteoclastogenesis and bone metastasis progression of breast cancer cells[63]. The stromal components other than osteoclasts and osteoblasts may also have important roles in facilitating the vicious cycle. Inhibition of the p38–MK2 pathway in stromal cells by small-molecule inhibitors could also limit bone metastasis progression of breast cancer in mice[205]. TGFβ has pivotal roles in multiple stages of colonization including early dormancy (FIG. 4a) and later vicious cycle, although the directions of effects may not be consistent. Nevertheless, TGFβ signalling has been targeted in myeloma preclinical models with the neutralizing antibody 1D11, which exhibits efficacy in combination with other therapies[206].

A common challenge for all the above therapies is potential toxicity due to the pleotropic roles of the targeted pathways. The acidic environment and the positively charged bone matrix may be leveraged to overcome this challenge. For instance, conjugation with negatively charged bisphosphonates can significantly enrich antibodies and chemical inhibitors in the BME, thereby reducing drug effects on other organs[207–209].

Immunotherapies. The bone marrow has unique immunological properties as it is where all immune cells are produced. For example, immature immune cells, especially myeloid cells, may negatively affect adaptive immunity. Moreover, the high level of TGFβ in the bone marrow may also blunt immune responses. Therefore, it is reasonable to hypothesize that the BME is immunosuppressive. In support of this notion, retrospective analysis suggests that patients with TNBC with bone metastases respond poorly to combined atezolizumab, an immune checkpoint inhibitor and nab-paclitaxel, despite overall significant responses in all patients[210]. Similarly, ipilimumab exhibited limited effects on castration-resistant prostate cancer[211], which may be due to skewing of T helper subsets towards the T_H17 subtype under the influence of TGFβ[212]. Future studies will be needed to further characterize the immune microenvironment in the bone marrow and to better understand

Periostin
An extracellular matrix component encoded by the *POSTN* gene. It is a ligand of integrins and has important roles in the niche supporting normal and cancer stem cells.

Endothelial tip cells
Endothelial cells that sprout branches of blood vessels.

how this microenvironment may affect responses to immunotherapies in bone metastasis.

Conclusions and perspectives

The colonization of DTCs in bone is driven by intimate interactions between cancer cells and the spatiotemporally dynamic environment. DTC fate regulation may be achieved through intricate organization of microenvironmental cells of various lineages and subtle differences between cells of the same lineage. Both normal homeostasis and pathological repair and/or remodelling induce reorganization and reprogramming of bone cells, which may in turn affect bone metastasis progression. Thus, future investigation of bone metastasis will benefit from approaches that can precisely map the BME at single-cell resolution. Complementarily, real-time intra-vital imaging will be needed to provide information about temporal dynamics of cancer and bone cells. Taken together, multidimensional models of bone colonization need to be established to fill the missing links of the journey of a cancer cell towards, within and beyond BME.

In addition to exerting pressure for genetic selection, the BME also seems to trigger adaptation of cancer cells through epigenomic reprogramming. Interestingly, the reprogramming appears to cause a dedifferentiation process and render metastatic cells more stem-like. As a result, the BME may fuel further metastasis to other organs, as demonstrated in preclinical models[46,78]. This hypothesis will need to be tested in more models, and detailed mechanisms will need to be elucidated. However, it is compelling to notice that the reprogramming may be in part driven by EZH2 (REFS[46,78]). EZH2 inhibitors are currently under clinical investigation[213]. Future studies are needed to further characterize this process, in terms of the onset, kinetics, reversibility and exact molecular drivers. Clinically, it will be interesting to examine whether EZH2 treatment can prevent patients with bone-only metastases from developing other metastases. If invisible bone metastases already begin to seed other organs, the treatment may even apply to all patients to stop the potential spread from bone. It also remains to be determined whether specific microenvironment niches in other metastatic sites can cause similar effects. The compound actions of clonal selection and epigenetic reprogramming may lead to more complicated metastatic evolution, which has been suggested by recent genomic sequencing studies.

Despite many commonalities, overt bone metastases of various cancer types exhibit important distinctions. For instance, strong osteomimicry and pivotal roles of osteocytes in the vicious cycle distinguish bone metastases of prostate cancer and kidney cancer, respectively. It is important to understand how various cancer types evolve to use different pathways and microenvironment factors to facilitate bone colonization. This knowledge may explain distinct therapeutic responses such as the resistance of kidney cancer to bisphosphonates and denosumab. Although it is difficult to compare cancer cells of different origins, their impact on various cell types in the microenvironment may be readily compared to delineate cancer type-specific interaction mechanisms.

Published online: 05 October 2021

1. Clarke, B. Normal bone anatomy and physiology. *Clin. J. Am. Soc. Nephrol.* **3** (Suppl. 3), S131–S139 (2008).
2. Ding, L., Saunders, T. L., Enikolopov, G. & Morrison, S. J. Endothelial and perivascular cells maintain haematopoietic stem cells. *Nature* **481**, 457–462 (2012).
3. Zhou, B. O., Yue, R., Murphy, M. M., Peyer, J. G. & Morrison, S. J. Leptin-receptor-expressing mesenchymal stromal cells represent the main source of bone formed by adult bone marrow. *Cell Stem Cell* **15**, 154–168 (2014).
4. Kunisaki, Y. et al. Arteriolar niches maintain haematopoietic stem cell quiescence. *Nature* **502**, 637–643 (2013).
5. Kusumbe, A. P. et al. Age-dependent modulation of vascular niches for haematopoietic stem cells. *Nature* **532**, 380–384 (2016).
6. Mendez-Ferrer, S. et al. Mesenchymal and haematopoietic stem cells form a unique bone marrow niche. *Nature* **466**, 829–834 (2010).
7. Brazill, J. M., Beeve, A. T., Craft, C. S., Ivanusic, J. J. & Scheller, E. L. Nerves in bone: evolving concepts in pain and anabolism. *J. Bone Min. Res.* **34**, 1393–1406 (2019).
8. McAllister, S. S. & Weinberg, R. A. The tumour-induced systemic environment as a critical regulator of cancer progression and metastasis. *Nat. Cell Biol.* **16**, 717–727 (2014).
9. Kaplan, R. N. et al. VEGFR1-positive haematopoietic bone marrow progenitors initiate the pre-metastatic niche. *Nature* **438**, 820–827 (2005).
10. Zeng, Z. et al. Cancer-derived exosomal miR-25-3p promotes pre-metastatic niche formation by inducing vascular permeability and angiogenesis. *Nat. Commun.* **9**, 5395 (2018).
11. Liu, Y. et al. Tumor exosomal RNAs promote lung pre-metastatic niche formation by activating alveolar epithelial TLR3 to recruit neutrophils. *Cancer Cell* **30**, 243–256 (2016).
12. Tyagi, A. et al. Nicotine promotes breast cancer metastasis by stimulating N2 neutrophils and generating pre-metastatic niche in lung. *Nat. Commun.* **12**, 474 (2021).
13. Catena, R. et al. Bone marrow-derived Gr1+ cells can generate a metastasis-resistant microenvironment via induced secretion of thrombospondin-1. *Cancer Discov.* **3**, 578–589 (2013).
14. Granot, Z. et al. Tumor entrained neutrophils inhibit seeding in the premetastatic lung. *Cancer Cell* **20**, 300–314 (2011).
15. Meyer, M. A. et al. Breast and pancreatic cancer interrupt IRF8-dependent dendritic cell development to overcome immune surveillance. *Nat. Commun.* **9**, 1250 (2018).
16. Cheng, P. et al. Inhibition of dendritic cell differentiation and accumulation of myeloid-derived suppressor cells in cancer is regulated by S100A9 protein. *J. Exp. Med.* **205**, 2235–2249 (2008).
17. Sinha, P. et al. Proinflammatory S100 proteins regulate the accumulation of myeloid-derived suppressor cells. *J. Immunol.* **181**, 4666–4675 (2008).
18. Fleming, V. et al. Targeting myeloid-derived suppressor cells to bypass tumor-induced immunosuppression. *Front. Immunol.* **9**, 398 (2018).
19. Markowitz, J., Wesolowski, R., Papenfuss, T., Brooks, T. R. & Carson, W. E. III Myeloid-derived suppressor cells in breast cancer. *Breast Cancer Res. Treat.* **140**, 13–21 (2013).
20. Welte, T. et al. Oncogenic mTOR signalling recruits myeloid-derived suppressor cells to promote tumour initiation. *Nat. Cell Biol.* **18**, 632–644 (2016).
21. Kim, I. S. et al. Immuno-subtyping of breast cancer reveals distinct myeloid cell profiles and immunotherapy resistance mechanisms. *Nat. Cell Biol.* **21**, 1113–1126 (2019).
22. Paget, S. The distribution of secondary growths in cancer of the breast. *Lancet* **133**, 571–573 (1889).
23. Kennecke, H. et al. Metastatic behavior of breast cancer subtypes. *J. Clin. Oncol.* **28**, 3271–3277 (2010).
24. Smid, M. et al. Subtypes of breast cancer show preferential site of relapse. *Cancer Res.* **68**, 3108–3114 (2008).
25. Zhang, X. H., Giuliano, M., Trivedi, M. V., Schiff, R. & Osborne, C. K. Metastasis dormancy in estrogen receptor-positive breast cancer. *Clin. Cancer Res.* **19**, 6389–6397 (2013).
26. Zhang, X. H. et al. Latent bone metastasis in breast cancer tied to Src-dependent survival signals. *Cancer Cell* **16**, 67–78 (2009).
27. Vanharanta, S. & Massague, J. Origins of metastatic traits. *Cancer Cell* **24**, 410–421 (2013).
28. Zhang, X. H. et al. Selection of bone metastasis seeds by mesenchymal signals in the primary tumor stroma. *Cell* **154**, 1060–1073 (2013).
29. Awolaran, O., Brooks, S. A. & Lavender, V. Breast cancer osteomimicry and its role in bone specific metastasis; an integrative, systematic review of preclinical evidence. *Breast* **30**, 156–171 (2016).
30. Bellahcene, A. & Castronovo, V. Increased expression of osteonectin and osteopontin, two bone matrix proteins, in human breast cancer. *Am. J. Pathol.* **146**, 95–100 (1995).
31. Tan, C. C. et al. Breast cancer cells obtain an osteomimetic feature via epithelial–mesenchymal transition that have undergone BMP2/RUNX2 signaling pathway induction. *Oncotarget* **7**, 79688–79705 (2016).
32. Shiozawa, Y. et al. Human prostate cancer metastases target the hematopoietic stem cell niche to establish footholds in mouse bone marrow. *J. Clin. Invest.* **121**, 1298–1312 (2011).
33. Ghajar, C. M. et al. The perivascular niche regulates breast tumour dormancy. *Nat. Cell Biol.* **15**, 807–817 (2013).
34. Price, T. T. et al. Dormant breast cancer micrometastases reside in specific bone marrow niches that regulate their transit to and from bone. *Sci. Transl. Med.* **8**, 340ra373 (2016).
35. Carlson, P. et al. Targeting the perivascular niche sensitizes disseminated tumour cells to chemotherapy. *Nat. Cell Biol.* **21**, 238–250 (2019).
36. Nobre, A. R. et al. Bone marrow NG2+/Nestin+ mesenchymal stem cells drive DTC dormancy via TGF-β2. *Nat. Cancer* **2**, 327–339 (2021).

37. Johnson, R. W. et al. Induction of LIFR confers a dormancy phenotype in breast cancer cells disseminated to the bone marrow. *Nat. Cell Biol.* **18**, 1078–1089 (2016).
38. Gawrzak, S. et al. MSK1 regulates luminal cell differentiation and metastatic dormancy in ER+ breast cancer. *Nat. Cell Biol.* **20**, 211–221 (2018).
39. Esposito, M. et al. Bone vascular niche E-selectin induces mesenchymal–epithelial transition and Wnt activation in cancer cells to promote bone metastasis. *Nat. Cell Biol.* **21**, 627–639 (2019).
40. Adams, G. B. et al. Stem cell engraftment at the endosteal niche is specified by the calcium-sensing receptor. *Nature* **439**, 599–603 (2006).
41. Wei, Q. & Frenette, P. S. Niches for hematopoietic stem cells and their progeny. *Immunity* **48**, 632–648 (2018).
42. Wang, H. et al. The osteogenic niche promotes early-stage bone colonization of disseminated breast cancer cells. *Cancer Cell* **27**, 193–210 (2015).
43. Zheng, H. et al. Therapeutic antibody targeting tumor- and osteoblastic niche-derived jagged1 sensitizes bone metastasis to chemotherapy. *Cancer Cell* **32**, 731–747 e736 (2017).
44. Wang, D. et al. NPNT promotes early-stage bone metastases in breast cancer by regulation of the osteogenic niche. *J. Bone Oncol.* **13**, 91–96 (2018).
45. Wang, H. et al. The osteogenic niche is a calcium reservoir of bone micrometastases and confers unexpected therapeutic vulnerability. *Cancer Cell* **34**, 823–839 e827 (2018).
46. Bado, I. L. et al. The bone microenvironment increases phenotypic plasticity of ER+ breast cancer cells. *Dev. Cell* **56**, 1100–1117.e1109 (2021).
47. Sethi, N., Dai, X., Winter, C. G. & Kang, Y. Tumor-derived JAGGED1 promotes osteolytic bone metastasis of breast cancer by engaging notch signaling in bone cells. *Cancer Cell* **19**, 192–205 (2011).
48. San Martin, R. et al. Tenascin-C and integrin alpha9 mediate interactions of prostate cancer with the bone microenvironment. *Cancer Res.* **77**, 5977–5988 (2017).
49. Oskarsson, T. et al. Breast cancer cells produce tenascin C as a metastatic niche component to colonize the lungs. *Nat. Med.* **17**, 867–874 (2011).
50. Lowy, C. M. & Oskarsson, T. Tenascin C in metastasis: a view from the invasive front. *Cell Adh. Migr.* **9**, 112–124 (2015).
51. Shupp, A. B., Kolb, A. D., Mukhopadhyay, D. & Bussard, K. M. Cancer metastases to bone: concepts, mechanisms, and interactions with bone osteoblasts. *Cancers* **10**, 182 (2018).
52. Lawson, M. A. et al. Osteoclasts control reactivation of dormant myeloma cells by remodelling the endosteal niche. *Nat. Commun.* **6**, 8983 (2015).
53. Guise, T. A. et al. Evidence for a causal role of parathyroid hormone-related protein in the pathogenesis of human breast cancer-mediated osteolysis. *J. Clin. Invest.* **98**, 1544–1549 (1996).
54. Guise, T. A. et al. Basic mechanisms responsible for osteolytic and osteoblastic bone metastases. *Clin. Cancer Res.* **12**, 6213s–6216s (2006).
55. Yasuda, H. et al. Osteoclast differentiation factor is a ligand for osteoprotegerin/osteoclastogenesis-inhibitory factor and is identical to TRANCE/RANKL. *Proc. Natl Acad. Sci. USA* **95**, 3597–3602 (1998).
56. Kingsley, L. A., Fournier, P. G., Chirgwin, J. M. & Guise, T. A. Molecular biology of bone metastasis. *Mol. Cancer Ther.* **6**, 2609–2617 (2007).
57. Waning, D. L. & Guise, T. A. Molecular mechanisms of bone metastasis and associated muscle weakness. *Clin. Cancer Res.* **20**, 3071–3077 (2014).
58. Ell, B. & Kang, Y. SnapShot: bone metastasis. *Cell* **151**, 690–690 e691 (2012).
59. Lu, X. et al. VCAM-1 promotes osteolytic expansion of indolent bone micrometastasis of breast cancer by engaging alpha4beta1-positive osteoclast progenitors. *Cancer Cell* **20**, 701–714 (2011).
60. Ross, M. H. et al. Bone-induced expression of integrin beta3 enables targeted nanotherapy of breast cancer metastases. *Cancer Res.* **77**, 6299–6312 (2017).
61. Welm, A. L. et al. The macrophage-stimulating protein pathway promotes metastasis in a mouse model for breast cancer and predicts poor prognosis in humans. *Proc. Natl Acad. Sci. USA* **104**, 7570–7575 (2007).
62. Andrade, K. et al. RON kinase: a target for treatment of cancer-induced bone destruction and osteoporosis. *Sci. Transl. Med.* **9**, eaai9338 (2017).
63. Luo, X. et al. Stromal-initiated changes in the bone promote metastatic niche development. *Cell Rep.* **14**, 82–92 (2016).
64. Coleman, R. E. Metastatic bone disease: clinical features, pathophysiology and treatment strategies. *Cancer Treat. Rev.* **27**, 165–176 (2001).
65. Esposito, M., Guise, T. & Kang, Y. The biology of bone metastasis. *Cold Spring Harb. Perspect. Med.* **8**, a031252 (2018).
66. Coleman, R. E. et al. Bone metastases. *Nat. Rev. Dis. Prim.* **6**, 83 (2020).
67. Soni, A. et al. Breast cancer subtypes predispose the site of distant metastases. *Am. J. Clin. Pathol.* **143**, 471–478 (2015).
68. Cummings, M. C. et al. Metastatic progression of breast cancer: insights from 50 years of autopsies. *J. Pathol.* **232**, 23–31 (2014).
69. Disibio, G. & French, S. W. Metastatic patterns of cancers: results from a large autopsy study. *Arch. Pathol. Lab. Med.* **132**, 931–939 (2008).
70. Lee, Y. T. Breast carcinoma: pattern of metastasis at autopsy. *J. Surg. Oncol.* **23**, 175–180 (1983).
71. Banys-Paluchowski, M., Fehm, T., Janni, W., Solomayer, E. F. & Hartkopf, A. Circulating and disseminated tumor cells in breast carcinoma: report from the consensus conference on tumor cell dissemination during the 39th Annual Meeting of the German Society of Senology, Berlin, 27 June 2019. *Geburtshilfe Frauenheilkd.* **79**, 1320–1327 (2019).
72. Tjensvoll, K. et al. Detection of disseminated tumor cells in bone marrow predict late recurrences in operable breast cancer patients. *BMC Cancer* **19**, 1131 (2019).
73. Coleman, R. E. & Rubens, R. D. The clinical course of bone metastases from breast cancer. *Br. J. Cancer* **55**, 61–66 (1987).
74. Coleman, R. E., Smith, P. & Rubens, R. D. Clinical course and prognostic factors following bone recurrence from breast cancer. *Br. J. Cancer* **77**, 336–340 (1998).
75. Early Breast Cancer Trialists' Collaborative Group. Adjuvant bisphosphonate treatment in early breast cancer: meta-analyses of individual patient data from randomised trials. *Lancet* **386**, 1353–1361 (2015).
76. Solomayer, E. F. et al. Influence of zoledronic acid on disseminated tumor cells in primary breast cancer patients. *Ann. Oncol.* **23**, 2271–2277 (2012).
77. Hartkopf, A. D. et al. Prognostic relevance of disseminated tumour cells from the bone marrow of early stage breast cancer patients – results from a large single-centre analysis. *Eur. J. Cancer* **50**, 2550–2559 (2014).
78. Zhang, W. et al. The bone microenvironment invigorates metastatic seeds for further dissemination. *Cell* **184**, 2471–2486.e20 (2021).
79. Kalhor, R., Mali, P. & Church, G. M. Rapidly evolving homing CRISPR barcodes. *Nat. Methods* **14**, 195–200 (2017).
80. Kalhor, R. et al. Developmental barcoding of whole mouse via homing CRISPR. *Science* **361**, eaat9804 (2018).
81. Kim, M. Y. et al. Tumor self-seeding by circulating cancer cells. *Cell* **139**, 1315–1326 (2009).
82. Nik-Zainal, S. et al. The life history of 21 breast cancers. *Cell* **149**, 994–1007 (2012).
83. Minn, A. J. et al. Genes that mediate breast cancer metastasis to lung. *Nature* **436**, 518–524 (2005).
84. Bos, P. D. et al. Genes that mediate breast cancer metastasis to the brain. *Nature* **459**, 1005–1009 (2009).
85. Kang, Y. et al. A multigenic program mediating breast cancer metastasis to bone. *Cancer Cell* **3**, 537–549 (2003).
86. Chen, Z., Orlowski, R. Z., Wang, M., Kwak, L. & McCarty, N. Osteoblastic niche supports the growth of quiescent multiple myeloma cells. *Blood* **123**, 2204–2208 (2014).
87. Crisan, M. et al. A perivascular origin for mesenchymal stem cells in multiple human organs. *Cell Stem Cell* **3**, 301–313 (2008).
88. da Silva Meirelles, L., Caplan, A. I. & Nardi, N. B. In search of the in vivo identity of mesenchymal stem cells. *Stem Cell* **26**, 2287–2299 (2008).
89. Muscarella, A. M. Unique cellular protrusions mediate breast cancer cell migration by tethering to osteogenic cells. *NPJ Breast Cancer* **6**, 42 (2020).
90. Willam, C., Schindler, R., Frei, U. & Eckardt, K. U. Increases in oxygen tension stimulate expression of ICAM-1 and VCAM-1 on human endothelial cells. *Am. J. Physiol.* **276**, H2044–2052 (1999).
91. Shen, S., Vagner, S. & Robert, C. Persistent cancer cells: the deadly survivors. *Cell* **183**, 860–874 (2020).
92. Eyre, R. et al. Microenvironmental IL1beta promotes breast cancer metastatic colonisation in the bone via activation of Wnt signalling. *Nat. Commun.* **10**, 5016 (2019).
93. Brown, D. et al. Phylogenetic analysis of metastatic progression in breast cancer using somatic mutations and copy number aberrations. *Nat. Commun.* **8**, 14944 (2017).
94. Ullah, I. et al. Evolutionary history of metastatic breast cancer reveals minimal seeding from axillary lymph nodes. *J. Clin. Invest.* **128**, 1355–1370 (2018).
95. Sturge, J., Caley, M. P. & Waxman, J. Bone metastasis in prostate cancer: emerging therapeutic strategies. *Nat. Rev. Clin. Oncol.* **8**, 357–368 (2011).
96. Wan, X. et al. Effect of transforming growth factor beta (TGF-beta) receptor I kinase inhibitor on prostate cancer bone growth. *Bone* **50**, 695–703 (2012).
97. Fournier, P. G. et al. The TGF-beta signaling regulator PMEPA1 suppresses prostate cancer metastases to bone. *Cancer Cell* **27**, 809–821 (2015).
98. Chen, C. et al. IL-17 and insulin/IGF1 enhance adhesion of prostate cancer cells to vascular endothelial cells through CD44-VCAM-1 interaction. *Prostate* **75**, 883–895 (2015).
99. Roudier, M. P. et al. Histological, immunophenotypic and histomorphometric characterization of prostate cancer bone metastases. *Cancer Treat. Res.* **118**, 311–339 (2004).
100. Furesi, G., Rauner, M. & Hofbauer, L. C. Emerging players in prostate cancer–bone niche communication. *Trends Cancer* **7**, 112–121 (2021).
101. Knerr, K., Ackermann, K., Neidhart, T. & Pyerin, W. Bone metastasis: osteoblasts affect growth and adhesion regulons in prostate tumor cells and provoke osteomimicry. *Int. J. Cancer* **111**, 152–159 (2004).
102. Hagberg Thulin, M., Jennbacken, K., Damber, J. E. & Welen, K. Osteoblasts stimulate the osteogenic and metastatic progression of castration-resistant prostate cancer in a novel model for in vitro and in vivo studies. *Clin. Exp. Metastasis* **31**, 269–283 (2014).
103. Akech, J. et al. Runx2 association with progression of prostate cancer in patients: mechanisms mediating bone osteolysis and osteoblastic metastatic lesions. *Oncogene* **29**, 811–821 (2010).
104. Yang, Y. et al. PTEN loss promotes intratumoral androgen synthesis and tumor microenvironment remodeling via aberrant activation of RUNX2 in castration-resistant prostate cancer. *Clin. Cancer Res.* **24**, 834–846 (2018).
105. Zhang, H. et al. FOXO1 inhibits Runx2 transcriptional activity and prostate cancer cell migration and invasion. *Cancer Res.* **71**, 3257–3267 (2011).
106. Dai, J. et al. Prostate cancer induces bone metastasis through Wnt-induced bone morphogenetic protein-dependent and independent mechanisms. *Cancer Res.* **68**, 5785–5794 (2008).
107. Liao, J. et al. Tumor expressed PTHrP facilitates prostate cancer-induced osteoblastic lesions. *Int. J. Cancer* **123**, 2267–2278 (2008).
108. Nelson, J. B. et al. Identification of endothelin-1 in the pathophysiology of metastatic adenocarcinoma of the prostate. *Nat. Med.* **1**, 944–949 (1995).
109. Lee, Y. C. et al. Secretome analysis of an osteogenic prostate tumor identifies complex signaling networks mediating cross-talk of cancer and stromal cells within the tumor microenvironment. *Mol. Cell Proteom.* **14**, 471–483 (2015).
110. Long, F. Building strong bones: molecular regulation of the osteoblast lineage. *Nat. Rev. Mol. Cell Biol.* **13**, 27–38 (2011).
111. Nandana, S. et al. Bone metastasis of prostate cancer can be therapeutically targeted at the TBX2–WNT signaling axis. *Cancer Res.* **77**, 1331–1344 (2017).
112. Lin, S. C. et al. Endothelial-to-osteoblast conversion generates osteoblastic metastasis of prostate cancer. *Dev. Cell* **41**, 467–480 e463 (2017).
113. Yu-Lee, L. Y. et al. Bone secreted factors induce cellular quiescence in prostate cancer cells. *Sci. Rep.* **9**, 18635 (2019).
114. Ercole, C. J. et al. Prostatic specific antigen and prostatic acid phosphatase in the monitoring and staging of patients with prostatic cancer. *J. Urol.* **138**, 1181–1184 (1987).
115. Cramer, S. D., Chen, Z. & Peehl, D. M. Prostate specific antigen cleaves parathyroid hormone-related protein in the PTH-like domain: inactivation of PTHrP-stimulated cAMP accumulation in mouse osteoblasts. *J. Urol.* **156**, 526–531 (1996).
116. Dallas, S. L. et al. Preferential production of latent transforming growth factor beta-2 by primary prostatic epithelial cells and its activation by prostate-specific antigen. *J. Cell Physiol.* **202**, 361–370 (2005).

117. Cohen, P., Peehl, D. M., Graves, H. C. & Rosenfeld, R. G. Biological effects of prostate specific antigen as an insulin-like growth factor binding protein-3 protease. *J. Endocrinol.* **142**, 407–415 (1994).
118. Kirschenbaum, A., Liu, X. H., Yao, S., Leiter, A. & Levine, A. C. Prostatic acid phosphatase is expressed in human prostate cancer bone metastases and promotes osteoblast differentiation. *Ann. N. Y. Acad. Sci.* **1237**, 64–70 (2011).
119. Ishibe, M., Rosier, R. N. & Puzas, J. E. Human prostatic acid phosphatase directly stimulates collagen synthesis and alkaline phosphatase content of isolated bone cells. *J. Clin. Endocrinol. Metab.* **73**, 785–792 (1991).
120. Santoni, M. et al. Bone metastases in patients with metastatic renal cell carcinoma: are they always associated with poor prognosis? *J. Exp. Clin. Cancer Res.* **34**, 10 (2015).
121. Wood, S. L. & Brown, J. E. Skeletal metastasis in renal cell carcinoma: current and future management options. *Cancer Treat. Rev.* **38**, 284–291 (2012).
122. Chen, S. C. & Kuo, P. L. Bone metastasis from renal cell carcinoma. *Int. J. Mol. Sci.* **17**, 987 (2016).
123. Lin, P. P. et al. Patient survival after surgery for osseous metastases from renal cell carcinoma. *J. Bone Jt. Surg. Am.* **89**, 1794–1801 (2007).
124. Pan, T. et al. BIGH3 promotes osteolytic lesions in renal cell carcinoma bone metastasis by inhibiting osteoblast differentiation. *Neoplasia* **20**, 32–43 (2018).
125. Sasaki, H. et al. Beta IGH3, a TGF-beta inducible gene, is overexpressed in lung cancer. *Jpn. J. Clin. Oncol.* **32**, 85–89 (2002).
126. Yamanaka, M. et al. BIGH3 is overexpressed in clear cell renal cell carcinoma. *Oncol. Rep.* **19**, 865–874 (2008).
127. Zhang, W., Bado, I., Wang, H., Lo, H. C. & Zhang, X. H. Bone metastasis: find your niche and fit in. *Trends Cancer* **5**, 95–110 (2019).
128. Keizman, D. et al. Bisphosphonates combined with sunitinib may improve the response rate, progression free survival and overall survival of patients with bone metastases from renal cell carcinoma. *Eur. J. Cancer* **48**, 1031–1037 (2012).
129. Vrdoljak, E. et al. Bisphosphonates in patients with renal cell carcinoma and bone metastases: a sunitinib global expanded-access trial subanalysis. *Future Oncol.* **11**, 2831–2840 (2015).
130. Haber, T. et al. Bone metastasis in renal cell carcinoma is preprogrammed in the primary tumor and caused by AKT and integrin alpha5 signaling. *J. Urol.* **194**, 539–546 (2015).
131. Pan, T. et al. Three-dimensional (3D) culture of bone-derived human 786-O renal cell carcinoma retains relevant clinical characteristics of bone metastases. *Cancer Lett.* **365**, 89–95 (2015).
132. Satcher, R. L. et al. Cadherin-11 in renal cell carcinoma bone metastasis. *PLoS ONE* **9**, e89880 (2014).
133. Giuliani, N. et al. Increased osteocyte death in multiple myeloma patients: role in myeloma-induced osteoclast formation. *Leukemia* **26**, 1391–1401 (2012).
134. Riquelme, M. A., Cardenas, E. R. & Jiang, J. X. Osteocytes and bone metastasis. *Front. Endocrinol.* **11**, 567844 (2020).
135. Terpos, E., Ntanasis-Stathopoulos, I. & Dimopoulos, M. A. Myeloma bone disease: from biology findings to treatment approaches. *Blood* **133**, 1534–1539 (2019).
136. Pan, T. et al. Cabozantinib reverses renal cell carcinoma-mediated osteoblast inhibition in three-dimensional co-culture in vitro and reduces bone osteolysis in vivo. *Mol. Cancer Ther.* **19**, 1266–1278 (2020).
137. Choueiri, T. K. et al. Cabozantinib versus everolimus in advanced renal cell carcinoma (METEOR): final results from a randomised, open-label, phase 3 trial. *Lancet Oncol.* **17**, 917–927 (2016).
138. Choueiri, T. K. et al. Cabozantinib versus sunitinib as initial targeted therapy for patients with metastatic renal cell carcinoma of poor or intermediate risk: the alliance A031203 CABOSUN Trial. *J. Clin. Oncol.* **35**, 591–597 (2017).
139. Escudier, B. et al. Cabozantinib, a new standard of care for patients with advanced renal cell carcinoma and bone metastases? Subgroup analysis of the METEOR trial. *J. Clin. Oncol.* **36**, 765–772 (2018).
140. Betts-Obregon, B. S. et al. TGFbeta induces BIGH3 expression and human retinal pericyte apoptosis: a novel pathway of diabetic retinopathy. *Eye* **30**, 1639–1647 (2016).
141. Kim, J. E. et al. A TGF-beta-inducible cell adhesion molecule, betaig-h3, is downregulated in melorheostosis and involved in osteogenesis. *J. Cell Biochem.* **77**, 169–178 (2000).
142. Klamer, S. E. et al. BIGH3 modulates adhesion and migration of hematopoietic stem and progenitor cells. *Cell Adh. Migr.* **7**, 434–449 (2013).
143. Ivanov, S. V. et al. Two novel VHL targets, TGFBI (BIGH3) and its transactivator KLF10, are up-regulated in renal clear cell carcinoma and other tumors. *Biochem. Biophys. Res. Commun.* **370**, 536–540 (2008).
144. Thapa, N., Kang, K. B. & Kim, I. S. Beta ig-h3 mediates osteoblast adhesion and inhibits differentiation. *Bone* **36**, 232–242 (2005).
145. Raggatt, L. J. & Partridge, N. C. Cellular and molecular mechanisms of bone remodeling. *J. Biol. Chem.* **285**, 25103–25108 (2010).
146. Tian, E. et al. The role of the Wnt-signaling antagonist DKK1 in the development of osteolytic lesions in multiple myeloma. *N. Engl. J. Med.* **349**, 2483–2494 (2003).
147. D'Alterio, C. et al. Concomitant CXCR4 and CXCR7 expression predicts poor prognosis in renal cancer. *Curr. Cancer Drug Targets* **10**, 772–781 (2010).
148. Pan, J. et al. Stromal derived factor-1 (SDF-1/CXCL12) and CXCR4 in renal cell carcinoma metastasis. *Mol. Cancer* **5**, 56 (2006).
149. Wehler, T. C. et al. Strong expression of chemokine receptor CXCR4 by renal cell carcinoma correlates with advanced disease. *J. Oncol.* **2008**, 626340 (2008).
150. Motzer, R. J., Bander, N. H. & Nanus, D. M. Renal-cell carcinoma. *N. Engl. J. Med.* **335**, 865–875 (1996).
151. Chambers, A., Kundranda, M., Rao, S., Mahmoud, F. & Niu, J. Anti-angiogenesis revisited: combination with immunotherapy in solid tumors. *Curr. Oncol. Rep.* **23**, 100 (2021).
152. Geraets, S. E. W., Bos, P. K. & van der Stok, J. Preoperative embolization in surgical treatment of long bone metastasis: a systematic literature review. *EFORT Open Rev.* **5**, 17–25 (2020).
153. Chan, D. A., Sutphin, P. D., Yen, S. E. & Giaccia, A. J. Coordinate regulation of the oxygen-dependent degradation domains of hypoxia-inducible factor 1 alpha. *Mol. Cell Biol.* **25**, 6415–6426 (2005).
154. Blancher, C., Moore, J. W., Robertson, N. & Harris, A. L. Effects of ras and von Hippel–Lindau (VHL) gene mutations on hypoxia-inducible factor (HIF)-1alpha, HIF-2alpha, and vascular endothelial growth factor expression and their regulation by the phosphatidylinositol 3′-kinase/Akt signaling pathway. *Cancer Res.* **61**, 7349–7355 (2001).
155. Wiesener, M. S. et al. Constitutive activation of hypoxia-inducible genes related to overexpression of hypoxia-inducible factor-1alpha in clear cell renal carcinomas. *Cancer Res.* **61**, 5215–5222 (2001).
156. Ivanyi, P. et al. Does the onset of bone metastasis in sunitinib-treated renal cell carcinoma patients impact the overall survival? *World J. Urol.* **34**, 909–915 (2015).
157. Kalra, S. et al. Outcomes of patients with metastatic renal cell carcinoma and bone metastases in the targeted therapy era. *Clin. Genitourin. Cancer* **15**, 363–370 (2017).
158. Osanto, S. & van der Hulle, T. Cabozantinib in the treatment of advanced renal cell carcinoma in adults following prior vascular endothelial growth factor targeted therapy: clinical trial evidence and experience. *Ther. Adv. Urol.* **10**, 109–123 (2018).
159. Vanharanta, S. et al. Epigenetic expansion of VHL–HIF signal output drives multiorgan metastasis in renal cancer. *Nat. Med.* **19**, 50–56 (2013).
160. Atkinson, E. G. & Delgado-Calle, J. The emerging role of osteocytes in cancer in bone. *JBMR Plus* **3**, e10186 (2019).
161. An, G. et al. Osteoclasts promote immune suppressive microenvironment in multiple myeloma: therapeutic implication. *Blood* **128**, 1590–1603 (2016).
162. Maroni, P. & Bendinelli, P. Bone, a secondary growth site of breast and prostate carcinomas: role of osteocytes. *Cancers* **12**, 1812 (2020).
163. Zhou, M. et al. KLF10 inhibits cell growth by regulating PTTG1 in multiple myeloma under the regulation of microRNA-106b-5p. *Int. J. Biol. Sci.* **16**, 2063–2071 (2020).
164. Delgado-Calle, J. et al. Bidirectional notch signaling and osteocyte-derived factors in the bone marrow microenvironment promote tumor cell proliferation and bone destruction in multiple myeloma. *Cancer Res.* **76**, 1089–1100 (2016).
165. Terpos, E. et al. Circulating activin-A is elevated in patients with advanced multiple myeloma and correlates with extensive bone involvement and inferior survival; no alterations post-lenalidomide and dexamethasone therapy. *Ann. Oncol.* **23**, 2681–2686 (2012).
166. Roussou, M. et al. Increased expression of macrophage inflammatory protein-1alpha on trephine biopsies correlates with extensive bone disease, increased angiogenesis and advanced stage in newly diagnosed patients with multiple myeloma. *Leukemia* **23**, 2177–2181 (2009).
167. Costa, F. et al. Expression of CD38 in myeloma bone niche: a rational basis for the use of anti-CD38 immunotherapy to inhibit osteoclast formation. *Oncotarget* **8**, 56598–56611 (2017).
168. Chung, C. Role of immunotherapy in targeting the bone marrow microenvironment in multiple myeloma: an evolving therapeutic strategy. *Pharmacotherapy* **37**, 129–143 (2017).
169. Favaloro, J. et al. Myeloma skews regulatory T and pro-inflammatory T helper 17 cell balance in favor of a suppressive state. *Leuk. Lymphoma* **55**, 1090–1098 (2014).
170. Pratt, G., Goodyear, O. & Moss, P. Immunodeficiency and immunotherapy in multiple myeloma. *Br. J. Haematol.* **138**, 563–579 (2007).
171. Gagelmann, N. et al. Development of CAR-T cell therapies for multiple myeloma. *Leukemia* **34**, 2317–2332 (2020).
172. Mikhael, J. et al. Treatment of multiple myeloma: ASCO and CCO Joint Clinical Practice Guideline. *J. Clin. Oncol.* **37**, 1228–1263 (2019).
173. D'Oronzo, S., Coleman, R., Brown, J. & Silvestris, F. Metastatic bone disease: pathogenesis and therapeutic options: up-date on bone metastasis management. *J. Bone Oncol.* **15**, 004 (2019).
174. Henry, D. H. et al. Randomized, double-blind study of denosumab versus zoledronic acid in the treatment of bone metastases in patients with advanced cancer (excluding breast and prostate cancer) or multiple myeloma. *J. Clin. Oncol.* **29**, 1125–1132 (2011).
175. Lipton, A. et al. Effect of denosumab versus zoledronic acid in preventing skeletal-related events in patients with bone metastases by baseline characteristics. *Eur. J. Cancer* **53**, 75–83 (2016).
176. Scagliotti, G. V. et al. Overall survival improvement in patients with lung cancer and bone metastases treated with denosumab versus zoledronic acid: subgroup analysis from a randomized phase 3 study. *J. Thorac. Oncol.* **7**, 1823–1829 (2012).
177. Body, J. J. et al. Oral ibandronate improves bone pain and preserves quality of life in patients with skeletal metastases due to breast cancer. *Pain* **111**, 306–312 (2004).
178. De Marinis, F. et al. Bisphosphonate use in patients with lung cancer and bone metastases: recommendations of a European expert panel. *J. Thorac. Oncol.* **4**, 1280–1288 (2009).
179. Dearnaley, D. P., Mason, M. D., Parmar, M. K., Sanders, K. & Sydes, M. R. Adjuvant therapy with oral sodium clodronate in locally advanced and metastatic prostate cancer: long-term overall survival results from the MRC PR04 and PR05 randomised controlled trials. *Lancet Oncol.* **10**, 872–876 (2009).
180. McKay, R. R. et al. Prognostic significance of bone metastases and bisphosphonate therapy in patients with renal cell carcinoma. *Eur. Urol.* **66**, 502–509 (2014).
181. Cronin, K. A., Ries, L. A. & Edwards, B. K. The surveillance, epidemiology, and end results (SEER) program of the national cancer institute. *Cancer* **120** (Suppl. 23), 3755–3757 (2014).
182. Noone, A. M. et al. Cancer incidence and survival trends by subtype using data from the surveillance epidemiology and end results program, 1992–2013. *Cancer Epidemiol. Biomarkers Prev.* **26**, 632–641 (2017).
183. Woodward, E. et al. Skeletal complications and survival in renal cancer patients with bone metastases. *Bone* **48**, 160–166 (2011).
184. Kinnane, N. Burden of bone disease. *Eur. J. Oncol. Nurs.* **11** (Suppl. 2), S28–S31 (2007).
185. Mackiewicz-Wysocka, M., Pankowska, M. & Wysocki, P. J. Progress in the treatment of bone metastases in cancer patients. *Expert. Opin. Investig. Drugs* **21**, 785–795 (2012).
186. Sato, M. et al. Bisphosphonate action. Alendronate localization in rat bone and effects on osteoclast ultrastructure. *J. Clin. Invest.* **88**, 2095–2105 (1991).
187. Hughes, D. E. et al. Bisphosphonates promote apoptosis in murine osteoclasts in vitro and in vivo. *J. Bone Min. Res.* **10**, 1478–1487 (1995).
188. Lacey, D. L. et al. Bench to bedside: elucidation of the OPG-RANK-RANKL pathway and the development of denosumab. *Nat. Rev. Drug Discov.* **11**, 401–419 (2012).

189. Ghajar, C. M. Metastasis prevention by targeting the dormant niche. *Nat. Rev. Cancer* **15**, 238–247 (2015).
190. Risson, E., Nobre, A. R., Maguer-Satta, V. & Aguirre-Ghiso, J. A. The current paradigm and challenges ahead for the dormancy of disseminated tumor cells. *Nat. Cancer* **1**, 672–680 (2020).
191. Barbier, V. et al. Endothelial E-selectin inhibition improves acute myeloid leukaemia therapy by disrupting vascular niche-mediated chemoresistance. *Nat. Commun.* **11**, 2042 (2020).
192. Wang, H. et al. Bone-in-culture array as a platform to model early-stage bone metastases and discover anti-metastasis therapies. *Nat. Commun.* **8**, 15045 (2017).
193. Denefle, T. et al. Thrombospondin-1 mimetic agonist peptides induce selective death in tumor cells: design, synthesis, and structure-activity relationship studies. *J. Med. Chem.* **59**, 8412–8421 (2016).
194. Allen, M. R. & Burr, D. B. Bisphosphonate effects on bone turnover, microdamage, and mechanical properties: what we think we know and what we know that we don't know. *Bone* **49**, 56–65 (2011).
195. Garnero, P., Sornay-Rendu, E., Chapuy, M. C. & Delmas, P. D. Increased bone turnover in late postmenopausal women is a major determinant of osteoporosis. *J. Bone Min. Res.* **11**, 337–349 (1996).
196. Chen, Q. & Massague, J. Molecular pathways: VCAM-1 as a potential therapeutic target in metastasis. *Clin. Cancer Res.* **18**, 5520–5525 (2012).
197. Nakazawa, Y. et al. Periostin blockade overcomes chemoresistance via restricting the expansion of mesenchymal tumor subpopulations in breast cancer. *Sci. Rep.* **8**, 4013 (2018).
198. Estey, E. et al. Use of granulocyte colony-stimulating factor before, during, and after fludarabine plus cytarabine induction therapy of newly diagnosed acute myelogenous leukemia or myelodysplastic syndromes: comparison with fludarabine plus cytarabine without granulocyte colony-stimulating factor. *J. Clin. Oncol.* **12**, 671–678 (1994).
199. Fischer, J. C. et al. Diagnostic leukapheresis enables reliable detection of circulating tumor cells of nonmetastatic cancer patients. *Proc. Natl Acad. Sci. USA* **110**, 16580–16585 (2013).
200. Boyerinas, B. et al. Adhesion to osteopontin in the bone marrow niche regulates lymphoblastic leukemia cell dormancy. *Blood* **121**, 4821–4831 (2013).
201. Becker, P. S. et al. Clofarabine with high dose cytarabine and granulocyte colony-stimulating factor (G-CSF) priming for relapsed and refractory acute myeloid leukaemia. *Br. J. Haematol.* **155**, 182–189 (2011).
202. US National Library of Medicine. *ClinicalTrials.gov* https://clinicaltrials.gov/ct2/show/NCT03292536?term=NCT03292536&draw=2&rank=1 (2021).
203. Soriano, P., Montgomery, C., Geske, R. & Bradley, A. Targeted disruption of the c-src proto-oncogene leads to osteopetrosis in mice. *Cell* **64**, 693–702 (1991).
204. Furuyama, N. & Fujisawa, Y. Regulation of collagenolytic protease secretion through c-Src in osteoclasts. *Biochem. Biophys. Res. Commun.* **272**, 116–124 (2000).
205. Murali, B. et al. Inhibition of the stromal p38MAPK/MK2 pathway limits breast cancer metastases and chemotherapy-induced bone loss. *Cancer Res.* **78**, 5618–5630 (2018).
206. Nyman, J. S. et al. Combined treatment with a transforming growth factor beta inhibitor (1D11) and bortezomib improves bone architecture in a mouse model of myeloma-induced bone disease. *Bone* **91**, 81–91 (2016).
207. Cole, L. E., Vargo-Gogola, T. & Roeder, R. K. Targeted delivery to bone and mineral deposits using bisphosphonate ligands. *Adv. Drug Deliv. Rev.* **99**, 12–27 (2016).
208. Farrell, K. B., Karpeisky, A., Thamm, D. H. & Zinnen, S. Bisphosphonate conjugation for bone specific drug targeting. *Bone Rep.* **9**, 47–60 (2018).
209. Tian, Z. et al. Harnessing the power of antibodies to fight bone metastasis. *Sci. Adv.* **7**, eabf2051 (2021).
210. Schmid, P. et al. Atezolizumab and Nab-paclitaxel in advanced triple-negative breast cancer. *N. Engl. J. Med.* **379**, 2108–2121 (2018).
211. Beer, T. M. et al. Randomized, double-blind, phase III trial of ipilimumab versus placebo in asymptomatic or minimally symptomatic patients with metastatic chemotherapy-naive castration-resistant prostate cancer. *J. Clin. Oncol.* **35**, 40–47 (2017).
212. Jiao, S. et al. Differences in tumor microenvironment dictate T helper lineage polarization and response to immune checkpoint therapy. *Cell* **179**, 1177–1190 e1113 (2019).
213. Italiano, A. et al. Tazemetostat, an EZH2 inhibitor, in relapsed or refractory B-cell non-Hodgkin lymphoma and advanced solid tumours: a first-in-human, open-label, phase 1 study. *Lancet Oncol.* **19**, 649–659 (2018).
214. Yoneda, T., Sasaki, A. & Mundy, G. R. Osteolytic bone metastasis in breast cancer. *Breast Cancer Res. Treat.* **32**, 73–84 (1994).
215. Corey, E. et al. Establishment and characterization of osseous prostate cancer models: intra-tibial injection of human prostate cancer cells. *Prostate* **52**, 20–33 (2002).
216. Yu, C. et al. Intra-iliac artery injection for efficient and selective modeling of microscopic bone metastasis. *J. Vis. Exp.* https://doi.org/10.3791/53982 (2016).
217. Kuchimaru, T. et al. A reliable murine model of bone metastasis by injecting cancer cells through caudal arteries. *Nat. Commun.* **9**, 2981 (2018).
218. Medina, D. The mammary gland: a unique organ for the study of development and tumorigenesis. *J. Mammary Gland Biol. Neoplasia* **1**, 5–19 (1996).
219. Sflomos, G. et al. A preclinical model for ERalpha-positive breast cancer points to the epithelial microenvironment as determinant of luminal phenotype and hormone response. *Cancer Cell* **29**, 407–422 (2016).
220. Sato, N. et al. A metastatic and androgen-sensitive human prostate cancer model using intraprostatic inoculation of LNCaP cells in SCID mice. *Cancer Res.* **57**, 1584–1589 (1997).
221. Valta, M. P. et al. Development of a realistic in vivo bone metastasis model of human renal cell carcinoma. *Clin. Exp. Metastasis* **31**, 573–584 (2014).
222. Kashtan, H. et al. Intra-rectal injection of tumour cells: a novel animal model of rectal cancer. *Surg. Oncol.* **1**, 251–256 (1992).
223. Sakamoto, S. et al. New metastatic model of human small-cell lung cancer by orthotopic transplantation in mice. *Cancer Sci.* **106**, 367–374 (2015).
224. Martin, C. K. et al. Zoledronic acid reduces bone loss and tumor growth in an orthotopic xenograft model of osteolytic oral squamous cell carcinoma. *Cancer Res.* **70**, 8607–8616 (2010).
225. Pinho, S. & Frenette, P. S. Haematopoietic stem cell activity and interactions with the niche. *Nat. Rev. Mol. Cell Biol.* **20**, 303–320 (2019).
226. Crane, G. M., Jeffery, E. & Morrison, S. J. Adult haematopoietic stem cell niches. *Nat. Rev. Immunol.* **17**, 573–590 (2017).
227. Mendez-Ferrer, S. et al. Bone marrow niches in haematological malignancies. *Nat. Rev. Cancer* **20**, 285–298 (2020).
228. Sivaraj, K. K. & Adams, R. H. Blood vessel formation and function in bone. *Development* **143**, 2706–2715 (2016).
229. Kusumbe, A. P., Ramasamy, S. K. & Adams, R. H. Coupling of angiogenesis and osteogenesis by a specific vessel subtype in bone. *Nature* **507**, 323–328 (2014).
230. Park, D. et al. Endogenous bone marrow MSCs are dynamic, fate-restricted participants in bone maintenance and regeneration. *Cell Stem Cell* **10**, 259–272 (2012).
231. Logan, M. et al. Expression of Cre Recombinase in the developing mouse limb bud driven by a Prxl enhancer. *Genesis* **33**, 77–80 (2002).
232. Greenbaum, A. et al. CXCL12 in early mesenchymal progenitors is required for haematopoietic stem-cell maintenance. *Nature* **495**, 227–230 (2013).
233. Pinho, S. et al. PDGFRalpha and CD51 mark human nestin+ sphere-forming mesenchymal stem cells capable of hematopoietic progenitor cell expansion. *J. Exp. Med.* **210**, 1351–1367 (2013).
234. Sugiyama, T., Kohara, H., Noda, M. & Nagasawa, T. Maintenance of the hematopoietic stem cell pool by CXCL12–CXCR4 chemokine signaling in bone marrow stromal cell niches. *Immunity* **25**, 977–988 (2006).
235. Baccin, C. et al. Combined single-cell and spatial transcriptomics reveal the molecular, cellular and spatial bone marrow niche organization. *Nat. Cell Biol.* **22**, 38–48 (2020).
236. Acar, M. et al. Deep imaging of bone marrow shows non-dividing stem cells are mainly perisinusoidal. *Nature* **526**, 126–130 (2015).
237. Bruns, I. et al. Megakaryocytes regulate hematopoietic stem cell quiescence through CXCL4 secretion. *Nat. Med.* **20**, 1315–1320 (2014).
238. Heazlewood, S. Y. et al. Megakaryocytes co-localise with hemopoietic stem cells and release cytokines that up-regulate stem cell proliferation. *Stem Cell Res.* **11**, 782–792 (2013).
239. Olson, T. S. et al. Megakaryocytes promote murine osteoblastic HSC niche expansion and stem cell engraftment after radioablative conditioning. *Blood* **121**, 5238–5249 (2013).
240. Zhao, M. et al. Megakaryocytes maintain homeostatic quiescence and promote post-injury regeneration of hematopoietic stem cells. *Nat. Med.* **20**, 1321–1326 (2014).
241. Quarta, G., Cattaneo, C. & D'Elia, M. Determining 14C content in different human tissues: implications for application of 14C bomb-spike dating in forensic medicine. *Radiocarbon* **55**, 1845–1849 (2013).
242. Rodan, G. A. Bone homeostasis. *Proc. Natl Acad. Sci. USA* **95**, 13361–13362 (1998).
243. Ribot, C. et al. Obesity and postmenopausal bone loss: the influence of obesity on vertebral density and bone turnover in postmenopausal women. *Bone* **8**, 327–331 (1987).
244. Compston, J. E. et al. Obesity is not protective against fracture in postmenopausal women: GLOW. *Am. J. Med.* **124**, 1043–1050 (2011).
245. Krakauer, J. C. et al. Bone loss and bone turnover in diabetes. *Diabetes* **44**, 775–782 (1995).
246. Einhorn, T. A. & Gerstenfeld, L. C. Fracture healing: mechanisms and interventions. *Nat. Rev. Rheumatol.* **11**, 45–54 (2015).
247. Schell, H. et al. The haematoma and its role in bone healing. *J. Exp. Orthop.* **4**, 5 (2017).
248. Bidwell, B. N. et al. Silencing of Irf7 pathways in breast cancer cells promotes bone metastasis through immune escape. *Nat. Med.* **18**, 1224–1231 (2012).
249. Dobrolecki, L. E. et al. Patient-derived xenograft (PDX) models in basic and translational breast cancer research. *Cancer Metastasis Rev.* **35**, 547–573 (2016).
250. Hoffman, R. M. Patient-derived orthotopic xenografts: better mimic of metastasis than subcutaneous xenografts. *Nat. Rev. Cancer* **15**, 451–452 (2015).
251. Wang, D. et al. Isolation and characterization of MC3T3-E1 preosteoblast subclones with distinct in vitro and in vivo differentiation/mineralization potential. *J. Bone Min. Res.* **14**, 893–903 (1999).
252. Qiao, H. & Tang, T. Engineering 3D approaches to model the dynamic microenvironments of cancer bone metastasis. *Bone Res.* **6**, 3 (2018).

Acknowledgements
The authors thank H. Chan and L. Michie for editing the manuscript. X.H.-F.Z. is supported by US Department of Defense DAMD W81XWH-16-1-0073, DAMD W81XWH-20-1-0375, NCI R01CA183878, NCI R01CA251950, NCI R01CA221946, NCI R01CA227904, NCI U01CA252553, Breast Cancer Research Foundation and McNair Foundation. R.L.S. is supported by US DOD KCRP W81XWH-20-1-0895, and UT MD Anderson Cancer Center Knowledge Gap Award and Institutional Research Grant.

Author contributions
The authors contributed equally to all aspects of the article.

Competing interests
The authors declare no competing interests.

Peer review information
Nature Reviews Cancer thanks the anonymous reviewers for their contribution to the peer review of this work.

Publisher's note
Springer Nature remains neutral with regard to jurisdictional claims in published maps and institutional affiliations.